Université Lille 1 – Sciences et Technologies
Ecole Doctoral : Sciences de La Matière, du Rayonnement et de l’Environnement

Ph.D THESIS
Presented by
Eric OSEI-AGYEMANG
For obtention of the title of
DOCTOR
Specialty: Molecules and Condensed Matter

MODELING REACTIVITY AND FUNCTIONALIZATION OF ZrC/ZrO_2 SURFACES AND INTERFACES EN-ROUTE TO SYNTHESIS OF ZrC/SiC NANOCOMPOSITES

Thesis supervised by Sylvain CRISTOL
Defense on 4th Ocotober 2016 before the jury composed of

Referees : M **Pascal RAYBAUD**, (Researcher) IFP-Energie Nouvelles
Mme **Geneviève POURROY**, (Director of Research), CNRS/ IPCMS
Examiners : M **Philippe CARREZ**, (Professor), Université de Lille 1
M **Alexis MARKOVITS**, (Professor), UPMC
Supervisor : M **Sylvain Cristol** (Professor), UCCS- Université de Lille 1
Co-Supervisor : M **Romain Lucas** (Assistant Professor), Université de Limoges

Résumé

Le carbure de zirconium (ZrC) est une céramique non oxyde utilisée dans l'industrie nucléaire et aéronautique. Cependant, ses excellentes propriétés mécaniques et physiques sont entravées par la formation d'oxydes à des températures de 500 à 600 ° C. Il est ainsi nécessaire de protéger la surface de ZrC avec d'autres matériaux tels que du carbure de silicium (SiC). La théorie de la fonctionnelle de la densité (DFT) combinée à une approche thermodynamique a été utilisé pour étudier la structure, les propriétés et la réactivité des différentes surfaces de ZrC en vue de leurs fonctionnalisation. La stabilité des différentes surfaces à faible indice de ZrC a été étudiée afin de déterminer les surfaces exposées lors de la fonctionnalisation et le revêtement avec le SiC. Une étude préliminaire de la réactivité de petites molécules inorganiques telles que H_2O, O_2 et H_2 a été effectuée. Ensuite, les propriétés des surfaces dans une atmosphère oxydante ont été modélisées pour développer des modèles pour les surfaces oxydées et les différents types de couches d'oxyde exposées. Plusieurs techniques expérimentales ont été combinées avec les études théoriques pour valider ces modèles. La Fonctionnalisation de ZrC a ensuite en partant des différents modèles de surfaces oxydées. Différentes molécules organiques ont été testées pour la fonctionnalisation. Les molécules utilisées classiquement telles que le 3-bromopropyne et le chloro-allylediméthylsilane interagissant très peu avec la surface, nous avons proposé l'acide 3-buténoïque comme molécule qui se lie très fortement à la surface tout en montrant une très réactivité très intéressante vis à vis du diphénylsilane qui est le précurseur de SiC (après une étape de pyrolyse).

Summary

ZrC is a non-oxide ceramic applied in the nuclear and aerospace industries but the excellent mechanical and physical properties are hampered by formation of low refractory oxides at temperatures of 500-600 ^{o}C. A need exists for coating the surface with other materials like SiC. Density functional theory (DFT) combined with thermodynamic modelling was used for this study. Stabilities of the various low index surfaces of ZrC are studied to determine the appropriate surfaces for coating with SiC. A preliminary study of reactivity of small inorganic molecules such as H_2O, O_2, and H_2 is carried out. The properties of ZrC surfaces towards

oxidation is then studied to develop proper models and understanding of the different types of oxide layers exhibited at real oxidizing conditions. Several experimental techniques were combined with the theoretical studies to analyse the oxide layers formed on ZrC surfaces. Mechanical and thermodynamic models were developed to characterize the interface formed between ZrC surfaces and the oxide layer. Functionalization of ZrC was finally carried out on the exposed facets of the oxidized ZrC. The functionalized surfaces were first grafted with 3-bromo propyne and allyl(chloro)dimethylsilane followed by hydrosilylation in a grafting-to approach from diphenylsilane and 1,4-diethynylbenzene monomers (these two monomers form a polymer macromolecule). The resulting particles are finally subjected to laser pyrolysis to yield the resulting ZrC/SiC core/shell nanocomposites. The use of H_2O as functionalizing group however did not yield grafted polymer units and hence a dual functional group organic molecule (3-butenoic acid) was used to yield the desired ZrC/SiC nanocomposites.

Remerciements

Je voudrais exprimer ma sincère gratitude à tous les étudiants des cycles supérieurs et tous les travailleurs sous la direction du professeur Sylvain Cristol. Tout d'abord, je suis très reconnaissant au professeur Cristol de m'avoir impliqué dans ce projet depuis ma deuxième année du programme de master ASC (Advanced Spectroscopy in Cemistry).

Cette implication avant la date prévue du début de projet, m'a permis d'acquérir les importantes notions fondamentales en chimie théorique, notamment les méthode de calcul *ab-initio* et de mettre en pratique toutes ces notions. Cela m'a également constitué une base de connaissance qui m'était utile par la suite durant la formation sur les outils de base utilisé dans ce projet telle que les logiciels de calculs.

En fait, sans cette participation au début du projet, je doute que je l'aurais eu toutes les compétences et les connaissances pour ce projet dans le temps pour une mise en œuvre réussie de la procédure prévue de ce travail. En effet, sans cette implication, je doute avoir eu toutes les compétences et le savoir-faire aussi rapidement pour la réussite de ce projet. De plus, je tiens a noter que l'aide du Pr. cristol, m'a permis de sentir la présence d'un père et de famille que je n'ai_ pas eu en France. Sans son soutien et ses conseils, j'aurais surement eu à affronter à beaucoup de difficultés à vivre en France. Je lui exprime ma grande reconnaissance

Les appréciations ne peuvent pas passer sans mentionner l'énorme contribution et une aide obtenue à partir de la tête du groupe 'modélisation spectroscopique' de l'Unité de Catalyse et de Chimie du Solide, Université Lille 1 (Professeur Jean-François Paul). Durant les moments où j'ai eu besoin d'aide, il m'a toujours guidé dans les étapes nécessaires dans la réalisation des plusieurs points. Je voudrais mentionner que beaucoup de fois que je n'ai pas de voie à suivre, il a été le seul à proposer des idées et des procédures pour mettre en place ce qui la plupart du temps a donné lieu à des résultats qui n'étaient pas prévu. Il a également été un acteur majeur qui a co-supervisé, relus, corrigés et contribué à toutes les publications évaluées de ce projet.

Je remercie tous les autres membres (étudiants, chercheurs et professeurs) du groupe de spectroscopie et de la modélisation, Unité de Catalyse et Chimie du Solide, comme Asma Tougerti pour fournir une assistance en cas de besoin, Anne-Sophie Mamede pour sa collaboration avec des caractérisations expérimentales de surfaces ZrC , Nicolas Nuns pour ses contributions sur l'analyse TOF-SIMS sur les particules ZrC oxydées, Dimitri Blank, Mireile Makhoul et Houssam Hijazi pour leur aide et assistance en cas de besoin.

Mes sincères remerciements vont aussi à tous le docteur en philosophie (PhD) et les étudiants dans le bureau 005 du bâtiment C3, Université Lille 1, plus précisément Marie Guehl, Marine Gaillard, Soraya Zaid et Guillaume Pomalaza pour leur aide à chaque fois que je me débattais avec les questions liées au Francais.

Dr. Romain Lucas du Centre Européen de la Céramique, Limoges a énormément contribué à la réalisation de ce projet grâce à ses conseils et son assistance. Je voudrais le remercier pour son soutien et le mentorat pendant mon temps à Limoges et de m'avoir aider à ce familiariser avec les différents procédés de synthèse pour obtenir les nano-particules ZrC. Sans ses arrangements et son l'assistance, j'aurai prouvé des difficultés avec l'hébergement durant la semaine passée à Limoges. Il a également été très utile dans la relecture et co-auteur de toutes les revues par les pairs des articles publiés à la suite de ce travail. Ma gratitude ne peut pas contourner le Centre Européen de la Céramique sans mentionner le professeur Sylvie Foucaud qui a également été utile dans la réalisation du succès obtenu dans ce projet. Comme auteru principal de ce projet, elle a coordonné et conçu la planification globale, la direction et l'exécution de ce projet à la réussite atteinte.

Je remercie tous les autres membres de ce projet multi-institutionnel dont la contribution m'a aidé à la réalisation de tous les résultats présentés dans cette écriture. Dr. Florence Babonneau et Cristina Coelho du Laboratoire de chimie de la matiére condensée de Paris (LCMCP) au ParisTech du Collège de France ont contribué à la caractérisation RMN des précurseurs et des surfaces polymères. En outre, je voudrais exprimer ma gratitude à Yann Leconte du Laboratoire Francis Perrin (LFP), CEA Saclay qui a effectué toutes les analyses de pyrolyse laser de la céramique de polymère en suspension. Je vous remercie de leurs discussions et sens de l'humour pendant les périodes de réunion entre les différents groupes de ce projet.

Enfin, ma profonde gratitude et mes sincères remerciements vont à toute ma famille qui m'ont soutenu et encouragé pour repousser les limites de mes capacités académiques. Ma mère, Dorcas Addai a toujours été la personne qui m'a soutenu durant les moments difficiles de mon voyage. Je la remercie pour l'amour, les soins, l'orientation et l'encouragement qui m'a amené à ce niveau d'éducation. Mes frères et sœurs Evelyn Addo, Anita Osei Wilson, Darlene Osei-Owusu, Sharon

Osei-Owusu, Nana Ansah Osei-Owusu et Cindy Marilyn Osei me ont tous appuyé la façon la plus aimante et attentionnée nécessaire pour une réussite de ce projet. Je ne peux pas quitter ma belle-mère Lydia Osei qui m'a montré amour et soins tout au long de ces années. Je suis très reconnaissant à mon père George Kwame Osei pour le montant de la pression soutenue il a continué à me lancer dans un programme de doctorat quand je pensais autrement. Son constant soutien, l'amour, les soins et l'orientation m'a toujours motivé. Ma femme Nana Yaa Owusu Agyapomaa a été toujours disponible pendant mes études. Je suis très reconnaissant et reconnaissante de ne pas avoir provoqué des problèmes familiaux qui pourraient avoir entravé les progrès de mon travail académique. Elle a été d'un grand secours en termes de soutien et d'encouragement.

Acknowledgements

I would like to express my sincere gratitude to all graduate students and all workers under the supervision of Professor Sylvain Cristol. First and foremost, I am very grateful to Professor Cristol for involving me in this project right from the beginning of my second year Master of Science degree program. This early involvement in this project prior to the stipulated and assigned date for commencement of the project granted me platform to learn the basic and most important theoretical, practical skills and knowledge in ab-initio simulation techniques. This stage also laid the foundation for me to learn all most of the ideas implemented in the software packages used for this project. In fact without this early involvement in the project, I doubt I would have had all the skills and knowledge for this project in time for a successful implementation of the planned procedure of this work. Moreover, aside being my supervisor, he has been the father and family I did not have in France. He has been very helpful in all aspects of my living in France. Without his support and guidance, I would have faced a lot of difficulties living in France. I give him the highest gratitude.

The appreciations cannot go by without mentioning the enormous contribution and help obtained from the head of the spectroscopy and modelling group of the Unité de Catalyse et Chimie du Solide, Université Lille 1 (Professor Jean-François Paul). In times when I needed assistance and my supervisor is on other duties, he has always been my go-to mentor who always guided me with the necessary steps forward in realizing the tasks ahead of me. I would like to mention that many times that I do not have an idea of way forward, he has been the one to suggest different ideas and procedures to try which mostly resulted in results that were not anticipated before. He has also been a major player who has co-supervised, proof-read, corrected and contributed to all the peer-reviewed publications that resulted from this project.

I thank all the other members (students, researchers and professors) of the spectroscopy and modelling group, Unité de Catalyse et Chimie du Solide such as Asma Tougerti for providing assistance whenever needed, Anne-Sophie Mamede for her collaboration with experimental characterizations of ZrC surfaces, Nicolas Nuns for his contributions on ToF-SIMS analysis on the oxidized ZrC particles, Dimitri Blank, Mireile Makhoul and Houssam Hijazi for their help and assistance whenever needed.

My sincere gratitude also goes to all the doctor of philosophy (PhD) students in bureau 005 of bâtiment C3, Université Lille 1, more specifically Marie Guehl, Marine Gaillard, Soraya Zaid and Guillaume Pomalaza for their help whenever I struggled with issues related to the French language.

Dr. Romain Lucas of the Centre Européen de la Céramique, Limoges has contributed enormously to the completion of this project through his guidance and assistance. I would like to thank him for his support and mentorship during my time at Limoges to familiarize myself with the various synthesis procedures for obtaining ZrC nano-particles. Without his arrangements and ever-present assistance, I would have struggled with accommodation and general up-keep for the one week period spent in Limoges. He has also been very helpful in proof-reading and co-authoring all the peer reviewed articles published as a result of this work. My gratitude cannot by-pass the Centre Européen de la Céramique without mentioning Professor Sylvie Foucaud who has also been helpful for realizing the success achieved in this project. As the Lead scientist of this project, she has coordinated and engineered the overall planning, direction and execution of this project to the current success achieved.

I thank all the other members of this multi-institutional project whose contribution has aided me in achieving all the results presented in this writing. Dr. Florence Babonneau and Cristina Coelho of Laboratoire de chimie de la matiére condensée de Paris (LCMCP) at the Collège de France – chimie ParisTech contributed in the NMR characterization of polymer precursors and surfaces. Additionally, I would like to extend my gratitude to Yann Leconte of the Laboratoire Francis Perrin (LFP), CEA Saclay who carried out all the laser pyrolysis analysis of the polymer suspended ceramics. I appreciate their discussions and sense of humor during the meeting periods amongst the various groups of this project.

Lastly, my heartfelt gratitude and sincere appreciation goes to my entire family whose support and encouragements motivated me at all times to push the boundaries of my academic abilities and prowess. My mother, Dorcas Addai has always been rock I could lean on during difficult times of my educational journey. I thank her for the love, care, guidance and encouragement that has brought me to this level of education. My siblings Evelyn Addo, Anita Osei Wilson, Darlene Osei-Owusu, Sharon Osei-Owusu, Nana Ansah Osei-Owusu and Cindy Marilyn Osei have all supported me in the most loving and caring fashion needed for a successful completion of this project. I cannot leave out my step-mother Lydia Osei who has showed me love and care throughout these

years. I am very grateful to my father George Kwame Osei for the amount of sustained pressure he kept on me to embark on a PhD program when I was thinking otherwise. His constant support, love, care and guidance has always motivated me. My wife Nana Yaa Owusu Agyapomaa has been very supportive and always available during my studies. I am very grateful and appreciative of her not giving me family problems that could have hinder the progress of my academic work. She has been of immense help in terms of support and encouragement.

Contents

Table of Contents

General Introduction

Transition metal carbides (TMC) are highly important ceramic materials with a wide range of applications. These materials are characterized by high hardness, high melting point, electrical conductivity and high strength. These excellent physical and mechanical properties renders them very useful in a wide range of applications. Due to their hardness, TMC materials can be used as drills and other tools that need to be abrasion resistant. Nanostructured TMC materials are also used in metallurgical, chemical and the aviation industries. They also find applications in the textile industry in making thermostat textiles in nylon, fiber. Majority of these materials have oxidation resistance at high temperatures, typically above 1400 ^{o}C.

Owing to the above mentioned properties, TMC's find applications in the nuclear industry where they are employed as nuclear reactor linings. Their applications in high temperature nuclear applications takes advantage of their favorable thermal and mechanical properties.[1] Zirconium Carbide (ZrC) among the TMC's has recently been considered as a structural and fission product barrier coating material for tri-isotropic (TRISO) coated nuclear fuel used in high temperature reactors (HTR's) for replacement or as an addition to the currently used silicon carbide (SiC) material.[2]–[4] The attractiveness for the use of ZrC in high temperature nuclear fuel material is due to its high melting point of more than 3400 ^{o}C as well as its resistance to fission product attack, low neutron absorption cross-sections and high thermal conductivity at extremely high temperatures.[1] ZrC satisfies a lot of property criteria for TRISO coatings. This makes it a good candidate material for high power density HTR fuels operating at temperatures above 1870 K which is considered as a limit for SiC used as TRISO coatings.[2]–[4] Various studies on ZrC as TRISO coatings has also shown minimal failure rate and superior fission product retention capabilities under various irradiation conditions.[2]–[4] Starting in the late 1970s, ZrC was demonstrated as a fuel coating for high temperature gas-cooled reactors (HTGR's) with a recent increase in interest in Japanese and US HTGR programs.[5] It should be noted that, the properties of the TMC composites depends strongly on the composition and microstructural homogeneity of the material.

Unlike SiC, ZrC is prone to oxidation at relatively low temperatures. ZrC is known to be susceptible to rapid oxidation depending on temperature, porosity, partial pressure of oxidative and reductive species from the reaction, carbon content and impurities.[6]–[8] Oxidation of ZrC does not occur at room temperature but takes place and leads to spallation at elevated temperatures above 870 K especially in high oxygen partial pressure environments[8], [9]. This spallation is due to the formation of weakly protective low refractory oxides.[10] The oxidation initiates at temperatures close to 550 K at low oxygen partial pressures (1-50 kPa)[11]. Significant oxidation has been observed above 970 K [6]. Formation of this oxide layer causes serious deterioration to the excellent physical and mechanical properties of ZrC. In order to overcome this, it is necessary to consider its alliance with a compound that forms a protective oxide layer in an oxidizing environment. No method of control of oxidation against systems of ZrC has been described. SiC however meets this requirement. SiC forms a protective layer of silica at temperatures above 1400 ^{o}C. It is also possible to consider the association of the oxidation products of SiC and ZrC, i.e. formation of $ZrSiO_4$[12]. With this approach, a composite material can be formed with SiC forming a protective shell around ZrC against oxidation while maintaining the excellent physical and mechanical properties of ZrC for applications in the nuclear industry.

For taking advantage of the oxidation protection of SiC, it has been proposed to use a pre-ceramic polymer for the SiC. Currently, SiC ceramics derived from polymers are known for their outstanding properties at high temperatures[13], [14]. The conventional method for producing ZrC/SiC composites is to use conventional powders of SiC and Zr which are mixed and then sintered. However, a problem with this method arises from the step of homogenization of the powder mixture and hence the pre-ceramic precursor route can be exploited [15], [16]. A recent preparation of ZrC/SiC composite has been achieved by the Laboratoire Science des Procédés Céramiques et de Traitements de Surface (SPCTS) in Limoges through coating of the pre-ceramic polymer SiC on the ZrC particles. This study has showed the interaction between the vinyl groups of polycarbosilane (PCS) and metallic zirconium in ZrC[17]. Thus the affinity of the vinyl groups on the ZrC surface has been exploited for the synthesis of polyvinylsilanes which allows improved microstructural homogeneity of the resulting composites[17]. However, the nature of the grafting of the polymer precursor of SiC on ZrC has not yet been addressed. As such, it is necessary to study the grafting of organic or covalent polymers onto the inorganic surface and follow the mechanisms of transformation of the ceramic material during pyrolysis. Additionally, strategies to promote strong interaction between the ceramic particles and the polymeric coating has to be developed.

In order to develop specific reactivity of the surface organic precursors, a prior step of modification of the inorganic ZrC particle surface is needed. For ZrC the available surface modification in the literature is oxidation[18]. Previous works have studied the adsorption of H_2O and methanol on single crystal oxygen modified ZrC, particularly on the surfaces (100) or (111) and XPS revealed formation of OH groups[19], [20]. Candidate molecules that can generate functionalization of the surface include H_2O, NH_3 and the radicals of azo initiators[21].

It is clear that no attempts have been made to provide control for the oxidation of ZrC nano particles in order to take advantage of its excellent mechanical and physical properties. In this context, there is the justification for carrying out such project. In this project, we aim at developing methods of control for ZrC oxidation. Our approach is to coat the surface of ZrC with another ceramic material, SiC which forms a protective layer at the temperatures at which ZrC easily oxidizes. The method we wish to develop here is first to study the surface properties and stabilities of the ZrC and then subsequently functionalize the surfaces with a modifying group that can be used for further grafting. A polymer precursor is then grafted onto the functional groups available from the molecules used in modifying the ZrC surface. In this respect, we intend to make use of modifying agents that satisfy such requirements. The organic polymer precursor used contains Si that can be utilized in forming the protective layer on the ZrC. In a final step, laser pyrolysis will be used to convert the polymer into SiC with residual carbon.

This project is therefore a bi-directional project which combines both experiments with theoretical studies for guidance and validations. Our part is to model the surface properties of ZrC, surface stabilities, surface reactions, surface modification, grafting of polymer precursors and interface between ZrC and SiC.

Chapter I is dedicated to a presentation on the current theoretical and experimental data on ZrC. A presentation on the current application areas of ZrC will be made. This review chapter will also present data on all current and available studies on the solid and bulk properties of ZrC. A part of this chapter will include the up to date review on the oxidation process of ZrC which leads to the formation of oxide layers on the surface. A survey of the available data on reduction of ZrC will be presented in addition to the current available data on the surface modification of ZrC nano particles with H_2O and other functional groups. In another part, a review of ZrO_2 formed on ZrC surfaces will be presented. A section on the grafting of polymeric precursors on ceramic surfaces and the current state of the art routes in achieving ceramic coatings on other ceramics through the organic precursors will be given.

Chapter II presents the theories and methodology used for this project. An account on the theory of many-body physics is given. In another section, Hartree-Fock theory is presented followed by post Hartree-Fock treatments. Density functional theory (DFT) is also presented in this chapter as well as ab-initio molecular dynamics method and atomistic thermodynamic treatments are discussed.

Chapter III will provide details analysis on the bulk and defect properties of ZrC. This chapter includes a section on obtaining accurate bulk parameters such as lattice parameter and bulk modulus as well as the elastic constants of ZrC. An insight into the formation and stability of point defects in ZrC will also be presented.

In chapter IV presents all studies done on the surface ZrC including stability of all low index surfaces, adsorption and reactivity of small molecules on the surfaces. This chapter is divided into three parts comprising three separate fully published articles. This first part gives a complete account on the oxidation of all the low index of ZrC is presented. This account is entailed in a fully published article entitled "*Oxidation and Equilibrium Morphology of Zirconium Carbide Low Index Surfaces Using DFT and Atomistic Thermodynamic Modeling*" and is published in **J. Phys. Chem. C,** 2016, 120, 8759−8771(DOI: 10.1021/acs.jpcc.6b01460).

The second part of chapter IV presents the reactivity of small molecules such as O_2, H_2 and H_2O on ZrC(100) surface. This part is presented as a fully published article as it contains all data on methodology, results, discussions and conclusions. This article is published entitled "*Periodic DFT and Atomistic Thermodynamic Modeling of Reactivity of H_2, O_2, and H_2O Molecules on Bare and Oxygen Modified ZrC (100) Surface*" in **J. Phys. Chem. C,** 2014, 118, 12952−12961(DOI: 10.1021/jp503208n).

The last part of chapter IV presents hydration and equilibrium morphology of ZrC(111) and ZrC(110) surfaces. This section consists of a fully published article entitled "*Stability, equilibrium morphology and hydration of ZrC(111) and (110) surfaces with H_2O: a combined periodic DFT and atomistic thermodynamic study*". The article is published in **Phys. Chem. Chem. Phys,** 2015, 17, 21401(DOI: 10.1039/c5cp03031e)

Chapter V is dedicated to all interfacial studies and it is divided into two parts. The first part provides studies on the interface between ZrC(100) and *c*-ZrO_2(100). This part is made up of a full article which is under review. The article is entitled "*Structure and Energetics of ZrC(100)||c-*ZrO_2*(001) interface: A Combination of Experiments, Finite Temperature Molecular Dynamics, Periodic DFT and Atomistic Thermodynamic Modeling*". The article is to be published in American Chemical Society, the **Journal of Applied materials and interfaces**. The article includes experimental analysis of oxidized ZrC nanoparticles using X-ray Photoemission Spectroscopy (XPS), Time of Flight Secondary Ion Mass Spectrometry (ToF-SIMS), Transmission Electron Microscopy Electron Diffraction (TEM-ED) for characterizing the oxide layer ontop of ZrC particles. A finite temperature molecular dynamics simulation was also used to gain more insight on the build-up of an oxide layer on the ZrC surface and DFT analysis combined with atomistic thermodynamics to characterize the ZrC||*c*-ZrO_2 interface.

The second part of chapter V provides studies on the characterization of ZrC(111) and *c*-ZrO_2(111) interface. The section is made up a full article which is under review. The article is entitled "*Characterizing the ZrC(111)//c-*ZrO_2*(111) Hetero-ceramic Inter-face: A First Principles DFT and Atomistic Thermodynamic Modeling*" and is to be published in American Chemical Society, the **Journal of Applied materials and interfaces.**

In chapter VI, the final part of this project is presented. In this chapter, studies on the functionalization of ZrC//ZrO_2 surfaces with organic molecules and subsequent grafting of polymeric precursors on the functionalized surface. This chapter is presented as a full article which is under review for publication.

In the last chapter, a general conclusion which links all parts of the project together is presented. This conclusion part starts with the general properties of ZrC through the studies on stabilities and functionalization of the surfaces to the grafting of polymeric precursors on the surface and final perspectives.

References

[1] Y. Katoh, G. Vasudevamurthy, T. Nozawa, and L. L. Snead, “Properties of zirconium carbide for nuclear fuel applications,” *J. Nucl. Mater.*, vol. 441, no. 1–3, pp. 718–742, Oct. 2013.

[2] G. H. Reynolds, J. C. Janvier, J. L. Kaae, and J. P. Morlevat, “Irradiation behavior of experimental fuel particles containing chemically vapor deposited zirconium carbide coatings,” *J. Nucl. Mater.*, vol. 62, no. 1, pp. 9–16, Oct. 1976.

[3] K. Minato, T. Ogawa, K. Fukuda, H. Nabielek, H. Sekino, Y. Nozawa, and I. Takahashi, “Fission product release from ZrC-coated fuel particles during postirradiation heating at 1600°C,” *J. Nucl. Mater.*, vol. 224, no. 1, pp. 85–92, Jul. 1995.

[4] T. Ogawa and K. Ikawa, *High Temp. Sci*, vol. 22, pp. 179–192, 1986.

[5] K. Sawa and S. Ueta, “Research and development on HTGR fuel in the HTTR project,” *Nucl. Eng. Des.*, vol. 233, no. 1–3, pp. 163–172, Oct. 2004.

[6] R. F. Voitovich and É. A. Pugach, “High-temperature oxidation of ZrC and HfC,” *Sov. Powder Metall. Met. Ceram.*, vol. 12, no. 11, pp. 916–921, Nov. 1973.

[7] J. B. Berkowitz-Mattuck, “High-Temperature Oxidation IV . Zirconium and Hafnium Carbides,” *J. Electrochem. Soc.*, vol. 114, no. 10, pp. 1030–1033, Oct. 1967.

[8] K. Tamura, T. Ogawa, and K. Fukuda, “The oxidation behavior of ZrC coating and powder studied by laser Raman spectroscopy and X-ray diffraction,” *J. Nucl. Mater.*, vol. 175, no. 3, pp. 266–269, Dec. 1990.

[9] Y. V. Miloserdin, K. V. Naboichenko, L. I. Laveikin, and A. G. Bortsov, “The high-temperature creep of zirconium carbide,” *Strength Mater.*, vol. 4, no. 3, pp. 302–305.

[10] H. Li, L. Zhang, L. Cheng, and Y. Wang, “Oxidation analysis of 2D C/ZrC–SiC composites with different coating structures in CH4 combustion gas environment,” *Ceram. Int.*, vol. 35, no. 6, pp. 2277–2282, 2009.

[11] G. A. Rama Rao and V. Venugopal, “Kinetics and mechanism of the oxidation of ZrC,” *J. Alloys Compd.*, vol. 206, no. 2, pp. 237–242, May 1994.

[12] N. Hun, Université Bordeaux 1, 2011.

[13] H. Li, L. Zhang, L. Cheng, Y. Wang, Z. Yu, M. Huang, H. Tu, and H. Xia, “Effect of the polycarbosilane structure on its final ceramic yield,” *J. Eur. Ceram. Soc.*, vol. 28, no. 4, pp. 887–891, 2008.

[14] P. Greil, “Polymer Derived Engineering Ceramics,” *Adv. Eng. Mater.*, vol. 2, no. 6, pp. 339–348, 2000.

[15] M. Gendre, A. Maître, and G. Trolliard, “A study of the densification mechanisms during spark plasma sintering of zirconium (oxy-)carbide powders,” *Acta Mater.*, vol. 58, no. 7, pp. 2598–2609, 2010.

[16] A. W. Weimer, *Carbide, nitride and boride materials synthesis and processing*, 80th ed. Chapman and Hall, 1997.

[17] D. Pizon, R. Lucas, S. Chehaidi, S. Foucaud, and A. Maître, “From trimethylvinylsilane to ZrC–SiC hybrid materials,” *J. Eur. Ceram. Soc.*, vol. 31, no. 14, pp. 2687–2690, 2011.

[18] M. D. K. Ingall, C. H. Honeyman, J. V. Mercure, P. A. Bianconi, and R. R. Kunz, “Surface Functionalization and Imaging Using Monolayers and Surface-Grafted Polymer Layers,” *J. Am. Chem. Soc.*, vol. 121, no. 15, pp. 3607–3613, Apr. 1999.

[19] H. Kitaoka, K. Ozawa, K. Edamoto, and S. Otani, “Interaction of water and methanol with oxygen-modified ZrC(100) surfaces,” *Surf. Sci.*, vol. 518, no. 3, pp. 225–233, 2002.

[20] T. Noda, M. Yamazaki, K. Ozawa, K. Edamoto, and S. Otani, “Oxygen adsorption on a ZrC(111) surface: angle-resolved photoemission study,” *Surf. Sci.*, vol. 450, no. 1–2, pp. 27–33, 2000.

[21] M. Iijima and H. Kamiya, “Surface Modification of Silicon Carbide Nanoparticles by Azo Radical Initiators,” *J. Phys. Chem. C*, vol. 112, no. 31, pp. 11786–11790, Aug. 2008.

Chapter I: Bibliographic Studies

Table of Contents

1. Introduction

ZrC is a non-oxide ultra-high temperature ceramic (UHTC) with a high melting point of ~ 3400 ^{o}C. With its excellent physical and mechanical properties, it is usually used in areas such as cutting tools, nano-structured composite part coatings, and can be used in harsh environmental conditions such as extreme temperature with applications such as the aerospace industry and nuclear fuel reactors. Its application is however limited due to the problem of the oxidation of the nano-particles at low temperatures in the regions of 300 ^{o}C to 600 ^{o}C[1]–[3]. This subsequently leads to spallation of the nano crystallites due to the low refractory oxides formed on the surface of ZrC particles.

Moreover, according to the literature, no attempt is being made to control this oxidation process and maintain the excellent physical and mechanical properties which makes ZrC advantageous in different applications. In this respect, this project aims at providing a solution for the control of oxidation of ZrC particles in order to make it useful for its intended purposes.

In order to proceed with developing methods for control of oxidation of ZrC surfaces, a thorough survey of the literature on ZrC systems has to be made. This survey is intended to shed light on what has actually been done on ZrC, the methodologies used, the challenges encountered, the synthesis processes used, how certain challenges are by-passed or solved and what has not been achieved so far. Such an analysis will provide guidance and direction for this research work. It will provide indications on which areas to focus and where to depend on results from works conducted by others. This survey is intended to be as exhaustive as possible so as to have a fair idea and knowledge on the system.

The literature survey is divided into many parts as follows: a section is devoted to the general class of transition metal carbide (TMC) ceramics, their properties, their applications and challenges faced in their synthesis and usage. As ZrC is a member of the TMC group of ceramics, a separation section is carved out and is dedicated to ZrC. This presents ZrC, the areas of application, the various synthetic methods and routes and the challenges in their synthesis. Another section is devoted to the crystal structure of ZrC, various bulk properties that has been addressed in the literature as well as studies on various compositions of ZrC phases and defect studies. In the next section, a literature account is given on the various low index surfaces of

ZrC. This section comprises studies on the stabilities of the various surfaces, their compositions and their properties in different environmental conditions. The last part of this section presents a survey on the reactivity of various small molecules on the low index surfaces of ZrC. The reactivity involves molecules like H_2, O_2, H_2O, their adsorption properties, their reactivity and mechanisms and their structure. In the subsequent studies, account is given on the various interfaces formed between ZrC and other oxide layers that form ontop of ZrC surfaces such as ZrO_2. Another section presents studies on the functionalization of ZrC surfaces, reactivity with organic molecules and the grafting of polymeric precursors on functionalized ZrC surface. A final account is given on the interaction and properties of siC with ZrC surfaces. The chapter is concluded with a general conclusion on the literature survey.

2. Transition Metal Carbides (TMC)

Transition metal carbides constitute a diverse class of materials with various technological applications. They have extensively been used in applications at extreme conditions of temperature and pressure owing to their great strength and durability. Such applications include drill bits and rocket nozzles as well as nuclear fuel reactor wall linens. They also exhibit an extreme hardness that make them usefu in applications such as cutting tools, show tires and shoe spikes[4]. Their hardness is also maintained at very high temperatures. They are also applied in ferrous alloys as the components responsible for the toughness of steel. The TMC's also have applications in other areas such optical coatings[5], electrical contacts[6], diffusion barriers[7] and several other uses.

These applications are feasible as these materials have extremely high melting points. They are sometimes referred to collectively as "refractory carbides". They have low chemical reactivity and are attacked only by concentrated acids and base in the presence of oxidizing agents at room temperature. They also maintain good corrosion resistance at high temperatures. They have good thermal shock resistance and good thermal conductivity. This permits heat to be drawn away from the surface when they are used as tools. For example, tungsten carbide (WC) is the most commonly used for fabrication as "cemented carbide" tool for cutting steel. In this tool, the carbide is normally bonded in a metal matrix such as cobalt. TiC, TaC and NbC are often used in conjunction with WC because TiC locally forms a layer of TiO[8] or TiO_2[9] which protects the tool from wear while TaC and NbC raise the melting temperature and oxidation resistance of the tool.

For high temperature applications, the carbides are used as pure material-sintered parts or in a Co/Mo/W carbide sintered composite. They outperform the standard alloys and superalloys in applications as rocket nozzles and jet engine parts where erosion resistance at temperatures above 2500 ^{o}C is crucial. For example, TiC_{1-x} and VC_{1-x} in particular maintain high strengths up to 1800 ^{o}C and therefore can be used as high temperature structural materials, provided that internal and surface flaws such as stress cracks, pores introduced during fabrication and sintering are removed. Such defects lead to a high room-temperature brittleness. Plastic flow relieves internal stresses caused by defects and leads to reduced brittleness at high temperatures. Plastic deformation occurs particularly via a mechanism of dislocation glide along {111} planes.

In addition to their technological uses, certain carbides have been examined for their catalytic properties in a number of reactions in addition to their being potential supports for more traditional catalytic materials (Ni, Pt, Rh, etc.) due to their high heat stability. Tungsten has been observed to be active as a catalyst and showed selectivity toward xylene formation during the isomerization and hydrogenolysis of 1,1,3-trimethylcyclopentane[10]. However, bare transition metals do not behave this way. This behavior was explained by invoking the formation of tungsten carbide on the surface of the metal; WC is similar to platinum in selectivity for neopentane isomerization as well[11]. Mo_2C has been found to behave similarly to Ru in CO-H_2 reactions[12]. Carbides of the group IV-VI metals have been studied for their activity in oxidation, hydrogenation/dehydrogenation, isomerization, hydrogenolysis, and CO-H2 reactions, and in many cases have been found to rival the performance of the less economic group VIII metals. Even though the refractory carbides do not show high activity for oxidation reactions, they are as active as the transition metals themselves for hydrogenations and dehydrogenation reactions. In isomerization reactions, WC, Pt, and Ir ar unique in their high activity and selectivity[13].

2.1 Structures of Transition Metal Carbides

Most transition metal monocarbides form in the *B*1 (NaCl) structure, *fcc* with carbon occupying the octahedral interstitial sites. Generally, the shortest metal-metal (M-M) distance is about 30% greater in the *B*1 carbide than in the pure metal for the group IV and V carbides but this drops to less than 10% greater for the group VI or VIII carbides[14]. At 100% site occupancy, the stoichiometry of the carbide is however $MC_{1.0}$ although this situation is not mostly realized. The resulting concentration ordering of the vacancies from the nonstoichiometric M-C ratio have a profound effect on thermodynamic, mechanical, electronic and magnetic properties of the metal carbides. Due to the difficulties inherent in synthesizing the pure compounds and measurement of the exact details of the crystal structure, there exists a matter of debate in the literature concerning the details of these effects. The metal carbides also share some characteristics with the metals themselves, having a plastic deformation like the fcc metals, which while lowering the high-temperature hardness also protects parts fabricated from the carbide from catastrophic failure in response to stresses.

Most group IV-V TMC’s obey the Hägg’s rules used for prediction of structures of the transition metal borides, carbides, halides and nitrides[15]. The radius of the non-metal atom (r_n) to that of the metal atom (r_m) determines the structure adopted by the TMC’s. For (r_n/r_m) < 0.59, the common structures adopted are the simple *A*1, *A*2, A3 and hexagonal lattices. More complex structures are however formed at ratios > 0.59 in order to avoid expansion of the lattice. The monocarbides take an fcc metal lattice with carbon atoms at the octahedral interstitial sites, while random occupation of half of the O_h sites in M_2C or M_3C leads to the *L3*’ (anti-NiAs) structure, and carbon occupation of the trigonal prismatic sites in the *hcp* lattice formed by the tungsten atoms leads to the CdI_2 structure[8]. Non-Hägg structures are known among the carbides as well, a major example being Cr_2C_3. A feature which is well known for TMC’s is that, the lattice adopted by the metal in the carbide is always different from that of the parent metal itself. For example, if the parent metal has an *fcc* lattice, it occupies a non-cubic lattice in the daughter carbide formed. The Engel-Brewer theory[16], [17] of metals has been used to explain this phenomenon. In this theory, the structure adopted by a metal or alloy depends on the *s-p* electron count[14]. Across the transition series, with increasing *s-p* electron count, the metal structure progresses from *bcc* to *hcp* to *fcc*. Moreover, the Group IV and V metal carbides form in the *B*1 structure rather than a hexagonal form because the incompletely filled bands of the host metals can accommodate a high ratio of sp-electron-rich carbon to metal. In Group VI the stoichiometry M_2C occurs often, while Groups VII and VIII, when they form carbides at all, take on metal-rich stoichiometries M_3C and M_4C, consistent with an attempt to avoid filling antibonding levels in the metal bands[18].

Concerning bonding in TMC's, investigations[19], [20] has shown that, the bonding is typically interactions of carbon 2*s* and 2*p* orbitals with metal d orbitals. The 2*s* orbitals are however localized at low energies so that the main interaction is between the 2*p* orbitals and the d orbitals of the metal (e_g and t_{2g} character) as shown in figure I.1.

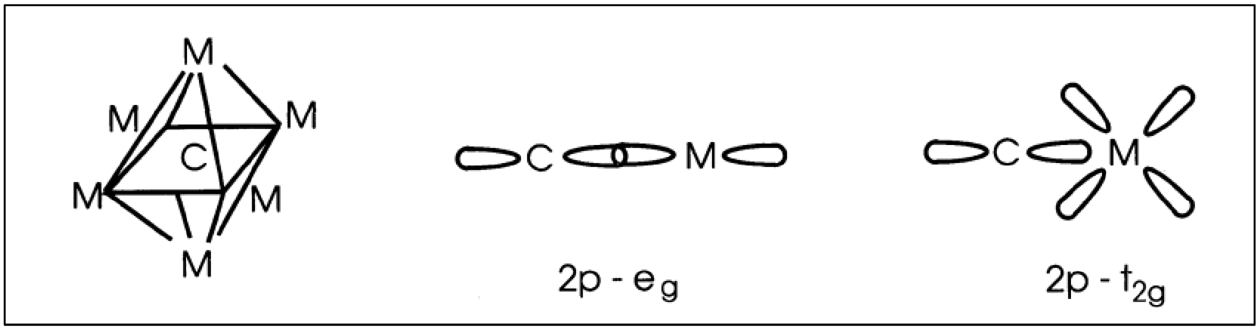

Figure I.1. Electronic Structure of transition metal carbides. Figure is adopted from reference[4]

Interest has long been developed in comparing the electronic structure of carbides to those of metals ever since WC was observed to have catalytic properties similar to Pt[11]. An area of controversy in the bonding of carbides is however on the direction of electron transfer. It was mentioned earlier that concerning properties like structure and composition, the carbon atoms appear to increase the density of *sp* electrons in the compounds. This phenomenon is supported by studies of the chemical and catalytic reactivity[14]. Moreover, measurements by X-ray photoemission (XPS)[21] and near-edge X-ray absorption fine-structure (NEXAFS) has shown that negative charge is concentrated around carbon and this result has been corroborated by augmented plane-wave (APW) calculations[20].

2.2 Synthesis and Characteristics of Transition Metal Carbides

The more common methods for preparing TMC's involves direct reaction of the metal or metal hydride powders with carbon. It is however difficult to achieve pure materials with homogenous compositions. However, other methods are available. The methods include routes that generally utilize high temperatures and therefore produce low surface area materials. Other methods lead to the production of powders, particles and supported forms and are generally moderate temperature methods that produce high surface area materials. The final group of methods discussed lead to the production of films and coatings.

2.2.1 Production of Low Surface Area Materials

For the low surface area materials methods, some processes involve *direct reaction of metals and elemental carbon*. This is done by contacting metallic powers and solid carbon in a protective atmosphere (H2 or vacuum) and sometimes in the presence of gaseous hydrocarbons, at temperatures between 1500 and 2300K[4]. Factors affecting the reactions are pressure, time and division of the metal. Some procedures also involve the reaction of metal oxide in powders in the presence of solid carbon. A mixture of metal oxide powder with carbon is heated again with the pure metal at temperatures between 1500 and 2300K with or without the presence of a hydrocarbon gas. These reactions are thermodynamically stable[4]. Another procedure is termed the *self-propagating method*. This method involves solid combustion synthesis[22]–[24]. The technique takes advantage of the exceptionally high thermodynamic stabilities of carbides. The preparation involves the reaction of a metal and a second component which may be a reactive gas in a self-sustaining manner, driven by the exothermicity of dissolution of carbon in the metals. In another procedure, single crystals are prepared. They are prepared by the Vernouil technique, the floating zone technique, and the methods involving precipitation from liquid metals[8].

2.2.2 Production of Powders, Particles and Supported forms

This part also involves several routes and procedures for obtaining the desired products. The first procedure involves the *reactions of metals or metal compounds with gas-phase reagents*. One such direct method of preparing carbides is the reaction of a metal or metal compound with a carbon-containing gas. Another procedure involves the *decomposition of metal halide vapors*. The carbides are prepared from volatile metal chlorides or oxychlorides by reacting them with gaseous hydrocarbons in the vicinity of a localized heat source at 1400-2900 K in the method known as the Van Arkel process. The reaction is a convenient method for producing small amounts of pure carbides. It is a thermodynamically stable reaction[4]. In another procedure, there is the use of *decomposition of metal compounds*. Various compounds can decompose to produce carbides. For example, the reaction of molybdenum and tungsten carbonyls with hydrogen can be used to make Mo_2C and WC[25], [26]. The reactions can be carried out in the gas phase if the compounds are volatile or in the solid state otherwise. In the *temperature-programmed methods*, the preparation consists of treating a precursor compound in a reactive gas stream while raising the temperature in a uniform manner. The precursor can be an oxide, sulfide, nitride or other compound while the reactive gas can be a mixture of hydrocarbon like methane and hydrogen for carbides. By monitoring changes in the exit gas phase composition, the end of the reaction can be ascertained and the product quenched. Also there is a method that utilizes *high surface area supports*. The use of supports offers the advantage of better usage of the active component and higher control of surface area and pore size distribution. Highly dispersed carbide phases may be prepared by depositing a precursor on a high surface area support and carburizing it[27]. An approach exists that uses *reaction between a metal oxide vapor and solid carbon*. This method is used in the preparation of ultra-high surface area carbides[28]–[30] and involves the reaction of solid carbon with vaporized metal oxide precursors like MoO_3 or WO_2. This synthesis approach uses high specific surface area activated carbons and the final product appears to retain a ‘memory’ of the porous structure of the starting material. The carbon acts as a skeleton around which the carbides are formed and the method can be used to prepare catalytically active samples with surface areas between 100 and 400 m^2g^{-1}. A last procedure is the *liquid-phase methods*. This method has been used to synthesize Mo_2C and W_2C via a chemical reduction method[31]. It is done by mixing tetrahydrofuran (thf) suspensions of the metal chlorides, $MoCl_4(thf)_2$, $MoCl_3(thf)_3$ and WCl_4 at 263K with lithium triethylborohydride, LiBEt3H to generate black colloidal powers (1.-2 µm diameter) composed of smaller 2 nm sized particles.

2.2.3 Production of Films and Coatings

The various methods which are used for producing films and coatings include *the plasma methods*. The plasmas are discharges in a low-pressure gas environment (0.01-0.02 Pa) that can be used for the direct synthesis of fine powders or the deposition of coatings[32], [33]. In thermal plasmas, electrons and gas molecules are at comparable temperatures which are typically thousands of degrees[34]. Solid reagents are atomized in this environment when they are used. Plasma processing is carried out in large-scale industrial deposition of protective coatings on metal pieces such as camshafts, springs and others[35], [36]. *The chemical vapor deposition* (CVD) method is also a well-known procedure for making thin films. It is also sometimes used to prepare supported particles[37], [38]. The films are formed by the chemical reaction of a gas phase species with the heated surface of a substrate. The CVD coatings are normally applied in the tooling, aerospace industries among others[39]. Another method for preparing films that is distinguishable from the CVD is called the *Physical vapor deposition* and it differs by the absence of surface chemical reactions that release ligands or other byproducts extraneous to the composition of the films. It may be viewed as the condensation of oligomeric units of the same composition as the film on the surface. The last method to be described in this section is the electrochemical reduction method. It involves the electrolysis of molten salts. Metal oxides are dissolved at 970 K in carbonate melts containing alkali metal fluoride and B_2O_3 and upon electrolysis, it yields millimeter sized crystallites on the walls of a graphite crucible which acted as the cathode[40], [41]

3. Zirconium Carbide

As a general description has been made for the TMC's, a quick transition can be made for Zirconium Carbide (ZrC) which is of interest in this project. ZrC is a group IV TMC and is used for most of the applications listed for the TMC's. However, the main area of application is in nuclear fuel reactor wall linens and also in cutting tools, aerospace and steel industries. In this discussion, the various methods of preparation of this material is considered with details for some synthesis procedures. A closer look is taken into the bulk properties, structural and mechanical properties that has been studied in the literature. A look at the properties of defects in the solid is also given. A survey is carried on the reaction of various molecules such as H_2, H_2O and O_2 with the ZrC low index surfaces.

3.1 Synthesis of ZrC

Several techniques amongst those discussed in section 2 are utilized in synthesizing ZrC. Several groups have synthesized ZrC from solid phase reactions using solution based precursors and also through vapor phase reaction methods such as CVD[8], [42]. The various fabrication techniques normally lead to samples with varying characteristics. Some of these characteristics include microstructure, chemical composition and impurity species as well as impurity concentrations[43]. However, certain characteristics are very important when synthesizing ZrC with various techniques. These characteristics include carbon-to-zirconium ratio which gives the product stoichiometry, porosity, pore size, pore distribution, pore morphology, chemical impurities, presence of secondary phases including grain boundary phases, grain size, morphology, orientation, texture and other forms of defects[43].

In the solid phase fabrication techniques, the most common approach usually involves the reduction of zirconia (ZrO_2) with carbon. The carbothermal reduction of ZrO_2 to produce ZrC is shown in a schematic representation in figure I.2.

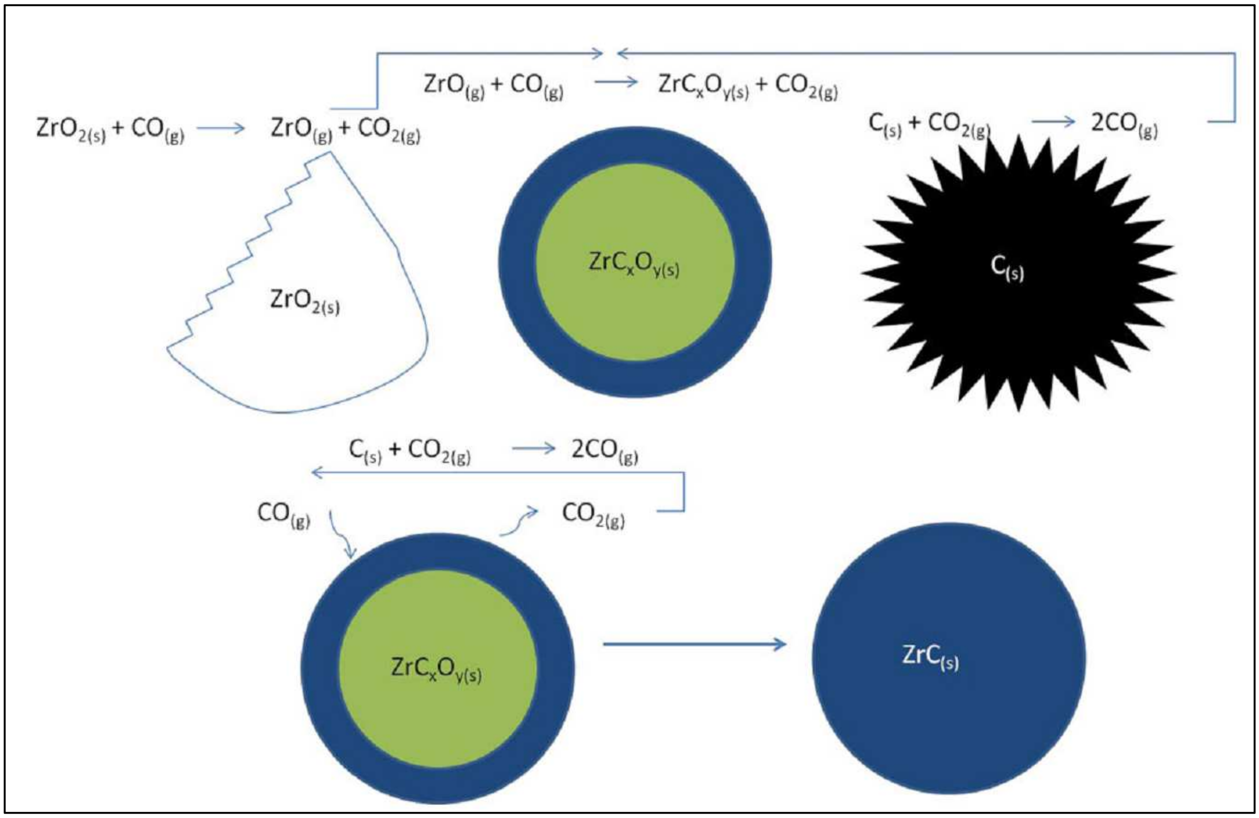

Figure I.2. Schematic representation on the process of carbothermal reduction in producing ZrC. Figure is adopted from reference[44]

The process however requires long time (16-24 h) and high temperatures of 2073-2873 K[45]–[47]. Repeated heating cycles is normally required for obtaining pure ZrC via this route. The main problem with this method is the presence of dissolved oxygen and also the inability to effectively remove the oxygen impurity at temperatures below around 2023 K. This subsequently results in the formation of intermediate oxycarbide which makes further processing difficult. [46], [47]. The degree of mixing at the microscale as well as the specific surface and surface chemistry or the reactants powders also affects the degree of carbonization as the process is a solid state reaction with powders. The reaction also requires a strictly controlled environment in order to ensure purity of the final product. The reaction involves the release of carbon monoxide (CO) gas[43]. This process is however endothermic:

$$ZrO_2 + 3C \rightarrow ZrC + 2CO \qquad (1.1)$$

$$ZrC_xO_y + (1 - x + y)C \rightarrow ZrC + yCO \tag{1.2}$$

The ZrC powder which is obtained is normally subjected to extra high temperature, long duration heat treatment cycles to obtain samples of required densities, grain sizes and shapes[43]. Equation 1.1 suggests the possibility of a simple manipulation of the carbon content but in reality, the formation of intermediate oxycarbide phases is expected to pose a formidable challenge[48].

In order to by-pass these problems, an alternate approach involves production of ZrC by direct combination of pure zirconium or zirconium hydride powder with carbon[48]–[50]. This reaction is known as a self-heating synthesis or combustion synthesis reaction[50]. The reactant mixture is initially pressed to form a green body and is heated to an ignition temperature after which the heat released by the reaction is sufficient to sustain and drive it to completion. This reaction is an exothermic reaction compared to the CO diffusion dependent carbothermic reaction and hence a quick process. The purity of the product obtained depends on the purity of the reactants used and the reaction environment. The reaction can be summarized as:

$$Zr + C \rightarrow ZrC \tag{1.3}$$

$$ZrH_2 + C \rightarrow ZrC + H_2 \tag{1.4}$$

As the product can reach very high temperatures, there is limited sintering during the combination reaction but this can be alleviated by providing adequate external pressure to keep the energetic product particles together during the reaction[51]. The main advantage of this method is the ability to produce relatively pure ZrC and the reduced reaction time scales. There is serious handling problem based on the combination reaction being highly exothermic and the size of the zirconium reactant being highly pyrophoric and susceptible to oxidation at room temperatures on the microscale. Control of the exact product stoichiometry in this method is challenging.

A different method such which is a solution based approach has also often been used to synthesize ZrC[52]–[54]. This method has to been used to produce ZrC by reaction of organic compounds containing zirconium and carbon solutions. Some common solutions used include zirconium-n-propoxide, zirconium 2,4-pentanedionate (ZPT) and zirconium n-butoxide. The use of Zr and C precursor solutions facilitates increased mixing on a molecular scale resulting in an efficient diffusion reaction. Extensive drying is used to separate the final product and heat treatment is used to initiate the carbothermic reaction. The method involves extra steps of drying (~ 24 h) prior to the carbothermic reaction but it increases the mixing of the products at the molecular level[52]. The solution based mixing method suffers from the disadvantage of residual oxygen impurity but the production of ZrC with varying stoichiometry can be achieved by varying the proportion of the reactant precursors.

The last method which is often used is the vapor phase fabrication method. This method has been the most commonly method applied for coating nuclear fuels in which impurities must be limited in the final product as well as low porosity must be achieved. The coating has to be deposited by vapor deposition methods such as CVD, evaporation or physical sputtering as the melting point of ZrC exceeds 3500 K[43]. Another process known as fluidized bed process provides pure and homogenous coatings on surfaces of spherical particles and typically employed when a dense, uniform and isotropic coating onto spherical kernels is required[43]. In a conceptual manner, this coating method involves conversion of Zr metal into zirconium halide by passing a halide gas over heated zirconium metal sponge. The zirconium halide is then reacted with a gaseous hydrocarbon compound such as methane. A gaseous ZrC which condenses onto a suitable substrate is then formed. Some groups have achieved this synthesis route using $ZrCl_4$[55], [56], ZrI_4[56], [57] while others have used $ZrBr_4$[58], [59] as the gaseous ZrC precursors. These reactions are normally carried out at 1573-1773 K and the processes can be summarized with the equation:

$$Zrx_4 + xCH_4 + 2(1-x)H_2 \rightarrow ZrC_x + 4HX \quad (X = Cl, I, Br, x \leq 1) \qquad (1.5)$$

The use of zirconium halides has been reported to cause extreme difficulties in controlling the rate of vapor supply. In a modified version Ogawa et al.[59] developed a spouted bed process supplying liquid bromine to form an initial source of Br_2 gas that reacts with metal Zr to produce

$ZrBr_4$. This bromide process was observed to successfully provide high purity and near-stoichiometric ZrC coatings[43]. Various studies have indicated that variation of the flow of methane and hydrogen, the C/Zr compositional ratio of the coating can be controlled and this method is known to produce high purity ZrC as compared to solid and solution based fabrication processes. Reasonable densities of the deposited ZrC can be achieved by further heat-treatment. The stoichiometry of ZrC can be controlled by varying the mixture of the hydrocarbon gas.

3.2 Structure, Bulk Properties and Defects of ZrC

ZrC forms in a cubic system in the NaCl ($B1$) structure. It belongs to the space group O_h^5- $Fm3m$ and has a closed packed fcc lattice structure. The carbon atoms occupy octahedral sites which leads to the formation of a monocarbide which is the most stable structure of ZrC. The ZrC structure consists of a mixture of different bonds. Ionic bonds, metallic Zr-Zr bonds and covalent C-Zr bonds are all present[60]. Among all the bonds present, the C-Zr bond is much stronger than the Zr-Zr bonds. It has been observed that, despite the considerable amount of charge transfer (~ 0.42 e^-/pair) from Zr to C atom[61], the contribution of the covalent bonding is predominant and hence the material is considered polar covalent[62]. The Zr-C bond energy has been estimated to be 5.812 eV[42] and is slightly higher than what is found in SiC, with Si-C bond energy being 4.677 eV. In terms of the electronic structure, ZrC is observed to have a characteristic bonding-antibonding structure with a pseudo-gap around the Fermi level[60]. The C –s states and Zr –p states are situated at the same energy (about 9 eV below the Fermi level and they are well separated (about 7 eV) from the bonding Zr 5d and C 2p states). Above the Fermi level, the states are derived from Zr-d (mostly by Zr t_{2g}-derived states) and C-p anti-bonding orbitals [60].

3.2.1 Lattice Parameter and Bulk Properties of ZrC

Due to the fact that carbon vacancy formation energies are low[43], most of the TMC's exist over a wide range of stoichiometry. These vacancies are caused by the removal of carbon atoms from the sub-lattice. The lattice parameter of ZrC has been observed to depend on the composition as shown in figure I.3[42].

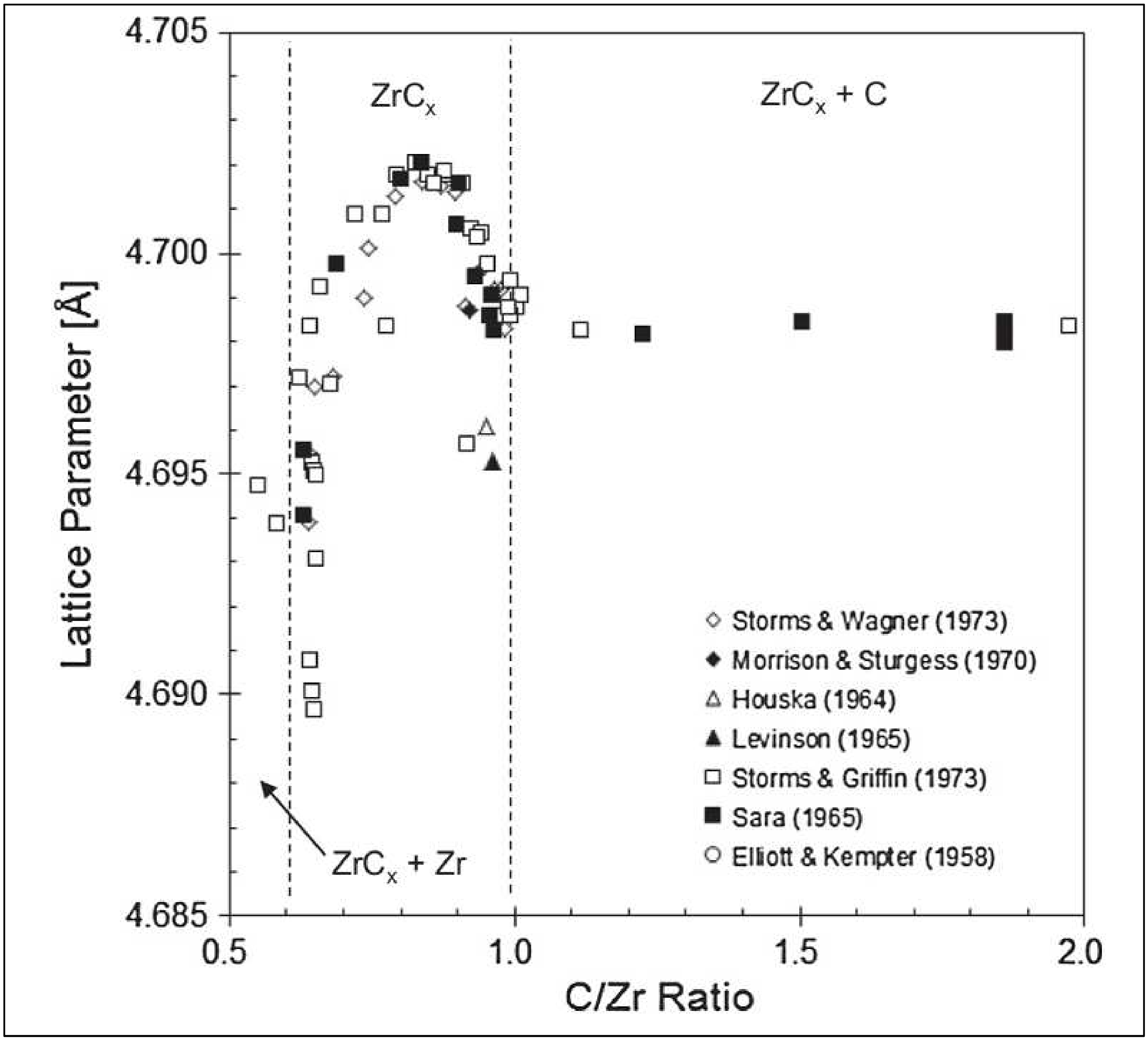

Figure I.3. Variation of ZrC lattice parameter with C/Zr ratio. The figure is adopted from reference [42]

The lattice parameter increases with increasing C/Zr ratio and a maximum value of ~4.702 Å is reached when C/Zr ratio is ~0.83 and after which the lattice parameter decreases[63]. Reports show that the lattice parameter is ~4.698 Å when the stoichiometry is $ZrC_{0.96\text{-}1.0}$ but the lattice parameter of carbon-rich ZrC shows no dependence on the C/Zr ratio[64], [65]. The attribution is that, when the C/Zr ratio exceeds 0.98, there is the precipitation of excess carbon. Also suggestions have been made that, the presence of undetectable oxygen and other impurities can result in the reduction of the lattice parameter[42]. An equation has been developed to theoretically calculate the lattice parameter for perfect lattices and is given by:

$$a = \left(\frac{4M}{d\,.\,N_A}\right)^{1/3} \tag{1.6}$$

M is the molecular weight, d is the mass density, N_A is the Avogadro's number and the value 4 denotes 4 units of ZrC in the unit cell. This equation predicts a maximum lattice parameter for ZrC at a C/Zr ratio of ~0.82 which agrees with experimental values but it fails to predict the lattice parameter for C/Zr ratio > 1.0 where carbon is present in a secondary phase precipitate along with near-stoichiometric ZrC[43].

Several other estimations of the lattice parameter including both experimental and theoretical calculations have been given in the literature. In an X-ray diffraction (XRD) experiment, the authors estimated the lattice parameter to be 4.69764 ± 00005 Å.[66]. In other experimental determinations, the lattice parameter is given as 4.70 Å[8] while a theoretical calculation based on density functional theory (DFT) calculated the lattice parameter of ZrC to be 4.731 Å[62]. All these values are in agreement with equation 1.6

The variable lattice parameter and composition yield a wide range of reported mass density. The density of ZrC has been observed to increase with the composition approaching stoichiometry[63]. However, carbon-rich ZrC with excess carbon (i.e. C/Zr > 1.0) shows lower density than near-stoichiometric ZrC[58]. The density is maximized near stoichiometry, which yields ~6.61 g/cm3 for $ZrC_{\sim 1.0}$[43].

3.2.2 Mechanical Properties of ZrC

The mechanical properties that are considered include most of the elastic constants of the ZrC material. These elastic constants can be used to characterize various deformation, hardness and brittleness of the ZrC material.

A first look is taken at the Young's modulus. Various accounts have been given on the Young's modulus of ZrC. These reports include those from Warren[67], Brown and Kempter[68], Chang and Graham[69] and Baranov[70]. Chang and Graham used the sonic resonance method with ZrC single crystal fabricated using the float zone method and C/Zr ratio from 0.89 to 0.94. Their estimated Young's modulus, *E* value was 406 GPa[69]. Brown and Kempter also used the sonic resonance method in determining the *E* of 386.6 GPa[68] but they used C/Zr ratio of 0.964 and the ZrC was prepared from hot press with 3% porosity. Warren used the Hertizan indentation technique with a C/Zr ratio of 0.95 using hot pressed ZrC with 8% porosity and calculated *E* as 400 GPa[67]. Baranov et.al used the sonic velocity method to calculate an *E* value of ~390 GPa[70] with C/Zr ratio of 0.96 and cold pressed ZrC powder sintered at 2600 K for 2h in Argon. In estimating the Young's modulus, Chang and Graham used the elastic coefficients C_{11} = 472 GPa, C_{12} = 98.7 GPa and C_{44} = 159.3 GPa[69]. Brown and Kempter also used coefficients C_{11} = 423 GPa, C_{12} = 40.8 GPa and C_{44} = 146.4 GPa[68]. It is apparent that the different methods used in preparing ZrC by the yielded different elastic coefficients as a result of the varying C/Zr ratio. Only limited amount of data is found on the Young's modulus of sub-stoichiometric and carbon-rich ZrC. Chang and Graham has reported only a small variation (about 1%) in the elastic constants between $ZrC_{0.94}$ and $ZrC_{0.89}$[69]. Leipold and Nielsen[71] has also reported a value of 358 GPa for hot pressed $ZrC_{0.81-0.85}$ with a free carbon content of 1.6-2.03% and a value of 353 GPa for the same hot pressed sample after annealing at 2070 K to reduce the amount of free carbon measured by dynamic techniques. Other groups have used theoretical studies to calculate the Young's modulus for ZrC. In reference [72], the authors used DFT to calculate the Young's modulus of ZrC as 408 GPa while in reference [73], *E* is calculated as 435 GPa using DFT as well.

The Poisson's ratio, *v* has also been calculated by several groups. Graham and Chang[69] used the same method as for the Young's modulus to calculate *v* of 0.187, Brown and Kempter[68] determined v as 0.191, Warren[67] determined v as 0.20 and Baranov et.al estimated[70] v to be 0.23. There is no exhaustive data on the dependence of v on temperature and C/Zr ratio[43]. However, Baranov et.al[70] has noted a marginal dependence of v on the C/Zr ratio at 300K, i.e 0.21-0.23 for $ZrC_{0.77}$-$ZrC_{0.96}$.

After obtaining the Young's modulus and Poisson's ratio, the shear modulus can be calculated. Chang and Graham[69] calculated a value of 172 GPa, Brown and Kempter[68] measured 162.3 GPa, Warren[67] measured 167 GPa and Baranov et.al measure 158 GPa[70]. This can be calculated from the equation:

$$G_V = \frac{1}{5}(C_{11} - C_{12} + 3C_{44}) \quad and \quad G_R = \frac{5(C_{11} - C_{12})C_{44}}{4C_{44} + 3(C_{11} - C_{12})} \tag{1.7}$$

G_v and G_R are the upper and lower bound of the shear modulus respectively. The average shear modulus is then calculated from the upper and lower bounds. For design purposes, a room temperature shear modulus of ~167 GPa for $ZrC_{1.0}$ is recommended[43]. No exact correlation of the shear modulus with temperature and C/Zr ratio has been determined due to the limited amount of information on the correlation of temperature and C/Zr with the Young's modulus and Poisson's ratio.

The hardness properties of ZrC has been studied using indentation hardness. Indentation hardness is a property used to represent the material's resistance to local plastic deformation. TMC's are generally known to be hard and is related to the strong hybrid ionic-covalent bonds. The strong Zr-C bonds tend to prevent plastic deformation, resulting in brittle failure in response to an applied load[43]. ZrC has anisotropy in hardness and strength[74]. Deformation in ZrC normally occurs on the preferred $\{111\}< 1\bar{1}1 >$ and $\{110\}< 1\bar{1}1 >$ [74]. In ZrC, the high directionality of the covalent bonds typically inhibits slip on the close-packed {111} planes and hence the strength of those bonds results in low dislocation mobility and brittle fracture at lower temperatures[43]. The critical resolved shear stress of the refractory ZrC is also dependent on the Zr/C ratio. The hardness depends on the bond strength and density, presence of second phase and elastic modulus. As such, there is the expectation that, presence of missing Zr-C bonds in sub-stoichiometric or excess carbon in a form of graphite in carbon-rich ZrC will alter the strength to a large extent.

3.2.3 Point Defects of ZrC

As ZrC is widely used in nuclear applications, there is the likelihood of atomic displacements in radiation environments which results in the creation of various defect structures such as point defects and defect clusters. These can lead to degradation of a material as a structural component as well as diffusion barrier for fission products[75]. There are reports that ion irradiation of a nearly stoichiometric ZrC results in an increase of the lattice parameter and that irradiation introduces high internal stress[76]. These phenomenon are all related to the generation of point defects in ZrC. There is lack of comprehensive studies on the most stable defect structures of ZrC.

ZrC is known to contain a large number of carbon vacancies and the properties of which are related to the broad compositional homogeneity of ZrC, normally at 38-50 at. % C at 500 ^{o}C[8], [61], [77]. A very common characteristic of group IV TMC's is a high vacancy concentration on the nonmetal sublattice[8].

A few groups have studied the formation and effect of defects in ZrC by theoretical means. Li et.al[61] calculated vacancy formation energies using ab initio methods. They calculated the carbon vacancy formation energy using a 63 atom supercell as 1.16 eV based on DFT calculations and 1.51 eV using interatomic potentials. Another group[78] has also used quantum mechanical calculations to study carbon vacancy formation in ZrC. They calculated the defect formation energies of substoichiometric ZrC structures ranging from 10% C to 75% C and they observed ZrC to be stable down to $ZrC_{0.5}$. Also, classical molecular dynamics has been used to study the radiation damage of ZrC and the associated defects produced[79]. The authors observed the most of Zr interstitials form a Zr-Zr dumbbell in the [111] direction and the C interstitials either remain isolated or they form a C-C dumbbell in the [111] direction. The number of anti-site defects found in the study was however small. Kim and Morgan[75] used ab initio calculations to study both vacancies and interstitial defects. They found C vacancy has the lowest formation energy, indicating the ease with which C vacancies in ZrC are formed and this corresponds to the C poor ZrC_x with wide compositional homogeneity. They also found the next most energetically favorable defect to be C interstitials. They examined the C and Zr interstitial structures by calculating defect formation energies (DFE) from initial interstitial atom positions displaced from an on-lattice atom along a high symmetry crystallographic orientation. The observed the most stable C interstitial to be a C-C-C trimer on the [101] direction, with a DFE of 3.56 eV/defect and a separation distance of 1.389 Å. A relatively close in energy, thus DFE of 3.82 eV/defect is the C tetrahedron in the [111] direction. These close values suggest that the C interstitial might diffuse easily using atom jumps between these two sites[75].

4. Reactivity of H_2, H_2O and O_2 on ZrC surfaces

In this section, a survey is presented on what has been studied so far concerning the reduction, oxidation and hydration of ZrC surfaces. It is necessary to study the reactivity of these molecules with ZrC as it yields in more insights on the functionalization of ZrC surfaces for further grafting polymeric precursors.

4.1 Reactivity of Oxygen with ZrC

ZrC is highly susceptible to oxidation. This oxidation begins at a relatively low temperature compared to SiC for example. Various parameters are used to characterize the oxidation of ZrC. These parameters include temperature and oxygen partial pressures. The affinity of ZrC for oxygen has in some cases been utilized by using the material as an oxygen getter in uranium oxide tri-isotropic (TRISO) fuels[80]. Reports on ZrC oxidation shows that ZrC is susceptible to rapid oxidation depending on temperature, porosity, partial pressure of oxidative and reductive gas species, carbon content and impurities[2], [3], [81]. Oxidation of ZrC results in complete spalling at elevated temperatures (T > 870 K) especially in high oxygen partial pressure environments (~130 kPa) [3], [82] even though oxidation does not affect ZrC at room temperatures. In temperatures exceeding 1500 K with sufficient partial pressures of oxygen, ZrC is known to passivate and the resulting zirconia undergoes limited but yet considerable sintering contribution to improved structural integrity in certain conditions[2].

According to Rama [83], the oxidation of ZrC initiates at temperatures close to 550 K in lower oxygen partial pressure environments (1-50 kPa) while significant oxidation has also been observed only above 970 K at atmospheric pressures[81]. The oxidation normally results in the formation of zirconia but ZrC goes through an intermediate oxycarbide phase before the zirconia appears[84], [85]. The formation of the oxycarbide is rapid and it is well expected as oxygen is known to dissolve in ZrC[86], [87]. At high oxygen partial pressures (~100 kPa), the reaction is controlled by the phase boundary reaction and the activation barrier is estimated to be ~2 eV at 723 < T < 853 K [83], [85]. At temperatures below 873 K, there is evidence in the literature[81], [83], [84] on the presence of zirconia and free carbon in the ZrC scales.

An overall reaction for the oxidation of ZrC as summarized by Rama [83] is given as:

$$ZrC + \tfrac{1}{2}(1-x)O_2 \rightarrow ZrC_xO_{1-x} + (1-x)C \tag{1.8}$$

$$ZrC_xO_{1-x} + \frac{1}{2}(1+3x)O_2 \rightarrow ZrO_2 + xCO_2 \tag{1.9}$$

The liberated carbon appears as uniformly suspended inclusions within the zirconia layer and the oxidized layer is reported to be amorphous (< 2 nm) and consisting of very small sized zirconia particles and free carbon[88]. With the formation of this layer, diffusion of oxygen assumes control of the reaction rate as the later starts to grow[81], [83]. The activation energies measured for this process are ~1.4 eV at 653 < T < 873 K [83], [84] under isothermal oxidation conditions and ~1.2 eV at 550 < T <1300 K [83] for non-isothermal conditions. The processes seems to be preferential zirconium oxidation since no significant carbon is expected to oxidize at these temperatures which results in the production of only limited amounts of CO_2[43]. As temperature is increased, > 870 K, cubic zirconia starts to nucleate from the amorphous zirconia and the crystals start to grow. Further increase in temperature causes the cubic zirconia crystals to grow larger, ~10 nm and carbon starts to oxidize to form CO_2 gas[83]. As the temperature is increased beyond 1070 K at lower oxygen partial pressures, < 50 kPa, there is the formation of tetragonal and monoclinic zirconia[3], [89] in the oxidized layers and the production of CO_2 gas increases with increased oxidation of carbon[81]. The escaping CO_2 gas leave behind voids which appear as additional porosity in the zirconia layer. At higher temperatures above 1270 K, stress is exerted by the growth of monoclinic zirconia at the grain boundaries and the pressure exerted by the increased CO_2 gas initiates inter-crystalline fracture in the already porous layer[2] and it is clear from these observations that the oxidation will have an adverse effect on the strength of ZrC. Increasing temperatures above 1470 K causes the porous monoclinic zirconia to sinter and densify, acting as a barrier for further diffusion of oxygen atoms[2] to reach the ZrC substrate and the oxidation turns passive as long as the zirconia scale remains intact[43].

Data in the literature indicates that the oxygen partial pressure affects the mode of oxidation and the rate of the reaction with the rate increasing with the pressure at low temperatures[83]. A mechanistic presentation of the oxidation process of ZrC assuming a constant partial pressure of oxygen and increasing temperature is shown in figure I.4.

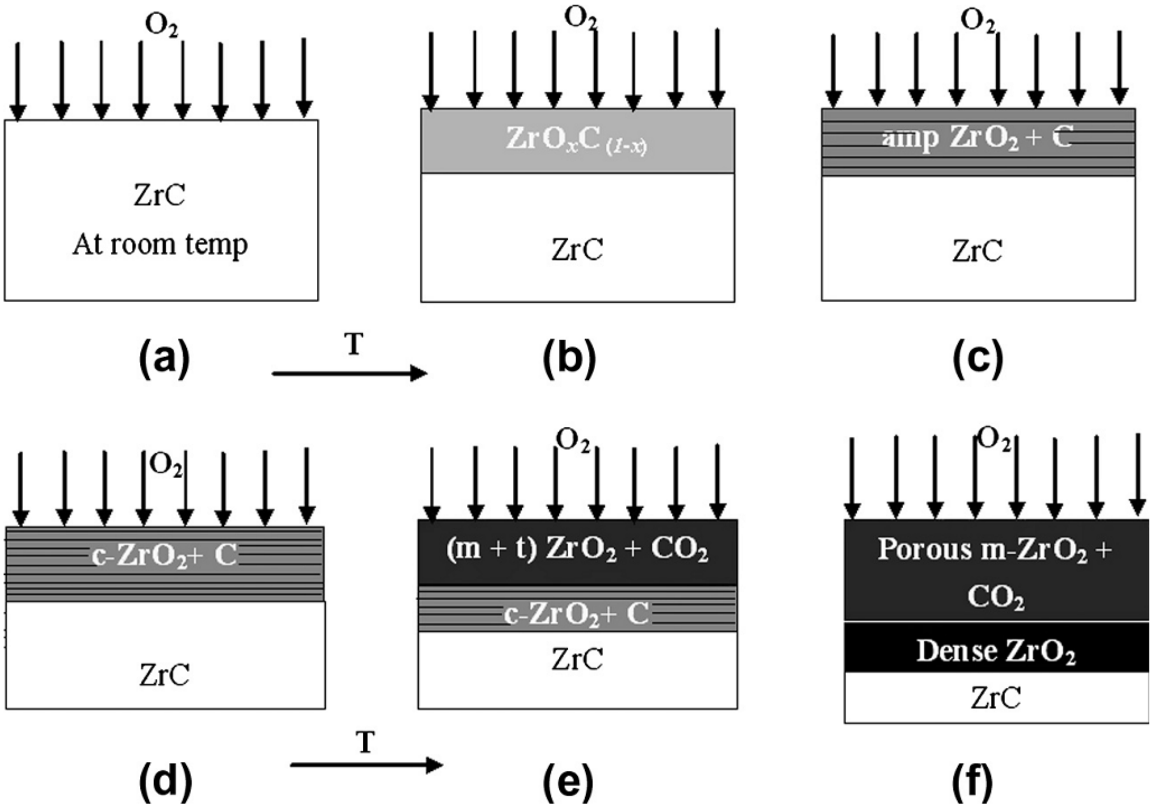

Figure I.4. Mechanism of oxidation on ZrC surface. The figure is adopted from reference [43]. (a) is ZrC at room temperature, (b) is formation of oxycarbide, (c) carbon precipitation with the formation of amorphous zirconia, (d) initiation of formation of low levels of CO_2 gas due to the oxidation of C, (e) monoclinic and tetragonal zirconia appears in addition to large (>10nm) cubic zirconia crystals still present at the interface, (f) zirconia starts to sinter as the temperature is increased and it creates a barrier for oxygen diffusion.

Several accounts are given in the literature concerning studies on the adsorption and reactivity of oxygen with the different facets of ZrC crystals.

Arya and Carter[62] had previously studied the stability of the different ZrC surfaces using surface energies and density of states calculations. They determined the stability of the surfaces to be in the order (100) > (111) > (110). The (100) surface being more stable than the (111) surface was confirmed by Ozawa et.al [90] when they used core level photo emission spectroscopy (PES) and X-ray absorption spectroscopy (XAS) studies to the co-adsorption O_2

and Cs on ZrC(111) surface. The authors concluded that the ZrC(111) surface is terminated with Zr layer. They also observed the (111) surface to be more reactive towards gas adsorption than the (100) surface.

Ozawa et.al. [91] used ultraviolet photoemission spectroscopy (UPS) to study the adsorption of oxygen on clean and potassium modified ZrC(111) surface. Oxygen is observed to adsorb dissociatively to form a $(\sqrt{3}\,\mathrm{x}\,\sqrt{3})R30^{o}$ structure at 0.4-0.8 L coverage and a (1 x 1) structure after further exposure on the clean ZrC(111) surface at room temperature. Adsorption of the dissociated to oxygen atoms is at three-fold hollow site on the ZrC(111) from analysis of O 2p peaks. The authors used a single crystal of $ZrC_{0.9}$ and the oxygen atoms are in a single adsorption state irrespective of the oxygen coverage. Noda et.al [92] also used Angle resolved PES (ARPES) to study the adsorption of oxygen on a ZrC(111) surface. They used a $ZrC_{0.93}$ crystal for the analysis. They observed oxygen to dissociatively adsorb at room temperature and forms a $(\sqrt{3}\,\mathrm{x}\,\sqrt{3})R30^{o}$ overlayer at 0.4-0.8 L coverage and also a (1 x 1) overlayer is formed after further exposure to oxygen. The oxygen $2p_x, 2p_y\ and\ 2p_z$ derived bands are formed at nearly the same binding energy region indicating that the O $2p_x, 2p_y\ and\ 2p_z$ orbitals have equal contributions to the chemisorption bonding on the (111) surface.

Noda et.al [93] also used PES to study the oxidation of ZrC(111) surface between room temperature and 1000 ^{o}C. At room temperature, oxygen adsorbs dissociatively forming a (1x1) overlayer. Thus at room temperature, oxygen adsorbs dissociatively and settles at a site above the surface plane while it penetrates the surface and settles at a subsurface site at elevated temperatures. The O atom is proposed to adsorb on the three-fold hollow site (between three surface Zr atoms) beneath which the carbon atom in the second layer is absent at room temperature[93]. The authors observed an increase in the work function of the surface ($\Delta\emptyset = 1.0$ eV) at saturation. The work function decreased to ($\Delta\emptyset = -0.55$ eV) for oxidation at 1000 ^{o}C and the adsorbed oxygen penetrates the surface the surface and settles at a subsurface site at 1000^{o}C. A peak caused by O 2p induced bonding state of dissociatively adsorbed oxygen develops at 6.0 eV.

Vojvodic et.al [94] studied atomic and molecular adsorption of various species including oxygen on TMC (111) surfaces using DFT. They used a stoichiometric ZrC(111) slab with Zr terminated on one side and C terminated on the other side of the slab. They studied atomic adsorption of O on ZrC (111) surface and observed the O atom to adsorb at fcc hollow site between three surface Zr atoms. In a study on the adsorption of oxygen on the (100) surface of ZrC, Viñes et.al [95] used periodic DFT, employing both PW91 and PBE exchange correlation functionals. They studied different configurations of oxygen adsorption on the (100) surface and observed oxygen to preferentially adsorb at an mmc site (between two metal atoms and one carbon atom) and also ontop metal configurations of the oxygen atom were observed to be the most stable. They observed changes in the work-function of the (100) surface which is induced by the presence of adsorbed oxygen. The same group [96] also carried out a systematic DFT study of molecular O_2 adsorption and dissociation on the (001) surface of group IV-VI TMC's usnig the projector augmented wave (PAW) formalism using the PW91 GGA functional. An O_2 coverage of 0.5MLwas used with a $\left(\sqrt{2}\,\mathrm{x}\,\sqrt{2}\right)R45^{o}$ unit cell. O_2 was found to adsorb molecularly on two different sites with similar adsorption energies (either bridging two metal atoms or placed directly on top of a metal atom). In order to understand the nature of interaction of O_2 with the TMC surfaces, Bader charge analysis was used together with projected DOS and electron localization function (ELF) plots. They observed the most stable adsorption modes are oxygen bridging two metal atoms with adsorption energy 0.87 eV and oxygen ontop of metal with oxygen atoms pointing to the neighbor carbon atoms with adsorption energy of 0.69 eV. There is an elongation of oxygen molecule inter-nuclear distance from 1.24 Å in vacuum to values around 1.35 Å. The authors also calculated the activation barrier from the molecularly adsorbed O_2 to the dissociatively adsorbed oxygen atoms. Rate constants for O_2 dissociation were also calculated from transition state theory using the vibrational frequency in the harmonic approach to estimate the entropy contribution to the free energy. The reported rate constants are at 300 K and reveals the group IV TMC's as the most active systems for O_2 dissociation due to their high rate constants.

In a photoelectron study by Shin et.al [97] on a $ZrC_{0.93}$ crystal, UPS and XPS were used to study the oxidation of ZrC(100) surface with exposure to O_2 at room temperature. Carbon atoms on the surface get depleted and substrate Zr atoms are oxidized. A zirconium oxide layer is proposed to be formed at lower coverage of < 3 L and this ZrO-like layer becomes a ZrO_x ($1 < x <2$) state with further O_2 exposure. Oxygen adsorption is observed to be nearly saturated at ~30 L. At more than 10 L exposure of O_2, the O 1s peak state settles at 530.6 eV with an asymmetric line shape showing that at least, two types of adsorbed species are present on the ZrC(100) surface. The peak at higher binding energy (B.E) is termed α_1 and the peak observed at 530.6 eV is termed α_2. The authors tentatively assigned the α_1 *and* α_2 states to Zr=O species and Zr oxide respectively. These two peaks however overlap at low coverage. The C 1s peak intensity reduced significantly with O_2 exposure and hence shows C atoms in the surface region are depleted by O_2 exposure, probably due to their desorption as CO or CO_2 molecules. They also observed that, as the ZrC(100) surface is exposed to 100 L of O2 at 300 ^oC, a peak associated with the α_1 (532.3 eV) is removed and only a peak associated with the α_2 state is observed at 530.6 eV evidencing the formation of ZrO_2 on the carbide surface. As the surface is heated at > 500 ^oC, the peak shifts to higher B.E with increasing heating temperature and finally settles at 530.9 eV at $\geq 900^oC$. The extraction of C atoms and the oxidation of Zr atoms occur simultaneously at low coverage. The $3d_{5/2}$ and $3d_{3/2}$ peaks of oxidized Zr atoms are observed at 180-181 eV and 182-183 eV respectively at low coverage (< 3L) while for higher O_2 exposure, a shift at higher energy (182-184 eV) is observed. In a separate work by De Gonzalez and Garcia[98] observed the $3d_{5/2}$ and $3d_{3/2}$ at 179.7 eV and 182.0 eV respectively for $(ZrO)_1$ while assigning them as 180.7 and 183.0 eV for $(ZrO)_2$. They concluded that a ZrO_x (1 < x < 2) oxide layer is formed upon exposure to 10-100 L of oxygen at room temperature.

Håkansson et.al [99] conducted high resolution core level study of ZrC(100) surface and its reaction with oxygen. They used $ZrC_{0.92}$ crystal for the studies. A dissociative adsorption of oxygen on the ZrC (100) surface is recorded in the valence band. The binding energy of C 1s peak in the bulk was initially observed at 281.5 ($\pm$0.1) eV. For the clean surface, the binding energies were determined to be Zr $3d_{5/2}$ level at 179.05($\pm$0.05) eV and a spin orbit split of 2.40 eV. The authors identified ZrO_2 growth by a shifted Zr 3d component and this component is shifted by +4.2 eV. A suboxide is identified by an intermediary shifted Zr 3d component with a chemical shift of between +1 and +2 eV. However, the formation of suboxide complexes involving carbon seems unlikely. Oxidation studies on pure Zr metal has also revealed formation of suboxide layer at initial stages with exposure of < 10 L and ZrO_2 growth at larger exposures of oxygen[100].

Rodriguez et.al [101] combined photoemission spectroscopy with DFT to study the interaction of oxygen with ZrC(001) surface. ZrC0.96-0.99 bulk stoichiometry was used and O_2 was dosed to the surface at 300 or 500 K. Both PW91 and RPBE exchange functionals were used. Oxygen was observed to adsorb dissociatively into a site between two surface Zr and one surface C atom and the $O_{2(gas)} \rightarrow 2O_{ads}$ reaction is very exothermic. The oxygen coverage has substantial effect on oxygen adsorption energy. The observed O 1s peaks at 531-528 eV denotes presence of atomic oxygen on/in the carbide surface/interface. At higher oxygen exposure, curve fitting showed at least two types of oxygen species in the carbide samples. The O 1s peak at ~528.8 eV is close to the position of ZrO_2 as observed by other groups[102] and thus the presence of ZrO_x on the surface together with O atoms chemisorbed on ZrC can be suggested. However, the Zr $3d_{5/2}$ peak position never reached the value of 182.5 eV characteristic of pure ZrO_2[102] even after dosing at 100 L of O_2 at 500 K. C 1s spectra shows peaks at 283.4 and 281.9 eV and the relative intensities shows about 40% of the C atoms near the surface has been perturbed of oxygen and thus the C 1s peaks shift between 1.3-1.6 eV. This points to strong interaction of O and the C sites either by $O \leftrightarrow C$ exchange at the surface or Zr – C bond being replaced by Zr – O and C – C bonds. At 500 K, oxidation of the surface is observed to be fast and clear features of ZrO_x are seen in the O 1s and Zr 3d core level spectra. The calculations show a $C \leftrightarrow O$ exchange being exothermic on ZrC(001) surface and the displaced C atoms bond to mmc sites. In the O/ZrC(001) interface, the C atom plays an important role in determining the behavior of the system. More details into the process of oxidation on the surface was carried out with DFT calculations. The carbon atoms displaced from the surface could react with O adatoms to form gaseous COx species as observed by others[103] and thus the O and C could combine to generate adsorbed CO but this reaction pathway was found to be highly endothermic on the ZrC(001) surface. The formation and removal of CO on the surface is shown in figure I.5.

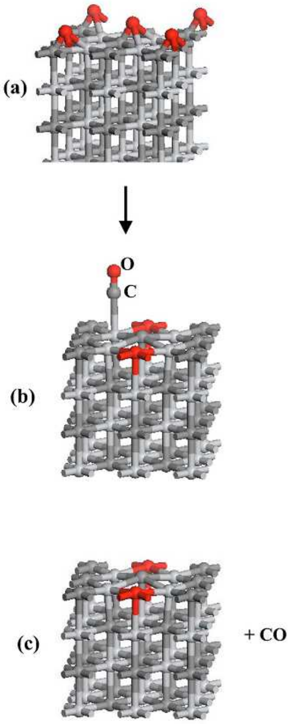

Figure I.5. Formation of CO on ZrC(001) surface. (a) is initial adsorption of 0.5 ML of O on the ZrC(001) surface with each unit cell containing two O atoms (red). One of the O atoms insert into the surface and the other forms CO with the displaced carbon as in (b). In (c), the CO has desorbed from the surface. C atoms are dark grey and Zr atoms are light grey. Figure adapted from reference [101]

As such, the removal of carbon by a single oxygen is essentially impossible. The unfavorable nature for such a process is due to the existence of carbon vacancies in the carbide surface but the vacancies can be avoided if the oxygen coverage is large. For further analysis, the authors observed two O atoms work in a cooperative way to remove one C atom from the surface as shown in figure I.5. The mechanism for removal of a C atom from ZrC(001) as CO gas involves a minimum of two O adatoms, one to take the place of the carbon atom in the surface and the other for the generation of CO.

Instead of focusing on the adsorption and oxidation process of the ZrC surfaces, other studies have concentrated on studying the electronic structure of the oxide layer formed on ZrC surfaces. Kitaoka et.al [104] used ARPES to study the electronic structure of Zr suboxide layer on

ZrC(100) surface. A $ZrC_{0.93}$ single crystal was used for the study. As the (100) surface is exposed to O_2 at room temperature, the C atoms in the substrate are depleted probably due to desorption as CO or CO_2 molecules and the substrate Zr atoms react with oxygen to form Zr oxides. A disordered ZrO_x ($1 < x < 2$) state was observed at more than 10 L oxygen exposure. At elevated temperatures of the exposed surface, the disordered ZrO_x layer is reduced without desorption of O atoms and the ZrO_x layer is formed by heating at ~1000 ^oC. The thickness of the ZrO-like layer could not be determined. The surface gave a well-defined sharp (1 x 1) LEED pattern and there was enhancement in the surface reactivity which is closely related to the modification of the surface electronic structure through the ZrO-like layer formation. Shimada et.al [105] also studied the electronic structure of suboxide films on ZrC (001) surface using DFT. The structure of ZrO-like film on the (100) surface is characterized by a band around 6 eV and a band around the Fermi-level in analysis of DOS plots. The film is observed to be mostly ionic. The suboxide has a rippled structure with the metal and oxygen atoms displaced vertically downward and upward respectively. The thickness of the experimentally obtained film was estimated to be 1.2-2.4 Å.

In a separate study, Shimada et.al [89] studied the $ZrC//ZrO_2$ interface by oxidation of the ZrC single crystals. A $ZrC_{0.97}$ crystal was oxidized isothermally at temperatures of 600-1500 ^oC in a mixed atmosphere of O_2 and argon with O_2 partial pressures of 0.02-2 kPa for 1-20 hrs. Preferred orientations of tetragonal or monoclinic ZrO_2 were occasionally observed on the surface with carbon films at the interface. The tetragonal ZrO_2 particles at several tens of nanometers in size were dispersed in the carbon films. XRD patterns on the crystal oxidized at 600 ^oC for 1 hr and O_2 pressure of 2 kPa shows the presence of cubic ZrO_2 together with the substrate ZrC. After 10 hrs oxidation, (110) orientation of tetragonal ZrO_2 occurs with appearance of small peaks of monoclinic ZrO_2. Further oxidation for 20 hrs still resulted in strong (200) peaks of tetragonal ZrO_2 with gradual growth of monoclinic ZrO_2. At 700 ^oC, mix phases of monoclinic and tetragonal ZrO_2 appears. The XRD results showed preferred (110) or (200) orientation of tetragonal ZrO_2 or a preferred (200) or (220) orientation of monoclinic ZrO_2 on oxidation of the (200) or (220) planes of a ZrC crystal respectively. Also high temperature oxidation at 1500 ^oC revealed tetragonal and monoclinic ZrO_2 from transmission electron microscopy electron diffraction (TEM-ED).

4.2 Reactivity of Hydrogen with ZrC

There is a limited amount of data in the literature concerning adsorption and reactivity of hydrogen with ZrC. Vojovodic et.al [94] used periodic DFT calculation to study the adsorption of atomic hydrogen on ZrC(111) surface. They used a stoichiometric ZrC(111) slab and applied polar corrections. The RPBE exchange correlation functional was used for the calculations. Hydrogen atom was observed to adsorb at fcc hollow sites between three surface Zr atoms.

Matskevich and Krachino [106] studied hydrogen adsorption on ZrC by thermodesorption method. Hydrogen thermodesorption curves were taken after various exposures at the temperatures between 300 – 1450 K. They determined an initial hydrogen adhesion coefficient of $S_0=0.03\pm0.02$ and desorption temperatures in the range of 750-1000 K.

Zhang et.al [107] studied the electronic structure of hydrogen-adsorbed ZrC(111) surfaces and observed that the adsorbed hydrogen atoms are preferably at hollow sites in which the third layer Zr atoms sit directly below them and in this case, the H 1s induced state is separated from the bulk states.

Aizawa et.al [108] studied hydrogen adsorption on TMC (111) surfaces. They also observed hydrogen to adsorb dissociatively on the (111) surface in a three-fold hollow site. They used ARPES to study the hydrogen adsorption and the H-induced site appeared at E_f - 6.5 eV where E_f is the Fermi energy level. Electron energy loss spectroscopy (EELS) was used to study the vibrational frequency of H and D on the ZrC(111) surface. The H-vibrational frequency was observed to vary with the coverage and this might be caused by a lateral interaction between the adsorbate for example a dipole – dipole interaction or an interaction through the substrate metal atom. The observed hydrogen frequency is 113.5 meV (915.4 cm^{-1})

Tokumitsu et.al [109] also studied the interaction of hydrogen with ZrC(111) surface with ARPES. $ZrC_{0.9}$ single crystal was used for the study. At room temperature, hydrogen adsorption was observed to attenuate the (111) surface induced states and causes an H 1s induced split-off state at 6.5 eV at the gamma point at saturation coverage. The hydrogen induced states appear at 6.0 – 6.5 eV and the saturation is reached at about 1.4 L exposure of H_2. The new H 1s band at ~6.0 eV indicates the state is a split-off from the bulk Zr 4d – C 2p band through the bonding interaction, similar to the case of many metal – H systems. The work function of the (111) surface is reduced from 4.6 eV to 4.3 eV at the saturation coverage.

4.3 Reactivity of Water with ZrC

The reactivity of water with ZrC surfaces is very important to consider due to the ubiquitous presence of traces of water in air and other environmental conditions. There is very limited amount of data concerning the hydration of ZrC nano particles.

There has been no reports on the hydration of ZrC(111) and (110) surfaces. The (100) surface is known to be inert towards H_2O adsorption. However, the (100) surface is also known to be activated and a ZrO-like layer is formed and covers the surface and this causes dissociative adsorption of H_2O into OH and atomic O species [104]. The authors in reference [104] observed that, and induced state at the Fermi-level due to the ZrO-like layer on the ZrC(001) surface was responsible for H_2O dissociation. Thus the suboxide film modifies the electronic structure of the (100) surface.

In a separate work, Kitaoka et.al [110] studied the interaction of H_2O with oxygen-modified ZrC(100) surface using XPS and UPS at room temperature with $ZrC_{0.93}$ single crystal. The ZrO-like layer on the (100) surface has an interesting property of a work function which is lower than that of the clean surface by 0.6 eV and the DOS around the Fermi level is increased. From the XPS analysis, a peak observed at 531 eV is ascribed to the O 1s level of O atoms in an ordered ZrO-like layer. A small peak appears at ~533 eV which is not resolved and is also observed in a spectrum of ZrC(100) surface exposed to 50 L O_2. This peak could be attributed to either O atoms which have less negative charge than those in the ZrO-like layer or O atoms surrounded by more positively charged Zr atoms than those in the ZrO-like layer but details of this peak is still not known. As the ordered ZrO-like surface is exposed to 1 L H_2O at room temperature, the two O 1s peaks grow at 530.4 and 532.3 eV, indicating that H_2O adsorbs forming two types of adsorbed species. No water-induced features are observed in XPS or UPS when the ZrC(100) clean surface is exposed to H_2O at least up to 10 L at room temperature. Moreover, as the ZrO-like surface is exposed to 1 L of O_2 instead of H_2O, two peaks appear at 530.4 eV and 532.3 eV but the peak at 530.4 eV now becomes dominant. As such, the authors confirmed the complete indication of the peak at 530.4 eV at the O 1s emission from an atomic O adsorbate formed from the complete dissociation of H_2O or O_2. The peak at 532.3 eV is thus attributed to the O 1s emission from the hydroxyl species formed through partial dissociation of water.

Moreover, according to Noda et.al [92] during the studies on oxygen adsorption on ZrC(111) surface, there was the appearance of an additional hump or peak grow at ~7.0 eV for 0.5 L O_2 exposure and they tentatively attributed this to the emission from the small amount of OH species formed by adsorption of H_2O included in the residual gas because previous studies (unpublished work by Noda et.al) had shown that H_2O adsorbs dissociatively on the unsaturated O/ZrC(111) surface to form OH species whose 1π state is found at 7.0-7.5 eV whereas H_2O does not adsorb on the saturated ZrC(111) (1 x 1) – O surface.

5. Grafting of Polymeric Precursors on ZrC

SiC ceramics derived from polymers are known for their outstanding properties at high temperature[112], [113]. The conventional method that has been used in producing ZrC/SiC composites is to use conventional powders of silicon carbide and zirconium which are mixed and then sintered. However, a problem with this method arises from the step of homogenization of the powder mixture which makes it suitable to use pre-ceramic precursors[114], [115]. The aim of our program is to coat the ZrC surface with SiC. The current method is to use a pre-ceramic polymer for the SiC, these polymers having silicon-bonded substituents. In this section, a survey is provided on all available studies carried out on grafting of organic and polymer precursors on ZrC surfaces. Only a limited number of investigations are available on the grafting of polymeric precursors on ZrC. This is done after initial functionalization of the ZrC surface with other molecules such as water to produce hydroxyl groups. However, the only available surface modification in the literature for ZrC is oxidation[111].

In a recent approach, a preparation of ZrC/SiC composites has been achieved by coating the pre-ceramic polymer SiC on the ZrC particles[116]. The study showed interactions between the vinyl groups of polycarbosilan (PCS) and metallic zirconium in ZrC. The affinity of the vinyl groups on ZrC surface has been exploited for the synthesis of polyvinylsilanes which allows improved microstructural homogeneity of the resulting composite[116]. The nature of the grafting of the polymer precursor of SiC on ZrC has however not been addressed. The molecules used for functionalizing the ZrC surface also has an effect on nature of grafting of the polymeric precursor. Aside oxidation, several other molecules for functionalizing the ZrC surface have been suggested and they include ammonia and radicals of azo initiators[117].

Instead of modifying the ZrC surface for the grip of polymers, other groups[118] have achieved the gripping of these polymers on inorganic surfaces by surface modification of silica particles, for example to modify the surface hydroxyl groups in more reactive functions such as Si-Cl. After this modification, a first step in functionalizing the surface of the nanoparticles is achieved using chloro-silanes with at least two functional Si-Cl groups in the case of Me_2SiCl_2. The Si-Cl residual having a group that has not reacted with the nanoparticle surface is then exploited to introduce an anionic macromolecular chain (polystyrene, polybutadiene) or others obtained by polymerization without transfer reactions or terminations[118]. This method is termed as *grafting-to* since it can covalently bind a macromolecular chain already synthesized. A scheme for the functionalizing inorganic surfaces with Me_2SiCl_2 is shown in figure I.6.

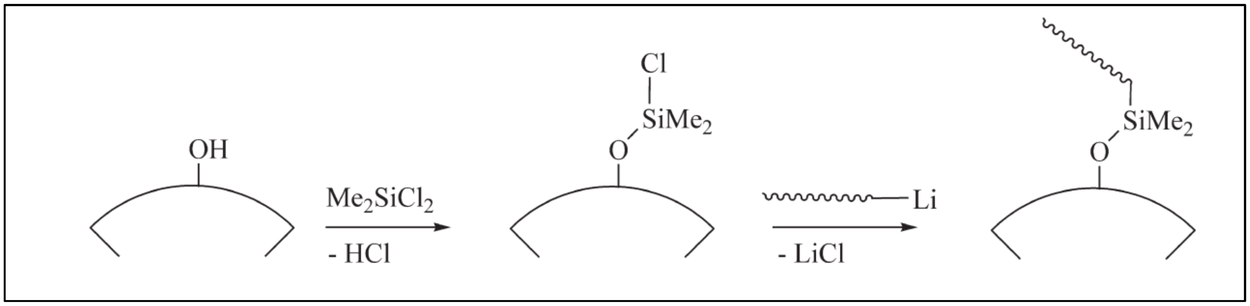

Figure I.6. A scheme for functionalizing inorganic silica surfaces with Me_2SiCl_2 after initial functionalization with water. Figure is adapted from reference [118]

The final *grafting-to* approach for grafting the macromolecule onto the functionalized nanoparticle surface is shown in figure I.7.

Another approach called grafting-from can be utilized to grow the macromolecules directly after attachment of a reactive monomer to the surface of the nanoparticle. Moreover, the hooking of covalent organic macromolecules on inorganic has not yet been described for ZrC.

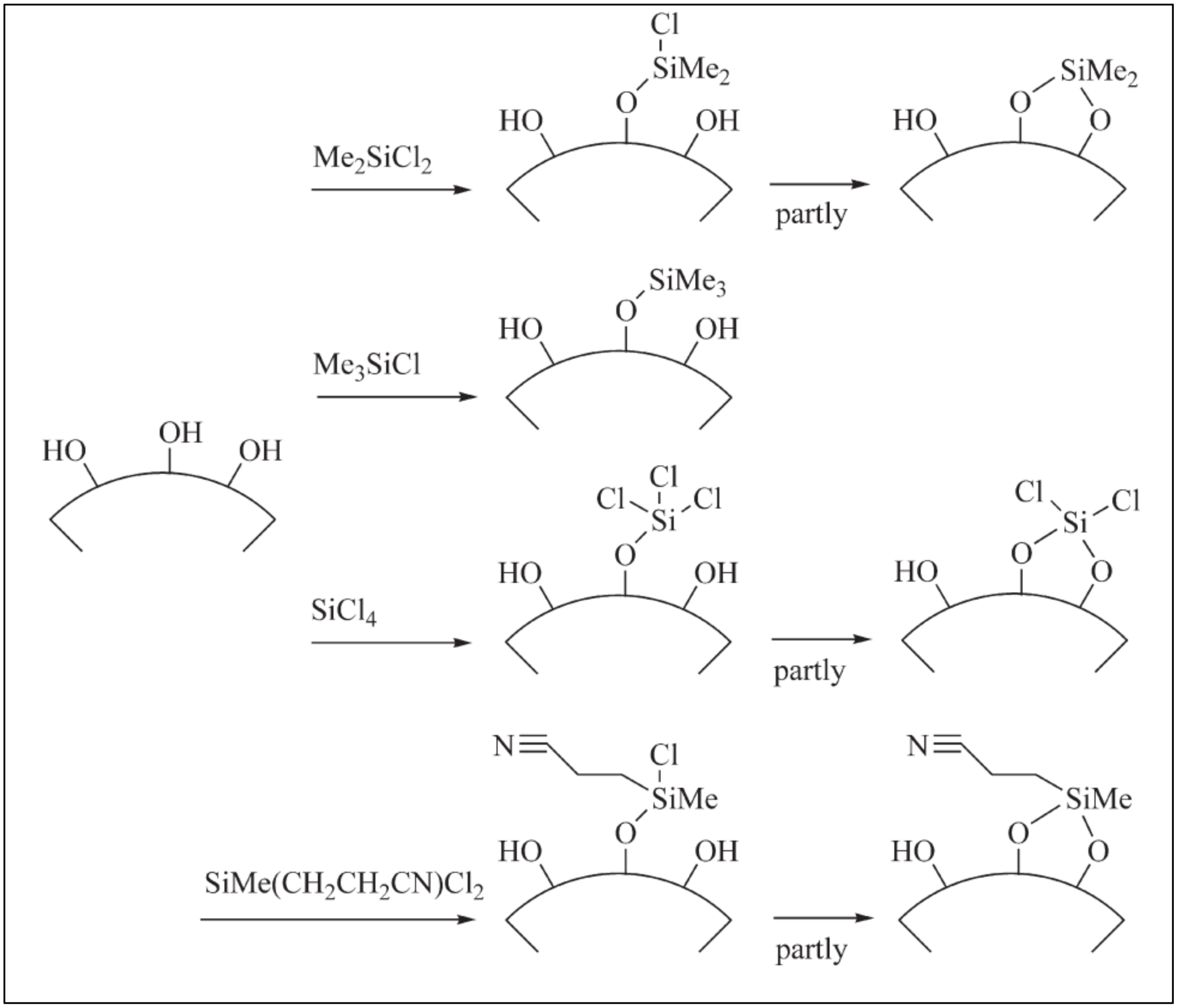

Figure I.7. Functionalization of silica surfaces with Me_2SiCl_2, Me_3SiCl, $SiCl_4$ and $SiMe(CH_2CH_2CN)Cl_2$ in the grafting-to approach. Figure is adapted from reference [118]

6. Program of Research

As has already been discussed in the literature survey, there has been no attempts or whatsoever to control oxidation of ZrC nano particles in order to make use of the excellent physical and mechanical properties that make ZrC suitable for a wide range of applications. Our goal is thus to develop a method for oxidation control on ZrC nano particles. Our method of choice is to coat the ZrC surface with SiC which forms protective layers on ZrC at higher temperatures but are resistant to the formation of oxides at lower temperatures of 300 – 600 ^{o}C, typical of ZrC. Our design approach is shown in figure I.8.

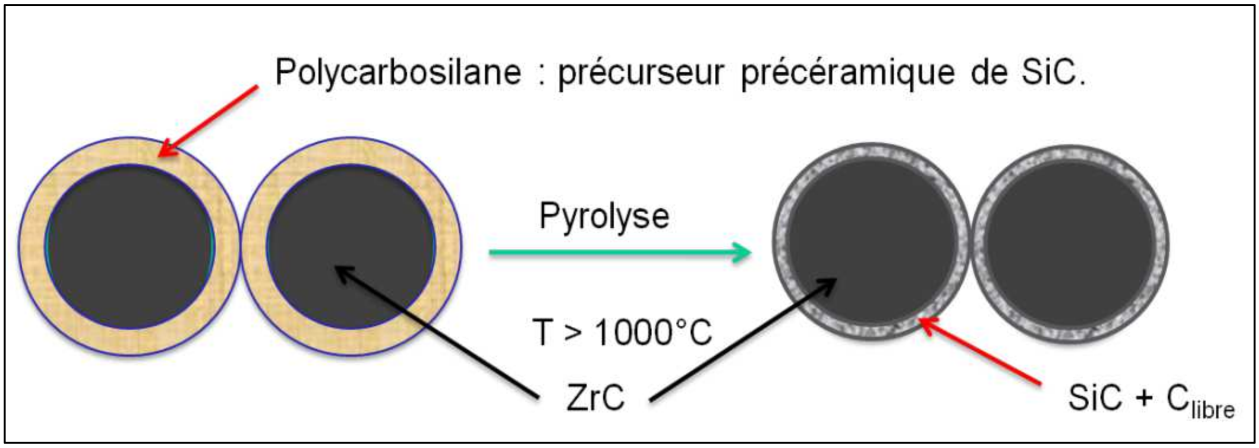

Figure I.8. Core/Shell strategy for synthesizing ZrC/SiC nanocomposites

The main questions that need to be addressed in this project are: (1) nature, stability and properties of the various ZrC low index surfaces (2) The reactivity of ZrC surfaces with oxygen, water and other small inorganic molecules of interest (3) Studies and characterization of interfaces existing between oxide layers and ZrC (4) Functionalization of of ZrC surfaces (5) grafting of polymeric precursors on functionalized ZrC surface.

As this work is part of a multi-institutional project, the theoretical and modeling part carried out will approach the listed problems in the following way:

- Initial studies and characterization of various bulk properties of ZrC

- Studies into all three low index surfaces of ZrC namely (100), (110) and (111) surfaces. The stability and properties of the various surfaces will be addressed and the most stable surfaces will be selected for the further reactivity studies.
- A different approach will be taken into studies on oxidation of ZrC nanoparticles by considering all three surfaces. The adsorption and reactivity studies at 0 K temperature in DFT will be linked to practical environmental conditions through atomistic thermodynamic modeling and equilibrium crystal shapes will identified. This part will also include studies on adsorption and reactivity with other small molecules like hydrogen
- Any interfaces existing between ZrC and oxide layers formed will be addressed with different approaches.
- Functionalization of ZrC surfaces will be done initially with water and if needs be, other organic molecules will be considered.
- Final grafting of polymeric precursors with different Si containing macromolecules will be studied in full detail.

References

[1] R. F. Voitovich and É. A. Pugach, “High-temperature oxidation of ZrC and HfC,” *Sov. Powder Metall. Met. Ceram.*, vol. 12, no. 11, pp. 916–921, Nov. 1973.

[2] J. B. Berkowitz-Mattuck, “High-Temperature Oxidation IV . Zirconium and Hafnium Carbides,” *J. Electrochem. Soc.*, vol. 114, no. 10, pp. 1030–1033, Oct. 1967.

[3] K. Tamura, T. Ogawa, and K. Fukuda, “The oxidation behavior of ZrC coating and powder studied by laser Raman spectroscopy and X-ray diffraction,” *J. Nucl. Mater.*, vol. 175, no. 3, pp. 266–269, Dec. 1990.

[4] S. T. Oyama, “Introduction to the chemistry of transition metal carbides and nitrides,” in *The Chemistry of Transition Metal Carbides and Nitrides*, S. T. Oyama, Ed. Springer Netherlands, 1996, pp. 1–27.

[5] M. Erola, J. Keinonen, A. Anttila, and J. Koskinen, *Solar Energy Mater.*, vol. 12, p. 353, 1986.

[6] C. Ernsberger, J. Nickerson, A. Miller, and D. Banks, “Contact resistance behavior of titanium nitride,” *J. Vac. Sci. Technol. A*, vol. 3, no. 6, pp. 2303–2307, Nov. 1985.

[7] M. Wittmer, “Properties and microelectronic applications of thin films of refractory metal nitrides,” *J. Vac. Sci. Technol. A*, vol. 3, no. 4, pp. 1797–1803, Jul. 1985.

[8] L. E. Toth, *Transition metal carbides and nitrides*. New York: Academic press, 1971.

[9] H. Tracy J., Ph.D, Massachusetts Institute of Technology, Cambridge, MA, 1990.

[10] J. Muller M. and F. Gault G., *Soc. Chim. Fr*, vol. 2, p. 416, 1970.

[11] R. B. Levy and M. Boudart, "Platinum-like behavior of tungsten carbide in surface catalysis," *Science*, vol. 181, no. 4099, pp. 547–549, Aug. 1973.

[12] L. Leclerq, K. Imura, S. Yoshida, T. Barbee, and M. Boudart, "Preparation of Catalysts III," Amsterdam: Elsevier, 1978, p. 627.

[13] M. Boudart and L. D. Ptak, "Reactions of neopentane on transition metals," *J. Catal.*, vol. 16, no. 1, pp. 90–96, Jan. 1970.

[14] S. T. Oyama, "Preparation and catalytic properties of transition metal carbides and nitrides," *Catal. Today*, vol. 15, no. 2, pp. 179–200, Jun. 1992.

[15] G. Hagg, *Z. Phys. Chem, Abt*, vol. 33, p. B12, 1931.

[16] N. Engel, *Ingenioren*, p. N101, 1939.

[17] L. Brewer, "Bonding and Structures of Transition Metals," *Science*, vol. 161, no. 3837, pp. 115–122, Jul. 1968.

[18] S. Ted Oyama, "Crystal structure and chemical reactivity of transition metal carbides and nitrides," *J. Solid State Chem.*, vol. 96, no. 2, pp. 442–445, Feb. 1992.

[19] L. I. Johansson, "Electronic and structural properties of transition-metal carbide and nitride surfaces," *Surf. Sci. Rep.*, vol. 21, no. 5–6, pp. 177–250, 1995.

[20] V. Gubanov A., A. Ianovsky L., and V. Zhukov P., "Electronic Structure of Refractory Carbides and Nitrides," Cambridge: Cambridge University Press, 1994.

[21] L. Ramqvist, K. Hamrin, G. Johansson, A. Fahlman, and C. Nordling, "Charge transfer in transition metal carbides and related compounds studied by ESCA," *J. Phys. Chem. Solids*, vol. 30, no. 7, pp. 1835–1847, Jul. 1969.

[22] H. Goldschmidt, “Process for Synthesis of Metals or Metalloids or Alloys,” DRP 96, 1895.

[23] H. Goldschmidt, *Z. Elektrochem*, vol. 4, p. 494, 1898.

[24] V. Hlavacek, *Ceram. Bull*, vol. 70, p. 240, 1991.

[25] I. Campbell E., *J. Electrochem. Soc.*, vol. 96, p. 318, 1949.

[26] J. Hojo, T. Oku, and A. Kato, *J. Less-Common Met*, vol. 59, p. 85, 1978.

[27] J. S. Lee, S. T. Oyama, and M. Boudart, “Molybdenum carbide catalysts,” *J. Catal.*, vol. 106, no. 1, pp. 125–133, Jul. 1987.

[28] M. J. Ledoux, C. Pham-Huu, S. Marin, M. Weibel, and J. Guille, *C. R. Acad. Sci. Paris*, vol. t. 310, p. 707, 1990.

[29] M. J. Ledoux, J.-L. Guille, C. Pham-Huu, and S. Marin, U.S Patent 5,308,597, 03-May-1994.

[30] M. J. Ledoux, C. P. Huu, J. Guille, and H. Dunlop, “Compared activities of platinum and high specific

surface area Mo2C and WC catalysts for reforming reactions,” *J. Catal.*, vol. 134, no. 2, pp. 383–398, Apr. 1992.

[31] D. Zeng and M. J. Hampden-Smith, “Room-temperature synthesis of molybdenum and tungsten carbides, Mo2C and W2C, via chemical reduction methods,” *Chem. Mater.*, vol. 4, no. 5, pp. 968–970, Sep. 1992.

[32] R. F. Baddour and R. S. Timmins, “The Application of Plasmas in Chemical Processing,” Cambridge: MIT Press, 1967.

[33] B. Ye Paton, “Plasma Processes in Metallurgy and Technology o Inorganic Materials,” Moscow: Nauka Publ. House, 1973.

[34] P. Ho, R. J. Buss, and R. E. Loehman, *J. Mater. Res*, vol. 4, p. 873, 1989.

[35] S. Dressler, *Indust. Heating*, vol. 38, Dec. 1991.

[36] D. Pye, *Indust. Heating*, vol. 38, Dec. 1991.

[37] C. F. Powell, J. H. Oxley, and J. M. Blocker, “Vapor Deposition,” New York: Wiley, 1966.

[38] D. P. Stinton, T. M. Besmann, and R. A. Lowden, *Am. Ceram. Soc. Bull*, vol. 67, p. 350, 1988.

[39] M. Podob, *Indust. Heating*, vol. 23, Dec. 1992.

[40] G. Weiss, *Ann. Chim*, vol. 1, no. 424, p. 446, 1946.

[41] L. Andrieux and G. Weiss, *Bull. Soc. Chim. France*, vol. 15, p. 598, 1948.

[42] E. K. Storms, *The refractory carbides*. New York: Academic Press, 1967.

[43] Y. Katoh, G. Vasudevamurthy, T. Nozawa, and L. L. Snead, “Properties of zirconium carbide for nuclear fuel applications,” *J. Nucl. Mater.*, vol. 441, no. 1–3, pp. 718–742, Oct. 2013.

[44] J. David, G. Trolliard, M. Gendre, and A. Maître, “TEM study of the reaction mechanisms involved in the carbothermal reduction of zirconia,” *J. Eur. Ceram. Soc.*, vol. 33, no. 1, pp. 165–179, Jan. 2013.

[45] A. Maitre and P. Lefort, “Solid state reaction of zirconia with carbon,” *Solid State Ion.*, vol. 104, no. 1–2, pp. 109–122, Dec. 1997.

[46] A. D. Mazzoni and M. S. Conconi, “Synthesis of Group IVB Metals Oxicarbides by Carboreduction Reactions,” *Mater. Res.*, vol. 5, no. 4, pp. 459–466, Oct. 2002.

[47] V. P. Bulychev and R. A. Andrievskii, *Poroshkovaya Metall*, vol. 4, pp. 38–42, 1977.

[48] A. Jain, Master of Science Thesis, Georgia Institue of Technology, 2004.

[49] G. Vasudevamurthy, T. W. Knight, E. Roberts, and T. M. Adams, “Laboratory production of zirconium carbide compacts for use in inert matrix fuels,” *J. Nucl. Mater.*, vol. 374, no. 1–2, pp. 241–247, Feb. 2008.

[50] J. B. Holt and S. D. Dunmead, *Ann. Rev. Mater. Sci*, vol. 21, pp. 305–334, 1991.

[51] I. L. Shabalin, M. V. Luchka, and L. I. Shabalin, *Phys. Chem. Solid State*, vol. 8, no. 1, pp. 159–175, 2007.

[52] M. D. Sacks, C. A. Wang, Z. Yang, and A. Jain, *J. Mater. Sci*, vol. 39, pp. 6057–6066, 2007.

[53] H. J. Ryu, Y. W. Lee, S. I. Cha, and S. H. Hong, “Sintering behaviour and microstructures of carbides and nitrides for the inert matrix fuel by spark plasma sintering,” *J. Nucl. Mater.*, vol. 352, no. 1–3, pp. 341–348, Jun. 2006.

[54] M. Dollé, D. Gosset, C. Bogicevic, F. Karolak, D. Simeone, and G. Baldinozzi, “Synthesis of nanosized zirconium carbide by a sol–gel route,” *J. Eur. Ceram. Soc.*, vol. 27, no. 4, pp. 2061–2067, 2007.

[55] G. H. Reynolds, J. C. Janvier, J. L. Kaae, and J. P. Morlevat, “Irradiation behavior of experimental fuel particles containing chemically vapor deposited zirconium carbide coatings,” *J. Nucl. Mater.*, vol. 62, no. 1, pp. 9–16, Oct. 1976.

[56] K. Ikawa, *J. Less-Common Met*, vol. 27, pp. 325–332, 1972.

[57] K. Ikawa and K. Iwamoto, “Coating Microspheres with Zirconium Carbide-Carbon Alloy by Iodide Process,” *J. Nucl. Sci. Technol.*, vol. 11, no. 6, pp. 263–267, 1974.

[58] K. Ikawa, *J. Less-Common Met*, vol. 44, pp. 207–213, 1976.

[59] T. Ogawa, K. Ikawa, and K. iwamoto, *J. Mater. Sci*, vol. 14, pp. 125–132, 1979.

[60] T. Das, S. Deb, and A. Mookerjee, “Study of electronic structure and elastic properties of transition metal and actinide carbides,” *Phys. B Condens. Matter*, vol. 367, no. 1–4, pp. 6–18, 2005.

[61] J. Li, D. Liao, S. Yip, R. Najafabadi, and L. Ecker, “Force-based many-body interatomic potential for ZrC,” *J. Appl. Phys.*, vol. 93, no. 11, pp. 9072–9085, 2003.

[62] A. Arya and E. A. Carter, “Structure, bonding, and adhesion at the ZrC(100)/Fe(110) interface from first principles,” *Surf. Sci.*, vol. 560, no. 1–3, pp. 103–120, 2004.

[63] E. K. Storms and P. Wagner, *High Temp. Sci*, vol. 5, pp. 454–462, 1973.

[64] R. V. Sara, *J. Am. Ceram. Soc*, vol. 48, pp. 243–247, 1965.

[65] B. H. Morrison and L. L. Sturgess, *Rev. Int. Hautes Temp. Et. Refract*, vol. 7, pp. 351–358, 1970.

[66] P. Haas, F. Tran, and P. Blaha, “Calculation of the lattice constant of solids with semilocal functionals,” *Phys. Rev. B*, vol. 79, no. 8, p. 85104, 2009.

[67] R. Warren, “Measurement of the fracture properties of brittle solids by hertzian indentation,” *Acta Metall.*, vol. 26, no. 11, pp. 1759–1769, Nov. 1978.

[68] H. L. Brown and C. P. Kempter, *Phys. Stat. Sol*, vol. 18, p. K21, 1966.

[69] R. Chang and L. J. Graham, “Low-Temperature Elastic Properties of ZrC and TiC,” *J. Appl. Phys.*, vol. 37, no. 10, pp. 3778–3783, 1966.

[70] V. M. Baranov, V. I. Knyazev, and O. S. Korostin, *Probl. Prochn*, vol. 9, pp. 45–47, 1973.

[71] M. H. Leipold and T. H. Nielsen, *J. Am. Ceram. Soc*, vol. 47, pp. 419–424, 1964.

[72] J. Wang, Y. Zhou, Z. Lin, T. Liao, and L. F. He, “First-principles prediction of the mechanical properties and electronic structure of ternary aluminum carbide Zr3Al3C5,” *Phys. Rev. B*, vol. 73, no. 13, p. 134107, Apr. 2006.

[73] H. Fu, W. Peng, and T. Gao, “Structural and elastic properties of ZrC under high pressure,” *Mater. Chem. Phys.*, vol. 115, no. 2–3, pp. 789–794, 2009.

[74] D. W. Lee and J. S. Haggerty, *J. Am. Ceram. Soc*, vol. 52, pp. 641–647, 1969.

[75] S. Kim, I. Szlufarska, and D. Morgan, “Ab initio study of point defect structures and energetics in ZrC,” *J. Appl. Phys.*, vol. 107, no. 5, p. 53521, Mar. 2010.

[76] D. Gosset, M. Dollé, D. Simeone, G. Baldinozzi, and L. Thomé, “Structural behaviour of nearly stoichiometric ZrC under ion irradiation,” *Nucl. Instrum. Methods Phys. Res. Sect. B Beam Interact. Mater. At.*, vol. 266, pp. 2801–2805, 2008.

[77] H. Baker, Ed., *ASM HANDBOOK, ALLOY PHASE DIAGRAMS*, vol. 3. Materials Park, Ohio: ASM International, 1992.

[78] H. W. Hugosson, O. Eriksson, U. Jansson, and B. Johansson, “Phase stabilities and homogeneity ranges in \$4d\$-transition-metal carbides: A theoretical study,” *Phys. Rev. B*, vol. 63, no. 13, p. 134108, Mar. 2001.

[79] L. Van Brutzel and J. P. Crocombette, *Nucl. Instrum. Methods Phys. Res. B*, vol. 255, p. 141, 2007.

[80] L. Rangaraj, S. J. Suresha, C. Divakar, and V. Jayaram, “Low-Temperature Processing of ZrB2,” *Metall. Mater. Trans. A*, vol. 39, no. 7, pp. 1496–1505, Mar. 2008.

[81] T. F. Viotovich and E. A. Pugach, *Metall*.

[82] Y. V. Miloserdin, K. V. Naboichenko, L. I. Laveikin, and A. G. Bortsov, “The high-temperature creep of zirconium carbide,” *Strength Mater.*, vol. 4, no. 3, pp. 302–305.

[83] G. A. Rama Rao and V. Venugopal, “Kinetics and mechanism of the oxidation of ZrC,” *J. Alloys Compd.*, vol. 206, no. 2, pp. 237–242, May 1994.

[84] S. Shimada and T. Ishi, *J. Am. Ceram. Soc*, vol. 73, 1990.

[85] R. W. Bartlett, M. E. Wadsworth, and I. B. Cutler, *Trans. Metall. Soc*, vol. 227, 1963.

[86] R. E. Bullock and J. L. Kaae, *J. Nucl. Mater*, vol. 115, pp. 69–83, 1983.

[87] S. Shimada, *Solid State Ionics*, vol. 101–103, pp. 749–753, 1997.

[88] S. Shimada, M. Inagaki, and M. Suzuki, “Microstructural observation of the ZrC/ZrO2 interface formed by oxidation of ZrC,” *J. Mater. Res.*, vol. 11, no. 10, pp. 2594–2597, 1996.

[89] S. Shimada, M. Yoshimatsu, M. Inagaki, and S. Otani, “Formation and characterization of carbon at the ZrC/Zro2 interface by oxidation of ZrC single crystals,” *Carbon*, vol. 36, no. 7–8, pp. 1125–1131, 1998.

[90] K. Ozawa, T. Yoshii, T. Noda, K. Edamoto, and S. Tanaka, “Coadsorption of oxygen and cesium on ZrC(111),” *Surf. Sci.*, vol. 511, no. 1–3, pp. 421–434, 2002.

[91] K. Ozawa, T. Fukunaga, T. Nakane, T. Noda, K. Edamoto, and S. Otani, “O2 adsorption on clean and K-modified ZrC(111) surfaces,” *J. Electron Spectrosc. Relat. Phenom.*, vol. 88–91, pp. 801–804, Mar. 1998.

[92] T. Noda, M. Yamazaki, K. Ozawa, K. Edamoto, and S. Otani, “Oxygen adsorption on a ZrC(111) surface: angle-resolved photoemission study,” *Surf. Sci.*, vol. 450, no. 1–2, pp. 27–33, 2000.

[93] T. Noda, T. Nakane, K. Ozawa, K. Edamoto, S. Tanaka, and S. Otani, “Photoemission study of the oxidation of ZrC(111),” *Solid State Commun.*, vol. 107, no. 4, pp. 145–148, 1998.

[94] A. Vojvodic, C. Ruberto, and B. I. Lundqvist, “Atomic and molecular adsorption on transition-metal carbide (111) surfaces from density-functional theory: a trend study of surface electronic factors,” *J Phys Condens Matter*, vol. 22, no. 37, p. 375504, Sep. 2010.

[95] F. Viñes, C. Sousa, F. Illas, P. Liu, and J. A. Rodriguez, “Density functional study of the adsorption of atomic oxygen on the (001) surface of early transition-metal carbides,” *J. Phys. Chem. C*, vol. 111, no. 3, pp. 1307–1314, 2007.

[96] F. Viñes, C. Sousa, F. Illas, P. Liu, and J. A. Rodriguez, “A systematic density functional study of molecular oxygen adsorption and dissociation on the (001) surface of group IV-VI transition metal carbides,” *J. Phys. Chem. C*, vol. 111, no. 45, pp. 16982–16989, 2007.

[97] K. Shin, O. Ken-ichi, E. Kazuyuki, and O. Shigeki, “Photoelectron Spectroscopy Study of the Oxidation of ZrC(100),” *Jpn. J. Appl. Phys.*, vol. 39, no. 9R, p. 5217, 2000.

[98] C. O. De González and E. A. García, “An X-ray photoelectron spectroscopy study of the surface oxidation of zirconium,” *Surf. Sci.*, vol. 193, no. 3, pp. 305–320, Jan. 1988.

[99] K. L. Håkansson, H. I. P. Johansson, and L. I. Johansson, “High-resolution core-level study of ZrC(100) and its reaction with oxygen,” *Phys. Rev. B*, vol. 48, no. 4, pp. 2623–2626, Jul. 1993.

[100] P. Sen, D. D. Sarma, R. C. Budham, K. L. Chopra, and C. N. R. Rao, “An electron spectroscopic study of the surface oxidation of glassy and crystalline Cu-Zr alloys,” *J. Phys. F Met. Phys.*, vol. 14, no. 2, p. 565, 1984.

[101] J. A. Rodriguez, P. Liu, J. Gomes, K. Nakamura, F. Viñes, C. Sousa, and F. Illas, “Interaction of oxygen with ZrC(001) and VC(001): Photoemission and first-principles studies,” *Phys. Rev. B - Condens. Matter Mater. Phys.*, vol. 72, no. 7, 2005.

[102] G. Liu, J. A. Rodriguez, J. Hrbek, J. Dvorak, and C. H. F. Peden, “Electronic and Chemical Properties of Ce0.8Zr0.2O2(111) Surfaces: Photoemission, XANES, Density-Functional, and NO2 Adsorption Studies,” *J. Phys. Chem. B*, vol. 105, no. 32, pp. 7762–7770, Aug. 2001.

[103] P. Frantz and S. V. Didziulis, “Detailed spectroscopic studies of oxygen on metal carbide surfaces,” *Surf. Sci.*, vol. 412–413, pp. 384–396, Sep. 1998.

[104] H. Kitaoka, K. Ozawa, K. Edamoto, and S. Otani, “Electronic structure of the Zr suboxide layer formed on a ZrC(1 0 0) surface,” *Surf. Sci.*, vol. 511, no. 1–3, pp. 359–365, 2002.

[105] T. Shimada, K. Imamura, K. Edamoto, and H. Orita, “Electronic structures of the suboxide films formed on TiC(100) and ZrC(100) surfaces: Density functional theory studies,” *Surf. Sci.*, vol. 603, no. 15, pp. 2340–2344, 2009.

[106] T. L. Matskevich and T. V. Krachino, “Hydrogen adsorption on zirconium carbide and its alloys with rhenium,” *Zhurnal Tekhnicheskoj Fiz.*, vol. 48, no. 3, pp. 534–540, 1978.

[107] Z. Yongfan, L. Junqian, C. Wenkai, and Z. Lixin, “Theoretical Study on the Electronic Structures of the Clean and Hydrogen-adsorbed ZrC(111) Surfaces,” *Acta Chimica Sinica*, vol. 60, no. 10, pp. 1798–1805.

[108] T. Aizawa, W. Hayami, R. Souda, S. Otani, and Y. Ishizawa, “Hydrogen adsorption on transition-metal carbide (111) surfaces,” *Surf. Sci.*, vol. 381, no. 2–3, pp. 157–164, 1997.

[109] S. Tokumitsu, T. Anazawa, A. Tanabe, R. Sekine, E. Miyazaki, K. Edamoto, H. Kato, and S. Otani, “Interaction of hydrogen with ZrC(111) surface: angle-resolved photoemission study,” *Surf. Sci.*, vol. 351, no. 1–3, pp. 165–171, 1996.

[110] H. Kitaoka, K. Ozawa, K. Edamoto, and S. Otani, “The interaction of water with oxygen-modified ZrC(100) surfaces,” *Solid State Commun.*, vol. 118, no. 1, pp. 23–26, 2001.

[111] M. D. K. Ingall, C. H. Honeyman, J. V. Mercure, P. A. Bianconi, and R. R. Kunz, “Surface Functionalization and Imaging Using Monolayers and Surface-Grafted Polymer Layers,” *J. Am. Chem. Soc.*, vol. 121, no. 15, pp. 3607–3613, Apr. 1999.

[112] H. Li, L. Zhang, L. Cheng, Y. Wang, Z. Yu, M. Huang, H. Tu, and H. Xia, “Effect of the polycarbosilane structure on its final ceramic yield,” *J. Eur. Ceram. Soc.*, vol. 28, no. 4, pp. 887–891, 2008.

[113] P. Greil, “Polymer Derived Engineering Ceramics,” *Adv. Eng. Mater.*, vol. 2, no. 6, pp. 339–348, 2000.

[114] M. Gendre, A. Maître, and G. Trolliard, “A study of the densification mechanisms during spark plasma sintering of zirconium (oxy-)carbide powders,” *Acta Mater.*, vol. 58, no. 7, pp. 2598–2609, 2010.

[115] A. W. Weimer, *Carbide, nitride and boride materials synthesis and processing*, 80th ed. Chapman and Hall, 1997.

[116] D. Pizon, R. Lucas, S. Chehaidi, S. Foucaud, and A. Maître, “From trimethylvinylsilane to ZrC–SiC hybrid materials,” *J. Eur. Ceram. Soc.*, vol. 31, no. 14, pp. 2687–2690, 2011.

[117] M. Iijima and H. Kamiya, “Surface Modification of Silicon Carbide Nanoparticles by Azo Radical Initiators,” *J. Phys. Chem. C*, vol. 112, no. 31, pp. 11786–11790, Aug. 2008.

[118] E. Hübner, J. Allgaier, M. Meyer, J. Stellbrink, W. Pyckhout-Hintzen, and D. Richter, “Synthesis of Polymer/Silica Hybrid Nanoparticles Using Anionic Polymerization Techniques,” *Macromolecules*, vol. 43, no. 2, pp. 856–867, Jan. 2010.

Chapter II: Methods and Models

Table of Contents

1. Theories and Backgrounds

As this part of the project involves the use of physical theories in modelling the properties of relevant material systems at the nano-scale level, this chapter introduces the many body theories utilized in condensed matter physics that is applied to the study of solid state systems and adapted for complex molecular systems as well. In this regard, a description of the relevant theories, equations and methods utilized in this project are provides. In this respect, the energy and all other observable physical quantities of a system can be obtained through the solution of a set of equations at the quantum level that embodies all relevant information of the system.

This chapter starts with a description of the quantum mechanical equations that governs the physical properties of many body systems through solution of the many body Halmitonian of the system. The different approaches used in solving the many body Halmitonian such as the Hartree Fock method are discussed with the higher order corrections for accurate description of the system. The density functional theory (DFT) method which is used for this work is further discussed. The theories behind implementation of DFT to periodic systems are included. A further description of the theories used in ab-initio molecular dynamics (MD) simulations, methods for calculating activation barriers, density of states (DOS) implemented in the DFT formalism and atomistic thermodynamic approaches that are combined with the electronic structure calculations are provided here.

2. Many body Hamiltonian

The total energy problem of many body systems are represented by the total Hamiltonian of the system, $\hat{\mathrm{H}}$. This Hamiltonian is given by:

$$\hat{\mathrm{H}} = -\frac{\hbar^2}{2m}\Delta + V \qquad (2.1)$$

Δ is the Laplacian operator and *V* is the potential energy of all particles. Application of the Hamiltonian to the total wavefunction of the system, Ψ yields the non-relativistic Schrödinger equation:

$$\hat{\mathrm{H}}\Psi = E\Psi \qquad (2.2)$$

The wavefunction Ψ is assumed to contain all information of the system and it depends on all the electronic and nuclear coordinates of the system. *E* is the total energy of the system. The Halmitonian operator, $\hat{\mathrm{H}}$ thus contains both kinetic energy and potential energy of the system. Equation 2.2 can then be rewritten as:

$$-\frac{\hbar^2}{2m}\Delta\Psi + V\Psi = E\Psi \qquad (2.3)$$

Equation 2.3 is an eigenvalue problem with the total energy *E* as the eigen value and the wavefunction Ψ as the eigenvector. Definition of boundary conditions are required to solve the eigenvalue problem. In order to relate the purely quantum mechanical property Ψ to physical properties, the concept of observables are introduced for which the total energy *E* is an example. According to the postulates of quantum mechanics, squaring the eigenvector (Ψ) yields the probability density of finding the system at a point in space, the integration over all space yields a probability of 1, for which the system is said to be normalized.

Since the many-body problem involves all particles such as electrons and nucleus of the system, the total Hamiltonian is divided into the kinetic and potential energy parts as:

$$\hat{H} = \hat{T} + \hat{V} \qquad (2.4)$$

The Laplacian kinetic energy operator $\hat{T}$ is divided into both the electronic part, $\widehat{T_e}$ for all N_e electrons and $\widehat{T_n}$ for all N_n nuclear cores. Thus the kinetic energy operator becomes:

$$\hat{T} = \widehat{T_e} + \widehat{T_n} \qquad (2.5)$$

Comparing equations 2.1 with 2.4, the kinetic energy operator can then be written as:

$$\hat{T} = -\sum_{i,k=1}^{N} \frac{\hbar^2}{2m}\Delta \qquad (2.6)$$

For $\widehat{T_e}$ the summation in equation 2.6 runs over i, the mass m of the electrons is m_e, N becomes N_e and the Laplacian operator becomes Δ_i. In terms of the nuclear kinetic energy operator, the summation runs over k, the mass m of nuclear cores become M_n and the nuclear Laplacian becomes Δ_k.

Moreover, the potential energy term $\hat{V}$ of equation 2.4 involves attractive and repulsive potentials between the electrons and the nuclear cores. The potential energy operator is separated into the electron-electron interaction term $\hat{V}_{ee}$, the electron-nuclear electrostatic interaction term $\hat{V}_{ne}$ and the nuclear-nuclear repulsive term $\hat{V}_{nn}$. The total Hamiltonian is then written as:

$$\hat{H} = \hat{T}_e + \hat{T}_n + \hat{V}_{ee} + \hat{V}_{ne} + \hat{V}_{nn} \qquad (2.7)$$

The different potential energy operator terms are defined as:

$$\begin{cases} \hat{V}_{ee} = \displaystyle\sum_{i=1}^{N_e}\sum_{j>i}^{N_e} \frac{e^2}{r_{ij}} \\ \hat{V}_{ne} = -\displaystyle\sum_{i=1}^{N_e}\sum_{k=1}^{N_n} \frac{e^2 Z_k}{r_{ik}} \\ \hat{V}_{nn} = \displaystyle\sum_{k=1}^{N_n}\sum_{l>k}^{N_n} \frac{e^2 Z_k Z_l}{R_{kl}} \end{cases} \qquad (2.8)$$

The many body Hamiltonian can finally be written as:

$$\hat{H} = -\sum_{i=1}^{N_e} \frac{\hbar^2}{2m_e}\Delta_i - \sum_{k=1}^{N_n} \frac{\hbar^2}{2M_n}\Delta_k + \sum_{k=1}^{N_n}\sum_{l>k}^{N_n} \frac{e^2 Z_k Z_l}{R_{kl}} + \sum_{i=1}^{N_e}\sum_{j>i}^{N_e} \frac{e^2}{r_{ij}} - \sum_{i=1}^{N_e}\sum_{k=1}^{N_n} \frac{e^2 Z_k}{r_{ik}} \qquad (2.9)$$

In equation 2.9, R_{kl} is the vector coordinate of k^{th} and l^{th} nuclear cores, r_{ij} is the vector coordinates between the i^{th} and j^{th} electrons, r_{ik} is the vector coordiates between the i^{th} electron and the k^{th} nucleus.

The main problem arising from equation 2.9 is that, we are now faced with a coupled system as the nucleus and electrons interact with each other. Thus the motion of any particle is completely influenced by all other particles. Solution to such a coupled equation (2.9) when inserted into equation 2.1 is non-trivial for most system, except the simplest systems such as the hydrogen atom. Materials of interest are however complex and simulation of realistic systems requires the use other techniques and approximations. This immediately leads to the Born-Oppenheimer approximation.

2.1. The Born-Oppenheimer Approximation

In order to solve the coupled system equation 2.9, an approximate method has to be used. In 1927, Max Born and Robert J. Oppenheimer introduced the Born-Oppenheimer approximation[1] in which the nuclear and electronic degrees of freedom are decoupled from each other. The nuclei are assumed to be much heavier than the electrons and hence the nuclei move much slower than the electrons. This allows the electronic motion to be decoupled from the nuclear motion since the two particles are on different time scales. The electrons are assumed to instantaneously follow the motion of the nuclei. In this respect, the nuclei appears almost stationary due to the timescale of motion of the electrons. The total wavefunction in equation 2.1 can consequently be decoupled into the electronic and nuclear parts:

$$\Psi(r_i\sigma_i, R_n) = \Phi_e(r_i\sigma_i, \{R_n\})\Phi_n(R_n) \tag{2.10}$$

In equation 2.10, $\Phi_e(r_i\sigma_i, \{R_n\})$ is the electronic wavefunction, $\Phi_n(R_n)$ is the nuclei wavefunction, σ_i is the electronic spin coordinate. The term $\{R_n\}$ denotes the nuclear spatial coordinates to be parameters and not variables. The total Hamiltonian in equation 2.1 can then be divided into the electronic and nuclear parts. The electronic part can be written as:

$$\begin{aligned}\widehat{H}_e \Phi_e(r_i\sigma_i,\{R_n\}) &= \left(-\sum_{i=1}^{N_e}\frac{\hbar^2}{2m_e}\Delta_i+\sum_{i=1}^{N_e}\sum_{j>i}^{N_e}\frac{e^2}{r_{ij}}-\sum_{i=1}^{N_e}\sum_{k=1}^{N_n}\frac{e^2Z_k}{r_{ik}}\right)\Phi_e(r_i\sigma_i,\{R_n\}) \\ &= E_e(R_n)\Phi_e(r_i\sigma_i,\{R_n\}) \qquad (2.11)\end{aligned}$$

$E_e(R_n)$ in equation 2.11 denotes the electronic energy which depends parametrically on the nuclear coordinates. This parametric dependence of the electronic energy means that for different arrangements of the nuclei, Φ_e is a different function of the electronic coordinates. If we solve the electronic problem, the motion of the nuclei can be solved under the same assumptions as used to formulate the electronic problem. This then generates a Hamiltonian for the nucleus motion in the average field of the electrons

$$\begin{aligned}\widehat{H}_n &= -\sum_{k=1}^{N_n}\frac{\hbar^2}{2M_n}\Delta_k+\left[-\sum_{i=1}^{N_e}\frac{\hbar^2}{2m_e}\Delta_i+\sum_{i=1}^{N_e}\sum_{j>i}^{N_e}\frac{e^2}{r_{ij}}-\sum_{i=1}^{N_e}\sum_{k=1}^{N_n}\frac{e^2Z_k}{r_{ik}}\right]+\sum_{k=1}^{N_n}\sum_{l>k}^{N_n}\frac{e^2Z_kZ_l}{R_{kl}} \\ &= -\sum_{k=1}^{N_n}\frac{\hbar^2}{2M_n}\Delta_k+E_e(R_n)+\sum_{k=1}^{N_n}\sum_{l>k}^{N_n}\frac{e^2Z_kZ_l}{R_{kl}} \qquad (2.12)\end{aligned}$$

Due to the slow motion of the nuclei compared to the electrons, the nuclear kinetic energy term of equation 2.12 can be ignored and the nuclear-nuclear repulsion term becomes a constant. The total energy for a fixed nuclei thus includes the constant nuclear repulsion term in addition to the electronic energy:

$$E(R_n)=E_e(R_n)+\sum_{k=1}^{N_n}\sum_{l>k}^{N_n}\frac{e^2Z_kZ_l}{R_{kl}} \qquad (2.13)$$

Thus the total energy, $E(R_n)$ provides a potential for nuclear motion and this function constitutes a potential energy surface obtained by solving the electronic problem. In applying the Born-

Oppenheimer approximation, the many-body problem can be restricted to only the electronic part (equation 2.11) which can only be solved exactly for one-electron systems. However, in order to solve the electronic part for many-electron systems, several approximations have to be employed. Several techniques are available for solving the Schrödinger equation. Two common such techniques are the Hartree Fock approximation which is a wavefunction based method and density functional theory among the density based approaches.

2.2 Hartree Fock Method

Even though the Born-Oppenheimer approximation reduces the many-body problem into an electronic problem, a problem which still exists is that, the electronic wavefunction $\Phi_e(r_i\sigma_i, \{R_n\})$ still depends on the spatial and spin coordinates of the electrons. In this section, the Hartree-Fock (HF) procedure for solving the Schrödinger equation which is normally considered as the basis of all *ab-initio* developments is described. The Hartree-Fock approximation however does not include correlation effects.

A procedure for obtaining the ground state energy E_o using the wavefunction of the ground state Ψ_o is the variational principle. According to this principle, the energy computed for the system as the expectation value of the $\hat{H}$ from any guessed wavefunction Ψ_{trial} will be an upper bound to the true energy of the ground state:

$$\langle\Psi_{trial}|\hat{H}|\Psi_{trial}\rangle = E_{trial} \geq E_o = \langle\Psi_o|\hat{H}|\Psi_o\rangle \qquad (2.14)$$

$E_{trial} = E_o$ if and only if $\Psi_{trial} = \Psi_o$

For the variational principle, in order to find the ground state energy, the energy functional $E[\Psi]$ needs to be minimized by searching through all acceptable N-electron wavefunctions. These trial wavefunctions must satisfy certain requirements to ensure they make physical sense. The lowest energy is given by the wavefunction Ψ_o and this lowest energy is the ground state energy E_o.

$$E_o = \min_{\Psi\rightarrow N} E[\Psi] = \min_{\Psi\rightarrow N}\langle\Psi|\hat{T} + \hat{V}_{ne} + \hat{V}_{ee}|\Psi\rangle \qquad (2.15)$$

The search for this wavefunction is however a tedious task and a subset of wavefuntions are usually employed for which the result is an approximation to the exact wavefunction. Thus it is practically impossible to solve equation 2.15 by searching through all acceptable N-electron wavefunctions. There is the need for a suitable subset that offers good approximation to the exact wavefunction. The HF method uses the simplest approximation to the complicated many-electron wavefunction.

Hartree considered the electron motions are independent and uncorrelated.[2] Within this approximation, each individual electron can be considered as moving in an average field generated by all other electrons. Later in 1930, Fock[3] combined the ideas from Hartree and expressed the overall wavefunction as a simple product of single particle wavefunctions in which the fermionic character of electrons is taken into account by using anti-symmetric sum products of the single particle wavefunctions $\varphi_i(r_i\sigma_i)$. A single Slater determinant Ψ_{SD} is used to represent the simplest ansatz of such representation.

$$\Psi_{SD} = \frac{1}{\sqrt{N!}} \begin{vmatrix} \varphi_1(r_1\sigma_1) & \varphi_2(r_2\sigma_2) & \dots & \varphi_1(r_N\sigma_N) \\ \varphi_1(r_1\sigma_1) & \varphi_1(r_1\sigma_1) & \dots & \varphi_1(r_N\sigma_N) \\ . & . & & . \\ . & . & & . \\ . & . & & . \\ \varphi_N(r_1\sigma_1) & \varphi_N(r_1\sigma_1) & \dots & \varphi_N(r_N\sigma_N) \end{vmatrix} \qquad (2.16)$$

The one electron wavefucntions $\varphi_i(r_j\sigma_j)$ describes electron *i* at the position of electron *j*. They are called spin orbitals and are composed of a spatial orbital and one of the spin functions. Replacing of the true N-electron wavefunction Ψ_{exact} with a single slater determinant is however a drastic approximation. The variational principle is then used to find the best slater determinant which yields the lowest energy. The spin orbitals are varied under the constraint that they remain orthonormal in such a way that the energy obtained from corresponding Ψ_{SD} is minimal:

$$E_{HF} = \min_{\Psi_{SD} \to N} E[\Psi_{SD}] \qquad (2.17)$$

The orthonormal constrain of the spin orbitals $\varphi_i(r_j\sigma_j)$ is given by:

$$\delta\left\{E_e - \sum_{i,j=1}^{N_e} \varepsilon_{ij}\ \langle\varphi_i|\varphi_j\rangle\right\} = 0 \tag{2.18}$$

This orthonormal constraint introduces the Langragian multipliers ε_{ij} in equation 2.18 which eventually leads to the HF equations which determines the best spin orbitals for which E_{HF} attains its lowest value:

$$\hat{F}(r_i)|\varphi_i\rangle = \sum_{j=1}^{N_e} \varepsilon_{ij}|\varphi_j\rangle,\ \ i = 1,2\ \ldots .N_e \tag{2.19}$$

These N_e equations have the appearance of eigenvalue equations were ε_{ij} are the eigenvalues of the operator $\hat{F}(r_i)$ with the physical interpretation of the ε_{ij} being orbital energies. $\hat{F}(r_i)$ is the Fock operator which is an effective one electron operator and can be written as:

$$\hat{F}(r_i) = \hat{t}_i - \sum_{n=1}^{N_n} \frac{Z_n}{|r_i - R_n|} + \sum_{j=1}^{N_e} \int \varphi_j^*(r') \frac{1}{|r_i - r'|} \varphi_j(r')\, dr' + V_x(r_i) \tag{2.20}$$

The kinetic energy term is given by $\hat{t}_i$ and $V_x(r_i)$ arises from the Pauli's exclusion principle. This term explains the non-local exchange for which there is no classical analogue. This non-local exchange term is given by:

$$V_x(r_i) = -\sum_{j=1}^{N_e} \frac{1}{|r_i - r'|} \frac{\varphi_j^*(r')\varphi_j(r_i)\varphi_i^*(r_i)\varphi_i(r')}{\varphi_i^*(r_i)\varphi_i(r_i)}\, dr' \tag{2.21}$$

Practical calculation of $V_x(r_i)$ is extremely difficult due to its non-local exchange nature. In this respect, the exchange integral for a free electron has been shown independently by Dirac[4] and

Bloch[5] that it can be expressed as a function of the electronic density. This idea was later generalized by Slater[6], [7] through the inclusion of a scaling factor X_β to the free electron gas expression.

$$V_x(r_i) = -3X_\beta \left(\frac{3}{8\pi}\,\varrho(r_i)\right)^{1/3} \tag{2.22}$$

This scaling factor is 2/3 for the free electron gas. Insertion of equation 2.22 into equation 2.20 yields the Hartree-Fock-slater equation (HFS).

2.2.1 Post Hartree-Fock Methods

As mentioned earlier, in the HF approximation, there is no consideration of electron correlation. This is a serious limitation as it does not consider electrons interacting with each other. Thus Ψ_{SD} never corresponds to the exact wavefunction and due to the variational principle, E_{HF} is always larger (less negative) than the exact ground state energy E_o. The difference between them is the correlation energy, E_c^{HF}.

$$E_c^{HF} = E_o - E_{HF} \tag{2.23}$$

E_c^{HF} is always negative because Eo and EHF are less than 0 and is a measure of the error introduced through the HF scheme. Electron correlation is caused by instantaneous repulsion of the electrons. The correlation is separated into two parts. The first part called the *dynamical correlation* relates to the responsiveness of electrons to interacting with each other and is controlled by the $1/|r_i - r'|$ term in the Hamiltonian. The second part called the non-dynamical or static electron correlation relates to how real systems energy is due to contributions from several accessible electronic states. Thus this parts relates to the fact that in some cases, the ground state Ψ_{SD} is not a good approximation to the ground state because there are other Ψ_{SD} with comparable energies. In this respect, the HF theory treats neither of these contributions and hence is not adequate enough to make chemical determinations that are reliable. As such, additional corrections have been developed to account for these shortcomings. Among these corrections include the full configurational Interaction (CI), Møller-Plesset perturbation theory (MPn), complete active space (CAS), or the coupled cluster methods (CC). A major part of these methods are completely first principles based methods and introduces no empirical data into their calculations.

2.2.1.1 General Perturbation Theory

In perturbation theory, the assumption is that the magnitude of a perturbation on the calculation is very small as compared to the unperturbed system. This assumption can be used to the advantage of correcting the correlation energies in HF theory. This is valid because the electron correlation energy is small compared to the HF energy. In applying perturbation theory to quantum mechanics, the total Hamiltonian of the system is divided into the unperturbed reference Hamiltonian $\widehat{H}_o$ plus the Hamiltonian corresponding to the correction applied to the system, $\widehat{H}'$ multiplied by a scaling factor λ. The scaling factor determines the strength of the perturbation applied.

$$\widehat{H} = \widehat{H}_o + \lambda\widehat{H}' \tag{2.24}$$

The eigenvalue problem now becomes

$$\widehat{H}|\Psi\rangle = \left(\widehat{H}_o + \widehat{H}'\right)|\Psi\rangle = E|\Psi\rangle \tag{2.25}$$

Since the eigenvalues and eigenfunctions of unperturbed Hamiltonian $\widehat{H}_o$ are known, equation 2.25 can be expanded in a Taylor series as:

$$E_n = E_n^{(0)} + \lambda E_n^{(1)} + \lambda^2 E_n^2 + \cdots \tag{2.26}$$

$$|\Psi_n\rangle = \left|\varphi_n^{(0)}\right\rangle + \lambda\left|\varphi_n^{(1)}\right\rangle + \lambda^2\left|\varphi_n^{(2)}\right\rangle + \cdots \tag{2.27}$$

The unperturbed Hamiltonian is given by the HF theory and the other perturbations come from the electron correlation. The zeroth order energy is the expectation value of $\widehat{H}_o$ with the zeroth order wave function. The first two orders of correction in the Taylor expansion to the energy of an electronic state n are given by:

$$E_n^{(1)} = \left\langle \Psi_n^{(0)} \middle| \widehat{H}' \middle| \Psi_n^{(0)} \right\rangle \tag{2.28}$$

$$E_n^{(2)} = \sum_{j \neq n} \frac{\left| \left\langle \Psi_n^{(0)} \middle| \widehat{H}' \middle| \Psi_n^{(0)} \right\rangle \right|^2}{E_n^{(0)} - E_j^{(0)}} \tag{2.29}$$

In MØller-Plesset perturbation, $\widehat{H}_o$ is a sum of one electron Fock operators. The electronic HF energy is given by $E_n^{(0)} + E_n^{(1)}$ while the other terms $E_n^{(i>1)}$ corrects the HF energy for correlation effects. The MP2 method includes the first additional correction term $E_n^{(2)}$ while MP3, MP4, etc corrects with higher terms.

The main problem with MØller-Plesset perturbation is that, evaluation of even the first correction terms becomes very expensive as the number of electrons increases. Though the HF method's computational time scales as N^2, the MP2 scales as N^4 with N being the number of electrons.

2.2.1.2 Configuration Interaction (CI)

The main problem encountered in the HF method was the use of a single slater determinant which might be different from the exact wave function. In the CI method, the system's wave function is described with more than one Slater determinant. In this way, HF determinant is also called the ground state determinant. The slater determinants used in the CI method differs from that of the HF method by a number of additional orbitals. Thus instead of using a single slater determinant as in the HF method, a linear combination of Slater determinants is used. This allows for the introduction of excited Slater determinants. These excited determinants can be single, double, triple, etc. Since all possible determinants can be described by reference to the HF determinant, the exact wave function for any state of the system can be written as:

$$|\Psi\rangle = C_o|\varphi_o\rangle + \sum_{ra} C_a^r|\varphi_a^r\rangle + \sum_{\substack{a<b \\ r<s}} C_{ab}^{rs}|\varphi_{ab}^{rs}\rangle + \sum_{\substack{a<b<c \\ r<s<t}} C_{abc}^{rst}|\varphi_{abc}^{rst}\rangle + \cdots \tag{2.30}$$

The labels a, b, c are the occupied molecular states and r, s, t are the virtual states. The second, third and fourth terms on the right hand side of equation 2.30 is the single, double and third excitations. The infinite set of N_e-electron determinants can be written as $\{|\Psi_i\rangle\} = \{|\varphi_o\rangle, |\varphi_a^r\rangle, |\varphi_{ab}^{rs}\rangle, \dots\}$ is a complete set for the expansion of any N_e-electron wave function. The exact energies of the ground and excited states of the system are the eigenvalues of the Hamiltonian matrix formed from the complete set $\{|\Psi_i\rangle\}$. The lowest value of the Hamiltonian matrix denoted by $\mathcal{E}_o$ is the exact non-relativistic ground state energy of the system within the Born-Oppenheimer approximation. The difference between this exact energy $\mathcal{E}_o$ and the HF energy E_o is the correlation energy, E_{corr}.

$$E_{corr} = \mathcal{E}_o - E_o \tag{2.31}$$

In a full-CI, all possible determinants are included in the expansion of the CI wave function. However, the number of determinants that must be included in a full-CI is extremely large even for relatively small systems. In practice, the full-CI expansion must be truncated and only a small fraction of the possible determinants used. The most practical approaches takes into account only determinants to certain excitation levels. Examples of such approaches include single excitation CI (CIS), single and double excitations (CISD), and single, double, triple excitations (CISDT) among others. In all such approaches, the variational principle is applied to achieve minimization of the coefficients in order to obtain the ground state energy.

2.3 Density Functional Methods

The above HF and post-HF methods described uses many-body wavefunctions which are often expensive. However, the electron density is rather used at the only basic variable in evaluating the total energy and other physical properties of a system in density based methods. The earliest models using electron density as the basic variable was introduced by Thomas and Fermi in the Thomas Fermi (TF) model.

2.3.1 The Thomas-Fermi Model

The electronic part of the many-body problem is difficult to handle as it depends on 4*N_e* coordinates with Ne electrons, $\Psi\big(r_1\sigma_1, \dots\dots,\ r_{N_e}\sigma_{N_e}\big)$ and this $4N_e$ coordinates include the spin coordinates of the electrons. The Thomas-Fermi model[8], [9] is a simple approach where the electron density of the system ϱ(r) is used as the basic variable. Within a volume element *dr*, the electron density of Ne electrons depends on only three independent coordinates and this is a very important feature of this model. The electron density is thus given by:

$$\varrho(r) = \sum_{i=1}^{N_e} \int \Psi\big(r_1\sigma_1, \dots\dots, \sigma_{N_e}\big)^{*} \delta(r_i - r)\, \Psi\big(r_1\sigma_1, \dots\dots, r_{N_e}\sigma_{N_e}\big) d(r_1\sigma_1) \dots d\big(r_{N_e}\sigma_{N_e}\big) \quad (2.32)$$

By using the kinetic energy density of a homogenous electron gas to approximate for that of the system, the total energy functional $E^{TF}[\varrho(r)]$ formulated by Thomas and Fermi is given as:

$$E^{TF}[\varrho(r)] = \frac{3(3\pi^2)^{2/3}}{10} \int \varrho(r)^{5/3} dr - \sum_{j=1}^{N_n} \frac{Z_n \varrho(r)}{|r - R_n|} dr + \frac{1}{2} \iint \frac{\varrho(r)\varrho(r)'}{|r - r'|} dr dr' \qquad (2.33)$$

In equation 2.33, the second and third terms on the right side are the classical electrostatic electron-nucleus attraction and electron-electron repulsion while the first term is the kinetic energy of the non-interacting electrons. The exchange energy which has no classical analogue was later on introduced by Dirac[4] into the TF model.

$$E_x^{Dirac} = -\frac{3}{4}\left(\frac{3}{\pi}\right)^{1/3} \int \varrho(r)^{\frac{4}{3}}\, dr \qquad (2.34)$$

Though the energies calculated with the TF model are too high, the Thomas-Fermi-Dirac (TFD) model accounts for this by the inclusion of the exchange term. Due to the poor description of the kinetic energy in this model, it does not yield accurate calculations of total energies for chemical predictions even after the Dirac correction. Moreover, it is the starting point for density functional theory (DFT) for solving multi-electron system problems.

2.3.2 The Hohenberg-Kohn Theorems

Two fundamental theorems are the basis of DFT and they were mathematically formulated and proved by both Hohenberg and Kohn[10] for non-degenerate ground states of systems. Within the first theorem, the electron density of a system is considered to uniquely determine the external potential due to the ions or nuclei to within a certain constant. This means that the total electronic energy of a system E can be expressed as a functional of the electron density ϱ alone.

$$E[\varrho] = T[\varrho] + \int \varrho(r)V_{ext}(r)dr + E_{ee}[\varrho] \qquad (2.35)$$

In equation 2.35, $T[\varrho]$ and $E_{ee}[\varrho]$ are the kinetic energy and electron-electron interaction energies and are both functionals. A further definition of the Hohenberg-Kohn functional, $F_{HK}[\varrho]$ using these two above functionals give:

$$F_{HK}[\varrho] = T[\varrho] + E_{ee}[\varrho] \qquad (2.36)$$

Substitution of the Hohenberg-Kohn functional into equation 2.35 yields:

$$E[\varrho] = \int \varrho(r)V_{ext}(r)dr + F_{HK}[\varrho] \qquad (2.37)$$

For an explicit expression for the Hohenberg-Kohn functional, there will be an exact solution for the Schrödinger equation. However, the electron-electron interaction term $E_{ee}[\varrho]$ can be expressed as two parts:

$$E_{ee}[\varrho] = J[\varrho] + E^{non-loc}[\varrho] \tag{2.38}$$

The first part on the right side of equation 2.38 is the classical Coulomb repulsion term while the second term contains all other interactions such as the self-interaction correction, exchange, and Coulomb correlation energy.

The second aspect of the Hohenberg-Kohn theorem utilizes the variational principle to obtain the energy of the exact functional. Within this approach, the ground state density $\varrho_o(r)$ is the density which minizes $E[\varrho]$:

$$E_o = E[\varrho_o(r)] \leq E[\varrho(r)] \tag{2.39}$$

Equation 2.39 is satisfied when the following conditions are met

$$\varrho_o(r) \geq 0 \ \ and \ \int \varrho_o(r)dr - N_e = 0 \tag{2.40}$$

The Euler-Lagrange equation under the constraint of a constant number of electrons, N_e is fulfilled during the energy minimization procedure and this can be written as:

$$\mu = \frac{\delta E[\varrho(r)]}{\delta \varrho(r)} = V_{ext}(r) + \frac{\delta F_{HK}[\varrho(r)]}{\delta \varrho(r)} \tag{2.41}$$

The Lagrange multiplier μ in defines the chemical potential of the electrons. Even though the Hohenberg-Kohn theorem provides all the ground state properties of the system, it does not provide the means of finding the universal functional $F_{HK}[\varrho(r)]$ and the search for this functional is still an active field of research

2.3.3 The Kohn-Sham Equations

In the Hohenberg-Kohn theorem, the exact form of the kinetic energy functional $T[\varrho]$ is not given. In another approach, Kohn and Sham decomposed this kinetic energy functional into two parts in order to provide an approximation for the Hohenberg-Kohn functional $F_{HK}[\varrho(r)]$. This decomposition yields a first part as the kinetic energy of non-interacting electrons T_s given as while the second part contains all remaining and neglected interactions in the non-interacting system (T-T_s)

$$T_s = -\frac{1}{2}\sum_{i=1}^{N_e}\langle \emptyset_i|\nabla^2|\emptyset_i\rangle \qquad (2.42)$$

$\emptyset_i$ in equation 2.42 are the Kohn-Sham orbitals. The other part of the Hohenberg-Kohn functional (T_s-T) is a small correction and hence is included alongside the non-classical part of the electron-electron interaction $E^{non-loc}$ in equation 2.38. The combination of these two leads to the exchange correlation (xc) energy term which is defined as:

$$E_{XC}[\varrho] = (T[\varrho] - T_s[\varrho]) + (E_{ee}[\varrho] - J[\varrho]) \qquad (2.43)$$

By substituting the exchange correlation functional of equation 2.43 into the energy functional of equation 2.35, we obtain the following:

$$E[\varrho] = T_s[\varrho] + \int \varrho(r)V_{ext}(r)dr + J[\varrho] + E_{XC}[\varrho] \qquad (2.44)$$

The main challenge in DFT is finding suitable expressions for the $E_{XC}[\varrho]$ term as it contains all contributions that are not known in an exact manner. If we make the following definition:

$$V_{eff}(r) = V_{ext}(r) + \int \frac{\varrho(r')}{|r - r'|} dr' + V_{XC}(r) \tag{2.45}$$

The Euler-Lagrange expression of equation 2.41 can now be written as:

$$\varepsilon_i \frac{\delta\varrho(r)}{\delta\emptyset_i} = \frac{\delta E[\varrho(r)]}{\delta\varrho(r)} \frac{\delta\varrho(r)}{\delta\emptyset_i} = \frac{\delta T_s[\varrho(r)]}{\delta\emptyset_i} + V_{eff}(r) \frac{\delta\varrho(r)}{\delta\emptyset_i} \tag{2.46}$$

The exchange correlation potential $V_{XC}(r)$ in equation 2.45 is defined as:

$$V_{XC}(r) = \frac{\delta E_{XC}[\varrho(r)]}{\delta\varrho(r)} \tag{2.47}$$

In order to obtain the solution for the Euler-Lagrange expression in equation 2.46, the following set of one-particle equations are solved in a self-consistent field (SCF) procedure.

$$\left[-\frac{1}{2}\nabla^2 + V_{eff}(r)\right]\emptyset_i = \varepsilon_i \emptyset_i \tag{2.48}$$

The electron density of the real system is however constructed from the Kohn-Sham orbitals and is given as:

$$\varrho(r) = \sum_{i=1}^{occ} |\emptyset_i(r)|^2 \tag{2.49}$$

The summation in equation 2.49 runs over all the occupied orbitals. The Kohn-Sham equations are represented by equations 2.45, 2.48 and 2.49. In using the SCF approach, the procedure is started with an initial guess of $\varrho(r)$ to determine the V_{eff} and then obtain a new $\varrho(r)$ from equations 2.48 and 2.49. The procedure is repeated until the $\varrho(r)$ converges, at which point the total energy of the system is obtained.

2.3.4 The Exchange Correlation Functionals

Even though the density based methods reduced the complications of the many-body problem found in wavefunction based methods, the primary distinguishing feature of all DFT implementations is the different approaches used in approximating the exchange correlation functional.

2.3.4.1 Local (Spin) Density Approximation (L(S)DA)

In the Local density approximation, a uniform electron gas is used for estimating the exchange correlation energy of an inhomogeneous system. The exchange correlation energy can be calculated:

$$E_{XC}^{LDA}[\varrho] = \int \varrho(r)\varepsilon_{XC}\big(\varrho(r)\big)dr \qquad (2.50)$$

The $\varepsilon_{XC}\big(\varrho(r)\big)$ term is the exchange correlation energy per particle of the uniform electron gas and this term can be split into an exchange and a correlation part.

$$\varepsilon_{XC}\big(\varrho(r)\big) = \varepsilon_{X}\big(\varrho(r)\big) + \varepsilon_{C}\big(\varrho(r)\big) \qquad (2.51)$$

The Dirac expression in equation 2.34 is used to define the exchange part $\varepsilon_{X}\big(\varrho(r)\big)$ and the correlation part is normally calculated by Monte Carlo (MC) simulations. The LSDA is an extended version of the LDA where the spin of the electrons are taken into account. In this way, the electron density $\varrho(r)$ in equations 2.50 and 2.51 is split into the "spin-up" and "spin-down" configurations.

Though the LDA uses a uniform electron gas for the approximation, it turns out that it is very good and accurate in many applications such as electronic and structural ground state properties.

It overestimates bond energies even though molecular geometries and vibrational frequencies are reasonably estimated.

2.3.4.2 Generalized Gradient Approximation (GGA)

A modification is made to the LDA to account for the inadequacies of the homogenous electron gas assumption. This modification is the introduction of a density gradient into the LDA approximation.

$$E_{XC}^{GGA}[\varrho] = \int \varrho(r)\varepsilon_{XC}\big(\varrho(r)\big), \nabla\varrho(r)dr \tag{2.52}$$

Different implementations of the GGA are developed by several groups. One popular such form of the GGA is developed by Perdew, Burke and Ernzerhof (PBE)[11] is widely used. Physical properties calculated by the GGA are normally better than those obtained by the LDA and LSDA in most cases.

Several other improvements to the GGA such as the meta-GGA exists. This includes the kinetic energy density. It however does not provide significant improvement to the results obtained by GGA.

2.4 Periodic Systems

The electronic structure calculation of extended systems such as bulk, surface, crystals with infinite number of electrons is an impossible task though the DFT formulation simplifies the many-body problem. The calculation of extended systems is however made feasible by assuming boundary periodic boundary conditions and utilizing Bloch's theorem.[12]

In the Bloch's theorem, the assumption is that, the electronic wavefunction of a periodic system can be represented as a product of a periodic function $u_{n,k}$(r) and a plane wave.

$$\vartheta_{n,k} = u_{n,k}(r)e^{ik.r} \tag{2.53}$$

The wave vector that lies inside the first Brillouin zone (BZ) is given by k, n defines the band index and provides labels for the wavefunctions of a given k. The periodic function however has the periodicity of the supercell used and hence can be expanded using a set of plane waves.

$$u_{n,k}(r) = \sum_{G} c_{n,k}(G)e^{iG.r} \tag{2.54}$$

The reciprocal lattice vectors which fulfills the boundary condition of the unit cell (G. L = 2πv) are defined by the wave vectors G. An integration into the reciprocal space yields the physical quantities of the system such as the electron density and the total energy. The numerical integration over the BZ can be performed as a sum over a finite number of k-points (mesh).

$$\int_{BZ}^{.} \frac{1}{\Omega_{BZ}} dk \rightarrow \sum_{k} w_k \tag{2.55}$$

The volume element of the BZ in the unit cell is given by Ω_{BZ}. The denser the k-points utilized, the minimal the error introduced by this approximation. However, the computational cost grows very quickly with the number of k-points used. Hence, one has to always check convergence of the system with respect to the k-points used in order to avoid unnecessary computational efforts. In molecules, liquids and large enough simulation cells, the BZ can be sampled using only the k = 0 (Γ) point.

Based on the above explanations of the periodic function, the electronic wavefunction should contain an infinite number of plane waves. This is less practical and in reality, only a finite number of the plane waves, up to a certain energy cutoff called the E_{cutoff} is used to provide a sufficiently accurate result.

$$\frac{1}{2}|k+G|^2 \le E_{cutoff} \tag{2.56}$$

With all these assumptions and simplifications, periodic systems can then be modelled by concentrating on the smallest unit cell that is periodically repeated over all space.

In this project, the energy cutoff for the ZrC system is tested for convergence from 200 eV up to 600 eV. This was done but calculating the ground state energy, E_o for the system at different E_{cutoff} values. A plot of this test is shown in figure II.1. The energy cutoff is found to converge at 500 eV. This value is used for all calculations involving ZrC.

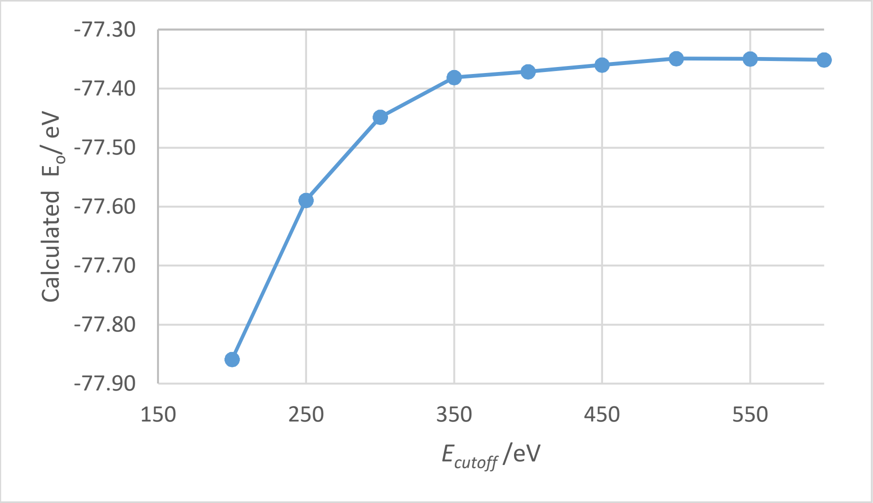

Figure II.1. Energy cutoff of ZrC bulk

A similar test was done for the k-point mesh. In this case, the standard Monkhorst-Pack[13] special grid was used for the evaluation starting from a 2 x 2 x 2 grid to 11 x 11 x 11 grid. The convergence criteria established was a 9 x 9 x 9 k-points for the BZ integration in bulk ZrC and 9 x 9 x 1 k-points for surface calculations.

2.5 Pseudo-Potentials

Valence electrons mostly govern chemical bonding, reactions and physical properties of systems. Thus the electrons found in the core regions of the atoms do not participate in chemical bonding. This serves as an advantage by separating the electrons of the system into the core and valence regions and using different descriptions for each. This greatly decreases the computational cost of involving all the electrons in the system for the calculation.

In the pseudopotential approach, the Pauli repulsion of the core electrons is described by an effective potential that expels the valence electrons from the core region. The resulting wavefunction is a smooth one and can however be well represented by plane waves. The pseudopotentials are introduced to avoid explicit description of the core electrons and also to avoid the rapid oscillations of the wavefunctions near the nucleus which normally requires complicated and large basis sets.

An augmentation region is used to separate the core region from the valence region. The augmentation region is characterized by a certain radius r_c from the nucleus. In the construction of the pseudopotential, an all-electron calculation is initially done to obtain the valence eigenvalues and wavefunctions that one seeks to reproduce within a pseudopotential calculation. The oscillations of the valence wavefunctions in the core regions are then smoothed out to create a pseudo-wavefunction which is then used to invert the Kohn-Sham equations for the atom to obtain the pseudopotential corresponding to the pseudo-wavefunction with the constraint that the all-electron eigenvalues are reproduced. The pseudopotential sub-sums the nuclear potential with those of the core electrons to generate an ion-core potential. The price to pay for pseudopotentials is that all information on the charge density and wavefunctions near the nucleus is lost.

3. Ab-initio Molecular Dynamics

In molecular dynamics (MD) simulation, the microscopic trajectory of each individual atom in the system is determined by integration of Newtons equations of motion. In classical MD, the system is considered to consist of massive, point-like nuclei with forces acting between them derived from empirical effective potentials. However, ab-initio MD maintains the same assumption of treating atomic nuclei as classical particle but the forces acting on them are considered quantum mechanical in nature and are derived from an electronic structure calculation. This approximation of treating only the electronic subsystem quantum mechanically is appropriate due to the mass difference between the electrons and the nucleus.

The ab-initio MD method is usually implemented in modern DFT codes by combining a Car-Parrinelo approach to determine the simultaneous evolution of the nuclear degrees of freedom and of the electronic wavefunctions bases on plane wave basis sets with pseudopotentials (PP) representing the electron ion interactions.

In ab-initio MD, two methods are commonly implemented in DFT packages, The Born-Oppenheimer and Car-Parrinello approaches. The assumptions made in both cases are as follows: all nuclei (together with their core electrons) are treated as classical particles, only systems for which a separation between the classical motion of the atoms and the quantum motion of the electrons can be achieved (systems satisfying the Born-Oppenheimer adiabatic approximation) are considered. It is possible to calculate the self-consistent electronic ground state and the forces on the ions using the Hellmann-Feynman theorem for any given ionic configuration. With the ionic forces at hand, the nuclear trajectories can be evolved in time using different algorithms such as the Verlet algorithm. Born-Oppenheimer MD implementations tries to achieve an accurate evolution of the ions by converging the electronic wavefucntions in an alternate manner to full self-consistency for a given set of nuclear coordinates. The ions are then evolved by a finite time step according to the quantum mechanical forces acting on them. Thus the nuclei moves along the Born-Oppenheimer surface with the electrons in their ground state for any instantaneous configuration of the nuclei. The time step involved is limited by the need to accurately integrate the highest ionic frequencies. Usually, a thermostat is required to compensate for a drift of the constants of motion due to imperfections in reaching electronic self-consistency.

On the other hand, the Car-Parrinello[14] approach combines “on-the-fly” simultaneous classical MD evolution of the atomic nuclei with the determination of the ground state electronic wavefunction for the electrons through introduction of a fictitious dynamics for the electronic degrees of freedom and defining a classical Lagrangian for the combined electronic and ionic degrees of freedom.

All the ab-initio MD calculations performed in this project are based on the Born-Oppenheimer implementation.

4. Geometry Optimizations

A simplified view of the geometry optimization process can be obtained by considering the Born-Oppenheimer potential energy surface (PES). This PES is a hypersurface and is defined by the electronic energy as a function of 3N dimensional nuclei positions R_n. A PES can be expressed in the neighborhood of any spatial positon R_n^o as:

$$E(R_n) = E(R_n^o) + g(R_n - R_n^o) + \frac{1}{2}(R_n - R_n^o)^T \mathrm{H}(R_n - R_n^o) + \cdots \qquad (2.57)$$

g and H are the gradients and Hessian with their components defined as:

$$g_n = \left.\frac{\partial E}{\partial R_n}\right|_{R_n = R_n^o} ; \qquad H_{n\mu} = \left.\frac{\partial^2 E}{\partial R_n \partial R_\mu}\right|_{R_n = R_n^o} \qquad (2.58)$$

A gradient calculation can be performed either analytically or numerically after an electronic energy is calculated. There are several optimization schemes available. With the calculated gradient, the scheme can change the atomic positions Rn of the molecule until the gradient value has reached a desired convergence threshold value at which point there is an indication of a stationary point on the PES. These stationary points define stable intermediates when they are found at a local minimum of the PES. This process is referred to as geometry optimization step. The multitude of such geometry optimization schemes available include *conjugate gradient, Newton-Raphson, steepest descent, or the Broyden-Fletcher-Goldfarb-Shanno (BFGS)* method. Some of these methods use only the first derivative of the energy while others use the Hessian as well.

4.1 The Climbing Image- Nudged Elastic Band (CI-NEB)

Usually during the course of a chemical reaction mechanism, the reactants and products or stable intermediates that are at local minima of the PES are connected by a transition state (TS). This difference in energy between the initial and state and the TS point gives the corresponding electronic activation barrier for that reaction. These TS points are usually first order saddle points where all but one internal coordinate are at a minimum. Several methods are available for finding the TS point along the potential energy surface (PES). These methods usually use a procedure where the optimization scheme successively moves along the normal mode of the Hessian with the lowest magnitude in an attempt to find the point of maximum negative curvature. These methods are usually efficient when the starting geometry is near the real TS and the utilized Hessian contains only one negative mode. When these conditions are not met, the method fails.

However, the NEB[15], [16] methods are efficient for finding the TS without using a Hessian. Within the NEB approach, a series of atomic configurations known as images are aligned in a row between the initial and final states along the reaction path through a linear interpolation scheme and then their energies are minimized as shown in figure II.2.

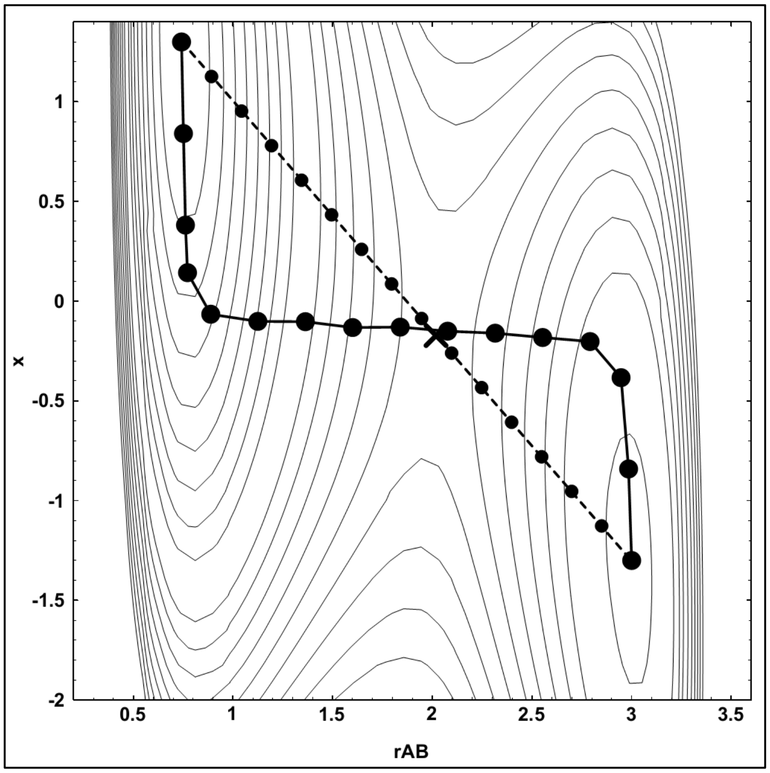

Figure II.2. A NEB plot along the minimum energy pathway (MEP). 16 images are used and connected by a dashed line with the images at points with filled small circles. The larger filled circles shows the images after optimization with force constant k = 0.5 near the end of the bands and k = 1 in the middle regions.

The images are connected by spring forces to ensure a quasi-equal spacing along the pathway. The images are arranged from an initial chain which connects the reactant and product minima. The images along the NEB are relaxed to the MEP through a force projection scheme in which potential forces act perpendicular to the chain but spring forces act along the chain.

During the NEB procedure, a set of images labelled Q_0, Q_1, Q_2, … , Q_P for which Q_0 is the reactant image and Q_P is the product image (P-1) intermediates are arranged along the guessed or interpolated reaction path and are optimized. An object function F is used to trace the optimization path by keeping the images Q_0 and Q_P fixed while the intermediate images are optimized. This object function is given by:

$$F(Q_i \dots Q_P) = \sum_{i=1}^{P-1} E(Q_i) + \sum_{i=1}^{P} \frac{k}{2}(Q_i - Q_{i-1})^2 \tag{2.59}$$

The force constant is represented by k in equation 2.59. Normally due to the stiffness of the elastic band, the path cuts the corner and misses the saddle point. Moreover, there is a down-sliding from the MEP during the optimization step. The corner-cutting results from the part of the spring force that is perpendicular to the path. The down down sliding however comes from the parallel component resulting from the interaction between the atoms in the system. Hence, a force projection scheme is used to relax the structures or images along the MEP. Within this procedure, the potential forces are perpendicular to the band and the spring forces act parallel to the band. Thus the NEB force on the image *i* is divided into two components:

$$F_i^{NEB} = F_i^{\perp} + F_i^{S||} \tag{2.60}$$

The force component which is due to the potential perpendicular to the band $F_i^{\perp}$ is given by:

$$F_i^{\perp} = -\nabla(Q_i) + \nabla(Q_i)\hat{\tau}_i\hat{\tau}_i \tag{2.61}$$

The spring force parallel to the band $F_i^{S||}$ is given by:

$$F_i^{S||} = k(|R_{i+1} - R_i| - |R_i - R_{i-1}|)\hat{\tau}_i \tag{2.62}$$

$\hat{\tau}_i$ is the unit vector at an image *i*, estimated from two adjacent images R_{i+1} and R_{i-1}, given by

$$\hat{\tau}_i = \frac{R_{i+1} - R_{i-1}}{|R_{i+1} - R_{i-1}|} \tag{2.63}$$

A modification of the NEB method called the climbing image nudged elastic band (CI-NEB)[15] method drives the image with the highest energy up to the saddle point. In this way, this image does not see the spring forces along the band but rather, the true force at this image along the tangent is inverted. In this way, the image tries to maximize its energy along the band and minimize in all other directions. As such, when this image converges, it will be at the exact saddle point.

All TS search calculations in this work are performed using the CI-NEB method.

5. Electronic Structure Calculation Implementation Packages

All electronic structure calculations including geometry optimizations are performed using the Vienna ab-initio simulation package (VASP)[17] based on Mermin's finite temperature DFT.[18] The core electrons as well as the core part of the valence electron wavefunction are kept frozen and replaced by the projector augmented wavefunction (PAW)[19] pseudopotentials. This implementation is done to reduce the number of plane waves required to effectively describe the electrons close to the nucleus. The generalized gradient approximation (GGA) parametrized by Perdew, Burke and Ernzerhof (PBE)[11] is used for all calculations. The Methfessel-Paxton[20] smearing scheme is used by setting the gamma parameter to 0.1 eV. In all calculations, the Monkhorst-Pack[13] special grid sampling scheme of the k-points for integration of the Brillouin zone. For resolution of the Kohn-Sham equations, the self-consistent field procedure is used by setting the energy changes for each cycle to 10^{-6} eV as the convergence criterion between successive iterations. This is convergence criterion is selected to ensure an accurate description of the electronic structure calculation.

6. Atomistic Thermodynamic Modelling

The total energies calculated from the electronic structure theories are obtained at 0 K temperature. This temperature however does not represent technologically important and real environmental conditions. As such, the microscopic electronic calculation needs to be linked with macroscopic physical properties. The microscopic contributions to the macroscopic energy can however be obtained through traditional statistical thermodynamics by using the ideal gas assumption. The partition function is the fundamental function that describes macroscopic properties. The combination of thermodynamics with the electronic structure calculation helps to take into account the effects of temperature, pressure and entropic contributions. This becomes very useful when considering the reactivity of molecules on surfaces as it accounts for the gas phase properties of the molecules as well as their properties when adsorbed on a surface.

All the atomistic thermodynamic models presented in this work are based on an already established thermodynamic scheme in which an adsorbed molecule is assumed to be in equilibrium with the gas phase which serves as a reservoir.[21] This scheme allows for the definition of the reaction Gibbs free energy (Δ_rG) of the adsorption process as follows:

$$\Delta_r G = G_{mol-surf} - G_{surf} - G_{mol} \tag{2.64}$$

The subscripts in equation 2.64 are defined as: *mol-surf* is for the surface with the adsorbed molecule, *surf* is for the free surface and *mol* is for the molecule in the gas phase. The Gibbs free energy terms in equation 2.64 are defined as:

$$G(T) = H(T) - TS(T) \tag{2.65}$$

The Gibbs free energy is divided into the enthalpic contribution *H(T)* and the entropic contribution *S(T)* with the following definitions:

$$H(T) = E(0K) + ZPE + E_{vib}(T) + E_{trans}(T) + E_{rot}(T) \tag{2.66}$$

$$S(T) = S_{vib}(T) + S_{trans}(T) + S_{rot}(T) \tag{2.67}$$

The indices in equations 2.66 and 2.67 vib, trans, rot provides account for the vibrational, translational and rotational contributions respectively. The ZPE in equation 2.66 is the zero point energy. This arises because even though there are no translational and rotational contributions at 0 K temperature, there is a vibrational energy at this temperature. For the entropic contribution, there is however an electronic entropy contribution which comes into play for systems with electronic degeneracies such as doublet, triplets and other states.

Combination of equations 2.64, 2.65, 2.66 and 2.67 yields the following sets of equations:

$$\Delta_r G = \left[\Delta E_O + \Delta E_{ZPE} - \Delta \sum n\, \mu(T,\ p) \right] \tag{2.68}$$

$\mu(T,\ p)$ is the chemical potential of the molecules involved in the reaction process. ΔE_o is the difference in the DFT energies of the species involved in the reaction at 0 K temperature and is defined as:

$$\Delta E_o = E^{el}_{mol-surf} - E^{el}_{surf} - E^{el}_{mol} \tag{2.69}$$

ΔE_{ZPE} in equation 2.68 is the difference in the ZPE of the gas phase molecule and the molecule adsorbed on the surface. The assumption here is that, the translational and rotational components of the adsorbed molecule are neglected with only the changes in the vibrational contributions taken into account. The thermal contributions to the chemical potential of the gas phase molecule consisting of temperature and pressure dependent terms are calculated as:

$$\Delta\mu(T,P) = \Delta\mu^o(T) + RT \ln\left(\frac{P}{P^o}\right) \tag{2.70}$$

R is the molar gas constant. The temperature dependent term of the gas phase molecules $\Delta\mu^o(T)$ is computed with statistical thermodynamics and calculated as:

$$\Delta\mu^o(T) = \left[E_{ZPE} + E_{vib(0\to T)} + E_{rot} + E_{trans} \right] + RT - T(S_{vib} + S_{rot} + S_{trans}) \tag{2.71}$$

The pressure p^o for all calculations was set to 1atm. The vibrational, rotational, translational and entropic energies in equation 2.71 are estimated as follows:

The translational contributions are

$$S_{trans} = k_B \left\{ \ln\left[\left(\frac{m_v}{2\pi\hbar^2}\right)^{3/2} \frac{V^o}{N_A} \right] + \frac{5}{2} \right\}; \qquad E_{trans}(T) = \frac{5}{2} RT \tag{2.72}$$

V^o is the molar volume of the gas at standard state, N_A is the Avogadro's number, k_B is the Boltzmann constant.

The rotational contributions are as follow: Linear molecules have energy of $E_{rot}(T) = k_B T$ while non-linear molecules have energy $E_{rot}(T) = \frac{3}{2} k_B T$. The entropy of rotation is given by:

$$S_{rot} = k_B \left\{ \ln \left[\frac{\sqrt{\pi I_A I_B I_C}}{\sigma} \left(\frac{2 k_B T}{\hbar^2} \right)^{3/2} \right] + \frac{3}{2} \right\} \tag{2.73}$$

The rotational symmetric number of the molecules point group is given by σ while I_A, I_B, and I_C are the molecules three principal moments of inertia.

The thermodynamic energy contributions from the molecular vibrations in the gas phase are calculated per the vibrational frequencies, ω_v for the vibrational modes. The vibrational energies are summed over all 3N-6 molecular vibrational modes for non-linear molecules and 3N-5 modes for linear molecules. The contributions are given as follows:

$$S_{vib} = k_B \sum_v \left[\frac{\hbar\omega_v}{k_B T (e^{\hbar\omega_v / k_B T} - 1)} - \ln\left(1 - e^{\hbar\omega_v / k_B T}\right) \right] \tag{2.74}$$

The vibrational energy contribution is given as:

$$E_{vib} = E_{vib}(0\,K) + RT \sum_v \left(\frac{h v_i}{kT} \right) \frac{e^{-h v_i / kT}}{1 - e^{-h v_i / kT}} \tag{2.75}$$

$E_{vib}(0\,K)$ is the ZPE and given by

$$ZPE = \frac{1}{2} h \sum_v v_i \tag{2.76}$$

All entropic, translational, rotational and vibrational contributions of the gas phase molecules are obtained from statistical thermodynamic tables.

References

[1] M. Born and R. Oppenheimer, “Zur Quantentheorie der Molekeln,” *Ann. Phys.*, vol. 389, no. 20, pp. 457–484, Jan. 1927.

[2] Hartree, D. R, *Pro. Cambridge Phil. Soc*, vol. 84, p. 457, 1927.

[3] V. Fock, “Näherungsmethode zur Lösung des quantenmechanischen Mehrkörperproblems,” *Z. Für Phys.*, vol. 61, no. 1–2, pp. 126–148, Jan. 1930.

[4] P. A. M. Dirac, *Pro. Cambridge Phil. Soc*, vol. 26, p. 376, 1930.

[5] F. Bloch, “Bemerkung zur Elektronentheorie des Ferromagnetismus und der elektrischen Leitfähigkeit,” *Z. Für Phys.*, vol. 57, no. 7–8, pp. 545–555, Jul. 1929.

[6] J. C. Slater, “A Simplification of the Hartree-Fock Method,” *Phys. Rev.*, vol. 81, no. 3, pp. 385–390, Feb. 1951.

[7] J. C. Slater, *Advances in Quantum Chemistry*, 6 vols. New York: Academic Press, 1972.

[8] L. H. Thomas, “The calculation of atomic fields,” *Math. Proc. Camb. Philos. Soc.*, vol. 23, no. 5, pp. 542–548, Jan. 1927.

[9] E. Fermi, *Rend. Accad. Naz. Lincei*, vol. 6, p. 602, 1927.

[10] P. Hohenberg and W. Kohn, “Inhomogeneous Electron Gas,” *Phys. Rev.*, vol. 136, no. 3B, pp. B864–B871, Nov. 1964.

[11] J. P. Perdew, K. Burke, and M. Ernzerhof, “Generalized Gradient Approximation Made Simple,” *Phys. Rev. Lett.*, vol. 77, no. 18, pp. 3865–3868, 1996.

[12] M. C. Payne, M. P. Teter, D. C. Allan, T. A. Arias, and J. D. Joannopoulos, “Iterative minimization techniques for \textit{ab initio} total-energy calculations: molecular dynamics and conjugate gradients,” *Rev. Mod. Phys.*, vol. 64, no. 4, pp. 1045–1097, Oct. 1992.

[13] H. J. Monkhorst and J. D. Pack, “Special points for Brillouin-zone integrations,” *Phys. Rev. B*, vol. 13, no. 12, pp. 5188–5192, 1976.

[14] R. Car and M. Parrinello, “Unified Approach for Molecular Dynamics and Density-Functional Theory,” *Phys. Rev. Lett.*, vol. 55, no. 22, pp. 2471–2474, Nov. 1985.

[15] G. Henkelman, B. P. Uberuaga, and H. Jónsson, “Climbing image nudged elastic band method for finding saddle points and minimum energy paths,” *J. Chem. Phys.*, vol. 113, no. 22, pp. 9901–9904, 2000.

[16] G. Henkelman and H. Jónsson, “Improved tangent estimate in the nudged elastic band method for finding minimum energy paths and saddle points,” *J. Chem. Phys.*, vol. 113, no. 22, pp. 9978–9985, Dec. 2000.

[17] J. Hafner, “Ab-initio simulations of materials using VASP: Density-functional theory and beyond,” *J. Comput. Chem.*, vol. 29, no. 13, pp. 2044–2078, 2008.

[18] N. D. Mermin, “Thermal Properties of the Inhomogeneous Electron Gas,” *Phys. Rev.*, vol. 137, no. 5A, pp. A1441–A1443, 1965.

[19] G. Kresse and D. Joubert, “From ultrasoft pseudopotentials to the projector augmented-wave method,” *Phys. Rev. B - Condens. Matter Mater. Phys.*, vol. 59, no. 3, pp. 1758–1775, 1999.

[20] M. Methfessel and A. T. Paxton, “High-precision sampling for Brillouin-zone integration in metals,” *Phys. Rev. B*, vol. 40, no. 6, pp. 3616–3621, 1989.

[21] K. Reuter and M. Scheffler, “First-principles atomistic thermodynamics for oxidation catalysis: Surface phase diagrams and catalytically interesting regions,” *Phys. Rev. Lett.*, vol. 90, no. 4, pp. 461031–461034, 2003.

Chapter III: Bulk Properties and Defects

Table of Contents

1. Introduction

In this section, studies on the bulk properties of zirconium carbide (ZrC) is presented alongside the analysis of structural defects.

In Order to apply all the theories and methods described in chapter II, it is better to gain a best description of the system. The DFT implementations in the VASP code has to be tested to ensure it yields accurate and reliable results for subsequent calculations on the ZrC and other systems of interest.

As the main purpose of this project is to study surface reactivity and modification of ZrC as well as the interface formed from ZrC and other materials such as ZrO_2 and SiC, it is imperative to set the ball rolling performing detailed testing of the DFT implementation in VASP. This testing is achieved by studying the properties of the bulk system in order to get accurate results that are comparable to those found in the literature. Several properties of the bulk are calculated for this purpose. Such properties include the lattice parameter of the system, bulk modulus, Young modulus, pressure derivative of the bulk modulus, elastic constants of the crystal material,

Moreover, studies on defect formation and structure is also carried out. This helps provide good description of the bulk ZrC system.

The chapter starts with development of slab models for ZrC, estimation of the lattice parameter, calculation of elastic constants and finally studies on defect formation.

2. Bulk Physical and Mechanical Properties of ZrC

Several properties of bulk ZrC are considered and studied in this section. Calculation of the lattice parameter from experimental data is described. Additionally other properties that provides proper description and characterization of the bulk such as cohesive energy, bulk modulus, and elastic constants are presented.

2.1 ZrC Lattice Parameter

The calculation of the lattice parameter is started using data obtained from experimental determinations.

ZrC having a cubic structure belongs to the octahedral (O_h^5) Fm-3m space group and it crystallizes in a NaCl type structure with four ZrC units per unit cell as shown in figure III.1. The Zr – C bond distance for this octahedral coordination is at least 2.349 Å with a theoretical density of about 6.56 g/cm^3 at 25 ^{o}C.[1]

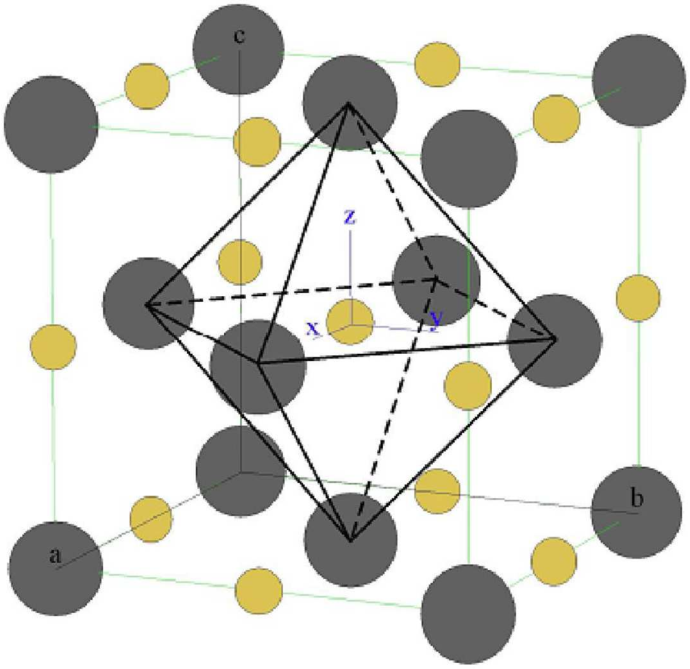

Figure III.1 Cubic structure of ZrC. Yellow balls denote C and big grey balls are Zr

The anions and cations independently form fcc lattices and these two interpenetrating lattices are displaced from each other by a $(^1/_2\ \ ^1/_2\ \ ^1/_2)$. Thus the primitive cell has two special positions, (0 0 0) and (0.5 0.5 0.5). The experimentally determined lattice parameter through X-ray diffraction (XRD) experiments is 4.69764 ± 00005 Å.[2] This experimental value of the lattice parameter was used as the starting point for determining the lattice parameter based on DFT studies. Thus a bulk unit cell of ZrC was built with the experimental lattice parameter and a series of calculations were performed on this structure. In determining the lattice parameter, the Energy- Volume approach was use. In this approach, the crystal structure is subjected to either volume compression or expansion of about 10% of the experimental value by applying a stress to the system. The electronic energy is then calculated for different volumes of the system. The set of calculated electronic energy values E(V) are plotted against the corresponding volume, V of the crystal. The resulting plot is then fitted with an appropriate equation of state (EOS). In this work, the Murnaghan's equation[3] of state was used for the fitting. This equation is given by:

$$E(V) = E_o - \left[\frac{BV_o}{B'-1}\right] + \left(\frac{BV}{B'}\right)\left[\left(\frac{V_o}{V}\right)^{B'}\frac{1}{(B'-1)} + 1\right] \qquad 3.1$$

E(V) is the calculated electronic energy at volume *V*, E_o is the fitted equilibrium energy, V_o is the fitted equilibrium volume, *B* is the bulk modulus and *B'* is the pressure derivative of the bulk modulus.

A fitting of the calculated energies at different volumes is shown in figure III.2.

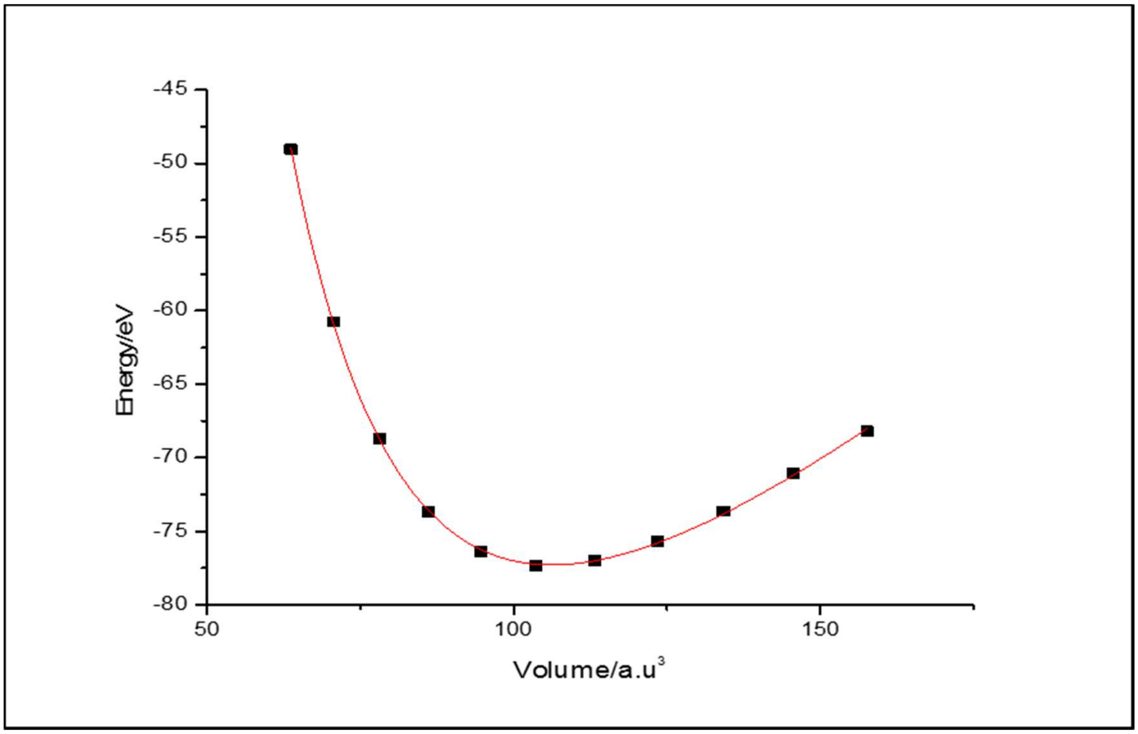

Figure III.2 Murnghan equation of state fitting of electronic energy $E(V)$ at different volumes V

The calculated equilibrium electronic energy is -77.37 eV with an equilibrium volume of 106.25 $Å^3$. As ZrC is cubic, the lattice parameter is obtained by taking the cube root of the equilibrium volume. This yields a calculated lattice parameter, a_o of 4.7363 Å. This value compares very well with the experimental values of 4.6976 Å[2] and 4.70 Å.[4]. The experimental value is thus overestimated by approximately 1% which is typical of GGA calculations. The calculated value is also compared with other theoretically determined values, 4.731 Å.[5]

The calculated bulk modulus B of ZrC is 217.9 GPa. This value compares well the with the experimental values of 223.1 GPa for $ZrC_{0.94}$ and 222.5 GPa for $ZrC_{0.89}$.[6] The Value also compares very well with other theoretical calculations, 217.7 GPa [7], 220.7 GPa [5]. This also provides a good description of the ZrC system. The calculated pressure derivative of the bulk modulus, *B'* is 3.84. A summary of the calculated bulk properties is provided in table III.1. This high bulk modulus value explains the covalent nature of the bonding in ZrC. Even though ZrC crystallizes in the NaCl structure which is associated with ionic bonding, they show properties associated with covalent bonding.[8] This covalent character between Zr and C is achieved through the charge distribution in the crystal.

Table III.1. Calculated bulk properties of ZrC

	a_o/ Å	*B*/ GPa	*B'*
This work	4.7363	217.9	3.84
Other GGA	4.7310[5]	217.7[7], 220.7[5]	3.80[9]
Experiment	4.6976[2], 4.7000[4]	223.1, 222.5[6]	

2.2 Density of States (Bulk ZrC)

A density of state (DOS) calculation is made on the optimized ZrC bulk structure to gain understanding of the type and strength of bonding present in ZrC.

The DOS plot of ZrC is shown in figure III.3. Figure III.3 shows the bonding structure of bulk ZrC. The Total DOS (TDOS) shows a broader valence band of ZrC. This broader band shows the delocalization of electrons in the bonds of ZrC. There is a slight dip at the Fermi level. Thus the Fermi level resides in a pseudo-gap and the density of electronic states at the Fermi level is very low.

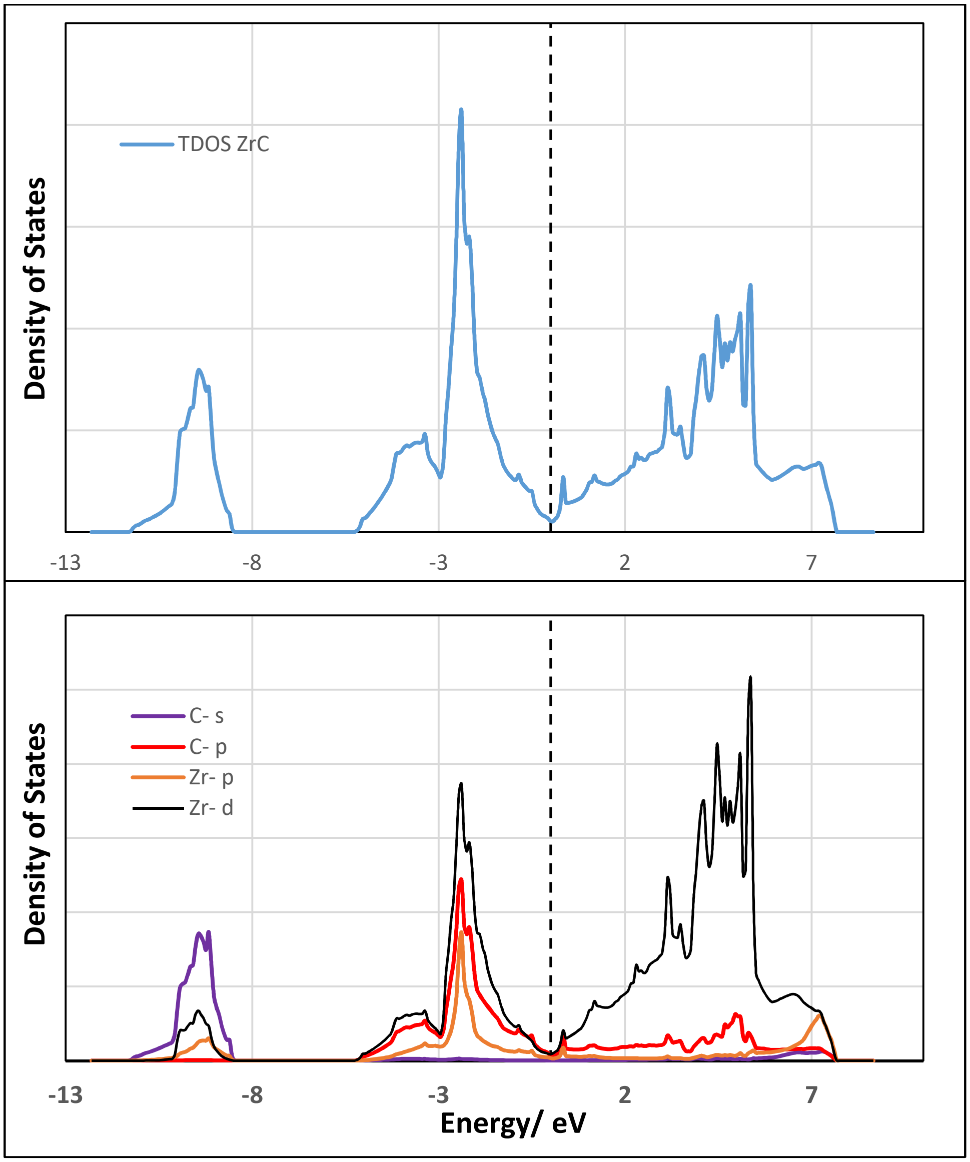

Figure III.3. Total DOS of ZrC (top) and Projected DOS onto Zr and C (bottom). The Fermi level is aligned at the 0 energy and marked with a dashed line.

A projection of the DOS onto the individual atoms is shown in the lower part of figure III.3. At the core bonding regions, the bonding is mainly C- s states and less diffuse. The conduction band is however made up of Zr –d states owing to the fact that Zr is a d^4 element. This huge conduction band of ZrC shows that it has more metallic nature than being an insulator. In the bonding region, the valence band is diffuse, spanning the energies between -5 eV to -0.8 eV. The covalent nature of the bonding in ZrC can be seen in the strong mixing of the Zr –d, Zr –p and C –p orbitals. This mixing spans all the region of the valence band. The strong covalent nature of the bonds explains the high bulk modulus calculated.

2.3 Elastic and Mechanical Properties of ZrC

In order to gain more understanding of the bulk properties of ZrC, an analysis of the elastic and mechanical properties is provided here. There are two methods for calculating the elastic properties of materials, the energy-strain method and the stress-strain method[10], [11]. The energy-strain approach is based on the computed total energies of properly selected strain states of the crystal. The second order elastic constants appear via Hooke's law in the second order Taylor expansion of the total energy of the system with respect to a small strain of the system:

$$E(V,\mathcal{E}) = E(V_o, O) - P(V_o)\Delta V + \frac{V_o}{2}\sum_{ij} C_{ij}\mathcal{E}_i\,\mathcal{E}_j + O\left[\mathcal{E}_i{}^3\right] \tag{3.2}$$

V is any considered volume, E is the total energy, C_{ij} are the elastic constants, V_o is the volume of the undistorted lattice, $P(V_o)$ is the pressure of the undistorted lattice at volume V_o, ΔV is the change in volume of the lattice due to the strain and $O\left[\mathcal{E}_i{}^3\right]$ indicates that the neglected terms in the polynomial expansion are cubic and a higher power of the $\mathcal{E}_i$ which is the strain.

For the cubic supercell, three independent elastic constants C_{11}, C_{12} and C_{44} are to be determined. Two deformation modes with keeping the unit cell volume constant[12] are employed and the bulk modulus is derived from the Birch-Murnaghan[13] equation of state.

The stress-strain approach is used for calculating the elastic constants and other elastic properties of ZrC in this work. In this method, the elastic constants are derived from the generalized Hook's law. A set of strains $\boldsymbol{\varepsilon = (\varepsilon_1, \varepsilon_2, \varepsilon_3, \varepsilon_4, \varepsilon_5, \varepsilon_6)}$ is imposed on a crystal by alternating the unit cell lattice vectors ($\bar{R}$) from the original vectors (R) as follows:

$$\bar{\boldsymbol{R}} = \boldsymbol{R}\begin{pmatrix} 1+\varepsilon_1 & {}^{\varepsilon_6}/_{2} & {}^{\varepsilon_5}/_{2} \\ {}^{\varepsilon_6}/_{2} & 1+\varepsilon_2 & {}^{4}/_{2} \\ {}^{\varepsilon_5}/_{2} & {}^{\varepsilon_4}/_{2} & 1+\varepsilon_3 \end{pmatrix} \tag{3.3}$$

ε_1, ε_2 and ε_3 are the normal strains and ε_4, ε_5 and ε_6 are the shear strains in Voigt's notation[14]. A 6x6 elastic constants matrix, C with components C_{ij} in Voigts' notation relates the strain vector ε with the stress vector $\boldsymbol{\sigma = (\sigma_1, \sigma_2, \sigma_3, \sigma_4, \sigma_5, \sigma_6)}$ as $\boldsymbol{\sigma = \varepsilon.\ C}$. Based on Hooke's law, the elastic stiffness constants matrix C is determined as $C = \varepsilon^{-1}\sigma$. Finally, the macroscopic cubic elastic constants are calculated as follows:

$$\hat{C}_{11} = \frac{C_{11} + C_{22} + C_{33}}{3} \tag{3.4}$$

$$\hat{C}_{12} = \frac{C_{12} + C_{13} + C_{23}}{3} \tag{3.5}$$

$$\hat{C}_{44} = \frac{C_{44} + C_{55} + C_{66}}{3} \tag{3.6}$$

$\hat{C}_{11}$, $\hat{C}_{12}$ and $\hat{C}_{44}$ are the three distinct elastic constants of a cubic crystal and C_{11}, C_{22}, … C_{66} are the elastic constants of the 6x6 matrix. The stress-strain approach is much more efficient as the six strains are sufficient to obtain a full elastic constants matrix.[11], [15]. Also, the method allows to obtain single crystal elastic constants without using the bulk modulus *B* from the EOS and thus to independently estimate *B*. At any volume, the bulk modulus *B* is related to the elastic constants by the equation:

$$B = \frac{(C_{11} + 2C_{12})}{3} \tag{3.7}$$

Thus, aside calculating the bulk modulus from the energy-volume approach using an EOS as described in section 2.1, it can as well be calculated from elastic constants of the crystal.

For isotropic materials, a calculation of the average shear modulus G is obtained from the upper and lower bounds of the shear modulus G_V and G_R [16], [17] respectively as follows:

$$G_V = \frac{1}{5}(C_{11} - C_{12} + 3C_{44}) \tag{3.8}$$

This upper bound can be derived assuming uniform strain throughout the sample. The lower bound is calculated as:

$$G_R = \frac{5(C_{11} - C_{12})C_{44}}{4C_{44} + 3(C_{11} - C_{12})} \tag{3.9}$$

This lower bound can be derived assuming uniform stress through the material. From the average shear modulus G and the bulk modulus *B*, the average Young's modulus E and the average Poisson's ratio *v* are derived as follows:

$$E = \frac{9GB}{3B + G} \tag{3.10}$$

$$v = \frac{3B - 2G}{2(3B + G)} \tag{3.11}$$

For cubic crystals, the elastic constants must fulfil the Born stability criteria[14] which are $C_{44} > 0$, $C_{11} > |C_{12}|$, $C_{11}+2C_{12} > 0$.

The stress strain calculation is done using the equilibrium volume V_o and the lattice parameter a_o obtained in section 2.1.

A summary of the calculated elastic constants and other mechanical properties that describes the deformation characteristics of ZrC is provided in table III.2

Table III.2. Elastic constants and bulk mechanical properties of ZrC

Parameter	This work	Experiment	Other GGA
$\hat{C}_{11}$/ GPa	480	470[18], 472[19]	455[9]
$\hat{C}_{12}$/ GPa	106	100[18], 99[19]	116[9]
$\hat{C}_{44}$/ GPa	149	160[18], 159[19]	152[9]
B/ GPa	231	223, 222[6]	229[9], 232[20]
G_V/ GPa	164	170[19]	
G_R/ GPa	170	162[19]	
E/ GPa	404	407[19]	408[9], 435[21]
v	0.2	0.19[19]	0.2[9]

The calculated bulk modulus using the stress-strain approach is 231 GPa. This value agrees quite well with the experimental values of 223 GPa and 222 GPa[6]. However, it is not in good agreement with the value calculated from the EOS fitting in section 2.1. Moreover, it compares very well with other GGA calculated values of 229 GPa[9] and in excellent agreement with 232 GPa[20]. As the bulk modulus is related to volume change, the high value calculated for ZrC indicates that, it is difficult to change the volume of the solid as it has a high electron density. The relatively large bulk modulus calculated with the stress-strain method is also consistent with the strong covalent bond character observed in the DOS plot of figure III.3. The established good agreement of the bulk modulus with other GGA based calculations provide indication of the reliability and accuracy of the method use.

Calculation of the three elastic constants involved both elongations and shear deformations. As can be seen from table III.2, all the calculated elastic constants are in excellent agreement with experimental data as well as other calculated GGA values. The elastic constant $\hat{C}_{11}$ which indicates stiffness against uniaxial strain is very high (480 GPa). This high stiffness constant of ZrC contributes to the excellent mechanical properties that makes it useful for applications in cutting tools and other harsh environments. $\hat{C}_{44}$ is determined by pure shear strain. The $\hat{C}_{44}$ corresponds to the resistance against {100}<110> shear deformations and the somewhat high value calculated is an indication of the mechanical strength of ZrC. From table III.2, the average shear modulus G can be calculated as 167 GPa. This value is in excellent agreement calculated in a different GGA work, 170 GPA[9] as well as with experimental value of 170 GPa[19]. The shear modulus as a ratio of shear stress to shear strain, it also measures the stiffness of the material. It is concerned with deformation of a solid when it experiences a force parallel to one of its surfaces whiles its opposite face experiences an opposition force such as friction. As such, this high shear modulus value of ZrC accounts for its deformation resistance when parallel forces are applied. Considering the Young's modulus E, it describes the materials strain response to uniaxial stress in the direction of the stress. The rigidness of ZrC is explained by the high Young's modulus value of 404 GPa calculated. This values is in excellent agreement with experimental value of 407 GPa[19]. The slight underestimation is however only 1% and the method employed in this work is considered reliable. An overestimation of the Young's modulus is however observed in other GGA calculations, 435 GPa[21] but excellent agreement is also found in another work, 408 GPa[9]

The calculated elastic constants obey the Born-stability criteria for cubic materials, i.e, $C_{12} < B < C_{11}$. The calculated Poisson's ratio of 0.20 is in excellent agreement with experiments, 0.19[19] and other theoretical calculations, 020[9]. This parameter is the coefficient of expansion on the transverse axial, and thus the negative ratio of transverse to axial strain. The Poisson's ratio is a measure of the Poisson effect. This effect explains the following phenomenon: when a material is compressed in one direction, it usually tends to expand in the other two directions perpendicular to the direction of compression. The same explanation is used for the situation when a material is stretched.

In summary, all the above physical, elastic and mechanical parameters for characterizing materials are calculated for ZrC. Accurate and reliable values are obtained for the calculations performed in this study.

3. Bulk Energetics of ZrC

Several energetic parameters are calculated to shed more light on the strength of bonds found in ZrC solids. In this respect, we use the formation energy and cohesive energy of ZrC to gain more understanding in the strength of bonds and interaction between Zr and C atomic species combining to form the solid ZrC. A comparison of the calculated values is made with both experimental and other theoretically calculated values to ascertain the accuracy and reliability of the method used in this work.

3.1 Cohesive (Binding) Energy

An initial assessment is made with the cohesive energy of ZrC bulk material. The cohesive energy of a substance is defined as the energy required to break all the bonds associated with one of its constituents. It is therefore a measure of the inter-molecular energy of a system. Thus, it is the energy that must be supplied to the solid to separate its constituents into neutral free atoms at rest and at infinite separation with the same electronic configuration.

The cohesive energy can be calculated as the energetic different between the solid and the separated atoms. The calculated cohesive energy E_{coh} for ZrC directly from VASP is given as -9.67 eV. This value is in complete agreement in another work, -9.64 eV/atom[5]. However, the experimental cohesive energy of ZrC is -7.92 eV/atom[4]. The discrepancy in the calculated value from the experimental value is that in the electronic structure calculation, the non-magnetic ground state configuration of Zr which is s^1d^3 is used instead of the high spin s^2d^2 (^3F)

configuration of Zr which is used in the experimental measurement. Part of this error is also due to know systematic errors in the DFT energies of the isolated atoms. Nevertheless, the cohesive energy is in excellent agreement with other GGA calculations and hence the method used is reliable. This high value of the cohesive energy for ZrC is also an indication of the strength in the bonds holding the atomic blocks that form the ZrC unit together. Thus an essentially high amount of energy is required to break the bonds in ZrC and hence its high mechanical and physical properties as corroborated by the elastic constants and bulk modulus calculated earlier.

3.2 Formation Energy of ZrC

The formation energy is calculated for ZrC so characterize the strength of bonds present in ZrC. It is the change in energy when a material is formed from its constituent elements in their reference states. The formation energy is also another means that reduces the systematic errors in the DFT energies of atoms in estimating the stability of compounds. The elements that form the compound are in their elemental states.

Considering the reaction for the formation of ZrC from Zr and C atoms in their elemental states as:

$$m(Zr_{hcp}) + n(C_{graphite}) \rightarrow m + n(ZrC_{solid}) \tag{3.12}$$

The formation energy of ZrC per atom can then be calculated as:

$$E_{form}^{ZrC} = \frac{(m+n)E(ZrC) - nE\left(C_{graphite}\right) - mE(Zr_{hcp})}{m+n} \tag{3.13}$$

The reference elements used in estimating the formation energy of ZrC are hcp Zr and graphite carbon. The calculated formation energy of ZrC is -0.89 eV/atom. This is in good agreement with other GGA calculations, -0.92 eV/atom[5]. It also agrees well with the experimental value of -1.04 eV/atom[22]. It is apparent that the high systematic error observed in the calculated cohesive energy of ZrC is somehow reduced.

In summary, the cohesive and formation energies of ZrC has been calculated to gain more understanding on the types and strength of bonds exhibited in this material.

4. Point Defects in ZrC

In order to complement all the other bulk properties studies, an analysis of solid defects is carried out for bulk ZrC. The defect studies is also carried out to check the precision of the elastic constant calculations. Defects in the solid can lead to imprecise calculation of the elastic constants. Experiments have shown that ZrC contains a large number of carbon vacancies, and their properties are related to the broad compositional homogeneity of the ZrC. They sometimes have C concentrations of 38-50% at 500 °C[4], [23], [24]. It is known that the perfectly stoichiometric cubic NaCl phase in transition metal carbides (TMC's) is unstable so that vacancies are always present. Among the different types of defects found in solids, vacancies and atomic insertions are considered in this study.

The energies of stoichiometric and defected ZrC structures are computed with different supercells. The volume of each supercell is fixed with the lattice parameter calculated for the stoichiometric ZrC in section 2.1 while the fractional atomic coordinates are relaxed. It has been observed that the most common form of defect in ZrC is carbon vacancy formation[25] and hence this type of defect is considered here. Four different concentrations of carbon were considered in this study; 75%, 88%, 94% and 97%. These were achieved using 1x1x1, 2x1x1, 2x2x1 and 2x2x2 supercells respectively. These concentrations also leads to the following formulae; $ZrC_{0.75}$, $ZrC_{0.88}$, $ZrC_{0.94}$ and $ZrC_{0.97}$ respectively. The volume of the supercells were kept fixed while the ions were allowed to relax.

The main parameter used in characterizing the defects and their stability is the defect formation energy (DFE). The DFE values were calculated for both carbon-rich and zirconium rich environments.

In the **carbon-rich** environment, the carbon removed from the stoichiometric structure is placed in a reservoir of carbon, diamond in this case. FCC diamond was used as the reference in calculating the energy of carbon. The lattice parameter used for FCC diamond was 3.5668 Å with 8 atoms per unit cell. A k-point mesh testing was done for carbon as was performed for ZrC. The resulting k-point mesh used for diamond carbon was 6x6x6.

In case of the Zr-rich environment, the carbon removed from the ZrC structure is placed in an excess of Zr to form ZrC units. In this case, the hexagonal closed pack (hcp) Zr is used as the reservoir for Zr. Thus the energy of carbon is computed in both diamond and hcp Zr reservoirs. A k-point mesh testing resulted in 9x9x5 grid.

The DFE is finally calculated as the difference in energy between the un-defected solid and the defected solid, taking into account the energy of the elemental specie being vacated as:

$$ZrC_{solid} \rightarrow ZrC_{(1-x)} + xC \tag{3.14}$$

The number of carbon vacancies is given by x. The DFE is in different environments is calculated as:

$$\boldsymbol{carbon - rich}\text{:} \quad DFE = E(ZrC_{(1-x)} + E[xC\{diamond\}] - E(ZrC_{solid}) \tag{3.15}$$

$$\boldsymbol{Zirconium - rich}\text{:} \quad DFE = (ZrC_{(1-x)} + E[xC\{hcp\ Zr\}] - E(ZrC_{solid}) \tag{3.16}$$

In the carbon-insertion type of defect, 1x1x1, 2x1x1, 2x2x1 and 2x2x2 supercells or ZrC were used and one carbon was inserted into the lattice of the structure. These give carbon concentrations of 125%, 112.5%, 106% and 103% respectively. The corresponding structures are $ZrC_{1.25}$, $ZrC_{1.13}$, $ZrC_{1.06}$ and $ZrC_{1.03}$ respectively. Corresponding DFE equations as in the carbon vacancies exist for the carbon insertion defects and the DFE values are calculated as for the carbon vacancies.

DOS calculations are performed for the two types of defect after geometry optimization of the supercells. The DOS include both total DOS and projected DOS to aid in explaining the defect features in solid ZrC.

4.1 Carbon Vacancy Defects

As explained earlier, the effects of carbon vacancy formation in sub-stoichiometric levels at different concentrations of carbon are computed in order to obtain understanding of the ease with which vacancies are formed in the stoichiometric structure. A summary of the DFE values calculated for the different concentrations of carbon vacancies is given in table III.3.

Table III.3. DFE at different concentrations of carbon in ZrC at different environments of carbon and zirconium

	Carbon-rich **(DFE/ eV)**		***Zr-rich*** **(DFE/ eV)**	
ZrC Formula	calculated	Reference	Calculated	Reference
$ZrC_{0.75}$	2.08		0.33	
$ZrC_{0.88}$	1.87		0.12	
$ZrC_{0.94}$	1.47		-0.28	
$ZrC_{0.97}$	1.04	0.93[26]	-0.71	-0.71[26]

According to table III.3, ZrC is more stable when carbon vacancy is formed at carbon concentrations of 94% and 97% in Zr-rich environments. The stabilities with which carbon vacancies are formed increased when large supercells are used. The vacancies are however not stable at low carbon concentrations, ie 75% and 88%. A pictorial view of the stability of the vacancies at different carbon concentrations is shown in figure III.4.

It is also obvious that the carbon vacancies are not stable in carbon-rich environments as the DFE values are all above zero, more than the equilibrium value for stoichiometric ZrC. The computed DFE values are moreover in excellent agreement with available theoretical values as can be seen in table III.3. The negative value for the vacancy in zirconium-rich conditions imply that, in the presence of Zr, ZrC will react to form ZrC_x ($x < 1$), i.e. the Zr will pull carbon from the stoichiometric compound to form bulk ZrC_x ($x < 1$) with carbon vacancies. The difference between the supercells is significant. In the larger supercells, the vacancies can be spread out more evenly in the structure, thereby minimizing the number of metal atoms with more than one carbon vacancy neighbor while this is not possible in the smaller supercells.

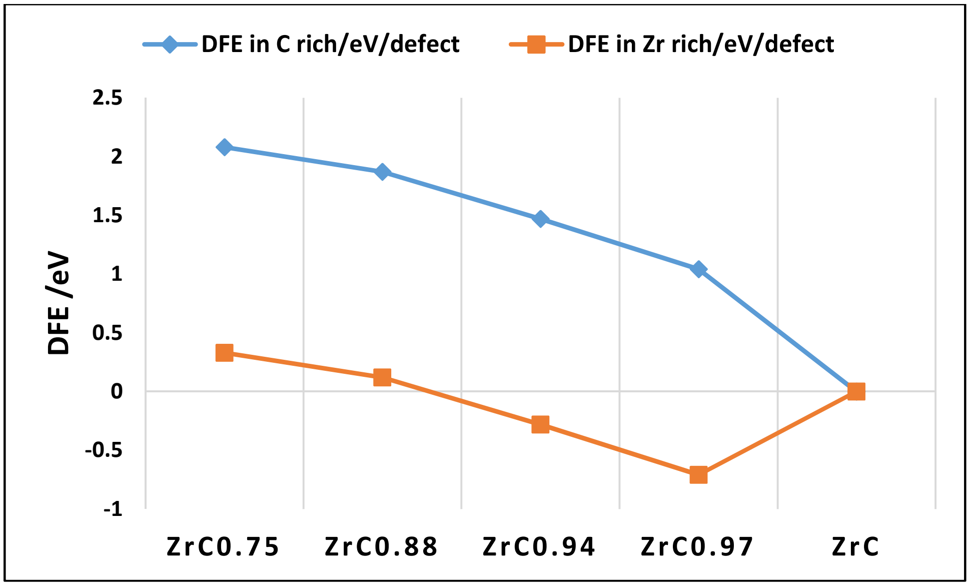

Figure III.4. DFE in carbon-rich and zirconium-rich environments at different carbon concentrations

In order to understand the electronic changes of the bulk structure upon carbon vacancy formation, different DOS plots were made for the defected structures and compared with those of the non-defected solid at different concentrations. The DOS for the different carbon vacancy concentrations can be seen in figures III.5, III.6, III.7 and III.8. The DOS will aid in understanding the bonding nature in the defected solids. Some characteristic features of the DOS plots can help to understand the differences and changes in chemical bonding between stoichiometric and sub-stoichiometric phases of ZrC.

For $ZrC_{0.75}$, the total DOS in figure III.5 for the stoichiometric structure can be divided into three regions: the lower core region (I) around -9.5 eV. This band is mainly made up of C –s orbitals. Region (I) is separated from the upper valence band region (II) by 5 eV in energy. Region (II) lies around -3.0 eV and is made up of large contributions from Zr -4d orbitals as well as significant contributions from C -2p orbitals. The fact that the low lying C -2s is separated far from the C -2p orbitals shows no hybridization of the carbon s and p orbitals.

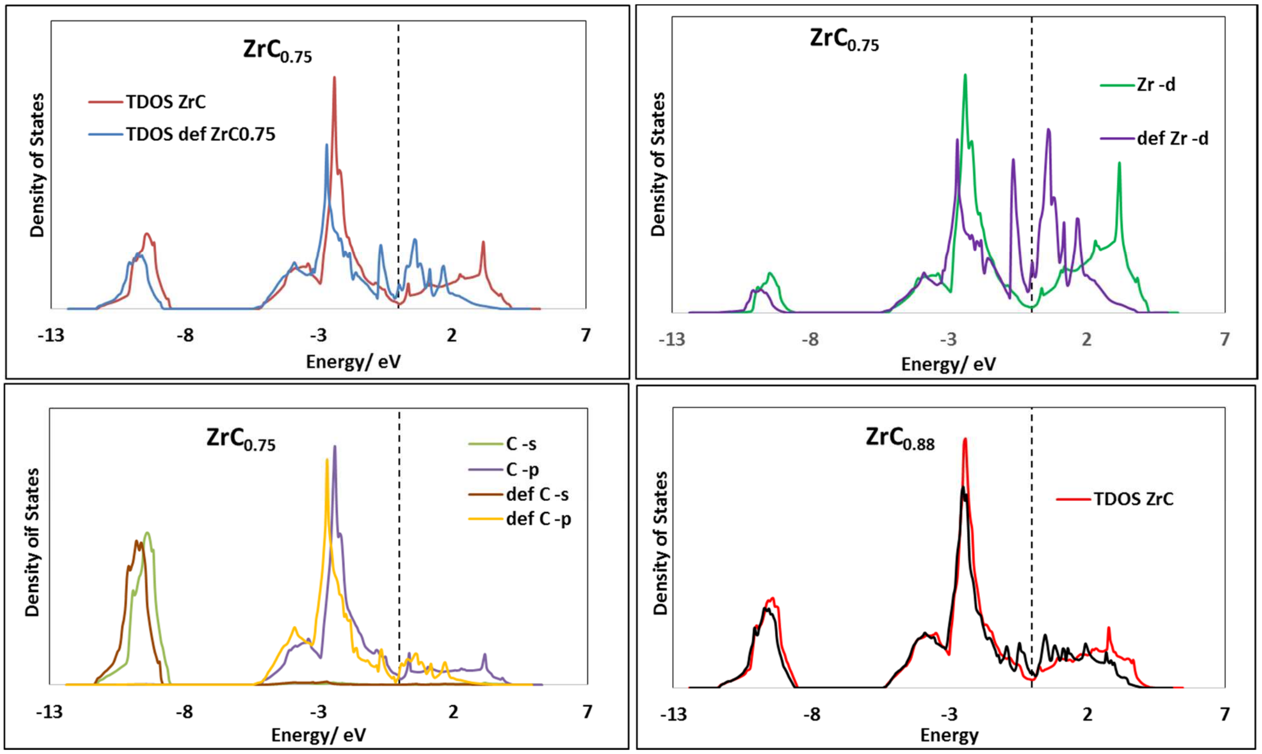

Figure III.5 TDOS and PDOS plots for $ZrC_{0.75}$ and $ZrC_{0.88}$ carbon vacancy structures. Labels with def means defected structure and without def are for the stoichiometric structures.

The region II explains the large covalent bond character between the C –p and the metal –d t_2g orbitals in ZrC. At the Fermi level, there is nearly zero states but a somewhat continuous band into the conduction band region which suggests the metallic nature of ZrC. The conduction band above the Fermi level is made up of unfilled states from the Zr e_g –d states. The large Zr -d states immediately after the valence band forms the Zr-Zr ddσ bond. The C –2s states are highly localized. Only when carbon is removed from the system does the ddσ bond begin to have a more significant influence and hence cannot be ignored during studies of carbon vacancies.

The occupied states at ~ -3.0 eV in the TDOS is due to the Zr –d t_2g orbitals mixing with C -2p orbitals to form t_2g-pdπ orbitals giving a strong covalent bond. This t_2g-pdπ is slightly metallic due to the larger contribution by the Zr t_2g-d orbitals than the C –p orbital. The conduction band is as a result of the metal e_g and the carbon antibonding p states mixing to form e_g pdσ bond which is rather weaker. A combination of the ZrC pdσ and pdπ bonds favor the octahedral arrangement and strongly resists shear.

As noted from the DFE values calculated, it is clear that the energy of formation of ZrC increases when vacancies are introduced into the structure. This indicates the states which are being unoccupied by the removal of carbon atoms are stabilizing states. When removing atoms in the carbon sub-lattice, the symmetry of the system is broken and hence there is more than one type of Zr and C atoms in the system.

Comparing the TDOS of ZrC and $ZrC_{0.75}$, there is no significant changes in the regions I and II. The largest difference in the TDOS is found in region III where the pseudo-gap which separates region II from region III is now pierced by two peaks. Upon projecting the TDOS onto the different atoms of Zr and C to see the details of changes, there is no significant change in the PDOS of the carbon atoms at the high vacancy concentration. At this concentration, all the remaining C and Zr atoms are close to the vacancy site. The C 2s localized state in region I is shifted slightly in energy by an amount of about 0.001 eV whiles the C –p states in the region II is shifted slightly to lower energies by about 0.05 eV and the Fermi level is shifted towards lower energies by about 0.02 eV. The antibonding states are shifted slightly towards lower energies. The major difference in the DOS is observed in the Zr –d states. The two peaks piercing the pseudo-gap between regions II and III are called vacancy peaks. This peak is caused by metal-metal bonds created through the vacancy site. As the carbon is removed, the unoccupied Zr –d states begin to shift to lower energy piercing the Fermi level to form an intense new state, which is now filled and are not hybridized with the C –p orbitals. Thus the formation of the metal-metal ddσ bond causes an increased in the states at the Fermi level and hence the $ZrC_{0.75}$ exhibits metallic properties. Additionally, the metal eg orbitals in the conduction band above the Fermi level become sharper and more localized. There is the appearance of new states in the region II of the Zr –d states. The low DFE of 0.33 eV in Zr-rich conditions for this defect concentration shows the possibility of its formation.

$ZrC_{0.88}$: As the carbon concentration is increased to 88%, there is still a slight change in the TDOS (figure III.5) as compared to the stoichiometric structure. At this concentration, there is symmetry breakage and the Zr and C atoms far and close to the vacancy area are different as shown in figure III.6. The regions I and II remains virtually unchanged. There is negligible change in the PDOS of carbon while a substantial change is observed in Zr. The Zr atoms far from the vacancy shows new states appearing at the Fermi level which are of metal d character while there are still intense new metal –d states appearing at the Fermi level for the Zr atom close to the vacancy region. It can be inferred that at higher vacancy concentrations such as $ZrC_{0.75}$ and $ZrC_{0.88}$, there are new metallic –d states introduced at the Fermi level and these states are not localized but exhibit long range effects.

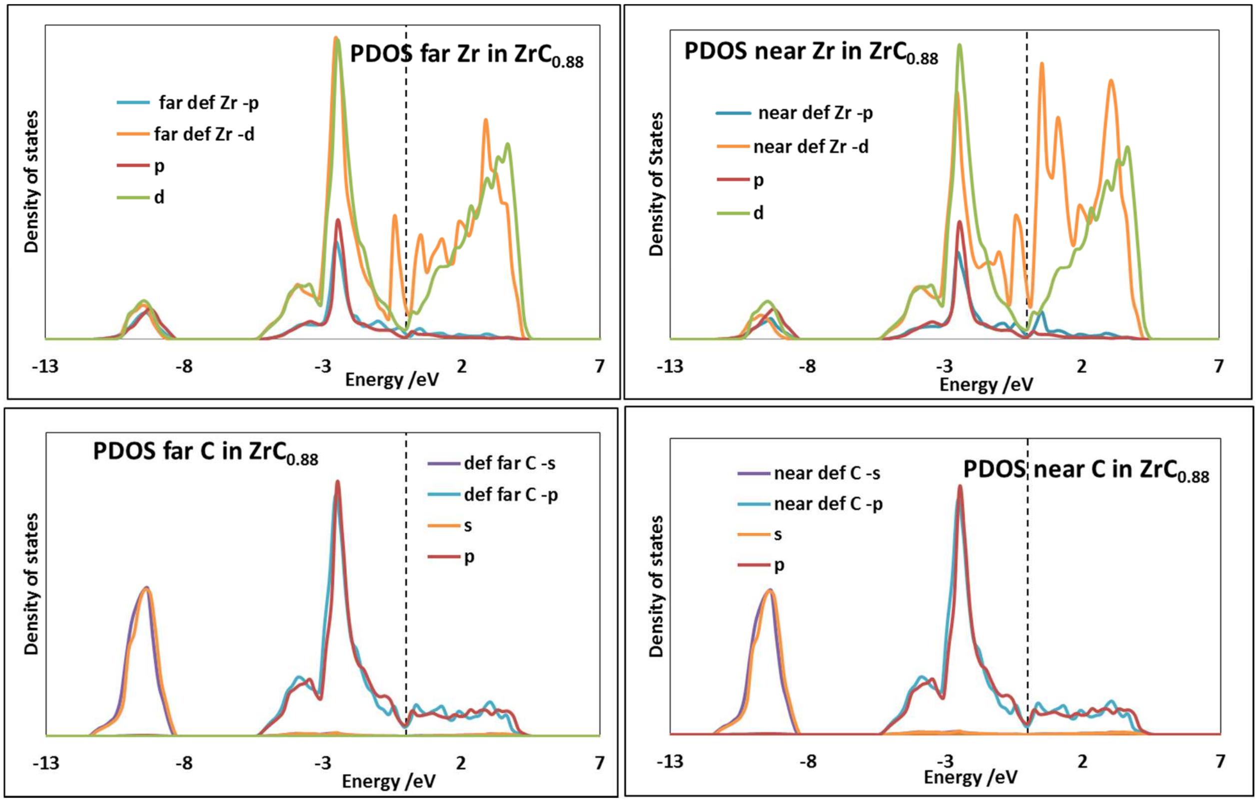

Figure III.6. TDOS and PDOS of $ZrC_{0.88}$ vacancy. Legend explanation is same as in figure III.5.

$ZrC_{0.94}$ and $ZrC_{0.97}$: The TDOS becomes nearly similar to the stoichiometric ZrC as shown in figure III.7. It is observed in figure III.7 that at these low vacancy concentration in $ZrC_{0.94}$, only a slight change in the TDOS is observed and there is the introduction of new –d states at the Fermi level for only the Zr close to the vacancy area while no significant changes or states appear in the other atoms. Thus the electronic structure of the sub-stoichiometric ZrC gets closer to that of the stoichiometric ZrC as the vacancy concentration gets lower as can be seen in $ZrC_{0.94}$ and $ZrC_{0.97}$ in figures III.7 and III.8. This explains the more stable nature of this low vacancy concentration formation as observed in the DFE values above with the $ZrC_{0.94}$ and $ZrC_{0.97}$ having DFE's of negative values as compared to those of $ZrC_{0.75}$ and $ZrC_{0.88}$.

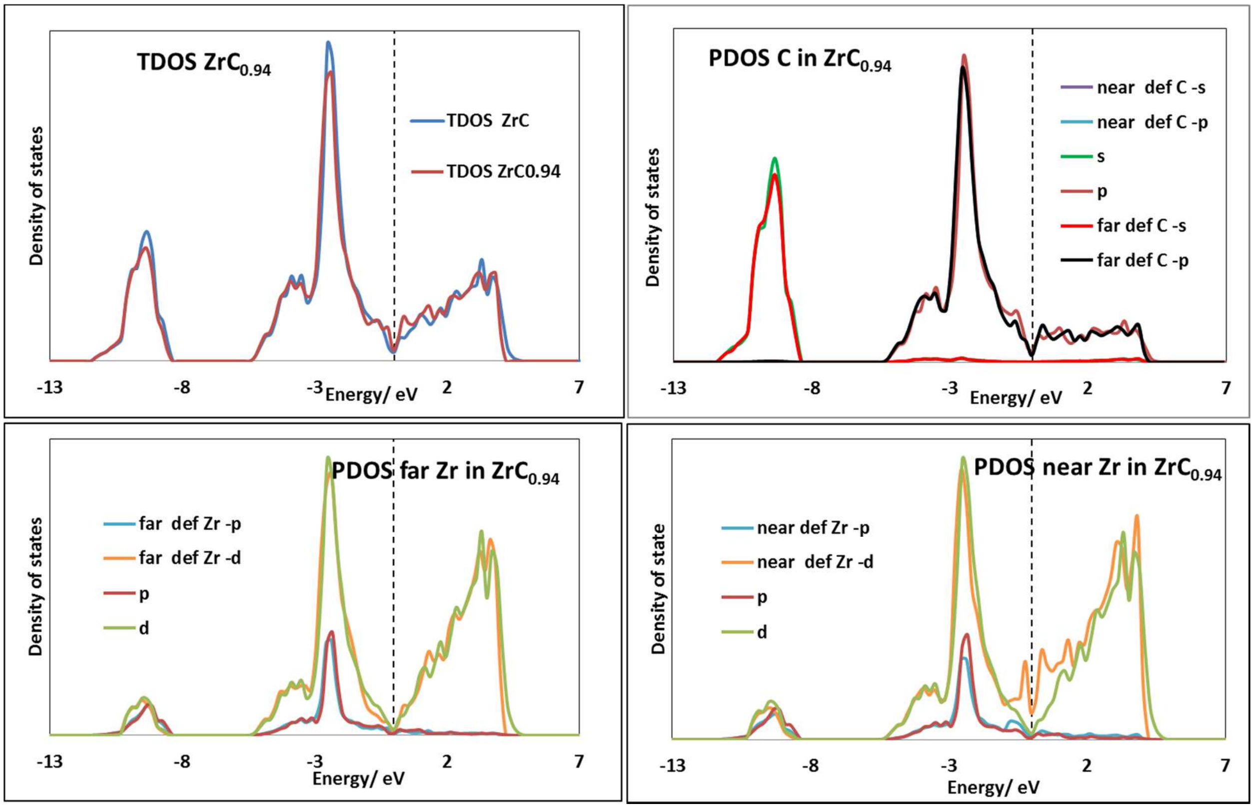

Figure III.7. TDOS and PDOS of $ZrC_{0.94}$ defect. Legend explanation is same as in figure III.5

Thus even though the new d- states appear in the low C vacancy solids, they are of very low intensities as compared to the high vacancy solids.

4.2 Carbon Insertion Defects

Aside the carbon vacancy defect, the Carbon insertion vacation is also studies. In this case, carbon is inserted into the bulk lattice of ZrC. The calculated DFE values for the different defect concentrations are shown in table III.4. Moreover, a plot of the DFE's at different C insertion concentrations is provided in figure III.9 to provide a pictorial view of the trend observed.

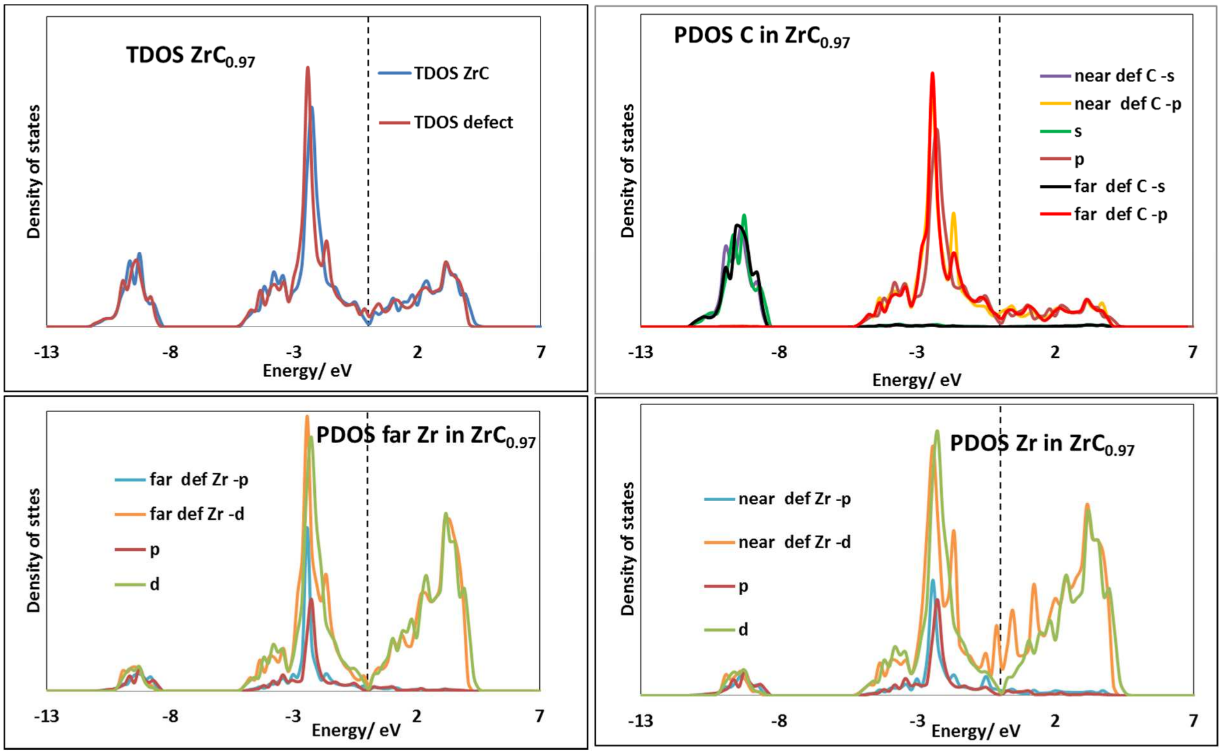

Figure III.8. TDOS and PDOS of ZrC$_{0.97}$ defect. Legend explanation is same as in figure III.5

High DFE values are calculated for both carbon-rich and zirconium rich environments. This shows the unstable nature of such solid defects. DOS plots are obtained for the Zr and C atoms close to and far from the inserted carbon.

Table III.4. Calculated DFE for carbon insertion defect in ZrC

ZrC formula	**C-rich DFE/ eV**	**Zr-rich DFE/ eV**
ZrC$_{1.250}$	5.76	7.51
ZrC$_{1.125}$	5.71	7.46
ZrC$_{1.063}$	5.36	7.41
ZrC$_{1.031}$	3.74	5.49

Even though structures of ZrC1.250, ZrC1.125, ZrC1.063 and ZrC1.031are studied, only diagrams for the ZrC1.250 and ZrC1.031 are shown figures III.10 and figure III.11.

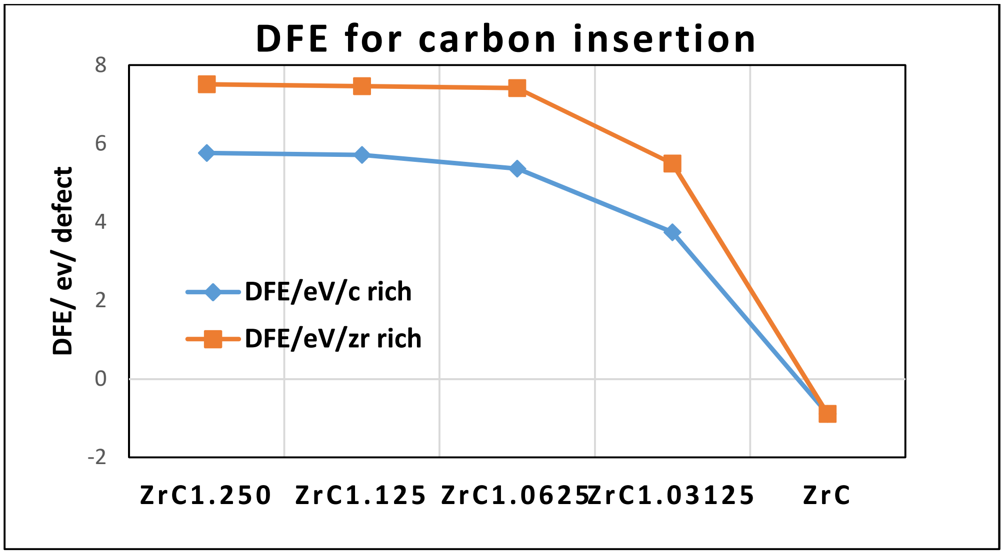

Figure III.9. DFE plot for Carbon insertion defects in ZrC at different insertion concentrations

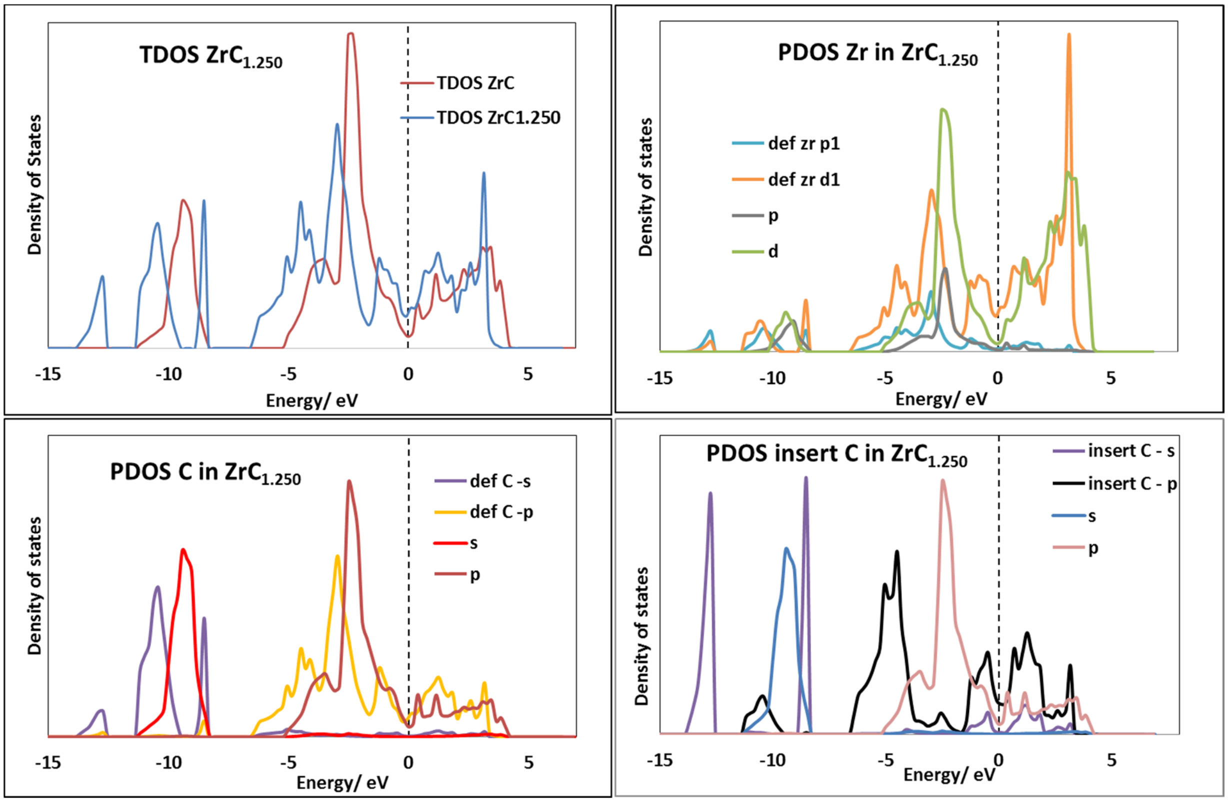

Figure III.10. TDOS and PDOS of $ZrC_{1.250}$ defect. Legend explanation is same as in figure III.5

There is no significant change in the DOS of carbon with only a slight shift in band energies while there are new d- states of metallic character at the Fermi level. There is change in symmetry for the carbon in the structure and hence the s- states split into new ones. The inserted carbon, having a different symmetry shows splitting of s- states into two bands and new p- states close to the Fermi level.

$ZrC_{1.031}$: for this concentration of defect, there is no change in the Zr atom far from the inserted carbon whiles new d- states with low intensity appears at the Fermi level for the Zr close to the inserted carbon. There is no change in the DOS for the carbon far from the inserted one while there is shift in p –states to higher energies for the near carbon and shift in s –states to higher energies. Similar DOS is observed for the near carbon even though there is a decrease in intensity for the p –states.

5. Conclusion

As a preliminary study to optimize the methodology for the subsequent parts of this project, bulk properties ZrC and solid defect studies have been carried out. These properties were studied to obtain accurate description of the properties found in solid ZrC bulk.

The principal and characteristic bulk properties such as lattice parameter and other mechanical properties were characterized to high accuracy. The lattice parameter was calculated within 1% of experimental value. The elastic constants, bulk modulus, shear modulus, Young's modulus and Poissons ratio were all calculated to a high level of accuracy. As such, the mechanical and physical properties of ZrC have been established with accurate results.

Two different types of defects in solids have been studied for ZrC. Carbon vacancy defects and carbon insertion defects were considered. All the types were considered in both carbon-rich and zirconium-rich environments. Among the different concentrations of carbon vacancy defects studied, only low vacancy concentration structures, i.e $ZrC_{0.94}$ and $ZrC_{0.97}$ were observed to be stable. The calculated DFE's are in excellent agreement with values found in the literature. Considering the carbon insertion defects, the observation is that such defect structures are unstable and hence unlikely to form. The effect of the defect is observed to be more local in both carbon vacancies and insertions.

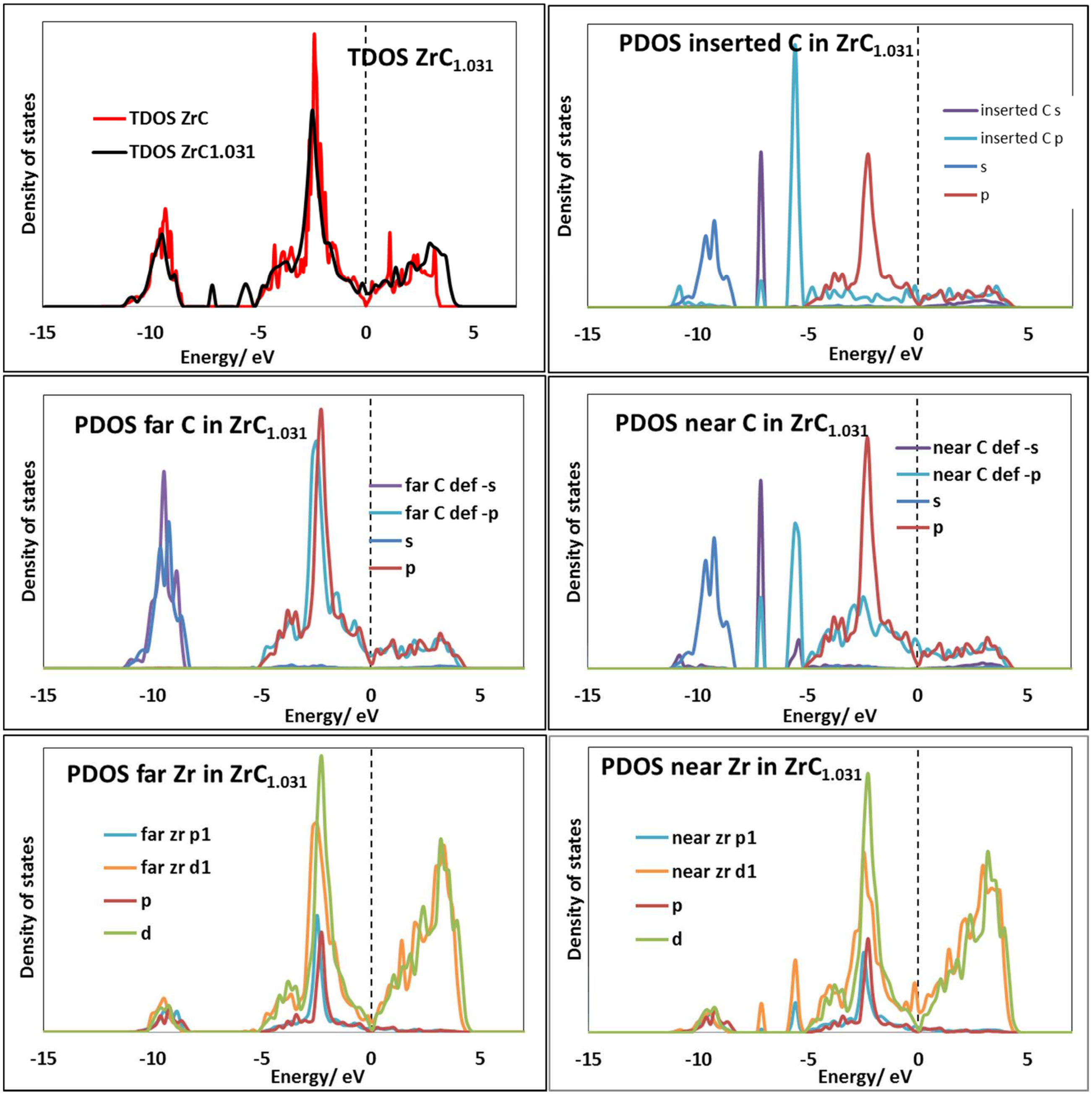

Figure III.11.TDOS and PDOS of $ZrC_{1.031}$ defect. Legend explanation is same as in figure III.5

Reference

[1] C. P. Kempter and R. J. Fries, .

[2] P. Haas, F. Tran, and P. Blaha, “Calculation of the lattice constant of solids with semilocal functionals,” *Phys. Rev. B*, vol. 79, no. 8, p. 85104, 2009.

[3] F. D. Murnaghan, “The Compressibility of Media under Extreme Pressures,” *Proc. Natl. Acad. Sci. U. S. A.*, vol. 30, no. 9, pp. 244–247, Sep. 1944.

[4] L. E. Toth, *Transition metal carbides and nitrides*. New York: Academic press, 1971.

[5] A. Arya and E. A. Carter, “Structure, bonding, and adhesion at the ZrC(100)/Fe(110) interface from first principles,” *Surf. Sci.*, vol. 560, no. 1–3, pp. 103–120, 2004.

[6] D. Douglass, *Superconductivity in d- and f-Band Metals: Second Rochester Conference*. Springer Science & Business Media, 2012.

[7] Z. Lv, H. Hu, C. Wu, S. Cui, G. Zhang, and W. Feng, “First-principles study of structural stability, electronic and elastic properties of ZrC compounds,” *Phys. B Condens. Matter*, vol. 406, no. 14, pp. 2750–2754, 2011.

[8] T. Das, S. Deb, and A. Mookerjee, “Study of electronic structure and elastic properties of transition metal and actinide carbides,” *Phys. B Condens. Matter*, vol. 367, no. 1–4, pp. 6–18, 2005.

[9] J. Wang, Y. Zhou, Z. Lin, T. Liao, and L. F. He, “First-principles prediction of the mechanical properties and electronic structure of ternary aluminum carbide Zr3Al3C5,” *Phys. Rev. B*, vol. 73, no. 13, p. 134107, Apr. 2006.

[10] Y. Le Page and P. Saxe, “Symmetry-general least-squares extraction of elastic coefficients from \textit{ab initio} total energy calculations,” *Phys. Rev. B*, vol. 63, no. 17, p. 174103, Mar. 2001.

[11] Y. Le Page and P. Saxe, “Symmetry-general least-squares extraction of elastic data for strained materials from \textit{ab initio} calculations of stress,” *Phys. Rev. B*, vol. 65, no. 10, p. 104104, Feb. 2002.

[12] D. Holec, M. Friák, J. Neugebauer, and P. H. Mayrhofer, “Trends in the elastic response of binary early transition metal nitrides,” *Phys. Rev. B*, vol. 85, no. 6, p. 64101, Feb. 2012.

[13] F. Birch, “Finite Elastic Strain of Cubic Crystals,” *Phys. Rev.*, vol. 71, no. 11, pp. 809–824, Jun. 1947.

[14] J. F. Nye, *PHYSICAL PROPERTIES OF CRYSTALS, THEIR REPRESENTATIONS BY TENSORS AND MATRICES*. Oxford: Oxford University Press, 1985.

[15] S. Shang, Y. Wang, and Z.-K. Liu, “First-principles elastic constants of α- and θ-Al2O3,” *Appl. Phys. Lett.*, vol. 90, no. 10, p. 101909, Mar. 2007.

[16] W. Voigt, *LEHRBUCH DER KRISTALLPHYSIK*. Leipzig: Teubner, 1928.

[17] A. Reuss, “Berechnung der Fließgrenze von Mischkristallen auf Grund der Plastizitätsbedingung für Einkristalle .,” *ZAMM - J. Appl. Math. Mech. Z. Für Angew. Math. Mech.*, vol. 9, no. 1, pp. 49–58, Jan. 1929.

[18] W. Weber, “Lattice Dynamics of Transition-Metal Carbides,” *Phys. Rev. B*, vol. 8, no. 11, pp. 5082–5092, Dec. 1973.

[19] D. J. Green, *AN INTRODUCTION TO THE MECHANICAL PROPERTIES OF CERAMICS*. Cambridge: Syndicate of the University of Cambridge Cambridge, 1998.

[20] S. Mecabih, N. Amrane, Z. Nabi, B. Abbar, and H. Aourag, *Phys. A*, vol. 285, p. 392, 2000.

[21] H. Fu, W. Peng, and T. Gao, "Structural and elastic properties of ZrC under high pressure," *Mater. Chem. Phys.*, vol. 115, no. 2–3, pp. 789–794, 2009.

[22] A. Fernández Guillermet, "Analysis of thermochemical properties and phase stability in the zirconium-carbon system," *J. Alloys Compd.*, vol. 217, no. 1, pp. 69–89, Jan. 1995.

[23] J. Li, D. Liao, S. Yip, R. Najafabadi, and L. Ecker, "Force-based many-body interatomic potential for ZrC," *J. Appl. Phys.*, vol. 93, no. 11, pp. 9072–9085, 2003.

[24] H. Baker, Ed., *ASM HANDBOOK, ALLOY PHASE DIAGRAMS*, vol. 3. Materials Park, Ohio: ASM International, 1992.

[25] Kim, Szlufarska, and Morgan, *J Appl Phys*, vol. 107, p. 53521, 2010.

[26] S. Kim, I. Szlufarska, and D. Morgan, "Ab initio study of point defect structures and energetics in ZrC," *J. Appl. Phys.*, vol. 107, no. 5, p. 53521, Mar. 2010.

Chapter IV: Adsorption and Reactivity of O_2, H_2 and H_2O with ZrC Low Index Surfaces

Table of Contents

1. Introduction

This chapter describes the adsorption and reactivity of small inorganic molecules namely H_2, O_2 and H_2O with ZrC low index surfaces. The analysis performed starts with studies on all three low index surfaces, (100), (110) and (111) surfaces including their structure, stability and all other properties. The chapter is made up fully published peer reviewed research articles. The chapter is divided into three sections covering each of the three molecules.

In the first section, the fully published article entitled "*Periodic DFT and Atomistic Thermodynamic Modeling of Reactivity of* H_2*,* O_2 *and* H_2O *molecules on Bare and Oxygen Modified ZrC(100) Surface*". This section describes work done on only the (100) surface and it is published in the American Chemical Society, Journal of Physical Chemistry C.

In the second section, another fully published article entitled "*Stability, Equilibrium Morphology and Hydration of ZrC(111) and (110) surfaces with* H_2O*: A Combined Periodic DFT and Atomistic Thermodynamic Study*". The article is published in the Royal Society of Chemistry journal, Physical Chemistry Chemical Physics. The paper describes the stability of ZrC(111) and (110) surfaces as well as their hydration and then the equilibrium morphology of the nanocrystallites at different temperatures upon hydration.

In the final section of this chapter, a full description of oxidation on all three ZrC surfaces is given. The section is also made of a fully published article entitled "*Oxidation and Equilibrium Morphology of Zirconium Carbide Low Index Surfaces using DFT and Atomistic Thermodynamic Modeling*". The article is published in the American Chemical Society, Journal of Physical Chemistry C.

2. Periodic DFT and atomistic thermodynamic modeling of reactivity of H_2, O_2 and H_2O on bare and oxygen modified ZrC(100) surface

A fully published article on the reactivity of H_2, O_2 and H_2O on ZrC(100) surface is given here.

THE JOURNAL OF PHYSICAL CHEMISTRY C

Article

pubs.acs.org/JPCC

Periodic DFT and Atomistic Thermodynamic Modeling of Reactivity of H_2, O_2, and H_2O Molecules on Bare and Oxygen Modified ZrC (100) Surface

Eric Osei-Agyemang,[†] Jean Francois Paul,[†] Romain Lucas,[‡] Sylvie Foucaud,[‡] and Sylvain Cristol*[,†]

[†]Unité de Catalyse et Chimie du Solide (UCCS), UMR-CNRS 8181, Université Lille 1, 59655 Villeneuve d'Ascq, Lille, France

[‡]Science des Procédés Céramiques et de Traitements de Surface (SPCTS), UMR-CNRS 7315, Centre Européen de la Ceramique—Institut des Procédés Appliqués aux Matériaux, Limoges, France

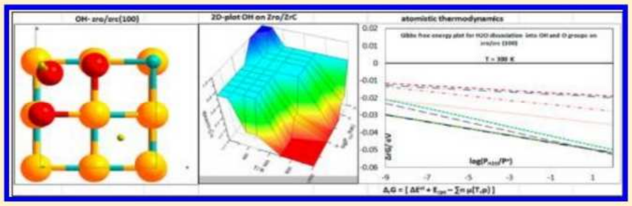

ABSTRACT: A comprehensive study was carried out using DFT calculation, together with statistical thermodynamics study of oxygen, hydrogen, and water sorption on the bare and ZrO-modified ZrC (100) surface. The bare ZrC (100) surface is found to be fully covered by oxygen whatever the temperature and pressure whereas it is free of hydrogen. Water adsorbs on the bare surface at temperatures below 200 K and dissociates into surface hydroxyl groups, but all water induced features are lost at room temperature. Oxygen modification further activates the (100) surface, and water adsorbs strongly as either atomic O with H_2 release or into surface OH and H groups. Thermodynamic stability plots at 300 K for different water coverage predict coverage of 0.75 ML at $>10^{-8}$ bar. These findings compare well with experimental photoemission studies published in the literature.

I. INTRODUCTION

Zirconium carbide (ZrC) is a non-oxide ultrahigh temperature ceramic (UHTC) used as thermostructural materials in applications and areas such as nuclear, aerospace, and steel. It belongs to the transition metal carbide (TMC) group of materials which have special properties such as high melting points. One of the major tasks for the nuclear and aerospace industries resides in the making of highly refractory ceramics whose properties would be compatible with the harsh working conditions of such processes.[1] For example the future fourth generation engines of nuclear plants are required to work at very high temperatures >1200 °C, and hence they would require materials whose physicochemical properties are compatible with such working conditions.[2] Other applications include the manufacture of hard materials such as cutting tools. ZrC among the TMC has very high refractory and excellent mechanical properties, and hence is suitable for these kinds of applications. The requirement of these structural materials to work under severe conditions, for instance, high temperatures and corrosive oxidizing environments, is not easily achieved. This is due to the fact that introduction of a small pressure of oxygen forms zirconium oxide layer on the surface, which leads to deterioration of the mechanical properties of the ceramic. Very low refractory oxides are thus formed at temperatures around 350−400 °C, and the oxidation resistance is very limited.[3]

The resistance to oxidation can be achieved by coating the surfaces with other ceramics such as SiC, which has outstanding properties at high temperatures.[4,5] In order to achieve such coating, the ZrC surface needs to be first modified with small molecules which can aid in the grafting of the SiC. Examples of such candidate molecules which can generate functionalization of the surface include water, ammonia, and azo-radical initiators.[6] The reactivity of the different surfaces of the ZrC material therefore requires extensive investigations to understand, first, the different processes taking place on the surface and, second, how such processes affect the physicochemical properties of the material. Several experimental and theoretical studies have been carried out including processes by which small molecules such as water, oxygen, and hydrogen among others interact with the surface. For example, the reactivity of oxygen on the (100) surface of ZrC has been extensively studied both experimentally and theoretically. Indeed, the (100) surface is found to be very reactive to oxygen exposure. Oxygen is observed to form a ZrO-like layer, after the ZrC (100) surface is exposed to 50 langmuirs (L) of O_2 and heated to about 1000 °C in an angle resolved photoemission spectroscopy (ARPES) study.[7] The oxidation process of the ZrC (100) surface was also studied using UPS and XPS. Upon exposure of the surface to O_2 at room temperature, carbon atoms in the surface get depleted and substrate Zr atoms are oxidized. ZrO-like layer was proposed to be at coverage of less than 3 L and to become a ZrOx ($1 < x < 2$) state with further exposure of O_2.[8] It was also observed that, upon heating of the oxidized surface over 1000 °C, the XPS O 1s peak intensity decreases rapidly while the C 1s peak intensity increases and becomes equal to the initial value at 1300 °C. Thus, oxygen is removed from the surface and bulk is recovered at temperatures

Received: April 1, 2014
Revised: May 22, 2014
Published: May 22, 2014

dx.doi.org/10.1021/jp503208n | J. Phys. Chem. C 2014, 118, 12952−12961

higher than 1300 °C.[8] Several theoretical studies have been undertaken on the oxidation process of the ZrC 100 surface. The preferred adsorption site of oxygen is found to be an mmc hollow site (bridge between two Zr atoms and one carbon atom)[9] thanks to density functional theory (DFT) calculations. The process involving the exchange of surface carbon atoms with oxygen using DFT predicts the removal of surface C atoms as CO gas involving a minimum of two O adatoms.[10]

The preparation of the ZrC material is normally difficult to perform at conditions void of gaseous water molecules, and as such the interaction of the individual surfaces with water is of paramount importance. Reactivity with water can lead to the formation of surface hydroxyl groups which can be used as precursors for subsequent grafting of other materials onto the ZrC surface. There is no extensive work both experimentally and theoretically on the reactivity of water with the ZrC (100) surface. The only experimental work performed on the reactivity of water on this surface is rather on an oxygen modified ZrC (100) surface.[7,11] According to the authors, water is inert on the ZrC (100) surface at room temperature but adsorbs dissociatively as OH and atomic O species on the oxygen modified surface. The authors observed no water induced features in XPS and UPS when the ZrC (100) clean surface is exposed to water at least up to 10 L at room temperature. As the surface covered with an ordered ZrO-like layer is exposed to 1 L H_2O at room temperature, two O 1s peaks grow at 530.4 and 532.3 eV indicating that H_2O adsorbs, forming two types of adsorbed species. There are however no reported theoretical studies on the reactivity of water on the ZrC (100) surface to our knowledge.

Not only is the oxidation of the ZrC (100) surface important but also the reduction process of the surface in reducing environments needs to be studied. However, there are no reports on the reactivity of the (100) surface with H_2 both experimentally and theoretically. It was suggested that H_2 shows no adsorption on the clean (100) surface at room temperature,[12] but the working pressure conditions were not reported.

In the present work, we investigate the reactivity of H_2O, O_2, and H_2 on the bare ZrC (100) surface as well as on a model of oxygen-modified ZrC (100) surface by means of periodic DFT calculations. The effects of temperature and pressure on the adsorption process are compared with experimental findings by mean of atomistic thermodynamic modeling.

The paper is divided as follows: section II describes the methods and materials used while section III.A provides the results for calculated bulk and surface properties. Sections III.B and III.C provide results and discussions on the reactivity of the small molecules on the bare and ZrO-modified (100) surface, respectively. Section IV finally draws conclusions on the current study.

II. CALCULATION SCHEME AND STRUCTURAL MODELS

All calculations were performed using the Vienna Ab initio Simulation Package (VASP),[13] which is based on Mermin's finite temperature DFT.[14] The electronic configurations used for Zr and C are [Kr]$4d^25s^2$ and [He]$2s^22p^2$ respectively. PAW pseudopotentials[15] were used to replace the core electrons which were kept frozen, as well as the core part of the valence electron wave functions, in order to reduce the number of plane waves required for electrons close to the nuclei. The GGA exchange correlation functional parametrized by Perdew, Burke, and Ernzerhof (PBE)[16] was employed, and the Methfessel−Paxton[17] smearing scheme was used by setting the sigma parameter to 0.1 eV. The accuracy of the calculation results was evaluated by changing the energy cutoff from 200 to 600 eV while the *k*-point sampling mesh was evaluated from 2 × 2 × 2 to 11 × 11 × 11 using the standard Monkhorst−Pack[18] special grid. From this evaluation, all subsequent bulk and surface calculations were performed by describing the valence electrons using the plane wave basis set with a cutoff of 500 eV while the integration of the Brillouin zone was performed with 9 × 9 × 9 *k*-points for the bulk and 9 × 9 × 1 for surface calculations. The Kohn−Sham equations are solved self-consistently until the energy difference between two successive iterations is lower than 10^{-4} eV.

Cubic ZrC belongs to the $Fm3m$ space group, with two special positions for Zr and C at (0 0 0) and (0.5 0.5 0.5) respectively with no degree of freedom in the bulk owing to the symmetry of the system. For bulk calculations, the positions of all ions were relaxed, while for all surface calculations, the positions of all the ions in the three topmost layers were relaxed in order to render the net forces acting upon them smaller than 10^{-2} eV/Å. The theoretical equilibrium lattice parameter for the ZrC was determined by calculating the energy at different volumes of the unit cell. The resulting data set was fitted using Murnaghan's equation of state (eq 1).

$$E(V) = E_o - [BV_o/(B' - 1)] + (BV/B') [((V_o/V)B'/(B' - 1)) + 1] \quad (1)$$

$E(V)$ is the energy obtained at different volumes, E_o is the fitted equilibrium energy, V is the volume of unit cell used, V_o is the equilibrium volume, B is the bulk modulus, and B' is the pressure derivative of the bulk modulus.

The stable (100) low index surface used in our calculations is shown in Figure 1. Their starting geometry was obtained by cleaving the optimized bulk structure along the corresponding normal direction. A (1 × 1) surface unit cell was used for all surface calculations except calculations on lower coverage adsorption structure where a (2 × 2) has been used. No surface reconstruction is observed.[19] In order to avoid surface−surface interactions, a vacuum of 12 Å was set as separation between two periodically repeated slabs. Eight atomic layers were used for the surface energy calculation and reactivity. The three outermost layers of the slab were allowed to relax in order to render the net forces acting upon them smaller than 1×10^{-2} eV/ Å while the remaining layers were kept fixed to mimic bulk properties. Cleaving of the ZrC (100) yields two equivalent surfaces, and then surface energy for the rigid surface is computed as $\gamma = (E_{slab} - nE_{bulk})/2A$ where E_{slab} denotes the slab energy, nE_{bulk} is the energy of n ZrC units in the bulk structure, and A is the surface area exposed by the surface plane. The surface energy for the relaxed surface is computed by adding the relaxation energy to that of the rigid surface and proceeding with the equation above for the unrelaxed surface. For the ZrO-like layer on the surface, the crystal structure is not yet determined. The observed thickness of this layer on the ZrC (100) surface is found experimentally to be 1.2−2.4 Å,[8] and it also gives a sharp (1 × 1) LEED pattern. Hence, we modeled this surface by replacing all the C atoms in the first layer with O atoms to form ZrO-like layer on the ZrC (100) surface.

The adsorption of small molecules has been investigated in both an associative and a dissociative way for water, hydrogen,

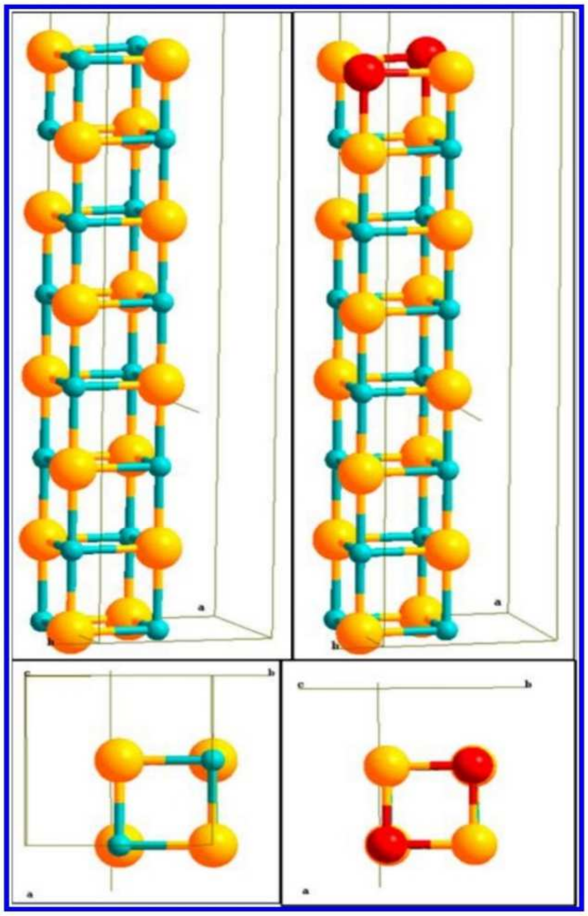

Figure 1. ZrC (100) [slab (left) and top view (bottom left)] and ZrO/ZrC (100) [slab (right) and top view (bottom right)]; blue (C), yellow (Zr), red (O).

and oxygen by testing different adsorption modes. While atomic and molecular oxygen are treated in a spin polarized way within the gas phase, O and O_2 adsorption was carried out without using spin polarization. Indeed, during its interaction with the surface, there is a dramatic weakening in the open shell nature of O_2 molecule and the subsequent dissociation into O atoms. Moreover, according to Rodriguez et al., during their first-principles calculations of O and O_2 adsorption on a ZrC (100) surface, they observed no need for spin polarized calculation after testing with several test calculations.[10] The adsorption energies are then computed as in eq 2.

$$E_{\mathrm{ads}} = -[E_{\mathrm{surf+molecule}} - E_{\mathrm{clean\_surface}} - E_{\mathrm{molecule}}] \tag{2}$$

$E_{\mathrm{surf+molecule}}$ is the energy of the surface with the adsorbed molecule, $E_{\mathrm{clean\_surface}}$ is the energy of relaxed clean surface, and E_{molecule} is the energy of the gaseous small molecules. After obtaining the preferred adsorption modes on the (100) surface, the effect of different coverage of the gaseous molecules on the (100) surface was evaluated using 0.25 monolayer (ML), 0.5 ML, 0.75 ML, and 1 ML coverages with (2 × 2) unit cells.

A. Thermodynamic Model. In order to establish relationship between the calculations performed and experimental working conditions, we used the already well-established atomistic thermodynamic scheme,[20] where the surface and the adsorbed molecule are assumed to be in equilibrium with the gas phase which serves as a reservoir. This then allows for the definition of the adsorption Gibbs free energy ($\Delta_r G$) as a function of thermodynamic parameters such as temperature, T, pressure, p, through the gas phase chemical potential μ using the general equation:

$$\Delta_r G = [\Delta E_o + \Delta E_{\mathrm{zpe}} - \sum n\mu(T, p)] \tag{3}$$

$\Delta E_0 = [E_{\mathrm{el(surface+molecule)}} - E_{\mathrm{el(surface)}} - nE_{\mathrm{el(molecule)}}]$ is the difference of the DFT energies computed at 0 K, and ΔE_{zpe} is the difference in the zero point energy (ZPE) of the gas phase molecule and the molecule adsorbed on the surface. The thermal contributions to the chemical potential of the gas phase molecule which consist of temperature and pressure dependent terms are calculated through eq 4.

$$\mu(T, p) = \mu^{o}(T) + RT \ln[P/P^{o}] \tag{4}$$

The temperature dependent term is computed with statistical thermodynamics as in eq 5.

$$\begin{aligned}\mu^{o}(T) = \Delta[E_{\mathrm{vib}}(0 \\ &\rightarrow T) + E_{\mathrm{rot}}(T) + E_{\mathrm{trans}}(T)] + RT \\ &- T(S_{\mathrm{vib}}(T) + S_{\mathrm{rot}}(T) + S_{\mathrm{trans}}(T))\end{aligned} \tag{5}$$

These thermal contributions introduce the changes in the vibrational, rotational, and translational degrees of freedom upon adsorption of the small molecules onto the surface. Part of the contributions of all such changes was observed to originate from the hard vibrations which are approximated with the ZPE as well as the entropic contributions of the gas phase molecules. The ZPE contributions of the adsorbed molecule on the surface as well as the gaseous molecule were taken into consideration. A value of P^{o} of 1 bar was used and a plot of ($\Delta_r G$) against pressure P was obtained at different constant temperatures. The lowest of such plots at different coverage is the most stable system in a given experimental condition.

B. Transition State (TS) Search. Transition state searches were carried out using the Climbing Image Nudged Elastic Band (CI-NEB)[21] method implemented in VASP. Eight images were used to connect reactants and products for the H_2O TS search while 16 images were required to observe all the features of the potential energy surface of the H_2 dissociation. It involved an initial calculation by fixing the substrate and relaxing the small molecule completely. The stationary points indicating the highest image in the CI-NEB above were characterized by vibrational frequency analysis obtained from the Hessian matrix of the energy to yield an imaginary frequency at the TS point.

The ZPE contribution of the reactant, TS, and product was taken into consideration, and the energies are corrected according to eq 6.

$$E_{\mathrm{corr}} = E + \sum_{i=1}^{MNV} \frac{1}{2} h\nu_i \tag{6}$$

E_{corr} is the corresponding energy of the reactant and TS image after the ZPE correction, and E is the electronic energy of the stationary point. The final energy barrier was then calculated as the difference in the corrected energies between the reactant and TS image.

III. RESULTS AND DISCUSSION

A. Bulk and Surface Structure Properties. Fitting of the energy against volume with the Murnaghan's equation of state yielded an optimized lattice parameter of $a_o = 4.736$ Å, which compares very well with the experimental values of 4.696 Å[22] and 4.70 Å.[1] The lattice parameter is summarized in Table 1, as well as the other fitted bulk properties such as the bulk modulus. The distance between the Zr and C atom sites in the bulk was calculated to be 2.368 Å after relaxation (experimental value: 2.349 Å[23]). The calculated value of the bulk modulus from the fitting, which is 217.9 GPa, is in also very good agreement with the experimental values (223 GPa;[24] 217.7 GPa[25]).

Table 1. Fitted Bulk Parameters

fitting parameter	fitted value
B	217.9 GPa
B'	3.84
V_o	106.25 Å^3
a_o	4.7363 Å

For the relaxation of the (100) surface, it was observed that the Zr atoms relax inward from the first layer, while the C atoms move upward in the first and second layers. This movement of the Zr and C atoms is in the form of ripples. The d_{1C-2M}, which is the vertical distance between C in first layer and Zr in second layer, is 2.346 Å, which agrees well with the value of 2.35 Å from other calculations.[26] The $d_{1M-2C} = 2.256$ Å and compares well with the experimental value of 2.200 Å[23] and calculated value of 2.260 Å.[26] The calculated surface energy for the ZrC (100) rigid surface is 105.7 meV·Å^{-2} as compared to the value of 105.0 meV·Å^{-2}.[27] There was a 9.93% relaxation energy yielding a relaxed surface energy of 95.2 meV·Å^{-2}, which is in excellent agreement with other calculations, 99.4 meV·Å^{-2},[27] 101 meV·Å^{-2},[28] and 96.8 meV·Å^{-2}.[29] The calculated surface energy of the (100) corroborates the fact that it is the most stable among all the surfaces of ZrC.[27] The stability of the (100) surface was further confirmed by computing the density of states (DOS) for the bulk structure and comparing with the projected DOS for the created surface. Figure 2 shows the DOS plot for the relaxed (100) surface. The DOS shows no significant change upon cleaving the bulk to obtain the (100) surface, but it however shows only a slight introduction of surface states around the Fermi level. Projection of the DOS revealed presence of Zr d states around the Fermi level. The near-bulk-like feature of the states around the Fermi level confirms the stability of this surface.

B. Reactivity of H_2, O_2, and H_2O on Bare ZrC (100) Surface. The most stable form of adsorption after testing with different configurations was used in computing the adsorption energies E_{ads}. The adsorption energy was also calculated for different coverage of the (100) surface.

i. H_2 Adsorption. Several adsorption modes were tested for different configurations to find the most stable form of adsorption. The only interaction observed for molecular H_2 with the (100) surface can be neglected: the hydrogen molecule interacts weakly with surface Zr atoms with very small adsorption energy (0.07 eV). In this mode of interaction, the distance between the hydrogen molecule and the surface Zr atoms is 2.47 Å and the distance between the hydrogen atoms is very close to the one observed in the gas phase (0.766 Å).

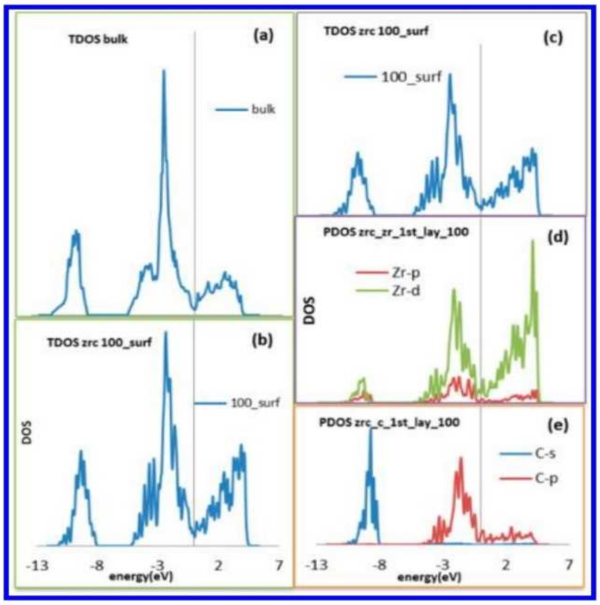

Figure 2. TDOS of bulk structure (a), TDOS of (100) surface (b, c), PDOS of Zr in first layer (d) and C in first layer (e) of ZrC 100 surface.

In the mode where H_2 dissociates into atomic species, the atomic hydrogen atoms are adsorbed on the surface carbon atoms with $E_{ads} = 0.44$ eV. The distance between the surface carbon atoms and the adsorbed H atom is 1.030 Å. Another possibility is the dissociation into H on Zr and the other on one surface C atom with the C−H bond distance as 1.150 Å and the Zr−H bond distance of 1.974 Å. This adsorption mode is however an endothermic process. The adsorption energies are summarized in Table 2.

Table 2. Calculated Adsorption Energies at Different Coverage H, Atomic O, ZrC (100) Surface

	E_{ads}/eV	
coverage/ML	H atom	O atom
0.25	0.51	2.60
0.50	0.44	2.70
0.75	0.37	2.71
1.0	0.26	2.75

In order to determine the effect of parameters such as temperature, pressure, and chemical potential of the gas phase hydrogen gas on the (100) surface, we obtained thermodynamic plots of stability. The Gibbs free energy plot is depicted in Figure 3 at 400 K. Our analysis revealed that hydrogen cannot be removed from the (100) surface by manipulation of temperature and pressure at temperature below 300 K, and hence we only report the thermodynamic plot at 400 K. No instance of full surface coverage was observed at any pressure condition. At extreme pressures above 30 bar, the surface is easily reduced and covered with three hydrogen atoms yielding 0.75 ML. As the pressure is reduced from around 30 to 10^{-2} bar, there is the removal of one hydrogen atom, resulting in 0.5 ML coverage. Going down further between 0.02 and 6×10^{-6} bar another hydrogen atom leaves the surface and results in low

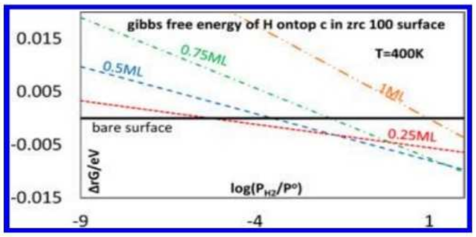

Figure 3. Gibbs free energy plot for atomic H adsorption on the ZrC (100) surface.

coverage of 0.25 ML, and at extremely low pressures of below 6 × 10^{-6} bar, the clean surface is recovered. A two-dimensional surface plot for the adsorption of H_2 on the bare (100) surface is provided in Figure 4. This plot is a function of temperature and pressure against coverage of hydrogen, and it provides better aid in observing the desorption characteristics of H_2 upon adsorption on the bare surface.

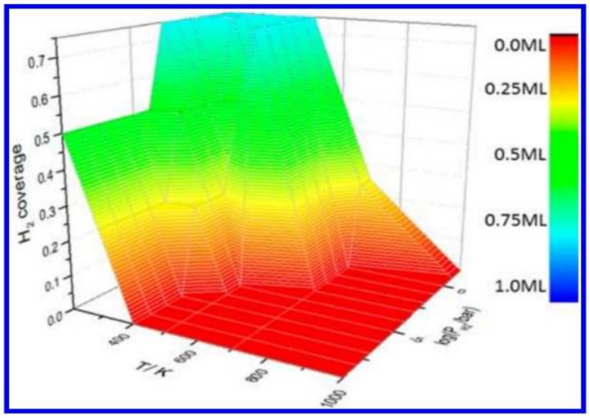

Figure 4. 2D plot of equilibrium hydrogen coverage on bare ZrC (100) as a function of temperature and partial pressure revealing desorption characteristics.

A transition state search was performed for the dissociation of H_2 into atomic H on the (100) surface. The reaction involved only one path, but an intermediate structure was observed, and hence the path was divided into two steps. The first reaction step involved the alignment of the H_2 molecule close to one C atom, with a bond distance between C and H of 1.362 Å and H−H bond distance of 1.186 Å at the first transition state (TS1) point. This later was characterized by only one imaginary frequency (Figure 5b) and an activation barrier of 0.58 eV. The intermediate species formed (Figure 5c) is dissociated H_2 into atomic H on both Zr and C atoms with a C−H bond distance of 1.150 Å and a Zr−H distance of 1.974 Å. This intermediate species was necessary as the two hydrogen atoms are far apart in the final state. As such, the two hydrogens first adsorb on one carbon and a closer Zr atom at this intermediate step before proceeding to the final step of the process. The reaction then proceeds through a second transition state (TS2) in which the H on Zr at the intermediate state is now moved and sits between that Zr and the adjacent C atom and characterized by one imaginary frequency (Figure 5d) and an activation barrier of 0.16 eV. The C−H bond distance is 1.143 Å while the H atom between Zr and C has bond distances of Zr−H = 1.996 Å and C−H = 2.032 Å. The activation energy between the reactant geometry and the highest TS image point (TS2) is then calculated to be 0.65 eV. This high energy barrier of the rate-determining step implies that reduction of the surface with H_2 is very slow at low temperature. Increasing the temperature slightly can drive the process past TS2, which can result in reduction of the ZrC (100) surface. At high temperature, the hydrogenated surface is however not stable. This competition between thermodynamic aspects (low temperature is required to obtain a stable hydrogenated surface state) and kinetic aspects (high temperature is required to overcome the activation barrier) is at the origin of our prediction of the absence of observation of H on the ZrC clean surface, even upon H_2 treatment. Indeed, there has been no experimental report on its observation on the clean (100) surface.

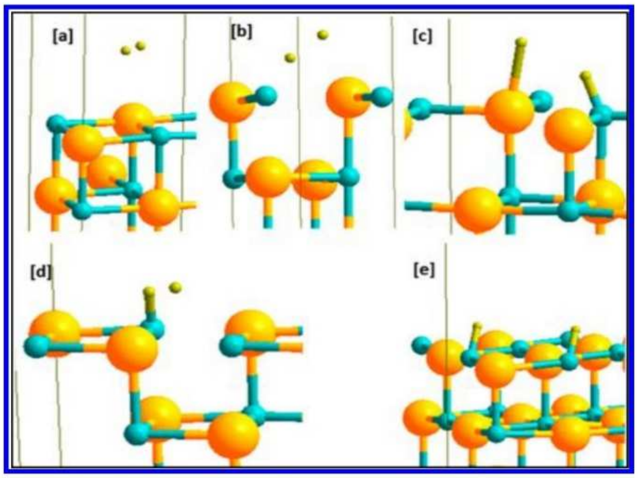

Figure 5. Dissociation process of H_2 to atomic H on clean ZrC (100) surface with their relative energies. Molecular H_2 on Zr (a, 0.0 eV), TS1 image (b, 0.58 eV), intermediate structure (c, 0.50 eV), TS2 (d, 0.65 eV), and atomic H on surface C (e, −0.48 eV). Blue (C), yellow (Zr), light green (H).

ii. O_2 Adsorption. There is detailed theoretical work in the literature concerning the adsorption of molecular and atomic oxygen,[30] as well as transition state search and kinetics[10] of the oxidation process of the ZrC (100) surface. However, there is no thermodynamic information concerning the working pressure and temperature regimes for such oxidation processes. We therefore tried to provide the missing thermodynamic data to the available information in the literature. Only two adsorption modes for molecular oxygen were observed with molecular O_2 sitting on top of Zr atoms on the (100) surface with E_{ads} = 0.52 eV compared to the value of 0.69 eV[30] reported previously. The other mode of adsorption was one in which the molecular O_2 bridges two surface Zr atoms with E_{ads} = 0.65 eV compared to 0.87 eV.[30] The slight difference in the adsorption energies can be attributed to the different GGA functional used as the PW91 functional was employed in ref 30. The authors in ref 30 also used spin polarized O_2 molecule in their calculation, and that accounts for the difference between their calculated values and what we obtained in this work. All other configurations of adsorption led to dissociative adsorption giving atomic oxygen on the surface with the O atom bridging two Zr atoms and one C atom on the surface in an mmc mode in agreement with what is discussed in ref 9. It was observed that dissociation of oxygen molecule into atomic oxygen is not affected by spin polarization, and hence our results involving atomic oxygen do not include spin polarized calculations. In this mode of adsorption, the O adatom is significantly closer to the surface carbon atom than the Zr atoms. The measured bond distance between the oxygen atom and carbon atom is 1.410 Å while the d_{OZr} is 2.24 Å. We obtained an adsorption energy of 5.77 eV for dissociation into atomic species on the ZrC (100) surface as compared to 5.69 eV, using the RPBE functional.[9] A summary of the adsorption energies at different coverages per oxygen atom is provided in Table 2.

It can be observed from Figure 6 that the surface (100) is easily covered with the smallest amount of oxygen at even extremely low pressures and temperatures below 1500 K. The surface is always covered with a full layer of oxygen at pressures between 3×10^{-7} bar and 100 bar even at 1500 K. Thus, even at such a high temperature of 1500 K, the surface cannot be easily cleaned from oxygen at a wide range of pressures through manipulation of pressure alone. This is in good agreement with the experimental report of the possibility of cleaning the (100) surface from oxygen by employing temperatures above 1500 K[8] in UHV.

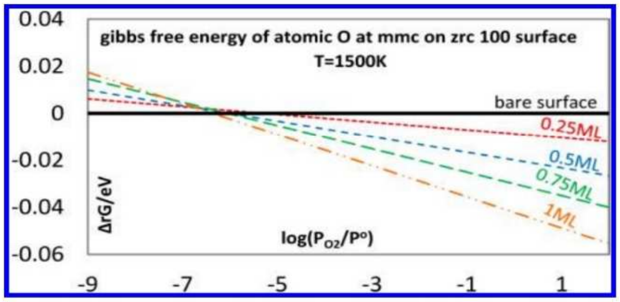

Figure 6. Gibbs free energy plot for atomic O adsorption on clean ZrC (100) surface at different temperatures.

iii. H_2O Adsorption. Several modes for water adsorption on the (100) surface were tested. Two stable modes of adsorption were observed. One associative mode where molecular H_2O sits directly on top of surface Zr atoms is obtained with an adsorption energy E_{ads} = 0.53 eV. Bonding of the water molecule to the surface is achieved through its O atom. The most stable dissociative mode of adsorption observed is the breaking of the H_2O molecule into surface hydroxyl and hydrogen atom with the OH group sitting on top of the surface Zr atom and the H atom on top of the surface C atom. This process is accompanied by an adsorption energy E_{ads} = 0.81 eV. The calculated adsorption energies at different surface coverage as well as the calculated bond distances of the adsorbed species onto the (100) surface are summarized in Table 3. Thus, at this point, it looks possible to functionalize the ZrC (100) surface with surface hydroxyl groups due to the significant adsorption energy calculated for the dissociative mode into surface OH and H groups.

We performed a transition state search for the dissociation of water into surface hydroxyl groups (Figure 7). The activation barrier for the above dissociation process is E_{barr} = 0.13 eV as shown in Table 3. This low energy barrier shows that water molecules will readily dissociate into hydroxyl and H species on the ZrC (100) surface.

Table 3. Adsorption Energies (E_{ads}) at Different Coverage for Associative (H_2O on Top of Surface Zr) and Dissociative Mode (OH on top of Zr, H on top of C)

	E_{ads}/eV/H_2O	
coverage/ML	H_2O on top of Zr	OH on top of Zr, H on top of C
0.25	0.49	0.85
0.50	0.53	0.81
0.75	0.56	0.98
1.0	0.48	1.00
	bond distances and activation barrier[a]	
	H_2O on top of Zr/Å	OH on top of Zr, H on top of C/Å
d_{OM}	2.50	2.05
d_{HC}		1.12
$E_{activation}$	0.13 eV	

[a] d_{OM} = O−$Zr_{surface}$ distance, d_{HC} = H−$C_{surface}$ distance. $E_{activation}$ = activation barrier for dissociation of H_2O to surface OH and H groups.

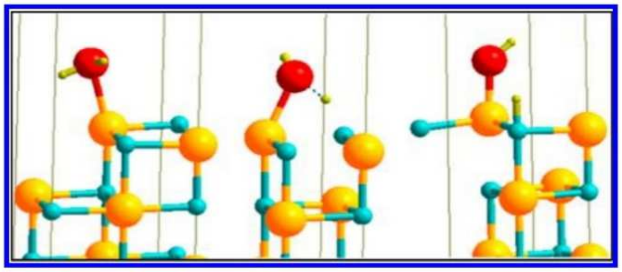

Figure 7. Dissociation of H_2O on clean ZrC (100) surface. Molecular H_2O on Zr (left), TS of H_2O dissociation (middle), surface hydroxyl and H groups (right). Blue (C), yellow (Zr), light green (H), red (O).

However, it is reported that no water induced features are observed on the ZrC (100) surface at room temperature[7] and hence it required the use of thermodynamic arguments to explain this apparent discrepancy. The adsorption energies obtained for both molecularly adsorbed water molecule and dissociatively adsorbed OH and H species on the ZrC (100) surface were used to obtain Gibbs free energy plots at different temperatures and pressures (Table 3). The plots of $\Delta_r G$ against different partial pressures of gaseous water molecules are shown in Figure 8 for the dissociative mode of water adsorption.

Our analysis shows that the surface can only be covered with 0.75 ML of H_2O molecules at very low temperatures (200 K) at pressures above 6×10^{-6} bar. Figure 8 provides details of the surface coverage at different pressures at 400 K when the surface is covered with hydroxyl and H groups. The surface is fully covered with OH at pressures above 7.5×10^{-4} bar. Below

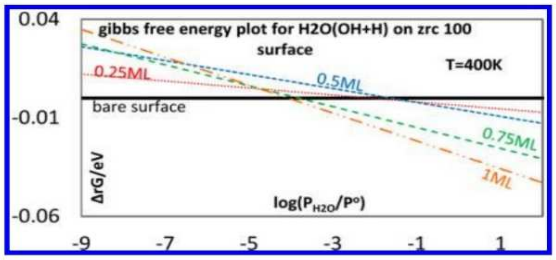

Figure 8. Gibbs free energy plot of molecular H_2O and dissociative H_2O to OH and H adsorption on clean ZrC (100).

7.5×10^{-4} bar, all surface hydroxyl and H groups are removed from the surface and the bare surface is recovered. The bare surface can also be recovered by working at 500 K and at pressures below 5×10^{-2} bar according to our analysis. In ref 7, the authors mentioned an observation in one of their experiments concerning water adsorption on the (100) bare surface and claim no observation of any water induced features at room temperature. This might however be due to the fact that the experiment was conducted in UHV so that the bare surface is always observed as can be seen in Figure 8.

C. Reactivity of H_2O on Oxygen Modified ZrC (100) Surface. The adsorption and energetics of water on the oxygen modified ZrC (100) surface were finally studied due to the established fact from the previous sections that there is always oxidation of the clean (100) surface upon introduction of even very small amounts of oxygen. The preparation of this surface requires conditions under which it is very difficult to control oxygen, and hence the surface is easily oxidized. Our model for the surface functionalization with water therefore needs to be modified by taking into account the oxidized layer on the surface. Details of the electronic structure of the ZrO-like layer on ZrC (100) have been studied, and a full description is provided elsewhere.[26] We however summarize the changes in surface properties and structure of the ZrO layer on the (100) surface. A summary of the interlayer distances between different layers in this model is provided in Table 4, and the relaxed structure of the ZrO layer on the ZrC (100) surface is shown in Figure 9. The calculated DOS after surface relaxation of the ZrO-like layer on the ZrC (100) surface is shown in Figure 10. ARPES of the ZrO thin layer on ZrC (100) has been studied.[31,32] This experiment revealed the formation of a band structure at 4−8 eV below E_f which was attributed to O 2p bands as well as new features at the Fermi level (E_f). The O 2p band was finally assigned at 6.1 eV. These features have been observed in our calculated DOS as can be seen in Figure 10. A comparison of the bulk, ZrC (100) surface and the ZrO-modified ZrC (100) surface TDOS as shown in Figure 10, panels a, b, and c, reveals a new valence band formed at 6 eV and also substantial amount of new states around the Fermi level. The TDOS was then projected onto the surface Zr and O atoms and compared to the TDOS of the ZrO layer. The band at 6 eV is solely from the O 2p orbitals (Figure 10f), and the new state formed at the E_f is mainly of Zr d character (Figure 10e). In comparison to the bare (100) surface, the ZrO-modified surface showed a shift of the Zr bands to higher energies into the unoccupied bands at the Fermi level and activates the surface for reactivity. The higher ionicity of the Zr−O bond with respect to the Zr−C bond is responsible for these changes in the DOS. Indeed the oxygen p state is filled and located at −6 eV whereas empty zirconium d states are pushed upward above the Fermi level by the π-donor nature of the oxygen ligands. The increased density of unoccupied Zr d states around the E_f provides further evidence for increase in activity of the modified surface.

Table 4. E_{ads} at Different Coverage for Complete Dissociation of H_2O to O + H_2, Dissociation to OH + H, and Interlayer Distances of Relaxed ZrO Layer on ZrC (100) Surface

coverage/ ML	E_{ads}/eV/H_2O	
	O as Zr−Zr bridge, H_2 in cell	OH on Zr, H on 4 hollow site
0.25	1.93	2.11
0.50	1.83	1.58
0.75	1.78	1.87
1.0	1.35	1.41
Interlayer Distances of Relaxed ZrO on ZrC (100) Surface/Å		
d_{1O-2M}	2.44	2.48[26]
d_{1M-2C}	2.14	2.14[26]
d_{2M-3C}	2.27	2.26[26]
d_{2C-3M}	2.42	2.42[26]

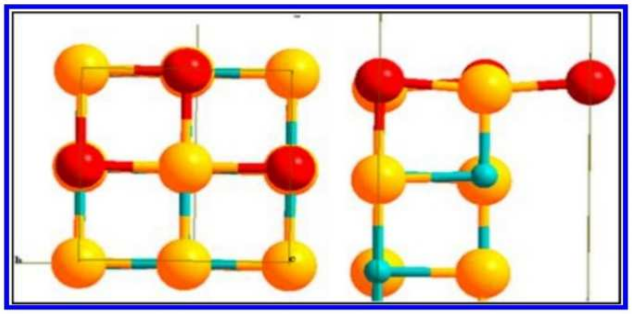

Figure 9. Top view (left) and side view (right) of relaxed ZrO layer on ZrC (100) surface. Blue (C), yellow (Zr), red (O).

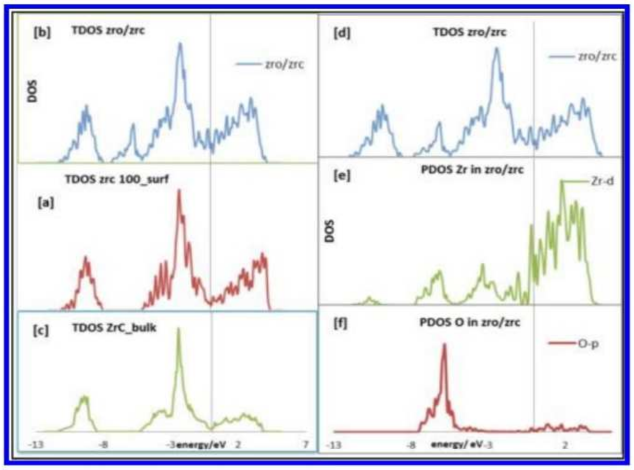

Figure 10. TDOS and PDOS of bulk, clean ZrC (100) and ZrO-like modified ZrC (100) surface aligned vertically at the E_f. TDOS panels a, b, and c show comparison of ZrC (100) clean surface (a), ZrO/ZrC surface (b), and bulk ZrC DOS (c), respectively. TDOS panels d, e, and f provide comparison of ZrO/ZrC surface (d) and projected DOS of Zr (e) and O atoms (f) on this surface, respectively.

Different adsorption modes, both associative and dissociative, for H_2O molecules on the ZrO modified (100) surface have been carried out. With respect to the observed reactivity on the clean surface mentioned earlier, there is a substantial increase in the reactivity of H_2O on this surface. Three stable modes of adsorption were observed: associative H_2O adsorption where H_2O bonds to surface Zr atoms through O of H_2O with E_{ads} = 0.54 eV, dissociative adsorption into O atoms adsorbed as Zr−Zr bridge on the surface and releasing molecular H_2 (Figure 11) with E_{ads} = 1.35 eV, and finally dissociative adsorption into OH group adsorbed on surface Zr and H sitting at the 4-hollow

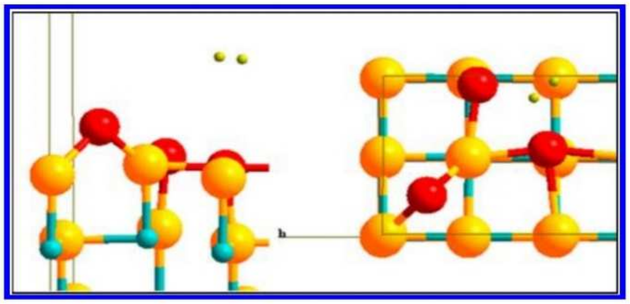

Figure 11. Complete H_2O dissociation into atomic O and molecular H_2 on ZrO-modified ZrC (100) surface. Side view (left) and top view (right). E_{ads} = 1.352 eV. Blue (C), yellow (Zr), light green (H), red (O).

site region between two Zr and two O atoms on the surface (Figure 12) with E_{ads} = 1.41 eV. Thus, we can have either hydroxylation of the surface or further oxidation of the surface with the liberation of H_2.

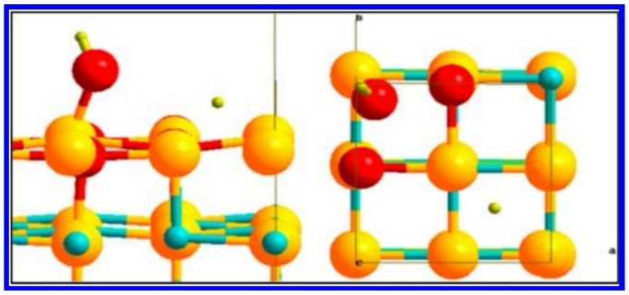

Figure 12. H_2O dissociation into surface hydroxyl and H atom on ZrO modified ZrC (100) surface. Side view (left) and top view (right). E_{ads} = 1.410 eV. Blue (C), yellow (Zr), light green (H), red (O).

Experimentally, H_2O, atomic O, and surface OH groups are observed on the ZrO modified ZrC (100) suface.[7] According to ref 7, UPS study of the adsorption of H_2O on the ZrO modified ZrC (100) surface revealed a band at 5.1 eV which was attributed to O 2p and two others at 7.0−7.7 eV and 9.5−10.0 eV attributed to 1 π and 3 σ states OH groups. Our projected TDOS in Figure 13a shows a comparison of the ZrO/ZrC (100) surface DOS to that of the completely dissociated water into atomic O and H_2, and we see completely new features at 5.1 eV mainly from atomic O 2p in agreement with experimental observations.[7] The TDOS comparison of the dissociation of H_2O into OH and H shows completely different structure to the atomic O adsorption. A new sharp band appears at 7.5 eV which originates from O 2p orbitals from surface OH groups (Figure 13c,d) and confirms the experimentally observed bands at 7.0−7.7 eV.[7] However, we did not observe the experimental bands at 9.5−10.0 eV in our DOS calculation. This can be explained by the fact that the OH 3 σ states are lying below the 1 π OH valence states and hence are difficult to observe in valence band spectra. As such, the assignment of these bands to OH 3 σ states in ref 7 is questionable. The surface states introduced at the E_f are reduced substantially in all cases upon the adsorption of H_2O as can be seen in Figure 13a,c.

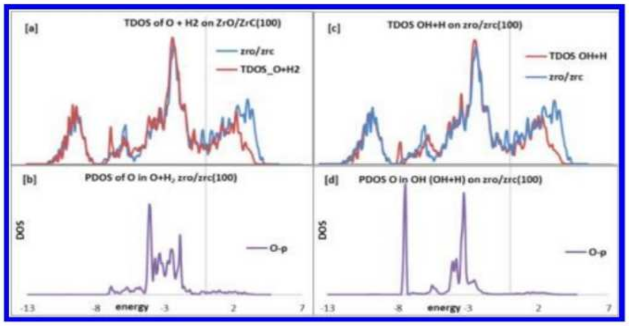

Figure 13. DOS plots for completely dissociated (O + H_2) and (OH + H) on ZrO/ZrC (100) surface.

After obtaining the adsorption energies at different coverage of H_2O on the ZrO/ZrC(100) surface, the stability plots are calculated for a wide range of pressures and at specified temperatures (Figure 14). In the stability plot of H_2O dissociation into atomic O and H_2, the plot is shown at 300 K in order to compare with the experimental findings in ref 7. It can be observed that at UHV or around 10^{-8} bar at 300 K, the surface is covered with the 0.75 ML layers of atomic O and OH groups in excellent agreement with what is observed in ref 7. A more detailed two-dimensional plot of the surface coverage against temperature and pressure, Θ_{hkl} (p, T) is provided in Figure 15. Such a diagram provides detailed understanding of the desorption process of adsorbed water molecules as functions of both temperatures (adsorption isobars) and water partial pressures (adsorption isotherms) in an easily understandable fashion. It provides more insights into the adsorbed species and coverage at pressures other than UHV conditions and different temperatures. For example, at 700 K, the surface is initially covered with three O atoms and three H_2 molecules are liberated at pressures >10^{-4} bar. However, between 10^{-4} and 10^{-5} bar, two O atoms leave the surface to give 0.25 ML coverage. The bare ZrO/ZrC (100) surface is recovered at pressures below 10^{-5} bar or at working temperatures above 700 K. A similar observation for atomic O in Figure 15b shows that, at pressures >10^{-3} bar, the surface is covered with three water molecules (0.75 ML). From 10^{-3} to 10^{-5} bar, there is desorption of two water molecules leaving one water molecule on the surface. Below 10^{-6} bar, the bare ZrO covered ZrC (100) surface is recovered. Thus, at the same

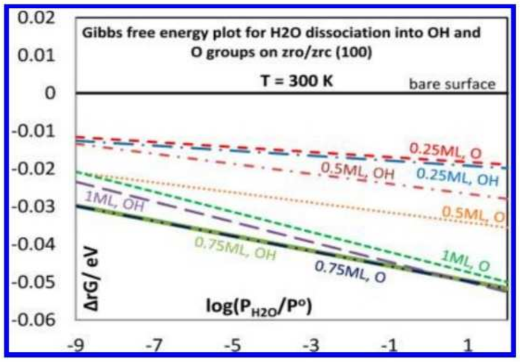

Figure 14. Gibbs free energy plot for H_2O adsorption on ZrO/ZrC (100) surface into either surface OH and H groups or O atoms with release of H_2.

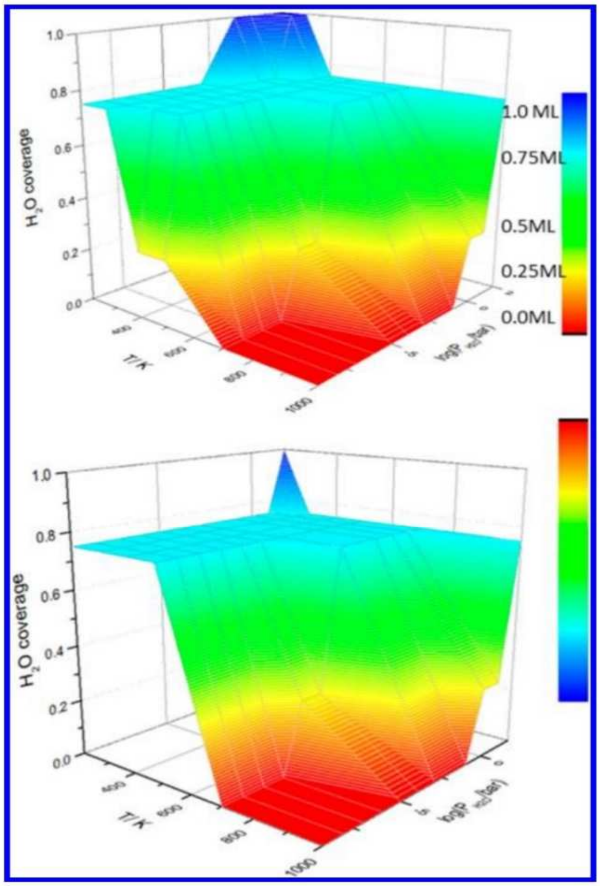

Figure 15. 2D plot of equilibrium water coverage on ZrO/ZrC (100), top (H_2O as OH + H) and bottom (H_2O as O + H_2) as a function of temperature and pressure, revealing a trimodal mode of desorption.

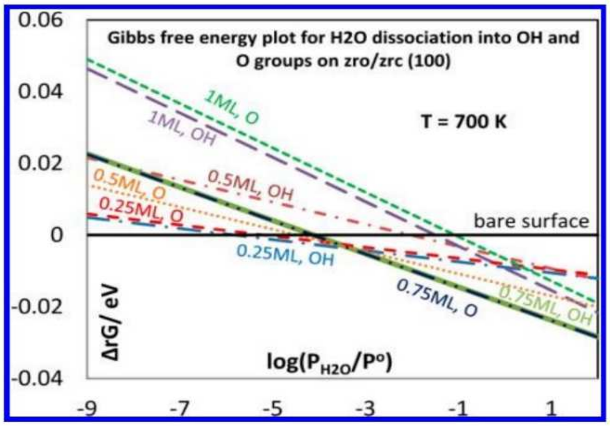

Figure 16. Gibbs free energy plot for H_2O adsorption on ZrO/ZrC (100) surface at 700 K into either OH and H groups or O atoms with release of H_2.

temperature upon water sorption, and in order to clear the surface, one needs much lower pressure for atomic O and H_2 than for OH and H (Figure 16). It reveals the trimodal desorption process of the hydroxylated and further oxidized ZrO/ZrC (100) surface.

IV. SUMMARY AND CONCLUSION

We have combined DFT and atomistic thermodynamic modeling to study reactivity of oxygen, hydrogen, and water molecules on bare and ZrO modified ZrC (100) surface. The calculated adsorption energies at different coverage for each of the small molecules were used to draw thermodynamic plots and study the effect of temperature and pressure on the adsorption of these small molecules on the (100) surface. The temperature range at which the oxidized (100) surface can be cleaned was established to be above 1500 K, confirming that the ZrC (100) surface readily oxidizes in the presence of even a small amount of oxygen. Studies of reduction of the surface with hydrogen reveal dissociative mode of adsorption into surface H atoms as the preferred one. The high activation barrier for H_2 dissociation prevents however the surface from being reduced at room temperature. Water adsorbs dissociatively on the bare (100) surface. The low activation energy barrier for the dissociation process makes it possible to obtain surface hydroxyl groups from molecular water for further functionalization. The surface is fully covered with hydroxyl and H groups at a wide pressure range at 400 K, and the bare surface can be recovered at temperatures above 500 K. This state is however not observed in XPS/UPS because vacuum induces water desorption. However, the oxygen modified ZrC (100) surface is further activated and dissociates water molecules leading to O atom (with H_2 release) and surface OH and H groups. These states are stable even at very low pressures at 300 K showing the oxidized surface is much easier to functionalize than the bare ZrC (100) surface.

■ AUTHOR INFORMATION

Corresponding Author

*Tel: +33 320 43 45 03. Fax: +33 320 43 65 61. E-mail sylvain.cristol@univ-lille1.fr.

Notes

The authors declare no competing financial interest.

■ ACKNOWLEDGMENTS

Numerical results presented in this paper were carried out using the regional computational cluster supported by Université Lille 1, CPER Nord-Pas-de-Calais/FEDER, France Grille, and CNRS. We highly appreciate and thank the technical staff of the CRI-Lille 1 center for their strong and helpful support. The project is supported by Agence Nationale de la Recherche under Contract No. ANR-12-BS08-004-02 (CollZSiC: Elaboration de nanocomposites coeur/coquille ZrC/SiC).

■ ABBREVIATIONS

UPS, ultraviolet photoemission spectroscopy; XPS, X-ray photoemission spectroscopy; L, Langmuir; LEED, low-energy electron diffraction; UHV, ultrahigh vacuum; ARPES, angle resolved photoemission spectroscopy

■ REFERENCES

(1) Toth, L. E. Transition metal carbides and nitrides; Academic Press: New York, 1971.

(2) Gosset, D.; Dollé, M.; Simeone, D.; Baldinozzi, G.; Thomé, L. Structural evolution of zirconium carbide under ion irradiation. *J. Nucl. Mater.* **2008**, *373*, 123−129.

(3) Li, H.; Zhang, L.; Cheng, L.; Wang, Y. Oxidation analysis of 2D C/ZrC−SiC composites with different coating structures in CH4 combustion gas environment. *Ceram. Int.* **2009**, *35* (6), 2277−2282.

(4) Li, H.; Zhang, L.; Cheng, L.; Wang, Y.; Yu, Z.; Huang, M.; Tu, H.; Xia, H. Effect of the polycarbosilane structure on its final ceramic yield. *J. Eur. Ceram. Soc.* **2008**, *28* (4), 887−891.

(5) Greil, P. Polymer Derived Engineering Ceramics. *Adv. Eng. Mater.* **2000**, *2* (6), 339−348.

(6) Iijima, M.; Kamiya, H. Surface Modification of Silicon Carbide Nanoparticles by Azo Radical Initiators. *J. Phys. Chem. C* **2008**, *112* (31), 11786−11790.

(7) Kitaoka, H.; Ozawa, K.; Edamoto, K.; Otani, S. The interaction of water with oxygen-modified ZrC(100) surfaces. *Solid State Commun.* **2001**, *118* (1), 23−26.

(8) Shin, K.; Ken-ichi, O.; Kazuyuki, E.; Shigeki, O. Photoelectron Spectroscopy Study of the Oxidation of ZrC(100). *Jpn. J. Appl. Phys., Part 1* **2000**, *39* (9R), 5217.

(9) Viñes, F.; Sousa, C.; Illas, F.; Liu, P.; Rodriguez, J. A. Density functional study of the adsorption of atomic oxygen on the (001) surface of early transition-metal carbides. *J. Phys. Chem. C* **2007**, *111* (3), 1307−1314.

(10) Rodriguez, J. A.; Liu, P.; Gomes, J.; Nakamura, K.; Viñes, F.; Sousa, C.; Illas, F. Interaction of oxygen with ZrC(001) and VC(001): Photoemission and first-principles studies. *Phys. Rev. B: Condens. Matter Mater. Phys.* **2005**, DOI: 10.1103/PhysRevB.72.075427.

(11) Kitaoka, H.; Ozawa, K.; Edamoto, K.; Otani, S. Interaction of water and methanol with oxygen-modified ZrC(100) surfaces. *Surf. Sci.* **2002**, *518* (3), 225−233.

(12) Nakane, T.; Noda, T.; Ozawa, K.; Edamoto, K. Adsorption of methanol on ZrC(100) and (111) surfaces. *Surf. Sci.* **1999**, *433−435* (0), 180−183.

(13) Hafner, J. Ab-initio simulations of materials using VASP: Density-functional theory and beyond. *J. Comput. Chem.* **2008**, *29* (13), 2044−2078.

(14) Mermin, N. D. Thermal Properties of the Inhomogeneous Electron Gas. *Phys. Rev.* **1965**, *137* (5A), A1441−A1443.

(15) Kresse, G.; Joubert, D. From ultrasoft pseudopotentials to the projector augmented-wave method. *Phys. Rev. B: Condens. Matter Mater. Phys.* **1999**, *59* (3), 1758−1775.

(16) Perdew, J. P.; Burke, K.; Ernzerhof, M. Generalized Gradient Approximation Made Simple. *Phys. Rev. Lett.* **1996**, *77* (18), 3865−3868.

(17) Methfessel, M.; Paxton, A. T. High-precision sampling for Brillouin-zone integration in metals. *Phys. Rev. B: Condens. Matter Mater. Phys.* **1989**, *40* (6), 3616−3621.

(18) Monkhorst, H. J.; Pack, J. D. Special points for Brillouin-zone integrations. *Phys. Rev. B: Condens. Matter Mater. Phys.* **1976**, *13* (12), 5188−5192.

(19) Johansson, L. I. Electronic and structural properties of transition-metal carbide and nitride surfaces. *Surf. Sci. Rep.* **1995**, *21* (5−6), 177−250.

(20) Reuter, K.; Scheffler, M. First-principles atomistic thermodynamics for oxidation catalysis: Surface phase diagrams and catalytically interesting regions. *Phys. Rev. Lett.* **2003**, *90* (4), 461031−461034.

(21) Henkelman, G.; Uberuaga, B. P.; Jónsson, H. Climbing image nudged elastic band method for finding saddle points and minimum energy paths. *J. Chem. Phys.* **2000**, *113* (22), 9901−9904.

(22) Haas, P.; Tran, F.; Blaha, P. Calculation of the lattice constant of solids with semilocal functionals. *Phys. Rev. B: Condens. Matter Mater. Phys.* **2009**, *79* (8), 085104.

(23) Tagawa, M.; Kawasaki, T.; Oshima, C.; Otani, S.; Edamoto, K.; Nagashima, A. TMC(100) surface relaxation studied with low-energy-electron-diffraction intensity analysis. *Surf. Sci.* **2002**, *517* (1−3), 59−64.

(24) Chang, R.; Graham, L. J. Low-Temperature Elastic Properties of ZrC and TiC. *J. Appl. Phys.* **1966**, *37* (10), 3778−3783.

(25) Lv, Z.; Hu, H.; Wu, C.; Cui, S.; Zhang, G.; Feng, W. First-principles study of structural stability, electronic and elastic properties of ZrC compounds. *Physica B* **2011**, *406* (14), 2750−2754.

(26) Shimada, T.; Imamura, K.; Edamoto, K.; Orita, H. Electronic structures of the suboxide films formed on TiC(100) and ZrC(100) surfaces: Density functional theory studies. *Surf. Sci.* **2009**, *603* (15), 2340−2344.

(27) Arya, A.; Carter, E. A. Structure, bonding, and adhesion at the ZrC(100)/Fe(110) interface from first principles. *Surf. Sci.* **2004**, *560* (1−3), 103−120.

(28) Li, J.; Liao, D.; Yip, S.; Najafabadi, R.; Ecker, L. Force-based many-body interatomic potential for ZrC. *J. Appl. Phys.* **2003**, *93* (11), 9072−9085.

(29) Vojvodic, A.; Ruberto, C.; Lundqvist, B. I. Atomic and molecular adsorption on transition-metal carbide (111) surfaces from density-functional theory: a trend study of surface electronic factors. *J. Phys.: Condens. Matter Mater. Phys.* **2010**, *22* (37), 375504.

(30) Viñes, F.; Sousa, C.; Illas, F.; Liu, P.; Rodriguez, J. A. A systematic density functional study of molecular oxygen adsorption and dissociation on the (001) surface of group IV-VI transition metal carbides. *J. Phys. Chem. C* **2007**, *111* (45), 16982−16989.

(31) Edamoto, K.; Nagayama, T.; Ozawa, K.; Otani, S. Angle-resolved and resonant photoemission study of the ZrO-like film on ZrC(1 0 0). *Surf. Sci.* **2007**, *601* (21), 5077−5082.

(32) Kitaoka, H.; Ozawa, K.; Edamoto, K.; Otani, S. Electronic structure of the Zr suboxide layer formed on a ZrC(1 0 0) surface. *Surf. Sci.* **2002**, *511* (1−3), 359−365.

3. Stability, equilibrium morphology and hydration of ZrC(111) and ZrC(110) surfaces with H2O: a combined periodic DFT and atomistic thermodynamic study

A fully published research article in Physical Chemistry Chemical Physics.

PCCP

PAPER

View Article Online
View Journal | View Issue

Cite this: *Phys. Chem. Chem. Phys.*, 2015, **17**, 21401

Stability, equilibrium morphology and hydration of ZrC(111) and (110) surfaces with H_2O: a combined periodic DFT and atomistic thermodynamic study

Eric Osei-Agyemang,[a] Jean-Francois Paul,[a] Romain Lucas,[b] Sylvie Foucaud[b] and Sylvain Cristol*[a]

Received 26th May 2015,
Accepted 14th July 2015

DOI: 10.1039/c5cp03031e

www.rsc.org/pccp

ZrC is a non-oxide ultra-high temperature ceramic (UHTC) material with excellent physical and mechanical properties used in nuclear plants and jet propulsion engines. However, the mechanical properties can be lost because of the easy oxidation of its grain surfaces. One way of dealing with such a problem is to coat the surface with inert carbides like SiC which can be grafted onto the ZrC surface by first modifying the exposed surfaces with reactive molecules. The stability of different terminations of the (111) facet was studied and the most stable is the termination on both surface layers by Zr atoms as it has been observed experimentally. A DFT calculation study jointly with atomistic thermodynamic modelling has been used to study the reactivity of the (111) and (110) facets with H_2O. H_2O dissociates into surface hydroxyl groups with the release of H_2 and the OH groups preferentially adsorb at high surface coverage (high adsorption energies at 1 ML coverage). The study of adsorption of H_2O onto other low index surfaces allows the determination of the equilibrium morphology of the ZrC nanocrystallites in different environments. In vacuum, ZrC nanocrystallites reveal a cubic structure with much of the (100) surface and a small amount of the (111) facets at the corners. Hydration of the (111) surface was a strong process and hence water can be removed from the surface at temperatures above 1200 K and pressures lower than 10^{-9} bar while higher pressures of H_2 in the gas phase enhance the removal of water. The Wulff construction of the nanocrystallites after hydration indicates only the (111) surface at lower temperatures while revealing the (100) facets at higher temperatures. Thus whatever the experimental conditions be, the (110) facet does not have to be considered.

I. Introduction

Zirconium carbide (ZrC) is a high temperature non-oxide material which exhibits mixed covalent, ionic and metallic bonding characters. It is widely used in nuclear reactor linings, aerospace engines and in the manufacturing of hard materials such as cutting tools. It is among the transition metal carbide (TMC) group of materials with high melting point (3430 °C). As it is a requirement for materials used in nuclear and aerospace industries to work in harsh environments, materials like high refractory ceramics are well suited.[1] As an example, nuclear plants with the future fourth generation engines are supposed to work at temperatures above 1200 °C. Hence these engines require materials with physico-chemical properties that are compatible with such working conditions.[2] According to its abovementioned properties, ZrC is a promising candidate for such applications. Working under severe conditions such as high temperatures and oxidizing environments is however not easily achieved due to the fact that introduction of a small dose of oxygen forms the zirconium oxide layer on the surface[3] which leads to deterioration of the mechanical and other properties of ceramics. Coating the surfaces with another ceramic material that is resistant to oxygen and maintains its physical properties at very high temperatures can help alleviate the oxidation problem.[4,5] Such coatings can be achieved by first modifying the ZrC surfaces with small molecules[6] in order to graft another material. In this context, the study of ZrC surfaces is of prime importance.

There are three distinct surfaces to be considered on the cubic structure of ZrC(100), (110) and (111) surfaces. In addition to the most stable (100), the (111) surface is also of considerable

---

[a] *Unité de Catalyse et Chimie du Solide (UCCS), UMR-CNRS 8181, Université Lille 1, 59655 Villeneuve d'Ascq, Lille, France. E-mail: sylvain.cristol@univ-lille1.fr; Fax: +33 320 43 65 61; Tel: +33 320 43 45 03*

[b] *Laboratoire Science des Procédés Céramiques et de Traitements de Surface (SPCTS), UMR-CNRS 7315, Centre Europ éen de la Céramique, 87068 Limoges, France*

stability[7] and has been prepared by many research groups.[8,9] Cleavage of the bulk ZrC crystal to form the (111) surface generates a surface which is either terminated by the Zr layer or the C layer. However, a recent Angle Resolved Photoemission Spectroscopy (ARPES) study has revealed that the electronic structure of the ZrC(111) surface is very similar to that of TiC, HfC, NbC and TaC(111) surfaces.[8] These other TMC(111) surfaces have been studied by Impact-Collision ion Scattering Spectroscopy (ICISS) which revealed that the first surface layer of these TMC's is terminated by the metal layer.[10–13]

Furthermore, the preparation of the ZrC material is normally difficult to perform under conditions void of gaseous water molecules and as such the interaction of the individual surfaces with water is of paramount importance. Reactivity with water can lead to the formation of surface hydroxyl groups which will modify the chemical properties of the surfaces but can also be used as precursors for subsequent grafting of other materials onto the ZrC surface. There is however no extensive work, neither experimental nor theoretical, on the reactivity of water with the ZrC(111) surface. The only experimental work performed on the reactivity of water on this surface is unpublished though mentioned in the paper by Noda *et al.*[8] Similarly, there is no report, neither experimental nor theoretical, on the adsorption of molecules onto the ZrC(110) surface even though a theoretical study on the surface energy has been carried out.[7]

In order to be able to determine the surface exposed by the ZrC crystallites in different environments and construct the crystal morphology, adsorption of water has been undertaken on these surfaces in order to obtain a complete picture. The stability of the surfaces is studied with different terminations and different water coverages by means of periodic DFT calculations and atomistic thermodynamic modelling. Adsorption of water onto the (100) surface which is also needed for constructing the equilibrium morphological shape is provided in a previous study.[14] The reactivity towards oxygen will be exposed in a subsequent paper.

The paper is divided as follows: Section II describes the calculation scheme and structural models used for the current work while Section III A provides the results regarding the calculated surface properties and description of the stability of the (111) surface with different terminations and its reactivity towards H_2O. Section III B provides results and description of the adsorption of H_2O onto the (110) surface. Section III C provides details of charge analysis for hydration of the ZrC surfaces. In Section III D, results and discussion on the equilibrium morphology of the bare nano-crystals as well as in hydrated environments at different temperatures are provided. Finally, Section IV draws conclusions on the current studies.

II. Calculation schemes and structural models

All calculations were performed using the Vienna Ab Initio Simulation Package (VASP)[15] which is based on Mermin's finite temperature DFT.[16] The electronic configurations used for Zr, O, H and C are [Kr]$4d^25s^2$, [He]$2p^6$, $1s^1$ and [He]$2s^22p^2$ respectively. PAW pseudopotentials[17] were used to replace the core electrons as well as the core part of the valence electron wavefunctions in order to reduce the number of planewaves required to describe the electrons close to the nuclei. The Generalized Gradient Approximation (GGA) exchange correlation functional parameterized by Perdew, Burke and Ernzerhof (PBE)[18] was employed and the Methfessel–Paxton[19] smearing scheme was used by setting the gamma parameter to 0.1 eV. The accuracy of the calculation results was evaluated by changing the energy cutoff from 200 eV to 600 eV while the *k*-point sampling mesh was evaluated from 2 × 2 × 2 to 11 × 11 × 11 using the standard Monkhorst–Pack[20] special grids. For this evaluation, all subsequent bulk and surface calculations were performed by describing the valence electrons using the plane wave basis set with the cutoff of 500 eV while the integration of the Brillouin zone was performed with 9 × 9 × 9 *k*-points for the bulk and 9 × 9 × 1 *k*-points for surface calculations. The self-consistent field (SCF) procedure for resolution of the Kohn–Sham equations is assumed to be converged when energy changes of 10^{-4} eV between two successive iterations are reached. For bulk calculations, the positions of all ions were relaxed while for all surface calculations, the positions of all the ions in the three top-most layers were relaxed in order to render the net forces acting upon them smaller than 10^{-2} eV Å^{-1}. The lattice parameter for the ZrC bulk was optimized by fitting the energy *versus* volume curve against the Murnaghan's equation of state as detailed in our previous work.[14]

According to the *Fm*3*m* space group of cubic ZrC, the non-equivalent, low index surfaces are (100), (110) and (111) surfaces as shown in Fig. 1. Their starting geometries were obtained by cleaving the optimized bulk structure along the corresponding normal directions. Unless otherwise stated, (1 × 1) surface unit cells were used for surface calculations. In order to avoid surface–surface interactions, a vacuum of 12 Å was set as a separator between two periodically repeated slabs.

For all calculations on the (111) surface, a (1 × 1) supercell was used with $\gamma = 60^\circ$ and a parameter of 6.698 Å. This surface has an exposed area of 38.854 Å^2. The surface exposes four Zr atoms (Fig. 1). In all (110) calculations, a (1 × 1) supercell with a and b parameters of 4.736 Å and 6.698 Å, respectively, was used. This surface has an exposed area of 31.724 Å and consists of two Zr atoms and two C atoms (Fig. 1). The (110) surface slab is stoichiometric.

All surface calculations with adsorption of small molecules onto the (110) surface were performed with at least 8 layer slabs and the three topmost layers were relaxed while keeping the remaining layers fixed to mimic bulk conditions. The surface energy for symmetric slabs with equivalent surfaces on both sides is computed as:

$$\gamma_{\text{surf}} = \frac{1}{2A}[E_{\text{slab}} - nE_{\text{bulk}}] \tag{1}$$

where E_{slab} denotes the slab energy and nE_{bulk} is the energy of n ZrC units in the bulk structure (n being the number of ZrC units in the slab) while A is the surface area exposed by the surface planes.

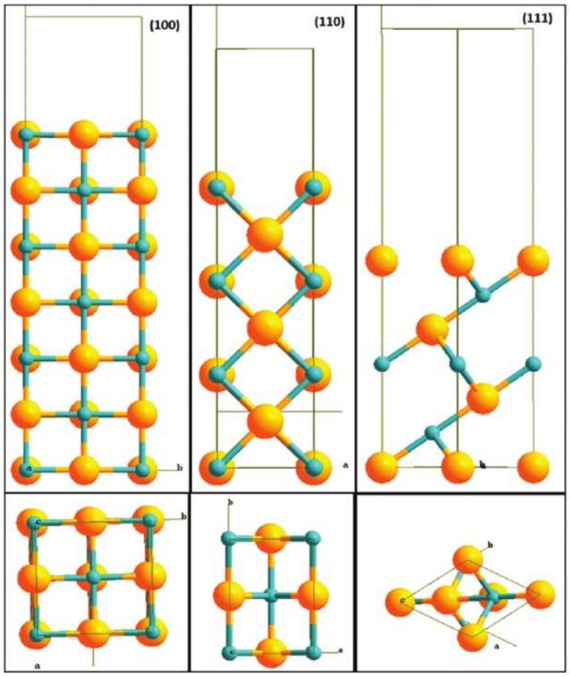

Fig. 1 Different surfaces of ZrC. Upper left (100), upper middle (110) and upper right (111) surfaces and the side view respectively. Bottom left, bottom middle, and bottom right are (100), (110) and (111) top views respectively. Yellow = Zr, blue = C.

Nine or ten atomic layers were used for the (111) surface stability calculations for stoichiometric and non-stoichiometric slab energy calculations and reactivity. The three outermost layers of the slab were allowed to relax while the remaining layers were kept fixed to mimic bulk properties. Cleavage of the ZrC(111) surface yields a stoichiometric slab with two inequivalent but complementary surfaces, one terminated with the Zr layer and the other with C.

For these two inequivalent surfaces, the cleavage energy is calculated by computing the surface energies for symmetric slabs terminating with the same atomic layer on both sides for each of the complementary surfaces. This enables estimation of the contributions made by each surface toward the cleavage energy. The surface energies of the two different surfaces are then added to obtain the cleavage energy.

The cleavage energy for the ZrC(111) surface with inequivalent surfaces (terminating with Zr on one surface layer and C on the other surface layer) is calculated using eqn (2).[21]

$$E_{\text{cleave}}^{(\text{Zr+C})} = \frac{1}{2A}\left[E_{\text{slab}}^{\text{Zr}} + E_{\text{slab}}^{\text{C}} - mE_{\text{bulk}}\right] \qquad (2)$$

where $E_{\text{slab}}^{\text{i}}$ is the total energy of the symmetric slab with i termination, A is the surface area, E_{bulk} is the bulk energy per unit formula in the ZrC cubic structure and m is the total number of bulk formula units in the two slabs.

This mode of termination leads to the introduction of electrostatic forces in the slab due to the polar nature of the resulting slab. This polarity can be cancelled out by different modifications either with stoichiometric slabs, in which Zr or C atoms are displaced from one termination to the other or with non-stoichiometric slabs in which extra Zr or C atoms are added to the surfaces. The following nomenclature is used for different terminations of the (111) surface in order to reduce the polarity of the surface slab. qA-(111)-rB is used as the notation where a layer of atom A terminates on one side of the slab and a layer of atom B terminates on the other side with q and r being the number of A and B atoms on both sides respectively. As an example, 2C-(111)-2Zr means 2C atoms are on one surface layer and 2Zr atoms are on the other surface of the slab. Different surface terminations are shown in Fig. 2. In order to account for the extra atoms in the slab, we used slabs which are symmetric with respect to the center of inversion.

The SOWOS program[22] was used for prediction of the Wulff[23] shapes using the calculated surface energies for the (100), (110) and (111) surfaces in the absence and presence of water.

The adsorption of water has been investigated in both associative and dissociative ways by systematically testing different adsorption modes. The adsorption energies are then computed as:

$$E_{\text{ads}} = -\left[E_{\text{surface-molecule}} - E_{\text{clean surf}} - E_{\text{molecule}}\right] \qquad (3)$$

where $E_{\text{surface-molecule}}$ is the energy of the surface with the adsorbed molecule, $E_{\text{clean surface}}$ is the energy of the relaxed clean surface and E_{molecule} is the energy of the gaseous molecules. After obtaining the preferred adsorption modes, the effect of different coverages of the gaseous molecules was evaluated using 0.25 Monolayer (ML), 0.5 ML, 0.75 ML and 1 ML.

In all cases, the coadsorption of different number of water molecules was tested but the step by step adsorption process of one water molecule followed by another was observed to yield the most stable configurations. The step by step adsorption of water was finally used. The different coverages were defined by the number of available Zr sites on the surface. For the (111) surface,

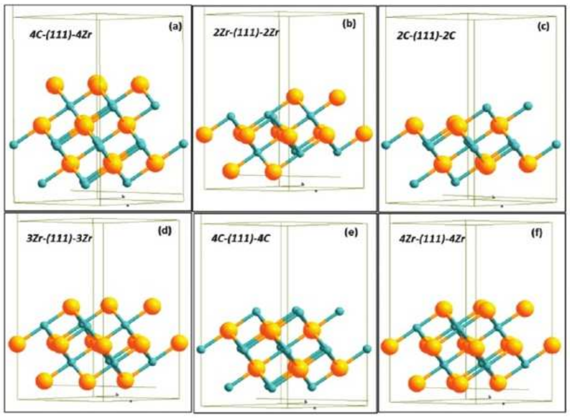

Fig. 2 Different polar correction schemes used for the (111) surface. Stoichiometric structures (a–c) have the same number of Zr and C atoms while non-stoichiometric structures have excess of either Zr or C atoms in the structure.

there are four Zr atoms and each site defines 0.25 ML. Moreover, for the (110) surface only two Zr atoms are present and easy to define the 0.5 ML and 1 ML coverages. In order to obtain 0.25 ML and 0.75 ML, (2 × 1) super cells were used revealing four Zr sites which makes it probable to define the 0.25 ML and 0.75 ML coverages.

Atomistic thermodynamic model

A thermodynamic treatment is needed to provide a more elaborate picture and explanations for the stability of different surface structures. The appropriate surface property which can be used to account for the contribution of each surface termination to the cleavage energy is the surface grand potential, Ω^{i}.[21] This implies a contact with reservoirs of Zr and C. The surface grand potential of the *i*th termination is as follows:

$$\Omega^{i} = \frac{1}{2A}\left[E^{i}_{\text{slab}} - N_{\text{C}}\mu_{\text{C}} - N_{\text{Zr}}\mu_{\text{Zr}}\right] \tag{4}$$

N_{C} and N_{Zr} are the number of C and Zr atoms in the surface slab while μ_{c} and μ_{zr} are the carbon and zirconium chemical potentials respectively. A is the surface area of the (111) termination. Since the chemical potentials of C and Zr are not independent because they are assumed to be in equilibrium with bulk ZrC, they are related through the expression: $\mu_{\text{ZrC}} = \mu_{\text{C}} + \mu_{\text{Zr}}$. μ_{ZrC} is the chemical potential of the bulk ZrC unit formula and it is approximated by the total energy of bulk ZrC unit formulae $E^{\text{bulk}}_{\text{ZrC}}$. Substituting this into eqn (4) yields:

$$\Omega^{i} = \frac{1}{2A}\left[E^{i}_{\text{slab}} - N_{\text{Zr}}E^{\text{bulk}}_{\text{ZrC}} + \mu_{\text{C}}(N_{\text{Zr}} - N_{\text{C}})\right] \tag{5}$$

Since it has already been established that the synthesis process of ZrC is accompanied by excess graphitic carbon,[6] we define eqn (5) in terms of the chemical potential of carbon. The chemical potential of C is defined relative to the chemical potential of C in its standard state and hence $\Delta\mu_{\text{C}} = \mu_{\text{C}} - \mu_{\text{C}}{}^{\star}$, where $\mu_{\text{C}}{}^{\star}$ is the chemical potential of C in its reference state and calculated as the bulk energy of graphitic carbon $E^{\text{bulk}}_{\text{C}}$. Substituting the expression of $\Delta\mu_{\text{C}}$ into eqn (5) yield the surface grand potential as:

$$\Omega^{i} = \frac{1}{2A}\left[E^{i}_{\text{slab}} - N_{\text{Zr}}E^{\text{bulk}}_{\text{ZrC}} + E^{\text{bulk}}_{\text{C}}(N_{\text{Zr}} - N_{\text{C}}) + \Delta\mu_{\text{C}}(N_{\text{Zr}} - N_{\text{C}})\right] \tag{6}$$

If we make the following definition:

$$\gamma_{\text{i}} = \frac{1}{2A}\left[E^{i}_{\text{slab}} - N_{\text{Zr}}E^{\text{bulk}}_{\text{ZrC}} + E^{\text{bulk}}_{\text{C}}(N_{\text{Zr}} - N_{\text{C}})\right] \tag{7}$$

Substituting eqn (7) into eqn (6) yields:

$$\Omega^{i} = \gamma_{\text{i}} + \frac{1}{2A}\left[\Delta\mu_{\text{C}}(N_{\text{Zr}} - N_{\text{C}})\right] \tag{8}$$

where γ_{i} is the surface energy of the selected (i = *q*A-(111)-*r*B) termination as defined in eqn (1). Thus the surface grand potential Ω^{i} is made up of the surface energy contributing part as well as the dependence and contribution of each atom on the surface.

Using eqn (8), a range of accessible Ω^{i} can be obtained if we have the minimum and maximum $\Delta\mu_{\text{Zr}}$ and $\Delta\mu_{\text{C}}$. It is assumed that the Zr and C forms do not condense on the ZrC(111) surface. To obtain the maximum Zr and C chemical potentials, the chemical potential of each of the species must be lower than the energy of the atom in the stable bulk phase of the considered species and hence:

$$\begin{cases} \Delta\mu_{\text{C}} = \mu_{\text{C}} - E^{\text{bulk}}_{\text{C}} < 0 \\ \Delta\mu_{\text{Zr}} = \mu_{\text{Zr}} - E^{\text{bulk}}_{\text{Zr}} < 0 \end{cases} \tag{9}$$

where $\Delta\mu_{\text{C}}$ and $\Delta\mu_{\text{Zr}}$ are the relative values of different chemical potentials with respect to $E^{\text{bulk}}_{\text{C}}$ and $E^{\text{bulk}}_{\text{Zr}}$ which are the energies of C in graphite and Zr in hcp zirconium bulk metal respectively. By combining $\mu_{\text{ZrC}} = \mu_{\text{C}} + \mu_{\text{Zr}}$ with the expression for $\Delta\mu_{\text{Zr}}$ and $\Delta\mu_{\text{C}}$ in eqn (9), we obtain the lower boundary for the Zr and C chemical potentials as:

$$\begin{cases} \Delta\mu_{\text{C}} > E^{\text{f}}_{\text{ZrC}} \\ \Delta\mu_{\text{Zr}} > E^{\text{f}}_{\text{ZrC}} \end{cases} \tag{10}$$

where $E^{\text{f}}_{\text{ZrC}}$ is the formation energy for bulk ZrC, computed using the equation $E^{\text{f}}_{\text{ZrC}} = E^{\text{bulk}}_{\text{ZrC}} - E^{\text{bulk}}_{\text{Zr}} - E^{\text{bulk}}_{\text{C}}$ and we calculated it as −1.59 eV. A plot of the surface grand potential Ω^{i} against the range of chemical potential values is then used to explain the thermodynamic stability of different terminations. Thus the surface grand potential accounts for both stoichiometric and non-stoichiometric slabs. It is obvious from eqn (6) that, for stoichiometric and symmetric surfaces, the third and fourth terms in the equation become zero and the expression reduces to surface energy while the cleavage energy is calculated as twice the surface energy. The surface grand potential is therefore the equivalent surface energy for both non-stoichiometric and stoichiometric slabs.

In order to establish the relationship between the calculations performed and the experimental working conditions, we used the already well-established atomistic thermodynamic scheme,[24] where the surface and the adsorbed molecule are assumed to be in equilibrium with the gas phase which serves as a reservoir. This then allows for the definition of the adsorption Gibbs free energy ($\Delta_{\text{r}}G$) as a function of thermodynamic parameters such as temperature T and pressure P using the general equation:

$$\Delta_{\text{r}}G = \left[\Delta E_0 + E_{\text{ZPE(surface-molecule)}} - \Delta\sum n\mu(T,P)\right] \tag{11}$$

where $\Delta\sum n\mu(T,P)$ is the difference in chemical potential of the reactant and product gas phase molecules. $\Delta E_0 = [E_{\text{el (surface-molecule)}} + E_{\text{el (released species)}} - E_{\text{el (surface)}} - nE_{\text{el(molecule)}}]$ is the difference in electronic energy of the considered surface and the small molecules according to the following process:

$$\text{ZrC surface} + n(\text{molecule}) \leftrightarrow \text{ZrC surface} - [n(\text{molecule})] + \text{released species} \tag{12}$$

ΔE_0 is also the adsorption energy E_{ads} in eqn (3).

Adsorption of the gas phase molecules onto the surface affects the chemical potential of the gaseous molecules due to the frustrations of the rotational and translational degrees of freedom as compared to the gas phase and consists of a temperature dependent term $[\Delta\mu^{\circ}(T)]$ and a pressure dependent term.

$$\Delta\mu(T,P) = \Delta\mu^{\circ}(T) + RT\ln\left(\frac{P}{P_0}\right) \tag{13}$$

The temperature dependent term can however be computed with statistical thermodynamics as below:

$$\Delta\mu^{\circ}(T) = [E_{\mathrm{ZPE}} + E_{\mathrm{vib}(0\to T)} + E_{\mathrm{rot}} + E_{\mathrm{trans}}] + RT - T(S_{\mathrm{vib}} + S_{\mathrm{rot}} + S_{\mathrm{trans}}) \tag{14}$$

These thermal contributions are introduced by the loss of rotational and translational degrees of freedom upon adsorption of the small molecules onto the surface as well as the change in the vibrational contribution. The values of $\Delta\mu^{\circ}(T)$ at different temperatures are obtained using standard statistical thermodynamic formulas with equilibrium geometry and calculated frequencies. A value of P_0 of 1 atm was used and a plot of (Δ_rG) against pressure P was obtained at different constant temperatures. The lowest of such plots is the most stable system under the given experimental conditions.

The surface energy, $\gamma_{hkl}(\mathrm{H_2O})$, as a function of n adsorbed water molecules at different temperatures can be calculated using the equation

$$\gamma_{hkl}(\mathrm{H_2O}) = \frac{1}{2n}\left[\gamma_{hkl}^{\circ} + \theta_{hkl}\Delta_r G_{hkl}(P,T,n)\right] \tag{15}$$

where $\Delta_rG_{hkl}(P,T,n) = \Delta E_0 + E_{\mathrm{ZPE(surface\text{-}molecule)}} - \Delta\sum n\mu(T,P)$, $\theta_{hkl} = 2n/A_{hkl}$ is the surface coverage by water, A_{hkl} is the surface area of the exposed *hkl* plane, and γ_{hkl}° is the surface energy of the bare surface ($\theta_{hkl} = 0$). The calculated $\gamma_{hkl}(\mathrm{H_2O})$ values were then used to predict the Wulff morphological structure of the ZrC nanoparticles at specified temperature and pressure. The Wulff shapes have been calculated using a water partial pressure of 0.01 bar.

III. Results and discussion

A. ZrC(111) surface

Surface structure properties of ZrC(111). The calculated surface and cleavage energies for different polar correction schemes are summarized in Table 1 and compared to the value of the polar surface (Fig. 2, 4C-(111)-4Zr).

Table 1 Calculated surface energies γ_i as in eqn (7) with different polar correction schemes for the ZrC(111) surface (Fig. 2). For symmetrically equivalent slabs, cleavage energy is calculated as twice the surface energy

	Surface energy		Cleavage energy	
Surface termination	γ_{rigid}/meV Å^{-2}	$\gamma_{\mathrm{relaxed}}$/meV Å^{-2}	γ_{rigid}/meV Å^{-2}	$\gamma_{\mathrm{relaxed}}$/meV Å^{-2}
4C-(111)-4Zr	—	—	638.6	597.7
2Zr-(111)-2Zr	287.7	236.6	575.4	473.2
2C-(111)-2C	265.1	233.3	530.3	466.6
3Zr-(111)-3Zr	229.6	190.7	459.2	381.4
4C-(111)-4C	444.0	428.8	888.0	857.6
4Zr-(111)-4Zr	194.6	168.9	389.2	337.8

Both relaxed and unrelaxed surface energies are reported. A comparison of the computed surface energies γ_i reveals that the structure in which both surface layers are covered with four Zr atoms, 4Zr-(111)-4Zr, is by far the most stable with the lowest surface grand potential within the range of C chemical potentials. It has been observed experimentally that there is always an excess of carbon in ZrC samples in the form of graphite[6] and hence the corrections made for the non-stoichiometric structures are done with bulk energy of carbon in graphite as in eqn (7). The calculated surface energy for this stable surface (Zr terminated on both sides) is 168.9 meV Å^{-2}. Arya and Carter[7] reported a value of 151.5 meV Å^{-2} for the ZrC(111) metal terminated surface. However, for the non-stoichiometric slabs, the authors used a correction that took into account only the number of atoms and not their chemical nature. As such it is difficult to compare the two surface energies. The relative stability of this (111) surface with the (100) and (110) surfaces is however consistent with the conclusions drawn by the authors. Comparing the cleavage energy of this termination with the as-cleaved (111) surface 4C-(111)-4Zr there is a high gain in stability. The thermodynamic stability plot of the surface grand potential against the chemical potential of carbon showing the stability regions of different surface terminations is shown in Fig. 3. Thus at all carbon chemical potentials $\Delta\mu_{\mathrm{C}}$ only the structure with 4Zr atoms terminated on both sides is thermodynamically stable. We also provide in Fig. 3, the surface grand potentials for the (100) and (110) surfaces for comparison.

For stoichiometric surfaces, the surface grand potential expression reduces to the surface energy. We predict that at low C chemical potentials $\Delta\mu_{\mathrm{C}} < -1.32$ eV, the 4Zr-(111)-4Zr surface termination is even more stable than the (100) surface. It can also be observed from Table 1 that all surface structures with carbon layer terminations yield extremely high surface energies and hence are not stable. The experimentally observed layer of Zr termination[25] is therefore corroborated by our stability studies.

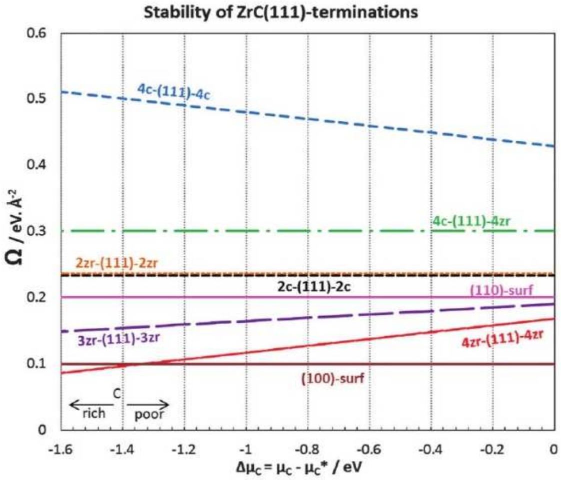

Fig. 3 Surface grand potential of (111) surface terminations at different Zr chemical potentials.

Table 2 Calculated surface energies (in meV Å^{-2}) for ZrC surface planes. γ_{rigid} is surface energy for the rigid slab and γ_{rel}. is surface energy for the relaxed slab. Ref. is reference

Surface	γ_{rigid}	γ_{rel}	Ref./γ_{rigid}	Ref./γ_{rel}
(100)	105.7	99.6	105.0[7]	99.4[7] 101.0[26] 96.8[27]
(110)	218.4	200.4	213.0[7]	199.7[7]
4Zr-(111)-4Zr	194.6	168.9	174.7[7]	151.5[7]

We selected the most stable structure 4Zr-(111)-4Zr for our subsequent calculations.

The calculated surface energies for the ZrC(111) polar surfaces are summarized in Table 2 in comparison with the values for the (110) and (100) surfaces.

This structure, which has four Zr atoms terminating both surface layers, was then further optimized and used for the calculation of the density of states (DOS). The total DOS (TDOS) and the projected DOS (PDOS) on the atoms are shown in Fig. 4. A comparison of the TDOS with that of the bulk structure shows a significant introduction of new surface states at the Fermi level (E_f), arising from Zr-d and Zr-p states. The metallic nature of the surface is evidenced and mostly due to the Zr-d occupied surface states at the Fermi level. The Zr d–C p mixing region arises at lower energies. Thus the very high electronic states observed for the (111) surface suggest a high reactivity of this surface compared to the (100) surface.[7]

There is no surface reconstruction of the relaxed ZrC bare (111) surface. It was observed that the interlayer spacing between the first and second layers is reduced while the second interlayer spacing increases substantially. The bond distance between the first and second layers, $d_{1\text{Zr}-2\text{C}}$, which is the distance between Zr in the first layer and C in the second layer is 2.24 Å and agrees well with values calculated by other groups, 2.22 Å,[27] and the second interlayer spacing between C in the second layer and Zr in the third layer $d_{2\text{C}-3\text{Zr}}$ = 2.45 Å. The other interlayer spacing and bond distances approach that of bulk.

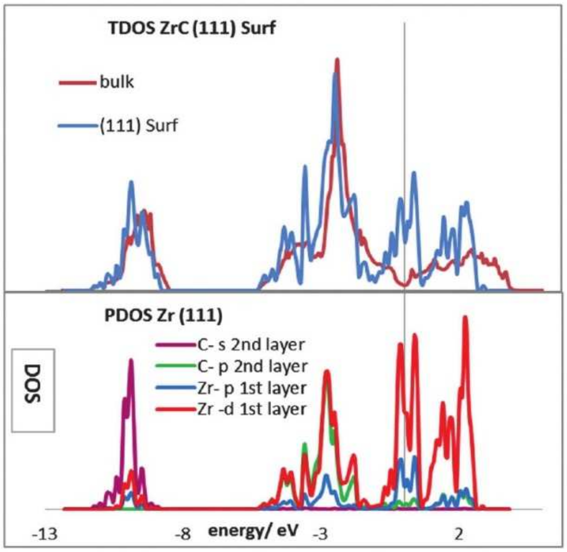

Fig. 4 TDOS and PDOS of the ZrC(111) surface.

Reactivity of H_2O on the bare ZrC(111) surface. After testing with different configurations, the most stable form of adsorption was used to compute the adsorption energies E_{ads}. The adsorption process was carried out in a stepwise manner, starting with one H_2O molecule, then two H_2O molecules, and so on. Both associative and dissociative modes of adsorption were tested. The adsorption energy was then calculated for successive water addition and as averages for different coverages of the (111) surface. All adsorption processes on the (111) surface are observed to favor complete dissociation into atomic species at fcc three-fold hollow sites just above Zr atoms in the third or fifth layers.

1 H_2O molecule adsorption. The observed reaction of a single H_2O molecule is a complete dissociation process where H_2O dissociates into atomic O and H species which adsorb very strongly at fcc three-fold hollow sites between three surface Zr atoms. This is accompanied by a very strong energy of adsorption, E_{ads} = 4.58 eV. Moreover, a calculation was made to ascertain the subsequent combination of the two adsorbed H atoms to form H_2 and released into the gas phase. This reaction was found to be endothermic.

O-(111)-2H ↔ O-(111) + $H_{2(\text{gas})}$, ΔE_{rxn} = 1.33 eV. The complete dissociation mode of adsorption is shown in Fig. 5a1 and a2.

The calculated bond distances between the O and surface Zr atoms were 2.36 Å, 2.15 Å and 2.15 Å while those of H and surface Zr atoms are between 2.15 Å and 2.20 Å.

2 H_2O molecule adsorption. In the presence of two H_2O molecules, there is a mixed mode of adsorption. There is a combination of complete and partial dissociation of H_2O molecules. This can be viewed as a process where the first H_2O molecule dissociates completely into O and H atoms, occupying three of the available four fcc hollow sites while the second water molecule dissociates partially into surface OH groups adsorbing at the remaining fcc hollow site and the H atom adsorbs at an fcc hollow site above the Zr atom in the fifth layer. The consecutive adsorption of the second H_2O molecule is accompanied by a high adsorption energy, E_{ads} = 3.25 eV. Thus even though the complete dissociation into atomic species has a very high adsorption energy, the partial dissociation also has a high energy. Fig. 5b1 and b2 shows the complete and partial dissociation of 2 H_2O molecules on ZrC(111) surfaces. The calculated bond distances between the surface O and Zr atoms are 2.170 Å, 2.21 Å and 2.10 Å, between O of the OH group and surface Zr atoms are 2.37 Å, 2.22 Å and 2.42 Å, while those between the H atoms and surface Zr atoms are between 2.003 Å and 2.663 Å.

3 H_2O molecule adsorption. Adsorption of three H_2O molecules resulted in partial dissociation into surface hydroxyl groups with the release of H_2 molecules. In the subsequent addition of the third H_2O molecule, there is the formation of three surface OH groups and H species all adsorbing at fcc three-fold hollow sites

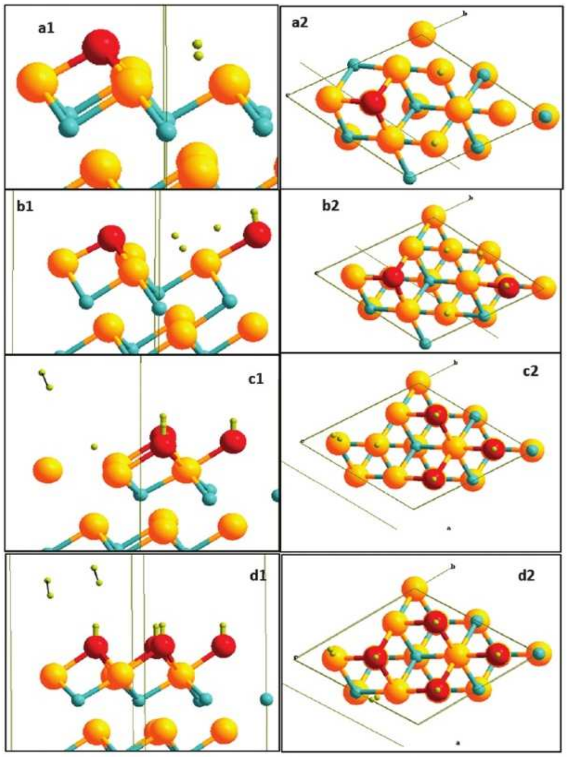

Fig. 5 Side view (left) and top view (right) for dissociation of water onto the ZrC(111) surface with 1, 2, 3 and 4 H_2O molecules. Blue (C), yellow (Zr), red (O), and light green (H).

with the release of the H_2 molecule. The successive adsorption of the third H_2O molecule is associated with adsorption energy, E_{ads} = 1.22 eV. This somehow low adsorption energy as compared to adsorption of one and two H_2O molecules may be due to the lateral repulsion between the three adsorbed OH species on the surface. Fig. 5c1 and c2 shows the adsorption of three molecules on the (111) surface with the release of H_2 into the gas phase. The measured bond distances between O of the OH group and the surface Zr atoms are in the range of 2.00 Å and 2.36 Å. The bond distances between the adsorbed H atom and the surface Zr atoms were 2.24 Å, 2.24 Å and 2.24 Å.

4 H_2O molecule adsorption. The adsorption of four H_2O molecules on the (111) surface leads to adsorption at all possible fcc three-fold hollow sites on the surface plane. There is the partial dissociation of H_2O molecules to form four OH groups adsorbing at the four available fcc sites with the release of two H_2 molecules into the gas phase. This adsorption process is governed by the equation: ZrC(111) + $4H_2O \leftrightarrow$ ZrC(111)–4(OH) + $2H_2$. The final geometry of adsorbed surface species is shown in Fig. 5d1 and d2. The adsorption energy for the successive addition of the fourth H_2O molecule, E_{ads} = 1.14 eV. This value is lower than that for adsorption of three H_2O molecules as part of the reaction energy is used in releasing two H_2 molecules into the gas phase. The calculated average bond distance between the surface Zr atoms and the O atom of the OH group is 2.37 Å. At this point, the surface is saturated with the maximum number of H_2O molecules as all the possible adsorption sites are occupied.

A complete picture of the potential energy surface showing all the adsorption process of water and the release of H_2 is shown in Fig. 6. This aids in easy visualization of the reaction process.

The calculated TDOS and PDOS of the fully hydroxylated (111) surface are shown in Fig. 7. A comparison of the TDOS (Fig. 7 top panel) of the clean and hydrated surfaces shows attenuation of the surface states around the Fermi level as well as introduction of a new band at around −5.5 to −7.0 eV due to the surface OH groups.

Since H_2 is a released gas, it has no effect on surface DOS and hence it is not shown. A projection of the DOS (Fig. 7 bottom) onto the O atom of the hydroxyl group shows attribution of the new state to the OH group. This is in good agreement with what is observed experimentally where the OH band is observed at ∼−7.0 eV.[8] This band is attributed to the 1π state of the OH group. Moreover, the unoccupied bands are shifted to higher energies as they interact with O-p electrons. The PDOS (Fig. 7 bottom panel) of the surface Zr atoms shows a considerable decrease in the surface d states and the newly observed band has a high contribution from the surface Zr d states. This shows a significant mixing of the metal-d and O-p from the OH group, yielding stable surface hydroxyl groups accompanied by high adsorption energy.

A summary of the successive adsorption energies of different amounts of H_2O molecules added to the surface as well as the calculated average adsorption energies per H_2O molecule at different water coverages on the (111) surface is provided in Table 3. These values show a decrease in the adsorption energies towards higher coverages as a result of the release of H_2 into the gas phase.

These calculated adsorption energies were then used to obtain thermodynamic stability plots using calculated Gibbs free energy of adsorption values at low and high temperatures. Due to hydrogen released by the hydration process, the stability plots are obtained as functions of both H_2O and H_2 pressures at

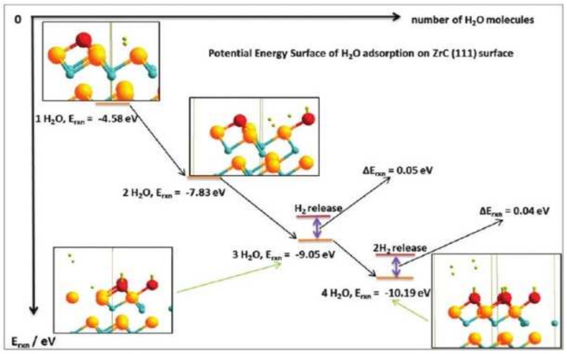

Fig. 6 Potential energy surface of H_2O adsorption on ZrC(111) surface. Blue (C), yellow (Zr), red (O), light green (H).

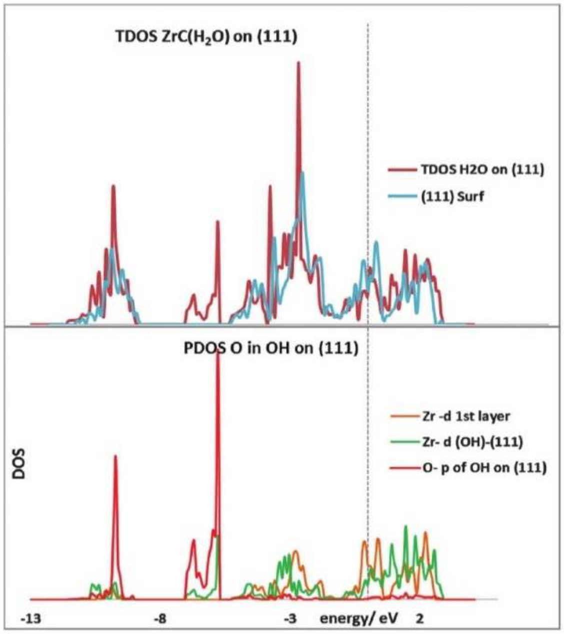

Fig. 7 TDOS and PDOS plots for dissociation of four water molecules on the ZrC(111) surface into OH and release of H_2 (full coverage). Blue legend: the clean (111) surface.

different temperatures. This type of plot is very useful when there is the need to remove surface hydroxyl groups to achieve the bare surface as hydrogen can be introduced into the system to drive the equilibrium to the left side of the reaction to produce water.

Plots of six different temperature regimes are provided (Fig. 8). This phase diagram is obtained as follows: at each temperature, the $\Delta_r G$ value is calculated for different pressures of both H_2 and H_2O gases at different coverages. The surface coverage which has the lowest $\Delta_r G$ value at a selected partial pressure of H_2 and H_2O is the most stable. Different coverages at different pressure combinations are then used to obtain the stability plots for different temperatures.

At lower temperatures between 200 and 400 K, the surface is fully covered with OH groups at all H_2O and H_2 pressures considered. As the temperature is increased to 500 K, small regions of the 0.5 ML begin to appear. This region is characteristic at H_2 pressures above 10^{-1} bar and H_2O pressures below 10^{-8} bar. The 0.5 ML is a mixture of partial and complete dissociation of H_2O molecules into surface O atoms and OH species. At 700 K, there is desorption of two H_2O groups at 10^{-9} to 10^{-10} bar of H_2O at H_2 pressures of 10^{-2} to 1 bar while three H_2O groups are desorbed from the surface at all H_2 pressures at 10^{-10} bar of H_2O. At 1000 K, a small region of 0.5 ML coverage still appears while there is a significant increase in the 0.25 ML region. The bare surface is recovered at higher temperatures above 1200 K at very low pressures of H_2O. At 1500 K, the bare surface is still recovered at H_2O pressures below 10^{-10} bar at all H_2 pressures while the 0.5 ML phase is totally lost. If only water molecules are introduced in the feed (without external addition of H_2), only the lower region of the diagram below the diagonal line Fig. 8 can be reached. This shows that partial or total surface dehydration can only be achieved at very high temperature.

Table 3 Adsorption energies E_{ads} for different coverages of H_2O on the (111) surface

Coverage	0.25 ML	0.50 ML	0.75 ML	1.0 ML
E_{ads}/per H_2O/eV	4.58	3.81	2.95	2.50
Successive adsorption energies of H_2O				
Number of H_2O molecules	1	2	3	4
E_{ads}/eV	4.58	3.25	1.22	1.14

It has to be noted that the 0.75 ML coverage is not stable at all studied temperatures for all the combinations of H_2 and H_2O partial pressures considered as the adsorption energies of the third and fourth water molecules are similar.

B. ZrC(110) surface

Surface structure of ZrC(110). The ZrC(110) surface structure was studied after full relaxation of the three topmost surface atom layers. There is no surface reconstruction after relaxation. The relaxation energy for the rigid surface is very small as compared to the (111) surface. Zr atoms of the first and second layers relaxed inwards while C atoms of the first and second layers relaxed upwards. Both the Zr–Zr and C–C bond distances of the surface layer remain the same as that of the bulk (3.35 Å). The first layer relaxes inwards while the second layer relaxes outward. The vertical distance between the C of the first layer and the C of the third layer decreases from 3.35 Å to 3.27 Å (d_{1C-3C} = 3.27 Å) and d_{2C-3C} = 2.33 Å. The vertical distance between Zr of the second layer and Zr of the fourth layer increases from 3.35 Å to 3.36 Å ($d_{2Zr-4Zr}$ = 3.36 Å). Thus surface relaxation causes an elongation of the Zr–C bonds between the second and third layers with the distance between Zr of the second layer and C of the third layer being d_{2Zr-3C} = 2.39 Å while the distance between C of the second layer and Zr of the third layer is d_{2C-3Zr} = 2.45 Å (the value in bulk ZrC is 2.37 Å). There is however a decrease in these inter-layer distances as one moves from the second layer to the first layer. The resulting d_{1Zr-2C} = 2.21 Å and d_{1C-2Zr} = 2.30 Å.

The high surface energy of the (110) surface is reflected in the TDOS as compared to that of the bulk (Fig. 9). Formation of the (110) surface from the bulk structure introduces a significant amount of new surface states just above the Fermi level. These new states are made of Zr d and C p orbitals. These new surface states are accounted for by the reduction in the coordination numbers of the surface Zr and C atoms to 3 as compared to coordination of 6 in the third and subsequent lower layers.

H_2O adsorption onto the ZrC(110) surface. Hydration of the (110) surface was also carried out in a successive fashion of H_2O molecule addition to the surface. The most stable form of adsorption of H_2O onto this surface is adsorption of O containing

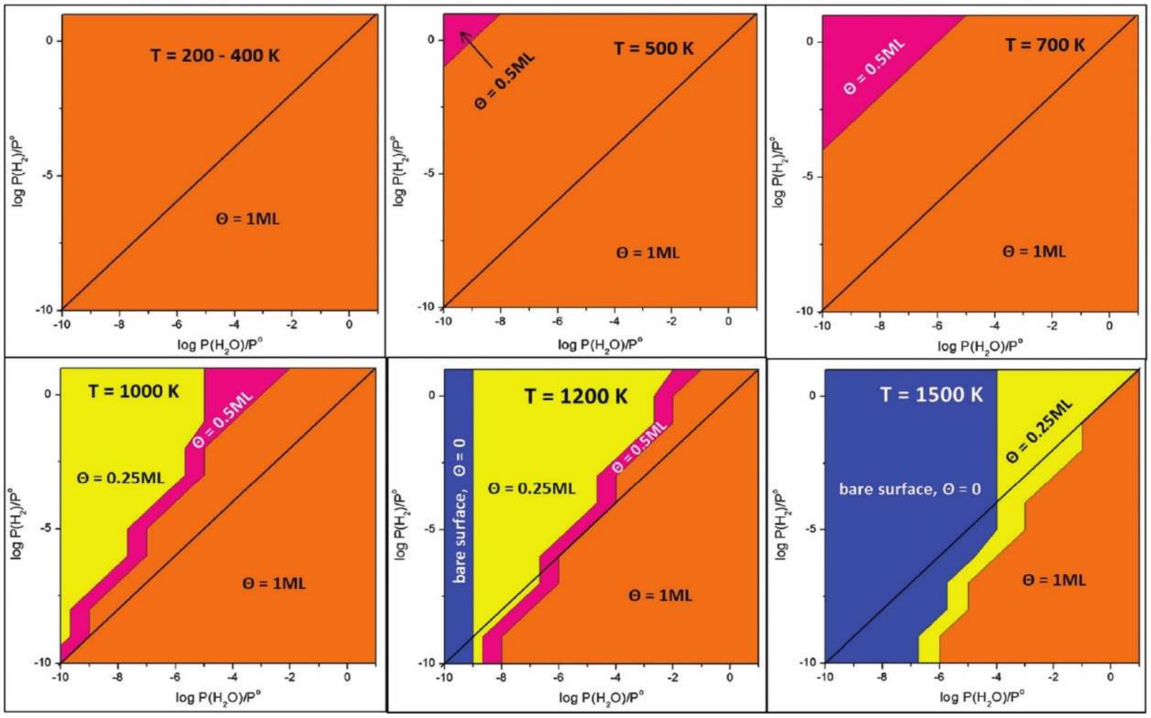

Fig. 8 2D-stability plot for H_2O adsorption onto the ZrC(111) surface at different temperatures. The 0.75 ML coverage is not stable at all studied partial pressures of H_2 and H_2O at all temperatures.

species as a bridge between two surface Zr atoms and on top of the C atom in the third layer whereas H atoms adsorbed on the top of surface C atoms.

1 H_2O molecule. The first H_2O molecule led to complete dissociation of water into atomic oxygen as a bridge between two Zr atoms and the resulting H atoms adsorbing on top of the two surface C atoms. This mode of adsorption yielded an adsorption energy, $E_{\text{ads}} = 4.22$ eV. The adsorption mode is shown in Fig. 10a1 and a2. The calculated bond distances between the O atom and the surface Zr atoms is 2.028 Å while the distances between the H atoms and the surface C atoms is 1.113 Å.

2 H_2O molecules. Adsorption of a second H_2O molecule led to partial dissociation of H_2O molecules into surface hydroxyl groups and H atoms. Thus two surface OH groups are formed as bridges between two surface Zr atoms and on top of the two available C atoms in the third layer as shown in Fig. 10b1 and b2. This adsorption of the second H_2O molecule was accompanied by a lower adsorption energy, $E_{\text{ads}} = 3.13$ eV, as compared to the adsorption energy of one H_2O molecule. At this point, the full surface coverage is achieved as all the stable adsorption sites are occupied. The calculated bond distances between the O atoms of the surface OH groups and the surface Zr atoms are within the range of 2.23 Å and 2.25 Å while those between the adsorbed H atoms and the surface C atoms is 1.12 Å. A (2×1) supercell was used to further obtain the adsorption energies for the 0.25 ML and 0.75 ML coverages which were calculated to be 4.21 eV and 3.44 eV per water molecule respectively.

The TDOS and PDOS of the partial dissociation of H_2O into surface hydroxyl groups are shown in Fig. 11. The TDOS shows the OH features appearing at about −7.5 eV which falls within the experimentally observed position range for the OH group.[8]

There is a slight attenuation in the surface states around the Fermi level upon adsorption of the OH groups and the PDOS shows a mixing of the Zr d orbitals with the O p orbitals during the adsorption of the OH groups onto the surface. There is also a large increase of the Zr d band above the Fermi level as the surface is hydrated.

Examination of the adsorption energies at different coverages of water (Table 4) shows strong adsorption at lower coverages.

The adsorption energies at different coverages were then used to obtain the thermodynamic stability plot in Fig. 12. This stability plot was obtained in a similar manner as that of Fig. 8. A 2D diagram is provided to aid easy viewing and interpretation. The full coverage of the surface with hydroxyl groups is achieved at low temperatures between 200 and 500 K at all H_2O partial pressures considered whereas the 0.5 ML phase which is made up of atomic O and H species on the surface is stable between 500 and 1000 K at low partial pressures of H_2O below 10^{-5} bar.

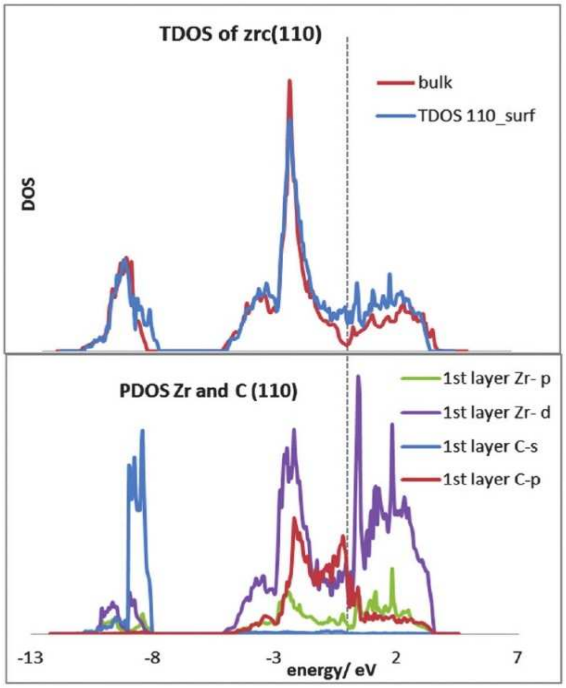

Fig. 9 TDOS and PDOS of the ZrC(110) surface.

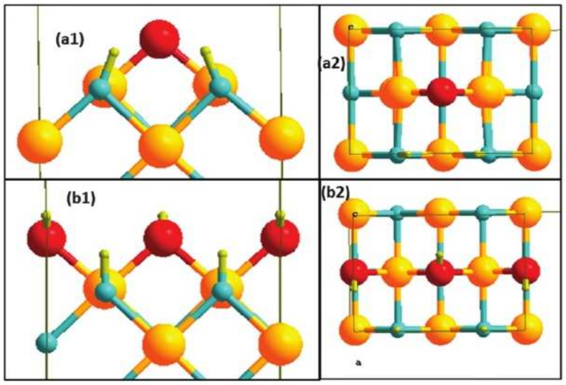

Fig. 10 Adsorption of H_2O onto the ZrC(110) surface. Left (side view), right (top view), blue (C), yellow (Zr), red (O), and light green (H).

It is also stable at higher temperatures up to 1800 K but at higher pressures of H_2O above 10^{-3} bar. The bare surface is recovered at temperatures above 1000 K in a wide range of H_2O partial pressures. It can be easily noted that both the 0.25 ML and 0.75 ML phases are not stable.

C. Characterization of surface oxidation

An analysis of oxidation of surface Zr and C atoms was carried out using the Bader code developed for VASP.[28] This was carried out for both the clean ZrC(110) and (111) surfaces. In order to provide a more complete picture of comparison, the same analysis was carried out for the adsorption of molecular water on the (100) surface.[14] Table 5 provides a summary of the Bader charge analysis.

In the case of hydration of the (100) surface with molecular water, there is clearly no change in the electron density of the surface Zr atoms as can be seen in Table 5. Moreover, upon hydration of the (110) surface, there is small charge transfer from the surface Zr atoms to O atoms and from surface C atoms to the attached H atoms. In the case of the (111) surface, upon hydration with the release of gaseous H_2, a clear redox process is evidenced and with a significant oxidation of surface Zr atoms (ΔQ_{Zr} = 0.68 electron) Table 5.

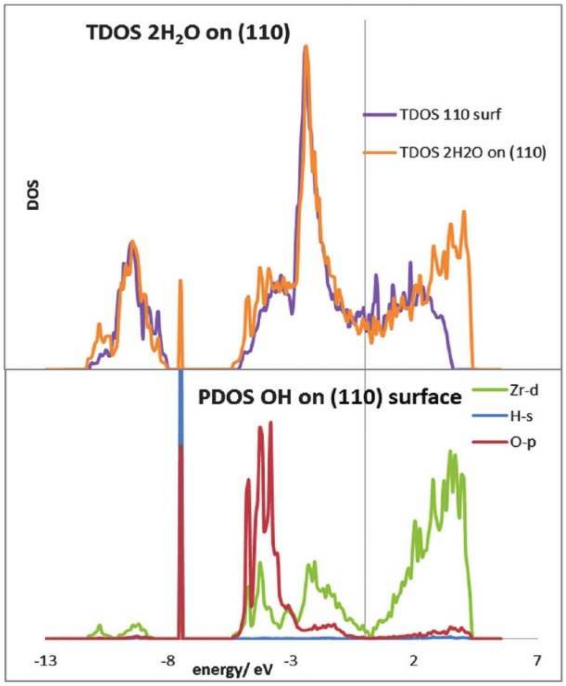

Fig. 11 TDOS and PDOS of H_2O adsorption onto the ZrC(110) surface; green legend: Zr on the surface layer.

Table 4 Adsorption energies E_{ads} for different coverages of H_2O on the (110) surface

Coverage	0.25 ML	0.50 ML	0.75 ML	1.0 ML
E_{ads}/per H_2O/eV	4.21	4.22	3.44	3.13

D. Equilibrium morphology of nanocrystallites

The equilibrium morphological shape of the ZrC nanocrystallites are predicted for the bare surface as well as for the hydrated surfaces at a range of selected temperatures.

Bare surface: the computed surface energies of the (100) and (110) surfaces, and the (111) surface (Zr-terminated) were used to predict the equilibrium Wulff morphology of the ZrC

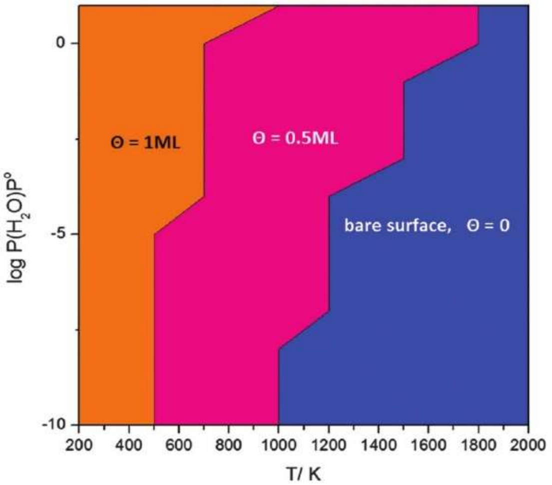

Fig. 12 2D surface stability plot for H_2O adsorption onto the ZrC(110) bare surface at different partial pressures of H_2O. 0.75 ML coverage is not stable at all studied temperatures and partial pressures of H_2O.

Table 5 Bader charge analysis of Zr and C atoms for clean and hydrated ZrC surfaces[a]

	Clean surface		
Parameter	ZrC-(100)	ZrC-(110)	ZrC-(111)
Net Q_C	−1.62	−2.27	−1.84
Net Q_{Zr}	1.65	2.47	1.09
	Hydrated surface		
Parameter	H_2O-(100)	HO-(110)	HO-(111)
ΔQ_{Zr}	0.06	0.27	0.68
ΔQ_C	0.05	0.51	0.05
ΔQ_O	−0.11	−0.22	−0.15

[a] The variation of the net charges (ΔQ_{Zr} and ΔQ_C) is defined with respect to the charges on Zr and C on the clean ZrC surfaces, while ΔQ_O is defined with respect to the charge of O in H_2O. The charge analysis was carried out using 1 ML coverage for both the (110) and (111) surfaces while 0.5 ML coverage was used for the (100) surface.

nanocrystallites in the absence of reactive molecules. The predicted Wulff structure is depicted in Fig. 13. The predicted morphology shows only the presence of (100) and (111) surfaces and the (110) surface does not appear. The crystallite structure is that of a cube with the small (111) facets at the corners which represents less than 1% of the exposed total surface area of the ZrC nanocrystallites. This is in excellent agreement with what has been observed experimentally as only the (100) surface is normally easily observed.[29]

H_2O adsorption: adsorption of water onto the (100) surface resulted in dissociative mode into surface OH groups on Zr atoms and H on surface C atoms with an adsorption energy of 1.0 eV. Details of H_2O adsorption on the (100) surface is provided in our previous paper.[14] A complete list of the surface energies of the individual facets of ZrC with their relative abundances upon hydration at different temperatures is compiled in Table 6.

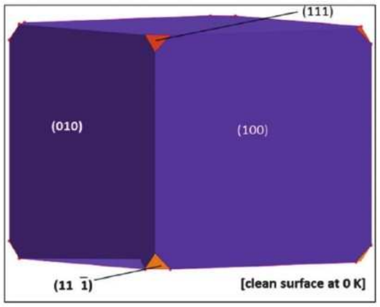

Fig. 13 Predicted Wulff solid for bare ZrC nanocrystallites.

For the (111) surface, there is a very strong interaction with water which provides much stability that overcompensates the surface energy of the bare facets at low temperatures and hence negative surface energies upon adsorption of water are reported. Thus (111) is highly stabilized relative to the other surfaces upon hydration in the range of 200 K to 500 K temperatures as shown in Table 6. This also reveals that the (110) surface is not present as compared to the other facets upon hydration of the nanocrystallites. The calculated surface energies at different temperatures after hydration were then used to obtain the Wulff construction of the equilibrium morphology of the nanocrystallites as shown in Fig. 14.

This construction was done at 0.01 bar H_2O pressure and 0.005 bar H_2 pressure. From 200 to 700 K, only the (111) facets are observed. This is due to the high stability of the (111) facets by four OH groups and subsequently stabilized further by the release of H_2 gas molecules. At 1000 K, 12 percent of the (100) surface is revealed as a result of removal of some OH groups from the (111) surface and the subsequent comparison of the resulting surface energies of the already bare (100) surface and the partially hydroxylated (111) facets. The surface energy for the (100) surface increases from 200 K to 500 K and remains fairly constant thereafter because at lower temperatures the surface is stabilized by the weakly adsorbed OH groups upon hydration, characterized by the low adsorption energy of the OH groups.[14] Thus at lower temperatures of 200 K to 700 K the extremely low surface free energy (negative values for surface energies) of the (111) surface results in smaller sized crystals. Moreover, at higher temperatures, the stabilizing OH groups are removed and the bare surface is exposed, resulting in an increased surface energy.

At 1200 K, more OH groups are removed from the (111) surface and the bare (100) surface increases in abundance to 35 percent with the (111) surface being 65 percent. As the temperature is increased further to 1500 K, the (111) facets decrease significantly in abundance while 76% of the surfaces is now made of the (100) facets. At all these temperatures, the full coverage with OH on the (111) surfaces is the most stable at 0.01 bar H_2O pressure and 0.005 bar H_2 pressure used while all (100) facets which appear are the bare surfaces. It can be clearly seen that at all temperatures, the (110) facets are not revealed. In order to functionalize the ZrC surfaces with hydroxyl groups

Table 6 Surface free energies of the exposed hydrated surface planes of ZrC at various temperatures with their relative abundance (in bracket) for $P(H_2O)/P_0$ = 0.01 bar and $P(H_2)/P_0$ = 0.005 bar

Surface energy/meV Å^{-2}	200 K	300 K	400 K	500 K
$\gamma_{(100)}(H_2O)$	43.0 (0%)	63.4 (0%)	84.5 (0%)	99.6 (0%)
$\gamma_{(110)}(H_2O)$	27.6 (0%)	42.1 (0%)	57.3 (0%)	73.0 (0%)
$\gamma_{(111)}(H_2O)$	−73.3 (100%)	−58.7 (100%)	−43.5 (100%)	−27.7 (100%)

Surface free energies at higher temperatures	700 K	1000 K	1200 K	1500 K
$\gamma_{(100)}(H_2O)$	99.6 (0%)	99.6 (12.3%)	99.6 (35.1%)	99.6 (76.4%)
$\gamma_{(110)}(H_2O)$	105.8 (0%)	144.6 (0%)	162.5 (0%)	190.3 (0%)
$\gamma_{(111)}$ (H_2O)	5.1 (100%)	56.9 (87.7%)	92.9 (64.9%)	147.0 (23.6%)

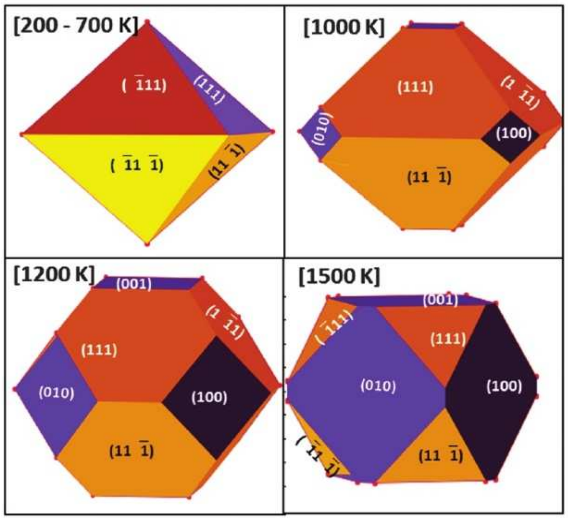

Fig. 14 Equilibrium Wulff shapes of hydrated ZrC at different temperatures. The (100) facets shown are bare surfaces while (111) are all shown for 1 ML full coverage which is the most stable at the chosen temperatures.

which can be obtained on the (100) facets or (111) facets, one can work in a wide range of temperatures and pressures and still achieve this aim. Thus there appear some changes in the morphology of the ZrC nanocrystallites when the surfaces are hydrated at different temperatures.

IV. Summary and conclusion

DFT and atomistic thermodynamic modelling have been combined to study the stability of ZrC(111) surfaces with different terminations of carbon atoms and zirconium atoms in an attempt to get rid of polarity in the slab. All cases tested yielded the most stable surface as the one with four Zr atoms in confirmation with experimental observations. The calculated surface energies of different facets were then used to obtain the equilibrium morphology of the ZrC nanocrystallites in a clean environment in vacuum. The equilibrium morphology at 0 K revealed the nanocrystallites as cubes exposing much of the (100) surface with truncations at the corners due to the appearance of small amounts of (111) facets and no (110) facets.

We have also studied the adsorption and reactivity processes of water on the (110) and (111) surfaces. A study of the adsorption of H_2O onto the (111) and (110) surfaces was carried out and we observed a complete dissociation into hydroxyl groups and the release of hydrogen molecules for the (111) surface. There is however a complete dissociation into oxygen as a bridge between two surface zirconium atoms with the dissociated hydrogens sitting on top of surface carbon atoms at low coverage for the (110) surface while a higher coverage results in surface hydroxyl groups. A thermodynamic stability plot shows the monolayer coverage with surface OH species as the most stable in a wide range of pressures until about 10^{-5} bar at 1200 K before the bare (111) surface is recovered. However, on the (110) surface the full coverage with OH and H atoms is stable at lower temperatures while the 0.5 ML coverage is stable between 700 K and 1000 K. The bare (110) surface is achieved at temperatures above 1000 K and lower H_2O partial pressures. Construction of the equilibrium morphology shows that from 200 to 1500 K temperature, the ZrC surfaces can be functionalized with surface hydroxyl groups, specifically on the (111) surface.

Acknowledgements

Numerical calculations presented in this paper were carried out using the regional computational cluster supported by Université Lille 1, CPER Nord-Pas-de-Calais/FEDER, France Grille, and CNRS. We highly appreciate and thank the technical staff of the CRI-Lille 1 center for their strong and helpful support. The project is supported by Agence Nationale de la Recherche under contract no. ANR-12-BS08-004-02 (CollZSiC: Elaboration de nanocomposites coeur/coquille ZrC/SiC).

References

1 L. E. Toth, *Transition metal carbides and nitrides*, Academic press, New York, 1971.
2 D. Gosset, M. Dollé, D. Simeone, G. Baldinozzi and L. Thomé, *J. Nucl. Mater.*, 2008, **373**, 123–129.
3 H. Li, L. Zhang, L. Cheng and Y. Wang, *Ceram. Int.*, 2009, **35**, 2277–2282.
4 H. Li, L. Zhang, L. Cheng, Y. Wang, Z. Yu, M. Huang, H. Tu and H. Xia, *J. Eur. Ceram. Soc.*, 2008, **28**, 887–891.
5 P. Greil, *Adv. Eng. Mater.*, 2000, **2**, 339–348.

6 M. Iijima and H. Kamiya, *J. Phys. Chem. C*, 2008, **112**, 11786–11790.

7 A. Arya and E. A. Carter, *Surf. Sci.*, 2004, **560**, 103–120.

8 T. Noda, M. Yamazaki, K. Ozawa, K. Edamoto and S. Otani, *Surf. Sci.*, 2000, **450**, 27–33.

9 T. Noda, T. Nakane, K. Ozawa, K. Edamoto, S. Tanaka and S. Otani, *Solid State Commun.*, 1998, **107**, 145–148.

10 A. Masakazu, O. Chuhei, Z. Shigeaki, O. Shigeki and I. Yoshio, *Jpn. J. Appl. Phys.*, 1981, **20**, L829.

11 W. Hayami, R. Souda, T. Aizawa, S. Otani and Y. Ishizawa, *Surf. Sci.*, 1992, **276**, 299–307.

12 W. Hayami, R. Souda, T. Aizawa, S. Otani and Y. Ishizawa, *Phys. Rev. B: Condens. Matter Mater. Phys.*, 1993, **47**, 13752–13758.

13 R. Souda, T. Aizawa, S. Otani and Y. Ishizawa, *Surf. Sci.*, 1990, **232**, 219–227.

14 E. Osei-Agyemang, J. F. Paul, R. Lucas, S. Foucaud and S. Cristol, *J. Phys. Chem. C*, 2014, **118**, 12952–12961.

15 J. Hafner, *J. Comput. Chem.*, 2008, **29**, 2044–2078.

16 N. D. Mermin, *Phys. Rev.*, 1965, **137**, A1441–A1443.

17 G. Kresse and D. Joubert, *Phys. Rev. B: Condens. Matter Mater. Phys.*, 1999, **59**, 1758–1775.

18 J. P. Perdew, K. Burke and M. Ernzerhof, *Phys. Rev. Lett.*, 1996, **77**, 3865–3868.

19 M. Methfessel and A. T. Paxton, *Phys. Rev. B: Condens. Matter Mater. Phys.*, 1989, **40**, 3616–3621.

20 H. J. Monkhorst and J. D. Pack, *Phys. Rev. B: Condens. Matter Mater. Phys.*, 1976, **13**, 5188–5192.

21 F. Bottin, F. Finocchi and C. Noguera, *Phys. Rev. B: Condens. Matter Mater. Phys.*, 2003, **68**, 035418.

22 D. Scopece, *J. Appl. Crystallogr.*, 2013, **46**, 811–816.

23 G. Z. Wulff, *Z. Kristallogr.*, 1901, **34**, 449–530.

24 K. Reuter and M. Scheffler, *Phys. Rev. Lett.*, 2003, **90**, 461031.

25 Y. Hwang, T. Aizawa, W. Hayami, S. Otani, Y. Y. Ishizawa and S.-J. Park, *Surf. Sci.*, 1992, **271**, 299.

26 J. Li, D. Liao, S. Yip, R. Najafabadi and L. Ecker, *J. Appl. Phys.*, 2003, **93**, 9072–9085.

27 A. Vojvodic, C. Ruberto and B. I. Lundqvist, *J. Phys.: Condens. Matter*, 2010, **22**, 375504.

28 W. Tang, E. Sanville and G. Henkelman, *J. Phys.: Condens. Matter*, 2009, **21**, 084204.

29 G. Mathieu, PhD thesis, Universite de Limoges, 2010.

4. Oxidation and equilibrium morphology of zirconium carbide low index surface using DFT and atomic thermodynamic modeling

A fully peer-reviewed article published in Journal of Physical Chemistry C.

THE JOURNAL OF PHYSICAL CHEMISTRY C
Article
pubs.acs.org/JPCC

Oxidation and Equilibrium Morphology of Zirconium Carbide Low Index Surfaces Using DFT and Atomistic Thermodynamic Modeling

Eric Osei-Agyemang,[†] Jean-François Paul,[†] Romain Lucas,[‡] Sylvie Foucaud,[‡] and Sylvain Cristol*[,†]

[†]Univ. Lille, CNRS, ENSCL, Centrale Lille, Univ. Artois, UMR 8181 - UCCS - Unité de Catalyse et de Chimie du Solide, F-59000 Lille, France

[‡]Laboratoire Science des Procédés Céramiques et de Traitements de Surface (SPCTS), UMR-CNRS 7315, Centre Européen de la Céramique, 87068 Limoges, France

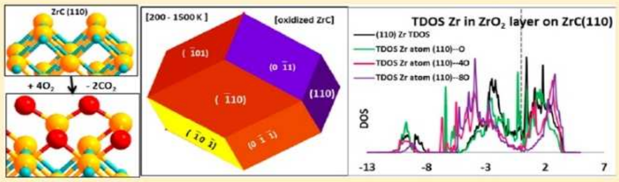

ABSTRACT: ZrC is a nonoxide high-temperature ceramic used for applications in harsh environments with corrosive and oxidizing conditions like nuclear reactor and nozzle flaps of jet propulsion engines. Moreover, easy oxidation of the crystal surfaces affects the excellent mechanical and physical properties. It is however imperative to study the oxidation processes on the different low index surfaces. DFT studies in conjunction with atomistic thermodynamic modeling have been used for this purpose. The (100) surface completely dissociates molecular oxygen into atomic species, and the surface is fully covered with oxygen atoms at a wide range of temperatures and pressures, recovering the bare surface at temperatures in excess of 1500 K. The (111) surface interacts strongly with O_2 by completely dissociating it into atomic species which adsorb at 3-fold fcc hollow sites. This surface is extremely difficult to clean of oxygen by manipulation of temperature and pressure alone. The bare surface cannot be recovered even at temperatures above 1800 K. The (110) surface on the other hand has a complex oxidation process, accumulating eight O atoms leading to the formation of surface ZrO_2 units with the release of CO_2. This ZrO_2-covered surface is highly stable and cannot be removed at temperatures below 2000 K by manipulating temperature and pressure alone. Wulff construction of the equilibrium morphology of the nanocrystallites upon oxidation reveals only the ZrO_2-covered (110) surface.

I. INTRODUCTION

Thermo-structural materials are often used in the aerospace industry (turbine components and flaps of nozzles) as well as the nuclear industry (as waterproof fuel jackets) and in the iron and steel industries (as refractory ceramics for the production of molten metals). Transition metal carbides (TMCs) meet these requirements due to their thermo-mechanical and chemical inertness properties.[1] Mostly in these areas of applications, the stakes are to make these structural materials lightweight while improving performance, to reduce the manufacturing cycles of the industrial processes by reducing the assembly operations, and finally to improve the shelf life of such materials. As such, these structural materials are required to work at extreme conditions of temperature and pressure as well as in oxidizing environments. These extreme requirements are met because of their high melting points of more than 3400 °C leading to their classification as ultrahigh temperature ceramics (UHTC).

ZrC has a cubic structure with three distinct low index surfaces (Figure 1) with stabilities in the following order: (100) > (111) > (110).[2] Details of surface energies of the different facets are provided elsewhere.[3]

The (111) surface is polar, terminated on one side by a carbon layer and a zirconium layer on the other side. However, the Zr-terminated side has been observed experimentally[4] and has been corroborated by our previous studies.[3] Aside from the excellent properties of the TMCs, they have not been widely utilized for extreme condition applications as compared to the ceramic-based borides such as zirconium diboride ($ZrBr_2$).

ZrC has the same mechanical properties as those of other TMCs at ambient conditions (SiC, TiC, etc.)[5] but forms weak refractory oxides at temperatures around 500−600 °C, and hence the oxidation resistance is limited.[6]

This eventually leads to a deterioration of the excellent mechanical properties. Different research groups have performed studies on the oxidation processes of surfaces of ZrC. There is an extensive amount of research carried out on the oxidation of the ZrC(100) surface.[7−10] In ref 8, the ZrC(100) surface is found to be very reactive to oxygen leading to the formation of a ZrO-like layer. Further exposure to oxygen leads to the formation of ZrO_x ($1 < x < 2$) layers on the surface.[8] Theoretical studies using DFT calculations revealed very high adsorption energies for oxygen on the (100) surface at a site between two surface Zr atoms and one carbon atom.[9,11] The oxidation mechanism on the (100) surface has been extensively studied by theoretical and experimental means.[10,12] The stable mode of adsorption is dissociative O_2 adsorption into atomic species bridging two surface Zr and one C atom. The authors observed an exothermic exchange of the adsorbed O atom and surface C atoms, and a subsequent second O atom adsorption

Received: February 11, 2016
Revised: April 1, 2016
Published: April 1, 2016

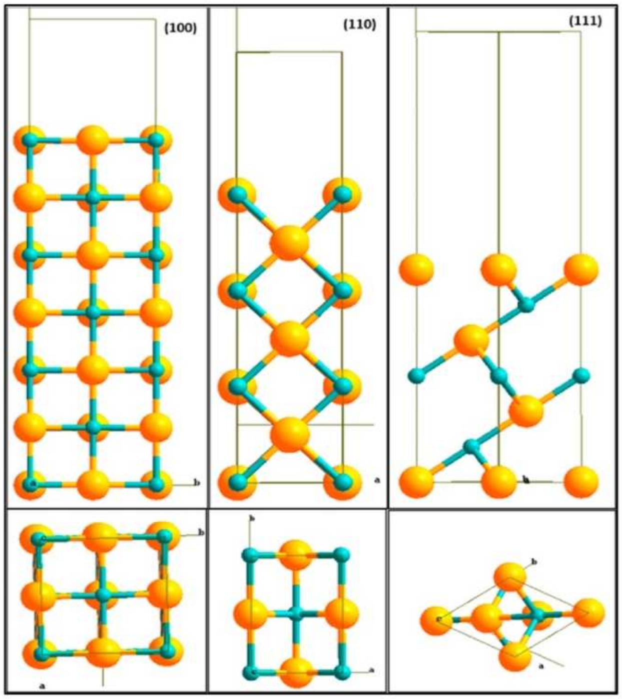

Figure 1. Different surfaces of ZrC. Upper Left (100), Upper middle (110), and Upper right (111) surfaces side view, respectively. Bottom left, bottom middle, and bottom right are (100), (110), and (111) top views, respectively. Yellow = Zr, Blue = C.

lead to a spontaneous formation and release of CO from the ZrC(100) surface. In a previous study, we reported details of the oxidation process on the (100) surfaces with the appropriate thermodynamic stability plots at different partial pressures of O_2.[11] All the adsorption energies and oxygen adsorption geometries concerning the (100) surface can be found therein.

Other experimental studies have revealed the dissociation of O_2 into atomic oxygen with very high adsorption energies on the ZrC(111) surface.[4,13,14] Some theoretical studies on the reactivity of oxygen on the (111) facets have been carried out.[15] All these studies have confirmed the very strong interaction of oxygen with the ZrC low index surfaces. Moreover, even though there is extensive experimental work on the oxidation of the surface, the reported theoretical studies do not provide information about oxidation at different coverage of oxygen and thermodynamic data concerning such processes.

In light of the above-mentioned studies of oxidation on the ZrC(100) and (111) surfaces, there is no extensive work done on the oxidation process of the (110) facets as well as information on oxidation at different coverage of oxygen and thermodynamic data. This is however needed in order to predict the equilibrium morphology of the nanocrystallites in oxidizing environments.

In this work, we have studied the reactivity of oxygen on ZrC(110) and (111) surfaces by means of periodic DFT.

The paper is structured as follows: in section II, we describe the methods and procedures used for the studies. Section IIIA presents the results and discussions of the oxidation on the (100) surface, while section IIIB discusses oxidation reaction on the (111) surface. Section IIIC provides detailed description of all reactions during oxidation of the (110) surface. Section IIID discusses the equilibrium morphology of the nanocrystallites upon oxidation. Section IV draws conclusions on the current work and provides future perspectives.

II. CALCULATION SCHEME AND STRUCTURAL MODELS

II.A. Calculation Methods and Parameters. We performed all calculations using the Vienna ab initio Simulation Package (VASP)[16] based on Mermin's finite temperature DFT.[17] The Zr, C, and O atoms were represented with the electronic configurations $[Kr]4d^25s^2$, $[He]2s^22p^2$, and $[He]2s^22p^4$, respectively. The core electrons as well as the core part of the valence electron wave functions were kept frozen and replaced with projector-augmented wave function (PAW) pseudopotentials.[18] This is done in order to reduce the number of planewaves required to effectively describe the electrons close to the nuclei. The generalized gradient approximation (GGA) exchange correlation functional as parametrized by Perdew, Burke, and Ernzerhof (PBE)[19] was used while employing the Methfessel–Paxton[20] smearing scheme by setting the gamma parameter to 0.1 eV. Testing of the energy cutoff for the accuracy of the calculations finally settled on 500 eV, while a Monkhorst–Pack[21] special grid sampling of the k-points for integration of the Brillouin zone yielded $9 \times 9 \times 9$ k-points representing 365 irreducible numbers of sampling points for all bulk calculations and $9 \times 9 \times 1$ k-points for surface calculations. Resolution of the Kohn–Sham equations using the self-consistent field procedure was performed by setting energy changes for each cycle at 10^{-4} eV as the convergence criterion between two successive iterations. Details of procedures used for all bulk calculations are provided elsewhere.[11] For all surface calculations, the positions of all the ions in the three topmost layers were relaxed until the net forces acting on them were smaller than 10^{-2} eV/Å.

(1×1) surface unit cells were used for all surface calculations with the exception of calculations involving lower coverage of O_2. A vacuum of 12 Å was used as separation between two periodically repeated slabs to avoid surface–surface interactions. For calculations on adsorption of oxygen on both (111) and (110) surfaces, 9 atomic layers were used. The topmost three layers of the surface slabs were relaxed, while the remaining layers were kept fixed to mimic bulk properties.

The (1×1) supercell used for the oxygen adsorption on the (111) surface has a lattice parameter of 6.698 Å and $\gamma = 60°$ with an exposed surface area of 38.854 Å^2. Four Zr atoms are exposed on this surface as shown in Figure 1. The (1×1) supercell used for oxygen adsorption on the (110) surface has a and b parameters of 4.736 and 6.698 Å, respectively, with an exposed surface area of 31.724 Å^2.

Oxygen was adsorbed on the surfaces in both associative and dissociative modes, and the adsorption energies are computed as in eq 1.

$$E_{\text{ads}} = -[E_{\text{O/Surf}} - E_{\text{Surface}} - E_{\text{O2}}] \quad (1)$$

$E_{\text{O/Surf}}$ is the energy of the oxidized surface; E_{Surface} is the energy of the clean surface; and E_{O2} is the energy of the gas-phase O_2 molecule.

The binding energy calculated for O_2 in our model is −6.04 eV compared to −6.08 eV in other studies.[22] In comparison to the experimental value of −5.17 eV,[23] the binding energy is overestimated by an amount of 0.87 eV. This is typical of GGA DFT calculations. It is therefore necessary to consider this overbinding issue. We therefore correct the adsorption energies by adding half of this overbinding energy (0.44 eV) for each O atom adsorbed.

After identifying the preferred mode of adsorption for O_2, we calculated the effect of different coverage of oxygen by using appropriate unit cells and increasing the number of oxygen atoms or molecules at the preferred adsorption sites. We evaluated 0.25 monolayer (ML), 0.5 ML, 0.75 ML, and 1 ML for the (100) and (111) surfaces, while up to 4 ML coverage was used for the (110) surface. The number of available Zr sites on the surfaces was used to define the different coverages. Each of the Zr atoms on the (111) surface defines 0.25 ML. For the (100) surface which has two surface Zr atoms, each Zr atom defines 0.50 ML, while for the (110) surface, each surface Zr atom defines 0.50 ML. Non-spin-polarized calculations were performed for O_2 adsorption on the surfaces as spin-polarized calculations have negligible contributions to the adsorption energies.

II.B. Atomistic Thermodynamic Model. The already well-established thermodynamic model[24] is used to provide a relationship between the calculated parameters and experimental working conditions. In this model, there is an assumption that the adsorbed molecules on the surfaces are in thermodynamic equilibrium with the gas phase which serves as a reservoir for the gas molecules. This then allows for a definition of the Gibbs free energy of adsorption ($\Delta_r G$) as a function of thermodynamic parameters like temperature, pressure. and chemical potential using the general eq 2.

$$\Delta_r G = [\Delta E_O + E_{ZPE(surf/molecule)} - \Delta \sum n\mu(T, p)] \qquad (2)$$

$E_{ZPE(surface/molecule)}$ is the zero point energy (ZPE) contribution of the gas molecule upon adsorption on the surface. ΔE_0 is the difference in the electronic energies of the oxidized surface and the gaseous O_2 molecule as well as any released species, while $\Delta\mu(T,p)$ is the difference in chemical potential of the gas-phase O_2 molecules and all other released species of the reaction. Thus, the ΔE_0 can be calculated according to the reaction in eq 3.

$$ZrC_{Surface} + n(O_2) \leftrightarrow ZrC_{oxid\_surface} + \text{released specie} \qquad (3)$$

From this surface reaction process, we can define ΔE_0 as $[E_{el(Oxid\ Surface)} + E_{Released\ specie} - E_{el(Surface)} - nE_{el(O2)}]$ which gives the corresponding reaction energies of the small molecules on the oxidized surface. The thermal contributions of the gas-phase molecules bring about changes in the chemical potential which are comprised of the temperature-dependent terms $\Delta\mu^0(T)$ and RT as in eq 4.

$$\Delta\mu(T, P) = \Delta\mu^0(T) + RT \ln\left(\frac{P}{P^0}\right) \qquad (4)$$

Statistical thermodynamics can be used to compute the change in chemical potential of the gas-phase molecules as in eq 5

$$\begin{aligned}\Delta\mu^0(T) = {} & [E_{ZPE} + E_{vib(0\to T)} + E_{rot} + E_{trans}] + RT \\ & - T(S_{vib} + S_{rot} + S_{trans})\end{aligned} \qquad (5)$$

The changes in the vibrational, rotational, and translational degrees of freedom provide the thermal contributions of the small molecules upon adsorption on the surfaces. Standard statistical thermodynamic formulas combined with equilibrium geometry and calculated frequencies are used to compute the values of $\Delta\mu^0(T)$ at different temperatures. The total pressure P^0 in eq 4 was set at 1 atm. Finally, the thermodynamic stability plots are obtained by plotting the calculated Gibbs free energies ($\Delta_r G$) against pressure p at different constant temperatures with the different coverages of O_2 molecules on the surface. The lowest-lying line of such plots is the most stable system at a given equilibrium condition.

In order to predict the equilibrium shape of the nanocrystals when small molecules are adsorbed on the surface, we calculate the surface energy $\gamma_{hkl}(O_2)$ as a function of the O_2 reacted with the surface at different temperatures and a partial pressure $P(O_2)/P^0 = 0.01$ bar as described in eq 6.

$$\gamma_{hkl}(O_2) = \frac{1}{2n}[\gamma^0_{hkl} + \theta_{hkl}\Delta_r G_{hkl}(P, T, nO_2)] \qquad (6)$$

$\gamma_{hkl}(O_2)$ is the corresponding surface energy after oxidation on the surface. γ^0_{hkl} is the surface energy of the clean or bare surface with no oxygen adsorbed ($\theta_{hkl} = 0$). $\theta_{hkl} = 2n/A_{hkl}$ provides a description for the surface coverage of the O_2, while $\Delta_r G_{hkl}(p, T, nO_2) = [\Delta E_0 + E_{ZPE(Surface+O2)} - \sum n\ \mu(T,p)]$. The resulting $\gamma_{hkl}(O_2)$ values at different temperatures are used to predict the equilibrium morphology of the nanocrystals using Wulff reconstruction.[25] The SOWOS[26] software package developed by Daniele Scopece is used for the Wulff construction.

The Bader code optimized for[27]VASP was used in analyzing the charged densities obtained for both the clean (100), (110), and (111) surfaces as well as for the oxidized surfaces

III. RESULTS AND DISCUSSION

Details about the bulk structural properties, lattice parameters, bulk modulus, surface energies, and surface relaxation of the ZrC low index surfaces are provided elsewhere.[3,11] The detailed oxidation processes on the ZrC(110) and (111) surfaces are provided here with a recount of the oxidation on the (100).

III.A. Reactivity of O_2 with the ZrC(100) Surface. Details of the reactivity of O_2 with the (100) surface are provided in a previous paper,[11] and hence we give a brief description of the oxidation process here.

One O Atom Adsorption. Molecular oxygen is found to adsorb in a dissociative mode on the ZrC(100) surface. The first O atom adsorbs at a 3-fold hollow site between two surface metal (Zr atoms) and one C atom in a configuration termed here as mmc configuration (Figure 2). The calculated adsorption energy for this process is 3.19 eV. The adsorbed O atom sits closer to the surface C atom than the two Zr atoms.

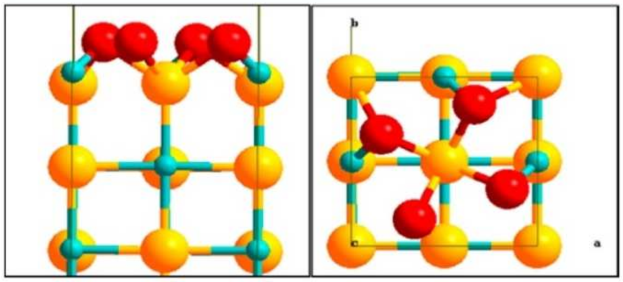

Figure 2. Side view (left) and top view (right) dissociated O atoms on the ZrC(100) surface. Blue (C), yellow (Zr), and red (O).

A Bader charge analysis was carried out for this adsorption process. The two Zr atoms in the mmc mode donate a charge of 0.04e$^-$. The C atom in the mmc donates 0.96e$^-$ which is understandable given that the adsorbed O atom sits closer to the C atom than the Zr atoms. The adsorbed O atom gains 1.06e$^-$. There is complete oxidation of the surface C atom with the Zr atoms being less affected.

Two O Atoms Adsorption. The second O atom also adsorbs in an mmc mode with high adsorption energy of 3.29 eV. At this stage the overall oxidation reaction on the surface is $\mathrm{ZrC(100)} + \mathrm{O_2} \rightarrow \mathrm{O{-}ZrC(110){-}O}$, $\Delta_r G = -6.48$ eV.

In the charge analysis, each of the Zr atoms donates a charge of 0.04e$^-$, while the C atoms transfer charge of 0.98e$^-$ to O atoms which receive a total charge of 1.05e$^-$. The surface C atoms are oxidized with little effect on the Zr atoms.

Three O Atoms Adsorption. The third O atom also adsorbed at an mmc site. However, the resulting 3 O atoms are now in alternating mmc modes. The calculated adsorption energy is 2.60 eV, and the $\Delta_r G = -9.08$ eV for the reaction.

The surface Zr atoms transfer a charge of 0.12e$^-$ each, while the O atoms receive an average charge of 1.03e$^-$. Due to the alternating nature of the mmc O atoms, one of the surface C atoms protrudes from the surface and transfers a charge of 1.86e$^-$, while the other C atom transfers a charge of 1.07e$^-$.

Four O Atoms Adsorption. In the addition of a fourth O atom the last possible mmc site on the surface is now adsorbed by an O atom with successive adsorption energy of 1.77 eV, and the overall change in Gibbs free energy at this stage is -10.85 eV.

Upon adding a fourth O atom, each of the two surface C atoms transfers a charge of 1.93e$^-$ to the O atoms, while the Zr atoms transfer charge of 0.16e$^-$ each. The four adsorbed O atoms receive a charge of 1.0e$^-$ each.

On this surface, the surface C atoms are easily oxidized.

A summary of all the successive adsorption energies and the average adsorption energy for each coverage of oxygen is provided in Table 1.

Table 1. Average Adsorption Energy, E_{ad}, per O Atom at Different Coverages and Successive O Addition Adsorption Energies on ZrC(100) and (111) Surfaces

		(100) Surface		
coverage	0.25 ML	0.50 ML	0.75 ML	1.0 ML
E_{ads}/eV/O	3.19	3.24	3.03	2.71
		Successive Adsorption Energies		
O number	1st	2nd	3rd	4th
E_{ad}/eV	3.19	3.29	2.60	1.77
(111) Surface				
coverage	0.25 ML	0.5 ML	0.75 ML	1.0 ML
E_{ads}/eV/O	6.24	6.20	6.08	5.83
		Successive Adsorption Energies		
O number	1st	2nd	3rd	4th
E_{ad}/eV	6.24	6.15	5.84	5.08

A fifth O atom was adsorbed on the surface, and the successive $E_{ads} = -1.47$ eV which is highly endothermic. The surface is therefore considered to be fully covered, and there is no further diffusion of oxygen into the bulk. Thus, the adsorbed O atoms passivate the surface.

In another work, the exchange between the surface C atoms with the adsorbed O atom was studied and found to proceed spontaneously. Subsequent addition of an O atom to form a surface CO moiety was also an exothermic process, but the final removal of CO from the surface was endothermic.[10] As such, we do not provide the details of such O ↔ C exchange process on the (100) surface here. We however present the thermodynamic stability plot of the oxidation process here (Figure 3). The surface is fully covered with O atoms at all pressures considered between 200 and 900 K temperature. At 1000 K, there is desorption of one O atom between pressures of 10^{-11} and 10^{-10} bar. Between 1100 and 1300 K, desorption of one O atom proceeds from 10^{-10} to 10^{-4} bar pressure. At higher temperatures of 1400 to 1500 K, the 0.50 ML coverage layer is recovered with the removal of two O atoms at pressures between 10^{-11} and 10^{-8} bar. At 1600 K, the bare surface is recovered at extremely low pressures of 10^{-11} bar, but between 1700 and 1800 K, the bare surface is fully recovered at pressures as high as 10^{-8} bar.

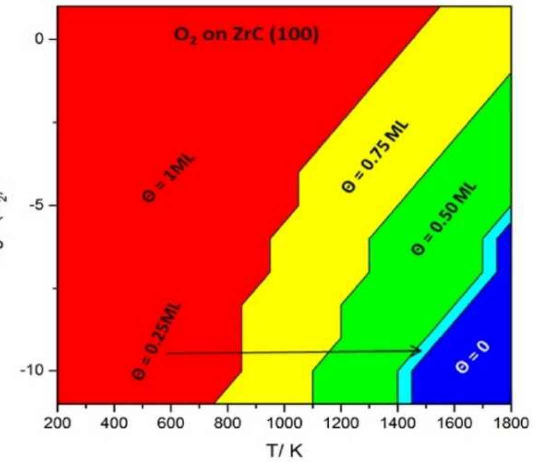

Figure 3. Thermodynamic stability plot for O_2 adsorption on the ZrC(100) surface (Θ is the surface coverage of oxygen).

III.B. Reactivity of O_2 with the ZrC(111) Surface. Both dissociative and associative modes of O_2 adsorption were tested for this surface. The ZrC(111) surface terminates with Zr and C layers at the two terminating surfaces. It has been observed experimentally to terminate with Zr layers, and a previous theoretical work[3] confirmed this observation. We therefore selected a (111) slab terminating on both sides with Zr layers comprised of four Zr atoms as described elsewhere.[3] Oxygen was found to adsorb dissociatively into atomic species on the (111) surface. This mode of adsorption was always accompanied by high adsorption energy. As such, we carried out the adsorption of O atoms in a successive fashion, adding one atom to the surface at a time.

One O Atom Adsorption. The first O atom added to the surface adsorbed at an fcc 3-fold hollow site between three surface Zr atoms and atop Zr atoms in the third layer (Figure 4). This was accompanied by a strong adsorption energy, $E_{ads} = 6.24$ eV. This is in excellent agreement with experimental observation for O adsorption.[4] The bond distances between the adsorbed O atom and surface Zr atoms are 2.110, 2.179, and 2.180 Å.

Using Bader charge analysis, the three Zr atoms forming the 3-fold hollow bond with the adsorbed O atom relax outward and transfer 0.34e$^-$ each to the oxygen atom, while the

DOI: 10.1021/acs.jpcc.6b01460
J. Phys. Chem. C 2016, 120, 8759−8771

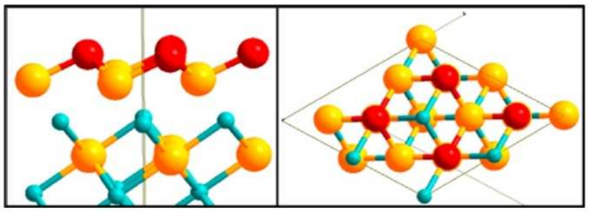

Figure 4. Side view (left) and top view (right) dissociated O atoms on the ZrC(111) surface. Blue (C), yellow (Zr), red (O).

remaining Zr atom receives 0.04e$^-$ from the transfer. Three of the second layer C atoms relax inward and donate 0.09e$^-$ each, while the remaining C atom moves upward receiving a charge of 0.05e$^-$. The adsorbed O atom receives a net charge of 1.17e$^-$.

Two O Atoms Adsorption. The second O atom adsorbed at a similar site to that of the first O atom adsorption. It is however accompanied by a slightly lower successive adsorption energy as compared to the first O atom, E_{ads} = 6.15 eV. At this point there are two out of the four possible adsorption sites occupied by the two O atoms. The calculated bond distances between the second O adatom and the surface Zr atoms are the same as those for the first O atom adsorption.

A Bader charge analysis was performed to provide a clear picture of the transfer of electrons at this stage of the oxidation process. Two of the four surface Zr atoms relax upward and donate 0.61e$^-$ to the adsorbed O atoms, while the other two Zr atoms relax inward and transfer 0.35e$^-$ to the oxygen during optimization. The second adsorbed O atom gains 1.16e$^-$. Two of the C atoms beneath the topmost Zr surface layer relax upward with no charge transfer, while the remaining two C atoms relax inward and transfer 0.14e$^-$ to the surface O atoms. Thus, in all, the two O atoms receive 2.32e$^-$ with 1.92e$^-$ from surface Zr atoms and 0.28e$^-$ from the second layer C atoms.

Three O Atoms Adsorption. Upon addition of the third O atom which adsorbs in a similar fashion as the first and second O atoms at the third of the four available adsorption sites, the successive adsorption energy is decreased further with E_{ads} = 5.84 eV. The bond distances between the adsorbed O atoms and the surface Zr atoms are 2.137, 2.136, and 2.189 Å.

During the optimization, one Zr atom moves outward and transfers a charge of 0.90e$^-$, while three Zr atoms move inward with a charge transfer of 0.67e$^-$ for a total of 2.91e$^-$. The O atom receives a net charge of 1.15e$^-$ for a total of 3.45e$^-$ for the three O atoms. Three of the second layer C atoms relax upward with charge transfer of 0.04e$^-$, while the remaining C atom relaxes inward with and transfers 0.19e$^-$ for a total of 0.31e$^-$. Thus, the Zr and C atoms transfer a total of 3.22e$^-$, and hence the remaining charge on the O atoms is from the third layer Zr atoms. It suddenly becomes apparent that the upward relaxing Zr atoms transfer more charge than the inward relaxing atoms. This is understandable as the protruding Zr atoms are readily accessible by the O atoms. This trend is however opposite for the C atoms in the second layer.

Four O Atoms Adsorption. Addition of a fourth O atom provides a full coverage of the available adsorption sites with atomic O species. This process is still accompanied by a strong successive adsorption energy, E_{ads} = 5.08 eV. This adsorption energy is lower than the adsorption energies of the first, second, and third O atoms. This reduction can be attributed to the lateral repulsion of the O atoms as the coverage on the (111) surface is increased. At this point, a fifth O atom was added, and the adsorption energy of −0.65 eV indicated a strong endothermic reaction. Hence we considered the full coverage up to four O atoms. The fully covered (111) surface with four O atoms is shown in Figure 4. The calculated bond distances between the adsorbed O atoms and the surface Zr atoms are 2.144 and 2.145 Å. The addition of four O atoms onto the ZrC(111) was a highly exothermic reaction yielding a combined adsorption energy of 23.31 eV.

With addition of the fourth O atom leading to full coverage on the surface, all four surface Zr atoms relax in the same direction, and each transfers a charge of 0.91e$^-$ to the adsorbed O atoms. Oxygen receives a charge of 1.14e$^-$ for a total of 4.56e$^-$. The second layer C atoms transfer 0.10e$^-$ for a total of 0.40e$^-$ to the O atoms.

From the charge transfer analysis, the oxidation process of this surface takes place on Zr atoms.

The average adsorption energy per O atom for different coverages was computed and summarized in Table 1. This table also includes the successive adsorption energy of each O atom added to the (111) surface. These adsorption energies at different coverages were used to obtain Gibbs free energies and used in the stability plot. It can be observed from Table 1 that the average adsorption energies per O atom remain nearly the same at different coverage, and thus the adsorption is not affected by the amount of oxygen on the surface. The thermodynamic stability plot for the different coverage at 2000 K is provided in Figure 5. At 2000 K, pressures as low as 10^{-9} bar are not enough to recover the bare surface. This is however not different from what has been reported experimentally as different groups used temperatures of above 1800 K at UHV pressures to clean the (111) surface during any experimental measurements.[14,28] The calculated PDOS and TDOS for the adsorbed oxygen on the (111) surface is shown in Figure 6(top). The TDOS shows a considerable attenuation of the surface states at the Fermi level upon adsorption of oxygen onto the surface. The unoccupied metal d-bands are shifted toward higher energies. The surface states are further examined by projecting the DOS of the Zr atoms on the oxidized surface as shown in Figure 6(bottom). There is a significant decrease in the intensity of the surface metal d states due to the mixing with O p bands resulting from the charge transfer from Zr.

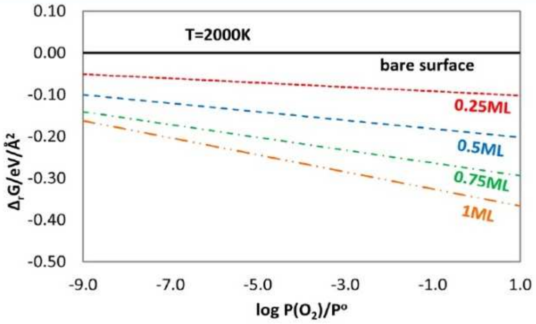

Figure 5. Gibbs free energy plot for dissociative O_2 adsorption on the ZrC(111) surface.

III.C. Oxidation of the ZrC(110) Surface. The oxidation process on the ZrC(110) surface was carried out for both associative and dissociative modes of adsorption. The observed

DOI: 10.1021/acs.jpcc.6b01460
J. Phys. Chem. C 2016, 120, 8759−8771

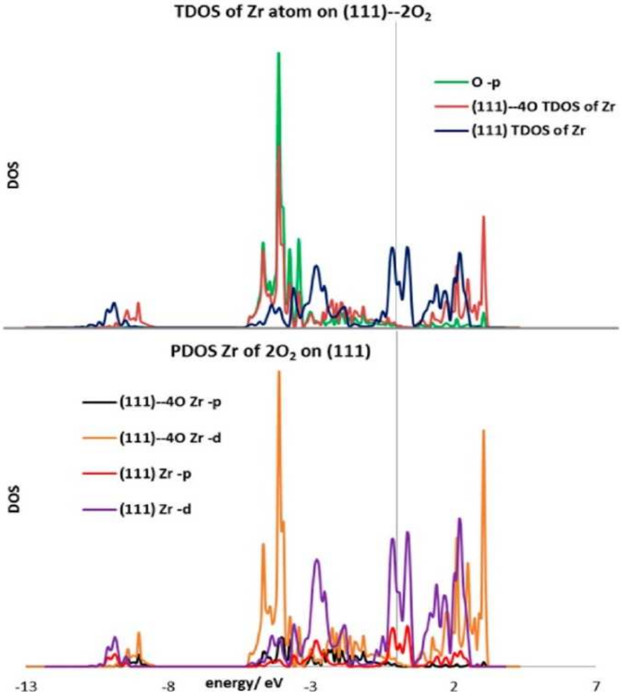

Figure 6. TDOS and PDOS of clean and oxygen-adsorbed ZrC(111) surface (top) and PDOS of Zr on clean and oxygen-adsorbed ZrC(111) surface (below) aligned vertically at the E_f. DOS in the vertical axis refers to density of states shown as bands.

stable mode of adsorption was always dissociative O_2 adsorption into atomic species. The reactivity study was thereafter carried out in a stepwise manner, starting from one O atom adsorption, then two O atoms, and so on. The different adsorption and chemical processes occurring on the (110) surface with different amounts of O atoms are as follows.

i. Initial Oxidation Phase. One O Atom Adsorption. Upon the addition of one O atom to the surface, there was a strong interaction with surface Zr and C atoms. The stable adsorption mode at this point was a bridge between one Zr and one C atom on the surface (Figure 7a).

This process was accompanied by a high adsorption energy, E_{ads} = 4.36 eV. Oxidation of the surface Zr atoms starts at this stage. The calculated bond distance between the adsorbed O atom and the surface Zr and C atoms is 1.31 and 1.12 Å, respectively. The C atom, which is bonded to the adsorbed O atom, is slightly displaced upward from its equilibrium position.

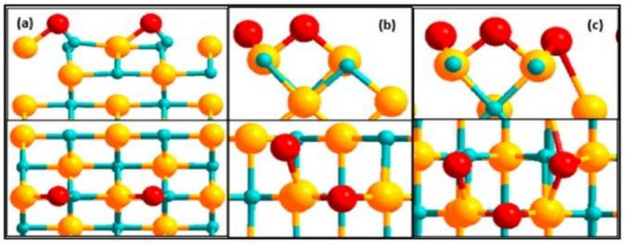

Figure 7. Oxidation of Zr atoms on the (110) surface showing side view (top) and top view (bottom). (a), (b), (c) are adsorption of 1, 2, and 3 O atoms, respectively. Blue = C, yellow = Zr, red = O.

$$\mathrm{ZrC}(110) + \frac{1}{2}\mathrm{O}_2 \rightarrow \mathrm{ZrC}(110){-}\mathrm{O},\ \ \Delta_r G = -4.36\ \mathrm{eV} \qquad (7)$$

$\Delta_r G$ is the change in Gibbs free energy of the considered process.

There is the transfer of 1.52e^- from the C atom bonding to the adsorbed O atom, while the free C atom transfers a charge of 0.26e^-. The Zr atom bonding with the O atom receives a charge of 0.19e^-, and the free Zr atom receives a charge of 0.49e^-. The adsorbed O atom receives a net charge of 1.11e^-. Upon O adsorption, the electronic reorganization leads to the Zr atoms receiving net charge as the Zr d states in the conduction band lie very close to the Fermi level (Figure 8) and the C p states from the valence band of the (110) surface occupy the Fermi level.

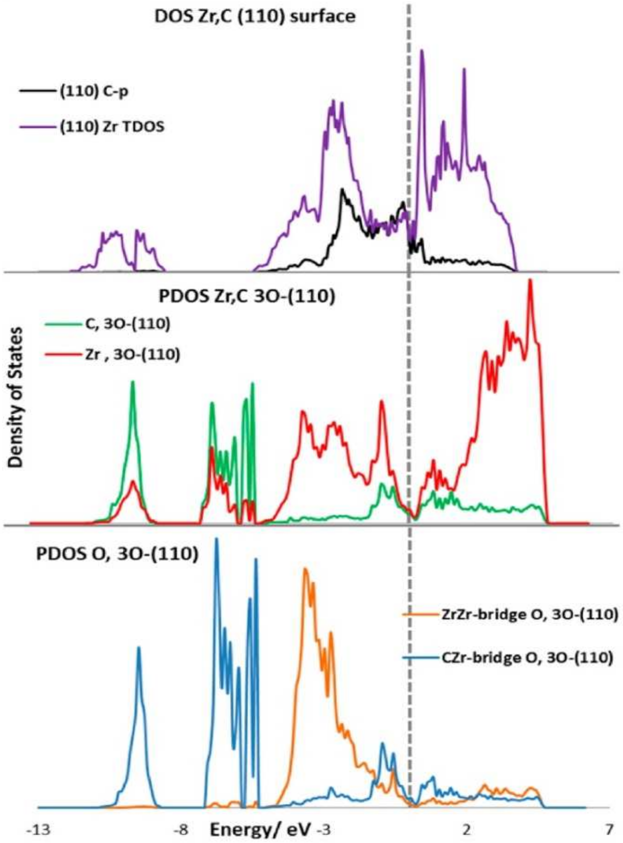

Figure 8. TDOS and PDOS for three O atoms adsorption on the (110) surface. The dashed vertical line is aligned at the Fermi level.

Two O Atoms Adsorption. When two O atoms are adsorbed on the surface, the second O atom adsorbs as a bridge between two surface Zr atoms (Figure 7b). This process is also characterized by a high successive adsorption energy of the second O atom, E_{ads} = 3.95 eV. Thus, the second Zr atom is oxidized at this point. The calculated bond distances between the adsorbed O atom and the surface C is 1.26 Å, while those between the adsorbed O and the surface Zr atoms are 2.26, 2.02, and 2.00 Å.

$$\mathrm{ZrC(110)} + \mathrm{O_2} \rightarrow \mathrm{ZrC(110){-}O},\ \ \Delta_r G = -8.31\ \mathrm{eV} \tag{8}$$

From this second oxygen addition to the last one, the Bader charge density analysis compares the oxidized surface with the bare surface. The C atom bonded to the first O atom transfers a net charge of 1.72e$^-$, and the other C atom transfers a charge of 0.48e$^-$. The two Zr atoms receive net charges of 0.19e$^-$ and 0.25e$^-$, while the adsorbed second O atom receives a charge of 1.25e$^-$. The charge on the first O atom is now 0.94e$^-$.

Three O Atoms Adsorption. Subsequent addition of a third O atom to the oxidized surface follows a similar pattern of adsorption mode as the ones for one and two O atoms (Figure 7c). The third O atom adsorbs as a bridge between the remaining surface C atom and a surface Zr atom with a successive adsorption energy, E_{ads} = 3.84 eV. This high adsorption energy shows strong interaction between the adsorbed O atom and the surface metal atoms. The bond distance between the surface C atoms and the adsorbed O atoms are 1.279 and 1.265 Å. The calculated bond distance between the adsorbed O atoms and the surface Zr units are 1.993 Å, 2.012 Å, 2.256 Å, and 2.270 Å. The adsorption process at this stage is governed by eq 9

$$\mathrm{ZrC(110)} + \frac{3}{2}\mathrm{O_2} \rightarrow \mathrm{ZrC(110){-}2O},\ \ \Delta_r G = -12.15\ \mathrm{eV} \tag{9}$$

The two surface Zr atoms receive charges of 0.13e$^-$ and 0.37e$^-$, respectively. The O atom adsorbed as a bridge between two Zr atoms receives a charge of 1.20e$^-$, while the two O atoms adsorbing as a bridge between Zr and C atoms receive charges of 0.88e$^-$ each. The two C atoms transfer charges of 1.61e$^-$ each to the O atoms. Thus, carbon atoms are oxidized at the end of this oxidation phase instead of Zr atoms.

The TDOS and PDOS are shown in Figure 8. A spin-polarized plot is shown to confirm that the adsorption energies are not affected by spin polarization as can be seen in the complete equivalence of the alpha and beta states. This provides information about changes in the surface states of the (110) surface and the introduction of new features by the adsorbed O atoms and their modifications of the (110) surface. The TDOS show Zr d unoccupied bands and C p valence bands close to the Fermi level reduced in intensity as they are being filled by the O electrons. The O introduced bands are found in the region between −5 and −7 eV. This region is typical of O bands as seen for the (111) surface. A projection of the DOS onto the surface Zr and C atoms shows a rigorous mixing of the O p orbitals with the C p and Zr d and p orbitals. This accounts for the observed high adsorption energy of the O atoms on the surface. The strong interaction also includes contributions from Zr s, Zr p, and C s orbitals.

ii. Further Oxidation of Surface C Atoms. After initial oxidation of one surface C atom, addition of extra O atoms further oxidizes the remaining surface C atoms.

Four O Atoms Adsorption. The fourth O atom commences the complete oxidation of the surface C atoms. At this point, there is an exchange between one of the surface C atoms and an O atom. This leads to the formation of a CO group which is strongly attached to the surface Zr atoms (Figure 9a). Thus, at this point, there are two Zr atoms, one C atom, and one O atom on the (110) surface plane as compared to two C atoms on the bare (110) surface. The successive adsorption energy at this stage is estimated to be 4.48 eV. The CO formation process is governed by eq 10.

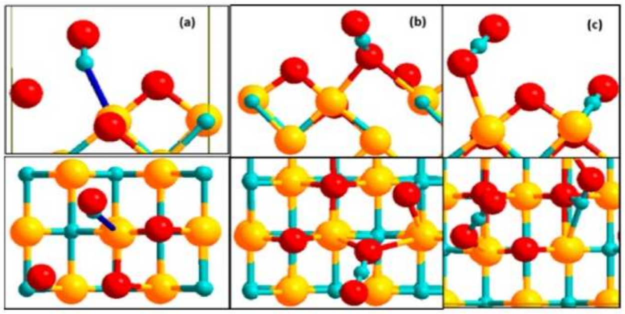

Figure 9. Oxidation of surface C atoms on the (110) surface showing side view (top) and top view (bottom). (a), (b), (c) are adsorption of 4 (with CO formed), 5, and 6 O atoms, respectively. Blue = C, yellow = Zr, red = O.

$$\mathrm{ZrC(110)} + 2\mathrm{O_2} \rightarrow \mathrm{3O{-}ZrC(110){-}CO},\quad \Delta_r G = -16.63\ \mathrm{eV} \tag{10}$$

It was necessary to check the spontaneity at which the CO can be removed from the surface (eq 11). Desorption of CO from the surface was however found to be an endothermic process.

$$\mathrm{3O{-}ZrC(110){-}CO} \rightarrow \mathrm{3O{-}ZrC(110)} + \mathrm{CO_{gas}},\quad \Delta_r G = 0.48\mathrm{eV} \tag{11}$$

Thus, the CO unit is adsorbed to the surface Zr atom with adsorption energy of 0.48 eV. Figure 9a does not however show this strong interaction, and a look at the charge density (Figure 10) provides a visualization of the strong adsorption of the CO group with surface Zr atoms.

In the Bader charge analysis, the Zr atom directly attached to the surface-incorporated O receives a charge of 0.11e$^-$, while the other Zr atom receives a net charge of 1.08e$^-$. The C atom in the CO group formed is highly oxidized and loses a charge of 3.14e$^-$ with the O atom in the CO group receiving a net charge of 0.92e$^-$. The surface incorporatered O atom gains a charge of 1.40e$^-$.

The bond distance between the incorporated surface O atom and the surface C atom is 3.257 Å, while that between the O and the attached surface Zr atom is 2.129 Å. The distance between C of the adsorbed CO and the surface Zr atom is 2.542 Å compared to 2.342 Å between the C atom in the second layer and Zr atom in the first layer. The surface is thus characterized by an O atom bridging two surface Zr atoms, an O atom bridging surface Zr and C atoms, one O atom incorporated into the surface plane, and an attached CO moiety.

Five O Atoms Adsorption. Addition of a fifth O atom further oxidizes the CO moiety which was formed in the previous step. This leads to the formation of CO_2 gas which is strongly attached to the surface (Figure 9b). The successive adsorption energy at this step is 3.59 eV. There is thus a complete oxidation of the first C atom on the surface at this point. The reaction process is shown in eq 12.

DOI: 10.1021/acs.jpcc.6b01460
J. Phys. Chem. C 2016, 120, 8759−8771

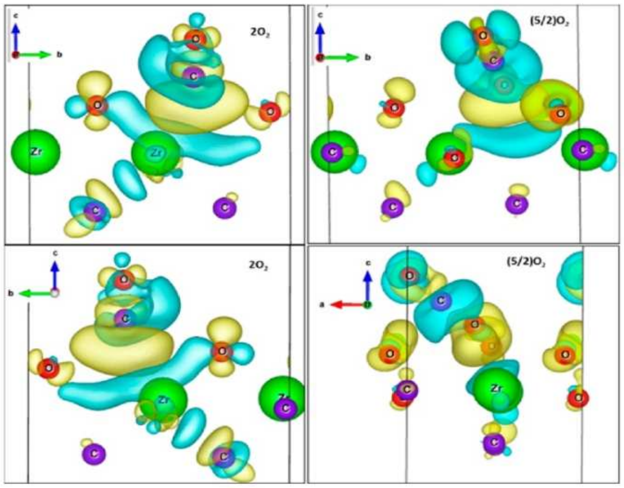

Figure 10. Electronic charge density for CO (top left and down left) and CO_2 (top right and down right) with 4O and 5O on (110), respectively, at different view angles. Positive charge density difference (light blue) and negative charge density difference (light yellow). Electronic charges near edges of the cell appear to be truncated and are a result of repetition in supercells due to periodic boundary contions. An isosurface level of 8.88×10^{-4} was used.

$$ZrC(110) + \frac{5}{2}O_2 \rightarrow 4O{-}ZrC(110){-}CO_2, \quad \Delta_r G = -20.22 \text{ eV} \tag{12}$$

The surface does not however release the attached CO_2 spontaneously as this process is endothermic with $\Delta_r G$ = 0.38 eV. As such, there is a strong interaction of the CO_2 with two surface Zr atoms through an O of CO_2 (Figure 10). The bond distance between O of CO_2 and the surface Zr atoms are 2.564 and 2.927 Å.

The O atom in CO_2 attached to the surface Zr atom gains a charge of $1.06e^-$ and the other O in CO_2 gains a total charge of $0.85e^-$, while the C of CO_2 $4.11e^-$. The Zr atom attached to the CO_2 receives a net charge of $0.10e^-$.

Six O Atoms Adsorption. There is a completion of the removal of all surface C atoms and a subsequent replacement with O atoms at this stage. Thus, the remaining surface C atom is now replaced by an O atom, while the O atom adsorbed as a bridge between the surface C and Zr atoms combines with the exchanged C atom to form an adsorbed CO moiety (Figure 9c). The already formed CO_2 is considered to be released into the gas phase though it has a slight interaction with surface Zr atoms (0.11 eV). This somewhat weak interaction is shown in the 2D charge density distribution plot of Figure 11. The successive adsorption energy of the sixth O atom is somehow lower than all previous O adsorptions (E_{ads} = 3.31 eV). Equation 13 depicts the chemical process on the surface at this stage.

$$ZrC(110) + 3O_2 \rightarrow 4O{-}ZrC(110) + CO_2, \quad \Delta_r G = -23.53 \text{ eV} \tag{13}$$

The adsorbed CO bridges a surface Zr and an O atom through its C atom. The bond distance between the C of the CO moiety and surface Zr and O atoms are 2.346 and 1.435 Å, respectively. There is also a strong interaction between O of CO and surface Zr atom with bond distance of 2.457 Å. The incorporated O atoms into the surface have bond distances of 2.157 and 2.362 Å. At this stage, there is still an O atom serving as a bridge between two Zr atoms on the surface.

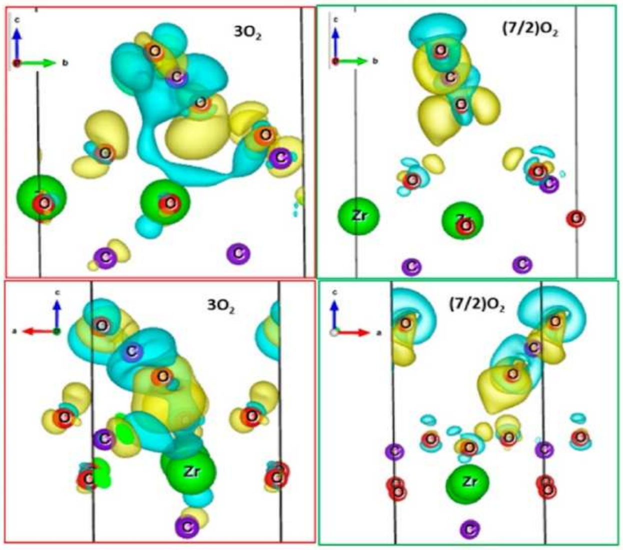

Figure 11. Electronic charge density difference for CO_2 in 6O adsorption (top left and bottom left), released CO_2 in 7O adsorption (top right and bottom right) at different view angles (positive charge density difference = light blue, negative charge density difference = light yellow). Electronic charges near edges of the cell appear to be truncated and are as a result of repetition in supercells due to periodic boundary conditions. An isosurface level of 8.88×10^{-4} was used to obtain the charge density plots.

The two surface Zr atoms receive net charges of $0.17e^-$ and $0.27e^-$, respectively, with the one attached to the CO group receiving the highest charge. C of CO transfers a charge of $3.01e^-$, and the two O atoms farthest from the surface receive charges of $1.23e^-$ and $1.06e^-$, respectively.

Figure 12 provides the TDOS and PDOS for the new surface formed. This surface lacks two C atoms replaced by two O atoms and hence looks like a ZrO layer. The Zr TDOS shows significant changes from the ideal (110) surface TDOS. The new surface shows sharp bands at the core level states. These sharp bands are attributed to the surface incorporated O p states with little contribution from the Zr d states. Thus, the O atoms on the surface show ionic bonding nature with the surface Zr atoms at this stage. The valence band structure is also altered by the O atoms on the surface. The PDOS for the adsorbed CO moiety shows an ionic bonding character as can be seen from the sharply isolated peaks at −11.18 eV and is strongly bonded to surface Zr d and O p orbitals. Also the interaction of the O atom in CO with the surface Zr atom can be seen in the PDOS at −8 eV. This surface is moreover slightly activated by the presence of unoccupied Zr d states around the Fermi level. The weakly bonded CO_2 appear as sharp peaks at −8.5 and −10 eV.

iii. Formation of Surface ZrO_2. As all the surface carbon atoms are replaced by O atoms, formation of ZrO_2 on the (110) surface commences.

Seven O Atoms Adsorption. This stage marks the complete conversion of the adsorbed CO group into CO_2 (Figure 13a).

DOI: 10.1021/acs.jpcc.6b01460
J. Phys. Chem. C 2016, 120, 8759−8771

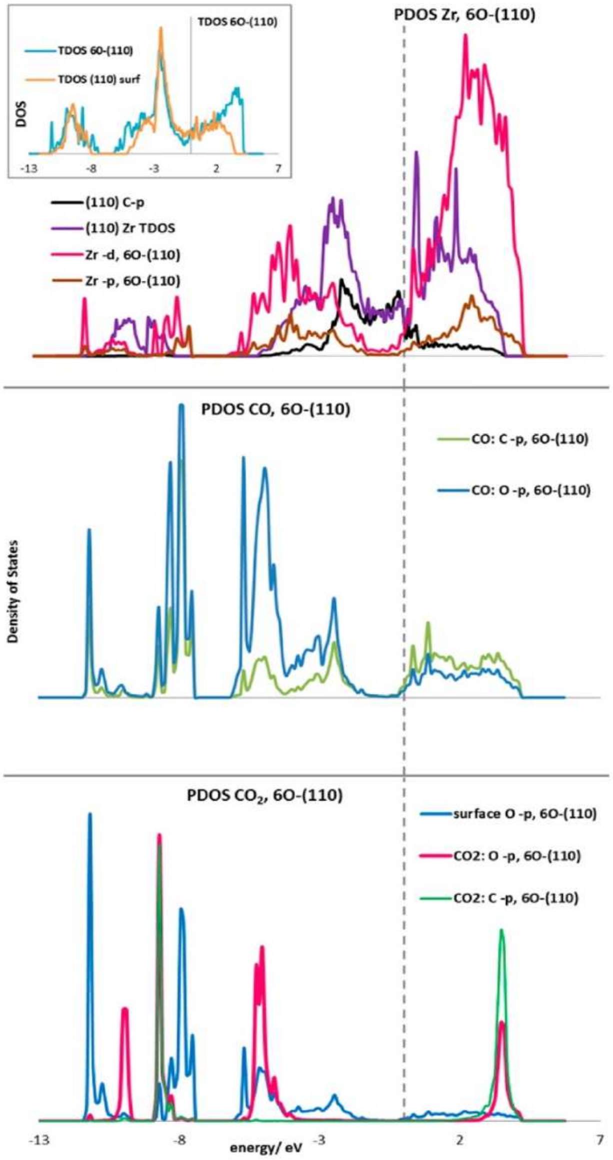

Figure 12. TDOS and PDOS for 6O atoms adsorption on the (110) surface, aligned vertically at the Fermi level.

Thus, the added oxygen oxidizes further the adsorbed CO and the resulting successive adsorption energy, E_{ads} = 4.25 eV. The formed CO_2 moiety interacts very strongly with surface O atoms through its C atom, while surface Zr atoms bond with O atoms of the CO_2. The surface reaction at this stage is governed by eq 14.

$$\mathrm{ZrC(110)} + \frac{7}{2}\mathrm{O_2} \rightarrow \mathrm{3O{-}ZrC(110){-}CO_2} + \mathrm{CO_2},$$
$$\Delta_r G = -27.78 \text{ eV} \tag{14}$$

Moreover, we estimated the reaction energy for desorbing the attached CO_2 from the surface, and this process is endothermic at this stage with $\Delta_r G$ = 0.42 eV. Thus, the Zr atoms in an attempt to form stable ZrO_2 units form additional bonds with

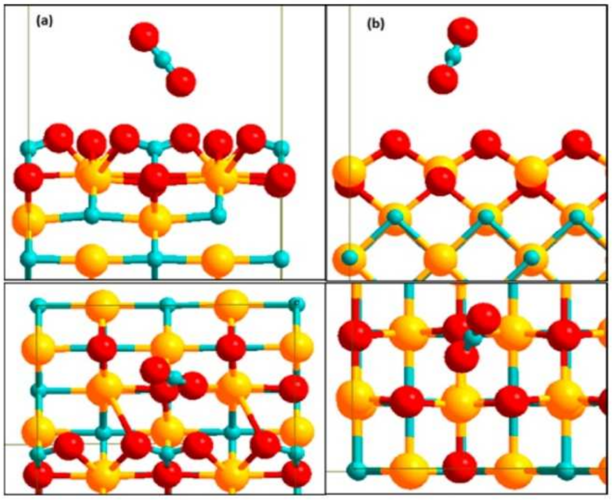

Figure 13. Formation of ZrO_2 on the (110) surface showing side view (top) and top view (bottom) and the released CO_2 molecule. (a), (b) are adsorption of 7 and 8 O atoms, respectively. Blue = C, yellow = Zr, red = O.

O atoms of CO_2. The free CO_2 group is shown in Figure 11 with virtually no interaction with the surface atoms. The calculated bond distance between C of CO_2 and surface O atoms is 1.409 Å, while the distances between O of CO_2 and surface Zr atoms are 2.277 and 3.007 Å.

The calculated charge transferred by the protruding surface Zr atom is 0.08e$^-$, while the inward relaxed Zr atom gains a charge of 0.08e$^-$. The C atom of the attached CO_2 transfers a charge of 4.16e$^-$, and the two O atoms of CO_2 gain charge of 1.16e$^-$ and 1.11e$^-$.

Eight O Atoms Adsorption. The adsorption of the eighth O atom marks completion of the total oxidation of the (110) surface. In order to form ZrO_2 on the surface, the added O atom adsorbs strongly on surface Zr atoms with a successive adsorption energy, E_{ads} = 3.51 eV. Figure 13b shows the geometry of the surface structure. The reaction process is shown in eq 15.

$$\mathrm{ZrC(110)} + 4\mathrm{O_2} \rightarrow \mathrm{4O{-}ZrC(110){-}CO_2} + \mathrm{CO_2},$$
$$\Delta_r G = -31.29 \text{ eV} \tag{15}$$

There is still a CO_2 group attached to the surface, and we estimated the reaction energy for the release of this CO_2 into the gas phase as in eq 16.

$$\mathrm{4O{-}ZrC(110){-}CO_2} \rightarrow \mathrm{4O{-}ZrC(110)} + \mathrm{CO_2},$$
$$\Delta_r G = -0.43 \text{ eV} \tag{16}$$

This process is found to be exothermic, and hence there is a spontaneous release of CO_2 into the gas phase. This exothermicity is related to the fact that the surface CO_2 group is not strongly bonded to the surface and has no interaction with the surface incorporated O atoms as is the case for 7O adsorption.

The overall change in Gibbs free energy for the eight O atom adsorption at this point is −31.29 eV. The final structure formed is a modified ZrC(110) surface with two ZrO_2 units on the surface. Two O atoms are in the surface plane of the Zr

DOI: 10.1021/acs.jpcc.6b01460
J. Phys. Chem. C 2016, 120, 8759−8771

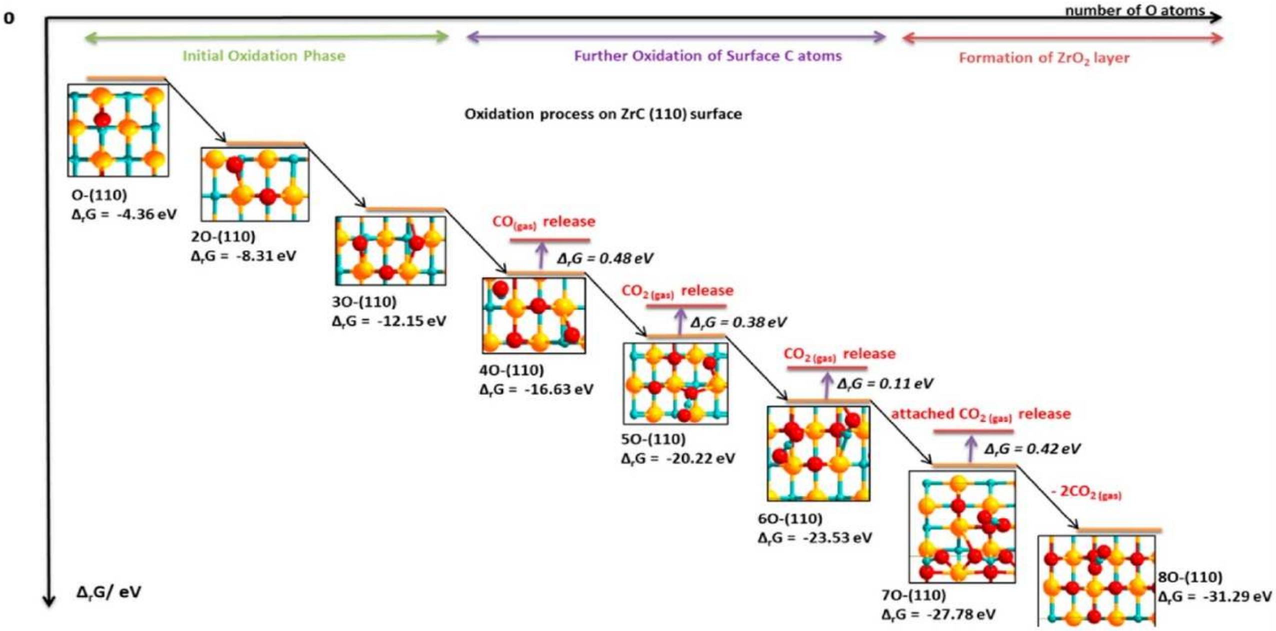

Figure 14. Reaction scheme for oxidation of the ZrC(110) surface. Red = O, Yellow = Zr, Blue = C.

atoms, while two O atoms form bridges between two adjacent Zr atoms. The Zr−O bond distances in the surface plane are 2.161 and 2.642 Å, while the distance between the two surface O atoms is 3.355 Å. The bridging O atoms have a distance of 2.008 Å from the surface Zr atoms. Figure 14 provides a complete picture for the oxidation process on the ZrC(110) surface.

A Bader analysis of the ZrO_2 layer formed on the ZrC(110) surface shows the two O atoms positioned at the surface plane gained charge of 1.54e$^-$, while the bridging O atoms gained a charge of 1.31e$^-$. The two surface Zr atoms donate charges of 0.24e$^-$ and 0.13e$^-$, respectively.

The overall conclusion from the charge transfer analysis at this final step is that the oxidation process of this surface will proceed with complete oxidation of all surface carbon atoms with subsequent removal of CO_2 before starting oxidation of zirconium atoms.

After forming the ZrO_2 layer on the (110) surface, it is worth mentioning here that there is further oxidation of the ZrO_2 layer formed. Thus, subsequent addition of O atoms to the ZrO_2 layer yielded reactions with negative $\Delta_r G$ values. We however talk about oxidation up to the formed ZrO_2 layer in this paper. A subsequent paper will discuss the oxidation process of the ZrO_2 layer formed.

Figure 15 shows the TDOS and PDOS for the ZrO_2 formed on the ZrC(110) surface. It can be easily noticed from the TDOS that the surface states around the Fermi level for the ZrC(110) surface are substantially decreased in both the occupied valence band and the unoccupied band by the formation of the ZrO_2 layer on the surface. This stabilizes the highly reactive (110) surface. Projection of the DOS to the surface Zr atoms which are typical of surface states for ZrC shows a gap at the Fermi level and virtually no d states at the surface. Thus, the metallic (110) surface is now transformed into a nonmetallic ZrO_2-covered (110) surface. The core band remains similar to that of the ZrC(110), while the new features introduced by the ZrO_2 layer in the valence band appear at around −4.0 eV. There is significant mixing of the surface Zr d and O p as well as the bridging O p orbitals. Moreover, the

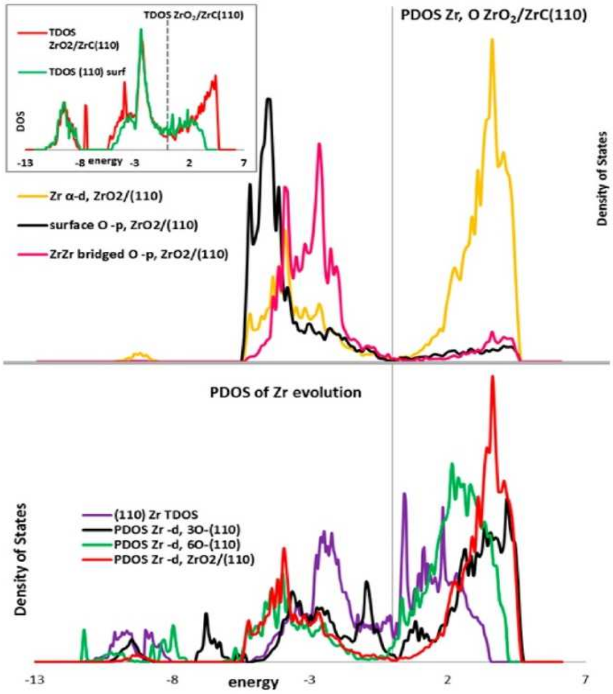

Figure 15. TDOS and PDOS for ZrO_2 formed on the ZrC(110) surface and evolution of the Zr atom DOS during oxidation of the ZrC(110) surface.

Table 2. Successive Adsorption Energy E_{ads} for Each Added O Atom and the Average Adsorption Energies at Different Coverages Defined As the Reaction Energy Divided by the Number of Adsorbed O Atoms for the ZrC(110) Surface

O atom number	1st	2nd	3rd	4th	5th	6th	7th	8th
E_{ads}/eV	4.36	3.95	3.84	4.48	3.59	3.31	4.25	3.51
Average Adsorption Energies at Different Coverages								
coverage/ML	0.5	1.0	1.5	2.0	2.5	3.0	3.5	4.0
E_{ads}/eV	4.36	3.98	3.93	4.07	3.97	3.86	3.92	3.87

unoccupied Zr d states around the Fermi level are decreased as compared to the ideal ZrC(110) surface.

It has been observed experimentally that the (110) orientation of t-ZrO_2 grows preferentially on ZrC(110) surfaces.[29,30] According to the authors, oxidation of ZrC(100) and (110) was carried out at temperatures of 600−1500 °C and O_2 partial pressures of 0.02−2 kPa for 1−20 h. Even at 1300 and 1500 °C, (110) orientations of t-ZrO_2 were found preferentially on the ZrC(110) surface. Thus, our ZrO_2 formation on the (110) surface is confirmed experimentally.

Figure 15 also contains the TDOS for the evolution of the Zr atom at three different stages of oxidation. For addition of only one O atom, the surface is further activated by Zr d states, and the noticeable changes in the DOS appear at −6.4 eV for the Zr d states in bonding with the O atom. At the beginning of oxidation of surface C atoms (addition of 4 O atoms), the surface d states of Zr are considerably decreased, and the appearance of new Zr d bands at −5.5 and −6.6 eV for the bonding of surface incorporated O atoms and formed CO groups, respectively. At the end of ZrO_2 surface layer formation, the changes in the Zr bands are due to those at −5.2 eV, −4.4 eV, and −3.9 eV, as well as −2.7 eV for mixing with surface incorporated and bridged O atoms, respectively.

Table 2 contains the calculated successive adsorption energies of each O atom added as well as the average adsorption energy per O atom at different coverages of O_2 on the ZrC(110) surface. The full coverage is defined for 1 O atom per surface Zr atom. These adsorption energies at different coverages were then used to obtain thermodynamic stability plots for the entire reaction process. The adsorption energy per O atom remains fairly constant at all coverages considered. The Gibbs free energy plot (Figure 16) at 2000 K and CO_2 partial pressure of 10^{-5} bar shows the ZrO_2 surface as the most stable. This explains the high stability of the ZrO_2 surface formed. A similar 2D plot (not shown) at all temperatures and partial pressures of O_2 and CO_2 shows only the fully oxidized (110) with a ZrO_2 surface layer being stable. Thus, manipulation of temperature and pressure alone cannot regain the bare ZrC(110) surface.

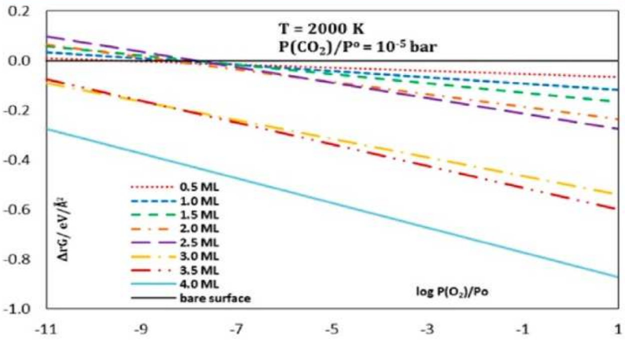

Figure 16. Gibbs free energy plot for ZrC(110) surface oxidation at 2000 K and CO_2 partial pressure of 10^{-5} bar.

It is worth mentioning here the difference in oxidation processes on the three different low index surfaces. The main difference in oxidation is due to the differential stability of the three surfaces. The lower surface energy of the (100) makes it more stable and less reactive to oxygen compared to the (110) and (111) surfaces. The very high reactivity of the (110) surface toward oxygen is due to the fact that this surface is highly unstable. It has a high surface energy, under saturation of surface atoms, and more dangling bonds and hence reacts vigorously with oxygen as compared to the (111) surface.

III.D. Equilibrium Morphology of Oxidized Nanocrystallites. The calculated Gibbs free energies of the different surfaces upon oxidation were then used to predict the equilibrium morphological shapes of the ZrC nanocrystallites. Table 3 provides the surface energies of the low index ZrC surfaces at different temperatures used for the Wulff construction. Figure 17 shows the equilibrium shape of the crystallites upon oxidation at temperatures of 200−1500 K. Only the (110) surfaces are revealed. This is due to the high stabilization of the surface by the formation of ZrO_2 layers on the surface. The (110) ZrC surfaces are not revealed for the bare crystallites as a result of the high surface energy associated with them and the subsequent significant surface states present at the Fermi level. However, these surfaces are completely transformed from the unstable ZrC(110) surface to a more stable ZrO_2 layer which drastically reduces the Zr d and C p states around the Fermi level that are responsible for the low stability of the surfaces. We therefore predict that, upon complete oxidation of all the surfaces of ZrC, the (110) surfaces are substantially increased in abundance and hence have to be considered.

IV. SUMMARY AND CONCLUSION

The oxidation process of low index ZrC surfaces was studied at different temperatures and oxygen partial pressures.

Oxidation of the (100) surface was reported in our previous studies[11] and has also been extensively studied by other groups.[10] We however report the thermodynamic stability plot here, and we observed the surface as completely oxidized over a wide range of temperatures and pressures. The bare surface is recovered at high temperatures above 1500 K and low O_2 partial pressures below 10^{-4} bar.

Oxidation of the (111) surface is a highly exothermic process of complete dissociation of oxygen into atomic species leading to the adsorption of one O atom per surface Zr atom. The O atoms adsorb at fcc 3-fold hollow sites between three surface Zr atoms. Manipulation of temperature and pressure alone cannot be used to clean the surface from oxygen even at temperatures as high as 1500 K.

DOI: 10.1021/acs.jpcc.6b01460
J. Phys. Chem. C 2016, 120, 8759−8771

Table 3. Surface Free Energies of the Exposed Oxidized Surface Planes of ZrC at Various Temperatures with Their Relative Abundances (In Bracket) for $P(O_2)/P^0 = 0.01$

surface energy/meV/Å^2	200 K	300 K	400 K	500 K
$\gamma_{(100)}(O_2)$	−0.33 (0%)	−0.31 (0%)	−0.29 (0%)	−0.27 (0%)
$\gamma_{(110)}(O_2)$	−0.76 (100%)	−0.74 (100%)	−0.73 (100%)	−0.71 (100%)
$\gamma_{(111)}(O_2)$	−0.42 (0%)	−0.40 (0%)	−0.39 (0%)	−0.38 (0%)
Surface Free Energies at Higher Temperatures				
	700 K	1000 K	1200 K	1500 K
$\gamma_{(100)}(O_2)$	−0.22 (0%)	−0.14 (0%)	−0.09 (0%)	−0.02 (0%)
$\gamma_{(110)}(O_2)$	−0.68 (100%)	−0.63 (100%)	−0.60 (100%)	−0.54 (100%)
$\gamma_{(111)}(O_2)$	−0.35 (0%)	−0.31 (0%)	−0.28 (0%)	−0.23 (0%)

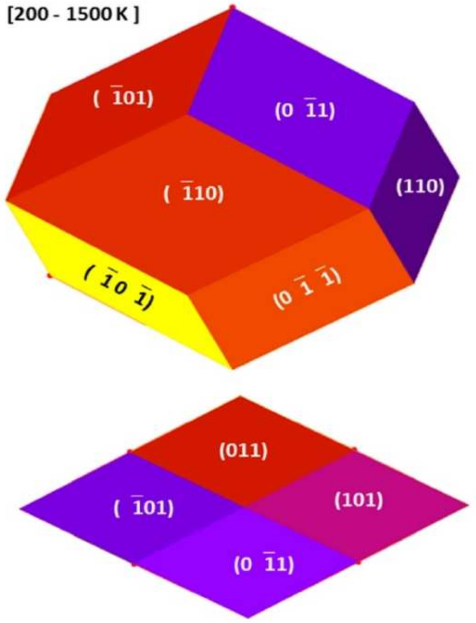

Figure 17. Equilibrium Wulff morphology for ZrC nanocrystallites upon oxidation (all (110) surfaces are covered by the ZrO_2 layer).

The (110) surface is highly reactive to oxygen and completely dissociates O_2 into atomic species. This surface incorporates high amounts of oxygen (8 O atoms) for its full oxidation process where we have followed the necessary steps. The surface is finally completely oxidized and forms ZrO_2 units on the surface layer with the release of CO_2 into the gas phase. This ZrO_2 layer formed is found to be highly stable and cannot be removed by temperature and pressure manipulations alone (even at 2000 K).

Wulff reconstruction of the equilibrium morphology of the ZrC nanocrystallites upon oxidation reveals only the (110) facets as a result of its enormous stabilization by the ZrO_2 layer formed on the surface.

■ AUTHOR INFORMATION

Corresponding Author

*Tel.: +33 320 43 45 03. Fax: +33 320 43 65 61. E-mail: sylvain.cristol@univ-lille1.fr.

Notes

The authors declare no competing financial interest.

■ ACKNOWLEDGMENTS

Numerical results presented in this paper were carried out using the regional computational cluster supported by Université Lille 1, CPER Nord-Pas-de-Calais/FEDER, France Grille, and CNRS. We highly appreciate and thank the technical staff of the CRI-Lille 1 center for their strong and helpful support. The project is supported by Agence Nationale de la Recherche under Contract No. ANR-12-BS08-004-02 (CollZSiC: Elaboration de nanocomposites coeur/coquille ZrC/SiC).

■ ABBREVIATIONS

TDOS, total density of states; PDOS, projected density of states; XPS, X-ray photoemission spectroscopy; DFT, density functional theory; PAW, projector-augmented wave function

■ REFERENCES

(1) Toth, L. E. *Transition Metal Carbides and Nitrides*; Academic press: New York, 1971.

(2) Arya, A.; Carter, E. A. Structure, Bonding, and Adhesion at the ZrC(100)/Fe(110) Interface from First Principles. *Surf. Sci.* **2004**, *560* (1−3), 103−120.

(3) Osei-Agyemang, E.; Paul, J.-F.; Lucas, R.; Foucaud, S.; Cristol, S. Stability, Equilibrium Morphology and Hydration of ZrC(111) and (110) Surfaces with H_2O: a Combined Periodic DFT and Atomistic Thermodynamic Study. *Phys. Chem. Chem. Phys.* **2015**, *17* (33), 21401−21413.

(4) Noda, T.; Yamazaki, M.; Ozawa, K.; Edamoto, K.; Otani, S. Oxygen adsorption on a ZrC(111) surface: angle-resolved photoemission study. *Surf. Sci.* **2000**, *450* (1−2), 27−33.

(5) Pastor, H. Les Carbures Réfractaires. *Ed. Ind. Céram. Fr.* **1977**.

(6) Li, H.; Zhang, L.; Cheng, L.; Wang, Y. Oxidation Analysis of 2D C/ZrC−SiC Composites with Different Coating Structures in CH4 Combustion Gas Environment. *Ceram. Int.* **2009**, *35* (6), 2277−2282.

(7) Kitaoka, H.; Ozawa, K.; Edamoto, K.; Otani, S. The Interaction of Water with Oxygen-modified ZrC(100) Surfaces. *Solid State Commun.* **2001**, *118* (1), 23−26.

(8) Kato, S.; Ozawa, K.-I.; Edamoto, K.; Otani, S. Photoelectron Spectroscopy Study of the Oxidation of ZrC(100). *Jpn. J. Appl. Phys., Part 1* **2000**, *39* (9R), 5217.

(9) Viñes, F.; Sousa, C.; Illas, F.; Liu, P.; Rodriguez, J. A. Density Functional Study of the Adsorption of Atomic Oxygen on the (001) Surface of Early Transition-metal Carbides. *J. Phys. Chem. C* **2007**, *111* (3), 1307−1314.

(10) Rodriguez, J. A.; Liu, P.; Gomes, J.; Nakamura, K.; Viñes, F.; Sousa, C.; Illas, F. Interaction of Oxygen with ZrC(001) and VC(001): Photoemission and First-principles Studies. *Phys. Rev. B: Condens. Matter Mater. Phys.* **2005**, DOI: 10.1103/PhysRevB.72.075427.

(11) Osei-Agyemang, E.; Paul, J. F.; Lucas, R.; Foucaud, S.; Cristol, S. Periodic DFT and Atomistic Thermodynamic Modeling of Reactivity of H_2, O_2, and H_2O Molecules on Bare and Oxygen Modified ZrC (100) Surface. *J. Phys. Chem. C* **2014**, *118* (24), 12952−12961.

DOI: 10.1021/acs.jpcc.6b01460
J. Phys. Chem. C 2016, 120, 8759−8771

(12) Viñes, F.; Sousa, C.; Illas, F.; Liu, P.; Rodriguez, J. A. A Systematic Density Functional Study of Molecular Oxygen Adsorption and Dissociation on the (001) Surface of gGroup IV-VI Transition Metal cCarbides. *J. Phys. Chem. C* **2007**, *111* (45), 16982−16989.

(13) Noda, T.; Nakane, T.; Ozawa, K.; Edamoto, K.; Tanaka, S.; Otani, S. Photoemission Study of the Oxidation of ZrC(111). *Solid State Commun.* **1998**, *107* (4), 145−148.

(14) Ozawa, K.; Yoshii, T.; Noda, T.; Edamoto, K.; Tanaka, S. Coadsorption of Oxygen and Cesium on ZrC(111). *Surf. Sci.* **2002**, *511* (1−3), 421−434.

(15) Vojvodic, A.; Ruberto, C.; Lundqvist, B. I. Atomic and Molecular Adsorption on Transition-metal Carbide (111) Surfaces from Density-functional Theory: A Trend Study of Surface Electronic Factors. *J. Phys.: Condens. Matter* **2010**, *22* (37), 375504.

(16) Hafner, J. Ab-initio Simulations of Materials using VASP: Density-Functional Theory and Beyond. *J. Comput. Chem.* **2008**, *29* (13), 2044−2078.

(17) Mermin, N. D. Thermal Properties of the Inhomogeneous Electron Gas. *Phys. Rev.* **1965**, *137* (5A), A1441−A1443.

(18) Kresse, G.; Joubert, D. From Ultrasoft Pseudopotentials to the Projector Augmented-wave Method. *Phys. Rev. B: Condens. Matter Mater. Phys.* **1999**, *59* (3), 1758−1775.

(19) Perdew, J. P.; Burke, K.; Ernzerhof, M. Generalized Gradient Approximation Made Simple. *Phys. Rev. Lett.* **1996**, *77* (18), 3865−3868.

(20) Methfessel, M.; Paxton, A. T. High-precision Sampling for Brillouin-zone Integration in Metals. *Phys. Rev. B: Condens. Matter Mater. Phys.* **1989**, *40* (6), 3616−3621.

(21) Monkhorst, H. J.; Pack, J. D. Special Points for Brillouin-zone Integrations. *Phys. Rev. B* **1976**, *13* (12), 5188−5192.

(22) Santos-Carballal, D.; Roldan, A.; Grau-Crespo, R.; de Leeuw, N. H. A DFT Study of the Structures, Stabilities and Redox Behaviour of the Major Surfaces of Magnetite Fe3O4. *Phys. Chem. Chem. Phys.* **2014**, *16* (39), 21082−21097.

(23) Haynes, W. M. *CRC Handbook of Chemistry and Physics*, 93rd ed.; Taylor and Francis: London, 2012.

(24) Reuter, K.; Scheffler, M. First-principles Atomistic Thermodynamics for Oxidation Catalysis: Surface Phase Diagrams and Catalytically Interesting Regions. *Phys. Rev. Lett.* **2003**, *90* (4), 461031−461034.

(25) Wulff, G. Zur Frage der Geschwindigkeit des Wachstums und der Auflösung von Krystallflächen. *Z. Kristallogr. - Cryst. Mater.* **1901**, *34*, 449−530.

(26) Scopece, D. SOWOS: an Open-source Program for the Three-dimensional Wulff Construction. *J. Appl. Crystallogr.* **2013**, *46* (3), 811−816.

(27) Tang, W.; Sanville, E.; Henkelman, G. A Grid-based Bader Analysis Algorithm Without Lattice Bias. *J. Phys.: Condens. Matter* **2009**, *21* (8), 084204.

(28) Tokumitsu, S.; Anazawa, T.; Tanabe, A.; Sekine, R.; Miyazaki, E.; Edamoto, K.; Kato, H.; Otani, S. Interaction ofHydrogen with ZrC(111) Surface: Angle-resolved Photoemission study. *Surf. Sci.* **1996**, *351* (1−3), 165−171.

(29) Shimada, S.; Yoshimatsu, M.; Inagaki, M.; Otani, S. Formation and Characterization of Carbon at the ZrC/ZrO_2 Interface by Oxidation of ZrC Single Crystals. *Carbon* **1998**, *36* (7−8), 1125−1131.

(30) Shimada, S.; Inagaki, M.; Suzuki, M. Microstructural Observation of the ZrC/ZrO_2 Interface Formed by Oxidation of ZrC. *J. Mater. Res.* **1996**, *11* (10), 2594−2597.

5. Conclusion

The chapter provided full account on studies on adsorption and reactivity of H_2, O_2 and H_2O on ZrC low index surfaces. Initial analysis was done on stability of all three low index ZrC surfaces. The established stability criteria is (110) < (111) < (100) surface. The as-cleaved ZrC (111) surface is a polar surface terminating with Zr layer on one side and C layer on the other side of the slab. Several correction schemes were applied and the most stable surface is Zr termination on both sides as confirmed by experiments.

Studies were carried out on the adsorption and reactivity of H_2 with ZrC (100) surface and hydrogen is observed to adsorb in a dissociative manner. The adsorption is however weak with a higher activation barrier from the molecular H_2 to atomic H species and hence the surface can be concluded to be free of hydrogen reactions. On the hydration of the (100) surface, molecular water is observed to adsorb on the surface at temperatures below 200 K but dissociates into hydroxyl groups at higher temperatures with a low activation barrier. Oxygen modification of the surface provides further activation of this surface and water dissociates further into both hydroxyl groups and atomic O with H_2 release.

Oxidation of all three surfaces were studied. Both ZrC (100) and (111) surfaces react very strongly with oxygen and after full coverage of the surface with a monolayer of oxygen, there is no further diffusion of oxygen into the bulk and the oxide layer passivates the surface. However, oxidation of the (110) surface leads to formation of ZrO_2 layer on the surface with the release of CO_2 into the gas phase. There is further diffusion of oxygen into the bulk and hence oxidation on this surface is not a passive process. Equilibrium morphology of the nano crystallites after oxidation shows appearance of only the (110) surface due to the irreversible formation of a stable ZrO_2 layer on the surface and the crystals are predicted to exhibit very small sized particles.

Hydration of the (110) and (111) surfaces showed the formation of hydroxyl groups on the surfaces with the process being much stronger on the (111) surface. There is the release of H_2 gas upon hydration of the (111) surface with the bare surface only recovered at temperatures in excess of 1200 K. From a Wulff reconstruction of the nanocrystallites, the equilibrium morphology after hydration shows the presence of only (111) surface at lower temperatures with the (100) surface appearing at higher temperatures. All surfaces can be functionalized with OH groups for grafting.

Chapter V: Structure and Properties at ZrC//ZrO$_2$ Interface

Table of Contents

1. Introduction

In this chapter a complete account is given on the nature, structure and properties of the oxide layer formed on surfaces of the ZrC nano crystallites used for our investigations. The determination of the structure and properties of this oxide layer observed on the ZrC surfaces is very crucial as different studies in the literature has identified different forms of the oxide layer on ZrC surfaces. The nature of the oxide layer will also determine the properties and structure of the final compounds used to functionalize the exposed surface. After determination of the nature of the oxide layer, it is very crucial to study and characterize the interface between ZrC and the oxide layer in order to build proper models for further studies.

The chapter is divided into two parts. The first part combines several experimental techniques in identifying the nature of the oxide layer and corroborated by molecular dynamics simulations. The structure and properties of the oxide layer formed on the ZrC(100) layer and the corresponding interface is characterized in this section. The section is made up of fully written article which has been submitted for publication and is reviewed. The article is to be published in the American Chemical Society, Journal of Applied Materials and Interfaces and is presented in this chapter in the form submitted for publication.

In the second section of this chapter, the properties and structure of the oxide layer formed on ZrC(111) surface as well as the interface is characterized. The section is also made up of a fully written article which has been submitted for publication and is under review. The manuscript is to be published in the American Chemical Society, Journal of Applied Materials and Interfaces. It is presented here in the exact format as submitted for publication.

2. Structure and Energetics of ZrC(100)||c-ZrO_2(001) interface: A Combination of Experiments, Finite Temperature Molecular Dynamics, Periodic DFT and Atomistic Thermodynamic Modeling

A fully written research article submitted for publication is presented in this section.

Structure and Energetics of ZrC(100)||*c*-ZrO$_2$(001) interface: A Combination of Experiments, Finite Temperature Molecular Dynamics, Periodic DFT and Atomistic Thermodynamic Modeling

Eric Osei-Agyemang[1], Jean-François Paul,[1] Romain Lucas,[2] Sylvie Foucaud,[2] Sylvain Cristol[1]*, Anne-Sophie Mamede[1], Nicolas Nuns[1], Ahmed Addad[3]

[1] Université de Lille 1, Univ. Lille, CNRS, ENSCL, Centrale Lille, Univ. Artois, UMR 8181 - UCCS - Unité de Catalyse et de Chimie du Solide.

[2] Université de Limoges, CNRS, ENSCI, SPCTS, UMR 7315, F-87000 Limoges, France.

[3] Unité Matériaux et Transformations, Université Lille 1, CNRS-UMR 8207

ABSTRACT: The oxidation process of ZrC is very important as it affects the excellent mechanical and Physical properties. ZrC, being a high temperature ceramic, forms low refractory oxides at lower temperatures of 500-600ºC. In order to develop core/shell materials by coating the ZrC surface with another material that forms protective layers on ZrC and prevents it from oxidation (such as SiC), there is the need to study and characterize the oxidized layer. We have used XPS, ToF-SIMS, TEM-ED and EDX analysis to study the oxidized layer and polycrystalline ZrO$_2$(mainly cubic phase) was identified. Some traces of the tetragonal phase are observed to be present as shells around the ZrC particles with a thickness of about 4 nm on the average. Periodic DFT was subsequently used to characterize the interface formed between ZrC(100) and *c*-ZrO$_2$(001) phases. A strong interface is formed mainly with charge transfer from Zr (c-ZrO2 side) at the interface to O and C (ZrC side) atoms at the interface. The interfacial properties are local to only the first and second layers of ZrO$_2$ and not on the third and fourth layers of ZrO$_2$ as Bader charge analysis revealed substantial charge transfer at the interface region with no charge redistribution in the second ZrO$_2$ layer and subsequent bulk layers. The main physical quantity, ideal work of adhesion (W_{ad}) used to characterize the interface remains fairly constant for all ZrO$_2$ layers and converges at three layers of ZrO$_2$. The interfacial bonds formed are observed to be stronger than the free surfaces in the corresponding ZrC and *c*-ZrO$_2$ used to generate the interface.

1 Introduction

One important transition metal carbide (TMC) known for its excellent physico-chemical and structural properties is Zirconium Carbide (ZrC). Being an Ultra High Temperature Ceramic (UHTC) with extremely high melting points of 3430 ºC, it is used in applications involving harsh conditions such as coatings of the inside walls of nuclear plants, hard materials like cutting tools and in the aerospace industries as nozzle flaps.[1,2]

ZrC belongs to the Fm3m space group, is a face centered cubic crystal and crystallizes in a NaCl crystal structure type.[3] It has three distinguishable low index surfaces with stabilities in the order of (100) > (111) > (110).[4,5]

Despite its excellent mechanical and physical properties, its use in extreme corrosive and oxidizing environments is limited. This is due to the fact that ZrC forms low refractory oxides at temperatures of around 500-600 ºC.[6] Several studies have been carried out on the different oxidation processes on the ZrC low index surfaces. A considerable amount of research has been done on the oxidation of the ZrC(111) surface, both experimental and theoretical.[7–10] (our oxidation paper under review). All these studies have shown very strong interaction of oxygen with the ZrC(111) surface. Oxygen is found to adsorb disscociatively as atomic oxygen and sits at three-fold hollow fcc sites between three surface Zr atoms. This adsorption process is found to be accompanied by extremely high reaction energies. (our oxidation paper under review).

In an experimental study on the oxidation of ZrC single crystals, ZrC crystals were oxidized isothermally at temperatures of 600-1500 ºC in a mixed atmosphere of O$_2$ and again with O$_2$ partial pressures of 0.02-2 kPa for 1-20 hours. Preferred orientation of tetragonal or monoclinic ZrO$_2$ were occasionally observed on the ZrC surfaces.[11] The authors further analyzed XRD patterns on the crystal oxidized at 600 ºC for one hour and PO$_2$ = 2 kPa showed the presence of cubic ZrO$_2$ together with the substrate ZrC. Subsequent XRD analysis showed a preferred (110) or (200) orientations of *t*-ZrO$_2$ or a preferred (200) or (220) orientation of m-ZrO$_2$ on oxidation of the (200) or (220) planes of a ZrC crystal respectively. In another work, a crystallographic relationship such as the (200) and (220) planes of ZrC being parallel to the (200) and (220) c-ZrO$_2$ is established at the ZrC/ZrO$_2$ interface.[12]

Even though there is not much work done on the oxidation process on the ZrC (110) surface, both experimental and theoretical, in a recent paper, a complete discussion on the adsorption process and mechanism of oxidation is provided.[13] The (110) surface is observed to adsorb oxygen dissociatively and leads to subsequent formation of a layer of ZrO$_2$ on the surface with the release of CO_2 into the gas phase. (Oxidation paper under review). This work complements the other oxidation studies done on the ZrC(100) and (111) surfaces.

Several studies have been reported on the adsorption and oxidation of ZrC(100) surface.[14–18] (our oxidation paper under review). Different accounts on a variety of oxidation processes are reported for the ZrC(100) surface. Theoretical studies have shown dissociative adsorption of oxygen into atomic species sitting at mmc sites (between two surface Zr atoms and one carbon atom).[16,18,19] In some of these reports, not only did the mode of oxygen adsorption alone studied but also the mechanism for subsequent exchange of adsorbed O atoms and surface C atoms with final removal of CO.[16,17,19]

In another report, the oxidation of ZrC(100) surface led to the formation of a ZrO-like layer in the form of ZrO_x $(1 < x < 2)$.[15] Details of the electronic structure of this oxidized layer (ZrO-like layer) are also reported in another paper.[20]

In a separate work, oxidation of the ZrC(100) surface led to the formation of c-ZrO_2 (200) on the ZrC facets.[12]

We have however carried out experimental measurements on ZrC nanocrystallites. We observed the presence of another phase coating the ZrC particles and TEM-ED measurements showed the presence of ZrO_2, mainly cubic ZrO_2. The *c*-ZrO_2 facets identified were (111), (002), (022) and (113) while *t*-ZrO_2 (101), (103) and (112) facets were also identified. Moreover, subsequent d_{hkl} indexation showed the *c*-ZrO_2 facets as predominant on the substrate ZrC.

In light of the above stated observations on the formation of ZrO_2 on the ZrC surfaces, it is necessary to study the structure, stability and energetics of the ZrC(100)/*c*-ZrO_2 interface.

The paper is organized as follows: Section 2 describes experimental conditions and setup for analyzing the ZrC particles. Section 3 describes the theories, methods and procedures used in this study. In section 4.1, we describe the results of the experiments carried out while section 4.2 discusses the results from molecular dynamics simulation of ZrO_2 growth on the ZrC(100) surface. Section 4.3 to 4.5 discusses the bulk, surface, interfacial strength, thermodynamic and electronic properties at the interface. Eventually, section 5 provides summary and conclusions on the current work.

2 XPS, ToF-SIMS and TEM-ED Experimental Analysis

A combination of XPS, ToF-SIMS and TEM-ED experiments were performed on the ZrC nanocrystallites to determine the nature and content of the oxidized layer.

The XPS analyses were performed using a Kratos Analytical AXIS Ultra^{DLD} spectrometer. A monochromatic aluminium source (Al Kα = 1486.6 eV) was used for excitation. The analyser was operated in constant pass energy of 40 eV using an analysis area of approximately 700 μm x 300 μm. Charge compensation was applied to compensate for the charging effect occurring during the analysis. The ZrO_2 phase O 1s (530.0 eV) binding energy (BE) was used as internal reference. Quantification and simulation of the experimental photopeaks were carried out using CasaXPS software. Quantification took into account a non-linear Shirley[21] background subtraction.

ToF-SIMS analyses were performed on a TOF.SIMS[5] instrument (IONTOF GmbhH, Münster, Germany) equipped with a 25keV bismuth primary ion source. Charging effect due to the primary ion beam was compensated with pulsed low energy electrons (20 eV). Static and dynamic acquisitions were performed in negative mode with Bi_3^+ primary ions. For static mode, a tableted powder was used to give better mass resolution and secondary ion yield. Negative and positive ToF-SIMS spectra were compared with a reference of ZrO_2. Dual beam mode was used for depth profiling. Cs^+ (0.5kV and 1kV) were used for sputtering in the non-interlaced mode and also to obtain low energy depth profiling on the ZrC to characterize the ZrO_2 surface layer.

TEM-ED experiments were performed on the ZrC particles to obtain the crystalline nature. A dry powder deposition on Cu grid with carbon film was used.

3 Calculation Scheme and Structural Models

3.1 General Interface Computational Details

All parameters used for the interface calculations are based on optimized parameters for the ZrC substrate.

We performed all theoretical calculations with the Vienna ab initio Simulation Package (VASP)[22] which is based on Mermin's finite temperature DFT.[23] For the Zr, O, H and C atoms, the electronic configurations used are $[Kr]4d^25s^2$, $[He]2p^6$, $1s^1$ and $[He]2s^22p^2$ respectively. The Projected Augmented Wavefunction (PAW) pseudopotentials[24] were used for representing the core electrons and the core part of the valence electrons wavefunctions. This helps to reduce the number of planewaves required to describe the electrons close to the nuclei. For the exchange correlation functional, the generalized gradient approximation (GGA) parameterized by Perdew, Burke and Ernzerhof (PBE)[25] was used and the Methfessel-Paxton,[26] smearing scheme was used by setting the gamma parameter to 0.1 eV. An optimized energy cut-off of 500 eV was used for the plane wave basis set in describing the valence electrons while the integration of the Brillouin zone was performed with a standard Monkhorst-Pack[27] special grid of 9 x 9 x 9 k-points for the bulk and 9 x 9 x 1 k-points for surface and interface calculations. The self-consistent field (SCF) procedure for resolution of the Kohn-Sham equations is assumed to be converged when energy changes of 1×10^{-4} eV between two successive iterations are reached.

3.2 Finite Temperature Molecular Dynamics

We performed finite temperature molecular dynamics to confirm the ZrO_2 phase formed on the ZrC surfaces as evidenced by the XPS, TOF-SIMMS and TEM-ED experiments. A (2 x 2) supercell was used for all MD simulations. This simulation was started with a thick layer of ZrC (100) surface slab while enough Zr and O atoms were deposited on the exposed ZrC surface to form about two layers of ZrO_2. Within the micro canonical ensemble, the ions were initially kept at T = 100 K and the velocities scaled upwards at different steps until a final temperature of 1000 K was reached. This temperature was selected to allow for the possibility of forming of the *m*-ZrO_2 phase which is stable at low temperatures below 1450 K. A time step of 1 fs was used. The resulting equilibrium structure was then quenched from

1000 K to 500 K and the final resulting structure was optimized at higher precision of calculation.

3.3 Bulk Phases of ZrC and ZrO_2

In order to facilitate discussions of the electronic and mechanical properties of the interfacial structure model used, we provide a brief discussion of the major characteristics of bulk electronic structure of ZrC and ZrO_2.

Cubic ZrC belongs to the *Fm3m* space group, crystallizes in an fcc structure and has two special atomic positions for Zr and C at (0 0 0) and (0.5 0.5 0.5) respectively as shown in figure 1. It has an experimental lattice parameter of 4.696 Å[28]. Details on calculation of optimized bulk parameters are found elsewhere.[18] In optimizing the geometrical structure, the positions of all ions were relaxed in order to render the net forces acting upon them smaller than 1 x 10^{-2} eV/Å. The lattice parameter for the ZrC bulk was optimized by fitting the energy vs volume curve against the Murnaghan's equation of state as detailed in our previous work.[18] Thus the optimized lattice parameter was calculated as 4.736 Å and this is less than 1% of the experimental value, typical of GGA functionals.[18]

All ZrC and ZrO_2 bulk calculations involved cells with 4 formula units (Figure 1).

The c-ZrO_2 has a $Fm\bar{3}m$ crystal structure. Starting from the experimental crystallographic positions, the volume of the cell was decreased and increased by about 10% and the resulting total energy calculated. The pairwise calculated values of volume and energy were fitted using the Murnaghan's equation of state.

The tetragonal ZrO_2 (t-ZrO_2) has the tetragonal symmetry $P4_2/nmc$ and only differs from the cubic phase in the small alternating distortion of the O atom columns along the 4_2 axes in the [001] direction. Compared to the *c*-ZrO_2, there is also a small elongation of the *c* lattice parameter along the [001] direction. Since optimizing the *c*-ZrO_2 structure along the c axis results in distortion of the O atoms in the perpendicular direction and subsequently yielding a tetragonal structure, we calculate lattice parameters for *t*-ZrO_2 as well. Optimization of the lattice parameter was started from the experimental cell with a = 3.596 Å and c = 5.187 Å[29] and the energy vs volume data fitted with the Murnaghan's equation of state.

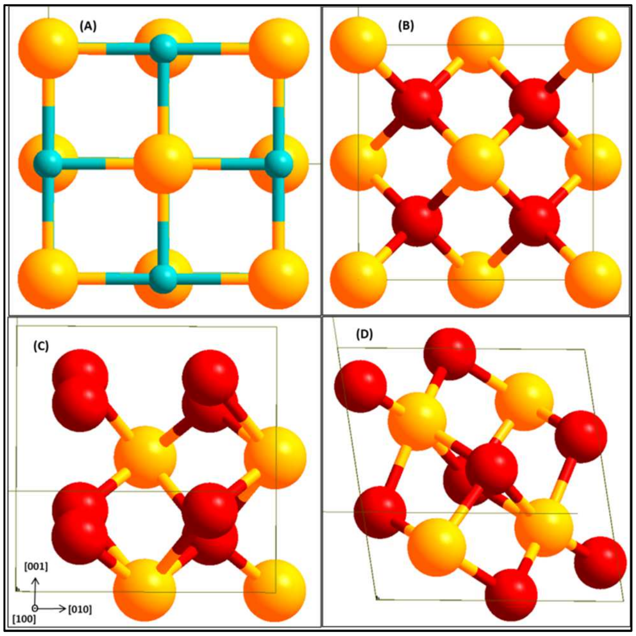

Figure 1. Bulk structures of ZrC(A), *c*-ZrO_2(B), *t*-ZrO_2(C) and *m*-ZrO_2(D). Yellow(Zr), light blue(C) and red(O).

The monoclinic ZrO_2, m-ZrO_2 belongs to the space group *P21/c*. This phase is also defined by another parameter, the angel β with an experimental value of 99.23°. Starting from experimental lattice parameters determined by Yashima et.al,[30] we calculated energies at different volumes and fitted the data with the Murnaghan's equation of state.

3.4 Construction of Interface Model

In developing an interface from two different bulk phases, a step by step approach is taken. An initial determination of the stacking direction at the interface needs to be selected and from this identified interface plane, the two different bulk phases should have a proper commensurability factor.[31] The two bulk phases are then cleaved to reveal the selected surfaces for the interfacial structure. These surfaces will have different terminations of different atomic layers. The two surfaces are then brought together in contact with each other to form the interfacial structure which is then fully relaxed to obtain the final optimized configuration at the interface.

3.4.1 Surface structures and commensurate phases

The different low index surfaces of ZrC have been extensively studied. The (100) surface is found to be the most stable compared to the other surfaces due to it being stoichiometric and non-polar.[4,5,18] With its lattice parameter of 4.736 Å, this surface has an exposed surface area of 22.468 $Å^2$. The ZrC(100) bulk phase is used as the substrate onto which the ZrO_2 is grown. Different studies have been made on the stability of the different surfaces of c-ZrO_2.[32,33] The c-ZrO_2 (111) surface is the most stable followed by the (110) and then the (100) surface for both relaxed and unrelaxed surfaces. In this work, we calculate the surface energies for 1 layer up to 6-

layers of ZrC. The surface energies are calculated with the expression $E_{surf} = (1/2A)\ [E_{slab} - nE_{bulk}]$ where E_{slab} is the total energy of the surface slab, E_{bulk} is the energy per formula unit of ZrC or ZrO_2 in the corresponding bulk, A is the surface area and n is the number of formula units in the surface slab.

Surface energies are calculated for the (001) terminations of *c*-ZrO_2, *t*-ZrO_2 and *m*-ZrO_2. The surface energies were calculated for different layers of ZrO_2 starting from 1 layer up to 6 layers of ZrO_2. These surface energies are needed to calculate the interface tension defined in section 3.4.3.

The c-ZrO_2 (001) surface can have different sequence of layering at the terminated surface. As can be seen in figure 1, it can be considered terminating as Zr|OO|Zr|OO|Zr|OO….. and in this case half of the oxygen atoms are located behind the front oxygen atoms on the same plane. The termination can be flipped to get another one. Another termination that can be built is O|Zr|OO|Zr|OO|Zr|O…. termination. With this configuration, oxygen layers terminate both exposed surfaces. Thus three different surface terminations can be used for building an interface with the ZrC(100) surface. A Zr-terminated, O- terminated or OO- terminated surface of c-ZrO_2 (001) can be used for the interface structure.

A problem which arises in interfacial studies is making two different phases commensurate with each other. This interface coherence requirement is as a result of the periodic boundary conditions used in the calculations at the interface. Thus a unit cell for the interface structure has to be selected. One geometrical principal measure used in ensuring this commensurability is the surface mismatch parameter ϒ.[34] With this measure, a surface unit cell of *c*-ZrO_2 with area of S_2 is coherently forced onto a substrate ZrC (100) surface with a surface unit cell of area S_1 (Figure 2). The mismatch parameter is then calculated as:

$$\Upsilon = 1 - \frac{2S_{1-2}}{S_1 + S_2} \ldots\ldots\ldots.eq.(1)$$

S_{1-2} is the overlapping area between the two commensurate surfaces (Figure 1). This misfit parameter does not measure an area mismatch but rather an average length scale misfit between the two unit cells.[35] Table 1 shows the calculated mismatch parameters for the different *c*-ZrO_2 surfaces on ZrC(100) surface using ZrC lattice parameter of 4.736 Å and c-ZrO_2 lattice parameter of 5.143 Å. It is obvious that the lattice mismatch for all c-ZrO_2 surfaces on the ZrC(100) surface is less than 40%. Thus from this table, it suddenly becomes apparent that the ZrC(100)||c-ZrO_2(001) interface combination choice with a misfit parameter ϒ of 8.2% is acceptable. This interface unit cell which is defined by the substrate ZrC(100) phase is cubic, small, 4.736 Å x 4.736 Å and can be easily managed.

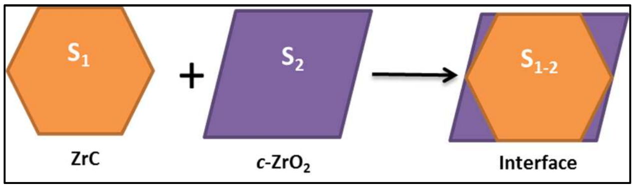

Figure 2. Bulk structures of ZrC(A), *c*-ZrO_2(B), *t*-ZrO_2(C) and *m*-ZrO_2(D)

Table 1. Surface mismatch parameter ϒ calculated for different combinations of ZrC and c-ZrO_2 surface

ZrC	c-ZrO_2	Overlap area(S_{1-2})/$Å^2$	Misfit (ϒ)
(100)	(001)	22.434	0.082
(100)	(110)	22.434	0.250
(100)	(111)	22.400	0.279

This mismatch parameter which is a geometrical measure cannot be used alone in building the interface structure. Other models and factors need to be considered. Two different methods for ensuring commensurability of two different phases can be found in the literature. In the first approach, sufficiently large unit cells of both phases are used. Thus the basic unit cells of each of the two different phases are increased in size in a subsequent manner until the two phases are commensurate with each other. This approach leads to interfacial structures with very small mismatch parameters and still some incoherent areas at the interface.[36] The interface models formed in this approach are however too huge and not suitable for ab initio methods.

In the second approach which is used in many interface calculation studies[37–42], a single unit cell is used at the interface plane and it is generally termed as the (1 x 1) model. One phase is considered as the substrate, its lattice parameters are used, the lattice parameters of the other phase are scaled until a perfect matching of the two lattice phases is obtained. This method is suitable for interface models with very little mismatch parameter and we adopt this approach for the current study.

3.4.2 Interface Model Geometry

A slab geometry model was used to study the interfacial structure and properties. The ZrC phase was selected as the substrate with a thickness of 10.945 Å thick which corresponds to 9 layers of ZrC. The selected substrate thickness is considered enough to form the required interfaces and also mimic electronic structure with ionic relaxations in the bulk ceramic.[33] The c-ZrO_2 units were then pinned onto the ZrC (100) exposed surface, layer by layer. Coherent interfaces were thus ensured by straining the c-ZrO_2 (001) units to match the dimensions of the ZrC(100) surface. Thus the bulk parameter and surface area of the ZrC(100) unit cell defines the interface structure model unit cell. In doing so, the c-ZrO_2 (001) unit cell lattice parameter is shrunk by about 8.6% relative to the equilibrium lattice of 5.143 Å. In fixing the orientation of the geometries of the two lattices at the interface, the remaining degrees of freedom in the final interface geometry after optimization is the perpendicular direction to the interface as well as the chemical composition of the interface.[43] Up to 5 layers of the *c*-ZrO_2 (001) units were built on the ZrC(100) surface.

Figure 3 shows side views of the different interface models used.

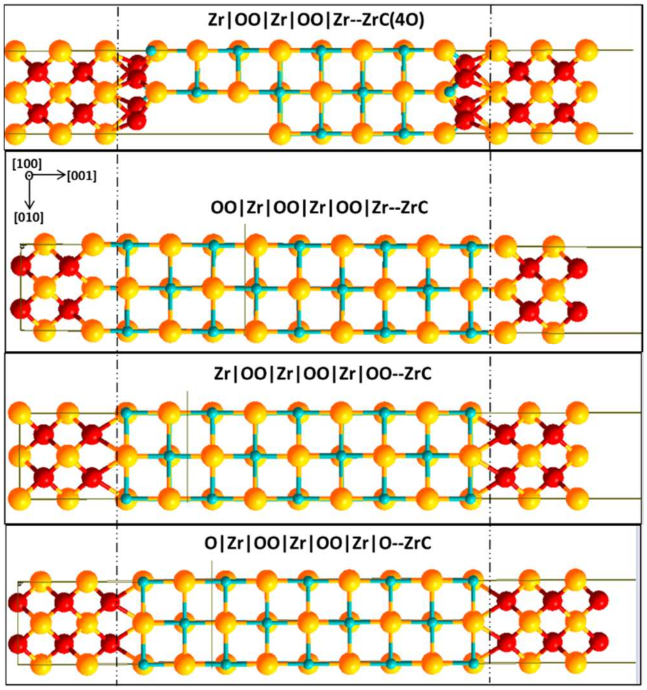

Figure 3. Interface structure models. Vertical dashed lines pass through bonds formed at the interface. Yellow(Zr), light blue(C), red(O)

Each *c*-ZrO_2 bilayer unit is approximately 3.5 Å thick. We ensured that all the models used are symmetric with respect to the center of the interface structure. This is done in order to ensure no long range dipole-dipole interaction between exposed surfaces of the interface slab. Thus each interface slab contains two identical interfaces. A vacuum of more than 13 Å was applied between two subsequent interface slabs in order to avoid any physical interactions between the slabs. Thus the interface slab configuration has a sequence of --- *c*-ZrO_2(001)||ZrC(100)||*c*-ZrO_2(001)|vacuum| *c*-ZrO_2(001)||ZrC(100)||*c*-ZrO_2(001)|vacuum| *c*-ZrO_2(001)||ZrC(100)||*c*-ZrO_2(001)|vacuum| *c*-ZrO_2(001) --

The ZrC(100) surface has a single layer terminating with the same number of Zr and C atoms. This surface is very compact and hence the interface chemical composition is defined by the terminating layer of the *c*-ZrO_2(001) phase. Along the [001] direction of bulk *c*-ZrO_2, three different terminations, Zr|OO|Zr|OO|Zr|OO-, O|Zr|OO|Zr|OO|Zr|O-, OO|Zr|OO|Zr|OO|Zr- and hence three different interface models can be built from these as shown in figure 3. Moreover, in a previous study[13], the oxidation of ZrC(100) surface led to the adsorption of 4 oxygen atoms on the surface, resulting in a full layer coverage. The synthesis of ZrC is mostly carried out in an oxidizing environment. It is therefore necessary to build another model with an oxidized ZrC(100) surface. Thus the fourth interface model consists of *c*-ZrO_2(001) terminating on both sides with Zr atoms on an oxidized ZrC(100) surface as shown in figure 3.

3.4.3 Interface Cohesion and Mechanics

An important parameter used in defining interface cohesion and stability is the interface tension γ_{int}, defined as the reversible work needed to separate the interface into two free surfaces.[44] With this definition, both plastic and diffusional degrees of freedom are assumed to suppressed and hence negligible. From this definition, the greater the γ_{int} value, the higher the energy needed to separate the two surfaces at the interface.

According to the Dupre equation, the interface tension can be defined in terms of the interface and free surface energies as[45,46]:

$$\gamma_{int} = \sigma_{ZrC} + \sigma_{c-ZrO_2} - \sigma_{ZrC||c-ZrO_2} \ldots\ldots eq.(2)$$

σ_{ZrC} and σ_{c-ZrO_2} are the relaxed surface energies of the ZrC and *c*-ZrO_2 surfaces respectively while $\sigma_{ZrC|c-ZrO_2}$ is the interface energy which is also defined as the adiabatic work of adhesion, $W_{ad} > 0$. Thus the relative strength of the interface versus the bulk bonds decides the preference for the interface formation or the open surfaces.[47] The adiabatic work of adhesion is defined as:

$$W_{ad} = \frac{E^{tot}_{ZrC} + E^{tot}_{c-ZrO_2} - E^{tot}_{ZrC||c-ZrO_2}}{2A} \ldots.eq.(3)$$

Where E^{tot}_{ZrC} *and* $E^{tot}_{c-ZrO_2}$ refers to the total energies of the full relaxed isolated ZrC and *c*-ZrO_2 slabs. $E^{tot}_{ZrC||c-ZrO_2}$ is the total energy of the fully relaxed interface slab and A is the interface area. The calculated W_{ad} value is usually a lower bound of values obtained by cleavage experiments due to dissipative processes in physically separating the interface.[44] Characterization of the interfacial strength is unrelated to the bulk strain in the deposited *c*-ZrO_2 and hence the $E^{tot}_{c-ZrO_2}$ value used is the total energy of the strained *c*-ZrO_2 in order to commensurate with the ZrC surface. Thus the strain energy component is cancelled between $E^{tot}_{c-ZrO_2}$ and $E^{tot}_{ZrC||c-ZrO_2}$ since the c-ZrO_2 is in the strained state.[47]

Another important parameter is the rigid work of adhesion, W^{rigid}_{ad} which provides maximum cancellation of the strain energy from the interface energy obtained.[43] This can be achieved by ensuring the same strain state exists in both the free surfaces and the interface. This quantity is very useful in comparing the stability of the various interfaces with respect to cleaving from the two different phases. This quantity is the only measure which holds information purely on the bonding at the interface irrespective of the free surfaces.[43] W^{rigid}_{ad} is calculated by rigidly cleaving the relaxed interface structure to produce the free surfaces and not allowing the free surfaces to fully relax.

The interface tension can be used to provide a measure of whether the interface formation or the formation of the free individual surfaces are preferred. The sign and magnitude of γ_{int} in equation 2 also provides a measure for whether the interface bonds are stronger than the internal bonds in each separate phase.[47] In this case, $0 < \gamma_{int} < \sigma_{ZrC} + \sigma_{c-ZrO_2}$ corresponds to weakly coupled interface and $\gamma_{int} < 0$ to strongly coupled interfaces. The calculated values of

σ_{ZrC} *and* σ_{c-ZrO_2} are obtained from their respective relaxed equilibrium bulk phases (strain free *c*-ZrO_2 (001) surface).

3.5 Interfacial Thermodynamic Stability

An assessment of the thermodynamic stabilities of the different interface models are carried out. In this manner, the thermodynamic stability of the three different models of c-ZrO2 on ZrC are assessed using the excess interface grand potential, $\Omega_{int}^{i/j}$ of an overlayer *j* on a substrate *i*, with respect to the ZrC and c-ZrO2 bulks as reference instead of the surface slabs. The excess interface grand potential is calculated as follows:

$$\Omega_{int}^{i/j} = \frac{1}{2}\left[\Omega_{slab}^{i/j} - N_{ZrC}\Omega_{ZrC} - N_{ZrO_2}\Omega_{ZrO_2}\right] - \Omega_{ZrO_2}^{surf} \;\ldots.eq.(4)$$

$\Omega_{ZrO_2}^{surf}$ is the surface grand potential of the exposed ZrO2 side of the interface slab which is in contact with the external environment. Assuming no temperature and pressure contributions to the grand potentials, the remaining bulk grand potentials can be defined as:

$$\begin{cases} \Omega_{slab}^{i/j} = E_{slab}^{i/j} - \sum_k N_k\mu_k \\ \Omega_{ZrC} = E_{ZrC}^{bulk} - \mu_{ZrC} \\ \Omega_{ZrO_2} = E_{ZrO_2}^{bulk} - \mu_{ZrO_2} \end{cases} \;\ldots..eq.(5)$$

N is the number of each chemical specie in the slab and μ is the corresponding chemical potential of that specie. E_{ZrC}^{bulk} *and* $E_{ZrO_2}^{bulk}$ are the total bulk energies of ZrC and ZrO_2 respectively. When the systems are in thermodynamic equilibrium, the chemical potentials of ZrC and ZrO_2 can be written as: $\mu_{ZrC} = \mu_{Zr} + \mu_C$ *and* $\mu_{ZrO_2} = \mu_{Zr} + 2\mu_O$. Substituting these with equation 5 into equation 4 with further rearrangements, we obtain the following equation:

$$\Omega_{int}^{i/j} = \frac{1}{2}\Big[E_{slab}^{i/j} - N_C E_{ZrC}^{bulk} - N_{ZrO_2}E_{ZrO_2}^{bulk} - \mu_{Zr}\left(N_{Zr} - N_C - N_{ZrO_2}\right) - \mu_O\left(N_O - 2N_{ZrO_2}\right)\Big] - \Omega_{surf}^{ZrO_2} \;\ldots\ldots\ldots eq.(6)$$

If we define a change in chemical potential related to the reference stable bulk Zr ($\Delta\mu_{Zr} = \mu_{Zr} - \mu_{Zr}^*$ with $\mu_{Zr}^* = E_{Zr}^{bulk}$) and O_2 gas ($\Delta\mu_O = \mu_O - (E_{O_2}^{Gas}/2)$) and substitute these in equation 6, we obtain the following equation:

$$\gamma_{int}^{i/j} = \frac{\Omega_{int}^{i/j}}{A} = \emptyset_{int}^{i/j} + \frac{1}{2A}\Big[\Delta\mu_{Zr}\left(N_C + N_{ZrO_2} - N_{Zr}\right) + \Delta\mu_O\left(2N_{ZrO_2} - N_O\right]\ldots eq.(7)$$

Where the interface dependent term $\emptyset_{int}^{i/j}$ is defined as:

$$\emptyset_{int}^{i/j} = \frac{1}{2A}\left[E_{slab}^{i/j} - N_{ZrC}E_{ZrC}^{bulk} - N_{ZrO_2}E_{ZrO_2}^{bulk} - E_{Zr}^{bulk}\left(N_{Zr} - N_C - N_{ZrO_2}\right) - \frac{E_{O_2}^{Gas}}{2}\left(N_O - 2N_{ZrO_2}\right)\right] - \gamma_{ZrO_2}^{surf}\,..eq.(8)$$

$\gamma_{ZrO_2}^{surf}$ is the surface energy of the exposed ZrO_2 surface to vacuum. The interface grand potential is dependent on the chemical potential of oxygen and zirconium. The upper limit of the chemical potentials are defined with respect to the total energy of bulk Zr and molecular O_2 while the lower limit is with respect to the formation energy of ZrO_2. The limits are defined in equations 9 and 10 as:

$$\begin{cases} \Delta\mu_O = \mu_O - \frac{E_{O_2}^{Gas}}{2} < 0 \\ \Delta\mu_O > \frac{E_{ZrO_2}^{f}}{2} \end{cases} \;\ldots\ldots.eq.(9)$$

$$\begin{cases} \Delta\mu_{Zr} = \mu_{Zr} - \mu_{Zr}^* < 0 \\ \Delta\mu_{Zr} > {}^1\!/_2\left(E_{ZrC}^{f} + E_{ZrO_2}^{f}\right) \end{cases} \;\ldots\ldots.eq.(10)$$

$E_{ZrO_2}^{f}$ is the formation energy of ZrO2, calculated as -4.98 eV and E_{ZrC}^{f} is the formation energy of ZrC. Thus the chemical potential ranges are $-5.78\,eV < \Delta\mu_{Zr} < 0$ and $-4.98 < \Delta\mu_O < 0$. A plot of $\gamma_{int}^{i/j}$ against $\Delta\mu_O$ and$\Delta\mu_{Zr}$ is obtained and the stabilities of the different interface models are analyzed.

4 Results and Discussion

4.1 XPS, ToF-SIMS and TEM-ED Experiments

The XPS analysis of $ZrC_{0.96}O_{0.04}$, summarised in Table 2, reveals that the surface is contaminated by adventitious carbon (C 1s Binding Energy, BE = 284.5 eV) and Zr oxide (Zr 3d BE = 182.3 eV).

Table 2. XPS characterization of $ZrC_{0.96}O_{0.04}$

Element	Binding energy (eV)	FWHM (eV)	Proportion (%)	Atomic concentration (%)
Zr $3d_{5/2}$ (ZrC)	178.8	1.1	57	25.3
Zr $3d_{5/2}$ (ZrO_2)	182.3	1.3	43	
O 1s (ZrO_2)	530.0	1.7	46	45.2
O 1s	531.7	1.7	54	
C 1s (ZrC)	281.1	0.9	44	26.9
C 1s	284.5	1.6	56	

S 2p (elemental)	162.1	2.1	37	2.6
S 2p (sulfates)	168.9	2.1	64	

The XPS analysis of $ZrC_{0.96}O_{0.04}$ clearly evidences the presence of two different chemical environments for zirconium with the observation of two doublets in the Zr 3d spectral region that are attributed to ZrC (Zr $3d_{5/2}$ BE = 178.8 eV)[48,49] and ZrO_2 (Zr $3d_{5/2}$ BE = 182.3 eV) (Figures 4 and 5). The decomposition of Zr 3d spectrum is performed using line shapes derived from data[50] of bulk reference materials of ZrO_2 and ZrC. The methodology consists in, on one hand by exposing $ZrC_{0.96}O_{0.04}$ to oxygen at 500°C for 1 h in a dedicated cell coupled to the XPS spectrometer then transferred into the XPS analysis chamber avoiding contamination.

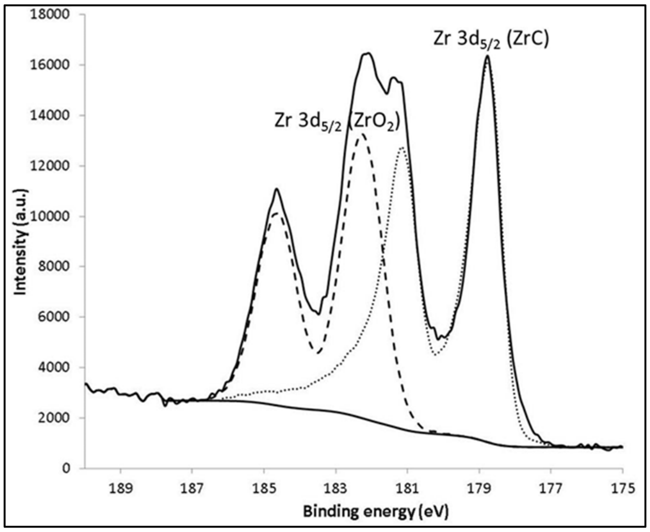

Figure 4. Decomposition of Zr 3d XPS spectrum for $ZrC_{0.96}O_{0.04}$ using line shapes defined from ZrO_2 and ZrC phases

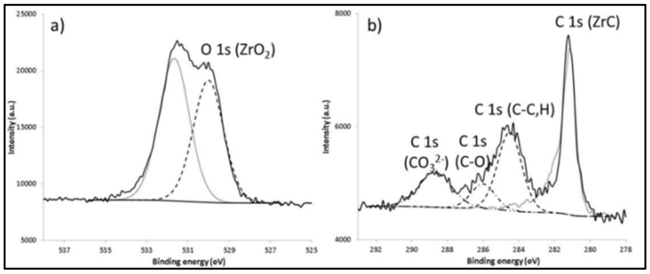

Figure 5. O 1s (a) and C 1s (b) XPS spectra for $ZrC_{0.96}O_{0.04}$

The oxidative treatment leads to the complete oxidation of the material into ZrO_2 (atomic Zr/O ratio of 0.5). On the other hand, the initial $ZrC_{0.96}O_{0.04}$ material was pressed into a pellet in order to operate an Ar^+ depth profile (2 keV, 3 mm x 3 mm). An extended (30 min) ion depth profile leads to the disappearance of the ZrO_2 contribution in Zr 3d region and to the appearance of asymmetric Zr 3d and C 1s photopeaks, characteristic of the metallic character of ZrC (atomic Zr/C ratio of 1.2). The atomic Zr / C ratio, calculated from the Zr 3d (ZrC) and C 1s (ZrC) contributions, is equal to 1.1, in good agreement with the expected ratio in ZrC phase. Furthermore, the atomic Zr / O ratio, calculated from the Zr 3d (ZrO_2) and O 1s (ZrO_2) components, is 0.6, close to the theoretical Zr / O ratio in ZrO_2 phase.

On the other hand, the ZrO_2 layer thickness (d_{ZrO_2}) can be evaluated using a homogenous and continuous layer model[51] of intensity attenuation in which the $\frac{I_{Zr\,3d\,(ZrO_2)}}{I_{Zr\,3d\,(ZrC)}}$ ratio is expressed as:

$$\frac{I_{Zr\,3d\,(ZrO_2)}}{I_{Zr\,3d\,(ZrC)}} = \frac{I^{\infty}_{Zr\,3d\,(ZrO_2)}\,(1-\exp(-\frac{-d_{ZrO_2}}{\lambda_{Zr\,3d\,(\rightarrow ZrO_2)}}))}{I^{\infty}_{Zr\,3d\,(ZrC)}\,\exp(-\frac{-d_{ZrO_2}}{\lambda_{Zr\,3d\,(\rightarrow ZrC)}}))}$$

where $I_{Zr\,3d\,(ZrO_2)}$ and $I_{Zr\,3d\,(ZrC)}$ are the intensities of the two respective components of the XPS Zr 3d signal of for $ZrC_{0.96}O_{0.04}$, $I^{\infty}_{Zr\,3d\,(ZrO_2)}$ and $I^{\infty}_{Zr\,3d\,(ZrC)}$ are the intensities of the XPS Zr 3d signal of ZrO_2 and ZrC reference samples (homogeneous material with infinite thickness), respectively, and $\lambda_{Zr\,3d\,(\rightarrow ZrO_2)}$ and $\lambda_{Zr\,3d\,(\rightarrow ZrC)}$ are the inelastic mean free paths of the electrons calculated from the TPP2M formula[52]. Their values are 2.2 nm. Then the ZrO_2 layer thickness (d_{ZrO_2}) is estimated to 3.2 nm.

In the static ToF-SIMS analysis, isotopic patterns detected at ZrC surface in positive mode match with ZrO_2 reference. During the dynamic SIMS depth profiling, an initial lower energy profiling showed ZrO_2^- peaks when the sputtering starts but the intensities of the ZrO_2^- and O^- peaks decrease with time. A similar pattern is observed at high energy sputtering (1kV) as shown in figure 6.

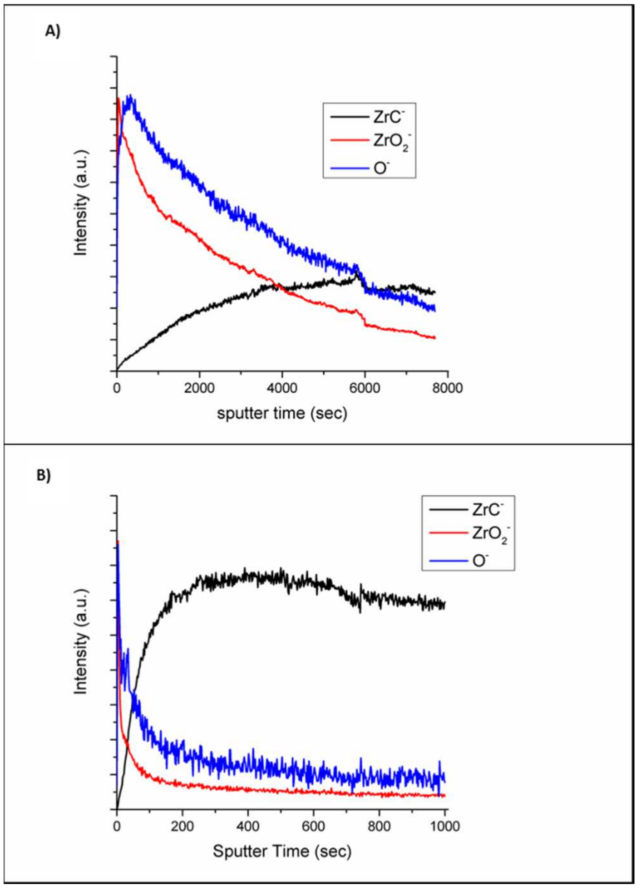

Figure 6. ToF-SIMS depth profiling with low energy (A) Cs^+ : 0.5kV – 30 nA – rastered over an area of 500µm x 500µm and high energy depth profiling (B) Cs^+: 1kV – 60 nA – rasterd over an area of 300µm

Moreover, even though the dynamic SIMS depth profile experiment was conducted under vacuum, there is still re-oxidation of the ZrC surface after some few minutes into the experiment. This is shown in figure 7 and these spectra shows that even under vacuum ($1x10^{-8}$ mbar) there is a quick re-oxidation of ZrC after Cs^+ etching. Thus the ZrC surfaces are highly reactive to oxygen as shown in several experimental[7–10] and theoretical works[13].

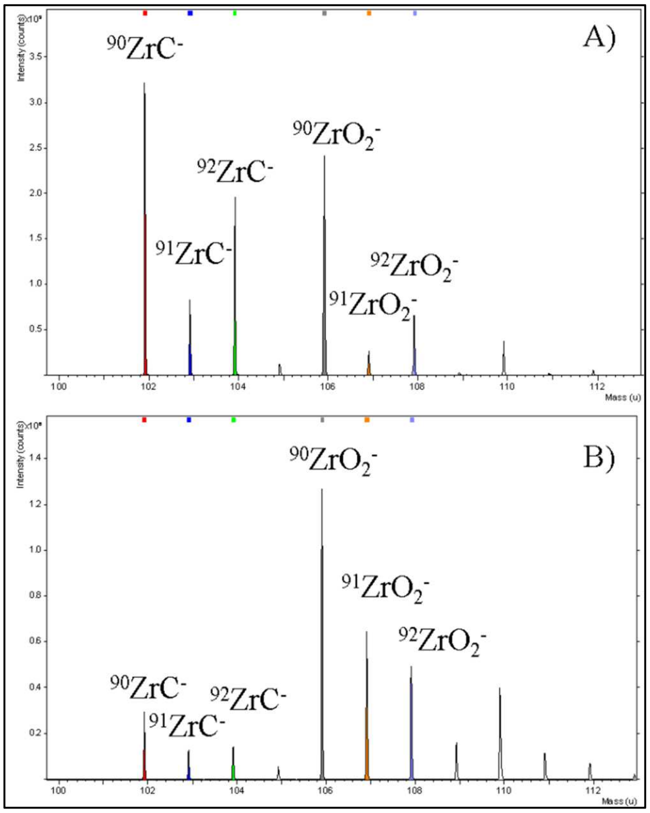

Figure 7. ToF-SIMS spectra in the m/z range (100-113). A) is a spectra acquired few seconds after a low energy depth profiling and B) is a spectra acquired about 5 minutes after low energy depth profiling.

The TEM-ED experiment revealed the presence of a phase different from the bulk ZrC at the particle surface. EDX elemental analysis showed this phase to be zirconium oxide (Figure 8). This oxide layer thickness was estimated to be around 5 nm. According to high resolution imaging, orientations are clearly observed. This reflects that the oxide layer is crystalline. Two different areas were observed to show different crystal orientations (Figure 9A). Thus the oxide is polycrystalline. Rings were observed from the diffraction pattern obtained from the oxide layer and this confirms the surface thin layer of oxide to be polycrystalline. A d_{hkl} indexation shows no possible correlation of the diffraction pattern with ZrC phase (Figure 9B). According to the lattice parameters calculated, there is no presence of monoclinic ZrO_2 but predominant amounts of cubic ZrO_2 and some traces of tetragonal ZrO_2.

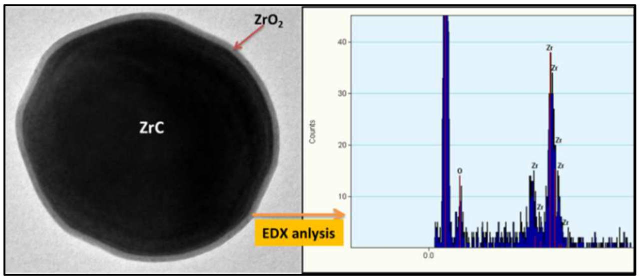

Figure 8. TEM and EDX identification of Zirconium Oxide on ZrC particles

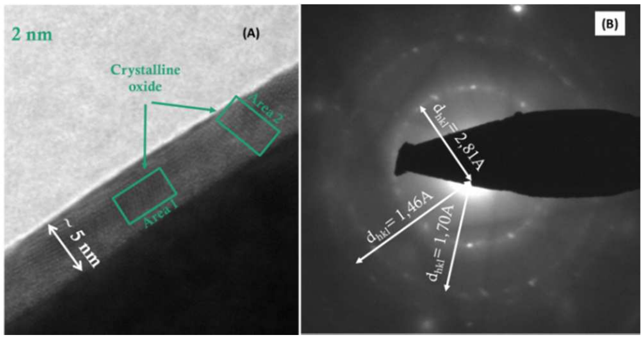

Figure 9. ED pattern and d_{hkl} indexation of Zirconium Oxide layer on ZrC particle surface

4.2 Finite Temperature MD

A brief discussion of the results obtained during the finite temperature MD simulations is provided here. At the higher temperature of 1000 K, there is a haphazard formation of ZrO_2 on the ZrC surface. Different coordinated O and Zr atoms are observed. Both 4- fold and 3- fold coordination are detected for O atoms while 5- fold and 6- fold coordination observed for Zr atoms. At the interface, all ZrO2 Zr atoms sit directly atop surface C atoms of ZrC and O atoms from ZrO_2 form mixed type of bonding at the interface. Some O atoms bond directly on top surface Zr atoms of ZrC while some O atoms forms a three- fold bond between two surface Zr atoms and a C atom of ZrC, as previously observed in other calculations on the oxidation of ZrC(100) surface.[18] The under coordinated O and Zr atoms at this stage are typical of *m*-ZrO_2.

Upon quenching the structure at 500 K temperature, a more ordered structure was obtained. 8- fold Zr and 4- fold O atoms are observed in the ZrO_2 structure formed, typical of t- and c-ZrO_2 as confirmed by the experimental results above.

4.3 Bulk and surface properties of ZrC and ZrO_2

Details of the optimized lattice parameter, bulk modulus and the pressure derivative of the bulk modulus for ZrC bulk phases are provided elsewhere.[18] Here, we consider optimized parameters for all three phases of ZrO_2.

Thus all characteristic bulk parameters needed to define all three ZrO_2 phases are well reproduced. Details on the lattice and bulk parameters are found in supporting information S.1. A summary of the bulk lattice parameters for ZrO_2 is provided in table S.1 (see supporting information).

The calculated surface energies for different layers of ZrC and all phases of ZrO_2 are summarized in table 3. For ZrC (100) surface, the surface energy quickly converges from 2 layers upwards and computed surface energy is in very good agreement with previous calculations.[4] A plot of the surface energies at different layers is shown in figure 10. It is obvious from table 3 that the surface energy converges after 4 layers for both *c*-ZrO_2 (001) and *m*-ZrO_2 (001) surfaces. The unrelaxed surface energy of 0.252 eV/ Å^2(not shown in table 3) is in very good agreement with other values of 0.222[32] eV/ Å^2. The surface energy of the relaxed structure is however 0.130 eV/ Å^2, about half of the unrelaxed structure. It is worth mentioning however that we only used stoichiometric surfaces with O terminations on both surfaces as this is found to be the predominantly exposed termination.[32] Relaxation in the c direction of the *c*-ZrO_2 surface resulted in distortion of the O atom positions along the *c*- axis.

The unrelaxed surface energy of the monoclinic (001) is 0.150 eV/ Å^2 and is in excellent agreement with the LDA calculated value of 0.152[33] eV/ Å^2 and the GGA value of 0.123[53] eV/Å^2. Upon relaxation, the surface energy quickly converges to a value of 0.100 eV/ Å^2 after 4 layers. This is also in very good agreement with the LDA calculated value of 0.113[33] eV/ Å^2 and the GGA value of 0.084 eV/Å^2.[53]

An oscillating feature is observed for the surface energies for different layers of *t*-ZrO_2 as seen in figure 10. This feature has been observed by other groups in their calculation of surface energy for different *t*-ZrO_2 layers[35]. This oscillating feature is a function of the odd/even nature of the number of layers used. Thus even numbered layers give very stable surfaces while odd numbered layers give high energy surfaces. This same feature was observed by Christensen and Carter[35]. This effect may be related to the fact that odd-layered crystalline *t*-ZrO_2 (001) surface slabs have $P\bar{4}m2$ symmetry while even-layered crystalline *t*-ZrO_2 (001) surface slabs have *Pmmn* symmetry.[35] In another study, 4- layers and 12- layers of *t*-ZrO_2 (001) surface energies were calculated to be 0.069 eV/ Å^2 and 0.070 eV/ Å^2 respectively.[54] Thus the surface energy for these even-layered slabs is the same and lower than our calculated values for the odd- layered slabs. However, our calculated surface energy for the 4- layered slab is 0.072 eV/ Å^2 and in excellent agreement with the value calculated by Eichler and Kresse[54]

Table 3. Calculated surface energies eV/Å^2 for different layers of ZrC (001), *c*-, *t*- and *m*-ZrO$_2$ (001) surfaces

Number of Layers	ZrC (001)		c-ZrO$_2$(001)		t-ZrO$_2$(001)		m-ZrO$_2$(001)	
	unrelaxed	relaxed	unrelaxed	relaxed	unrelaxed	relaxed	unrelaxed	relaxed
1 layer	0.135	0.135	0.229	0.144	0.231	0.205	0.257	0.069
2 layers	0.111	0.098	0.249	0.108	0.081	0.068	0.143	0.097
3 layers	0.108	0.098	0.252	0.109	0.205	0.175	0.149	0.090
4 layers	0.108	0.102	0.254	0.129	0.082	0.072	0.153	0.097
5 layers	0.107	0.100	0.255	0.130	0.203	0.193	0.158	0.102
6 layers	0.107	0.100	0.244	0.130	0.082	0.073	0.163	0.107

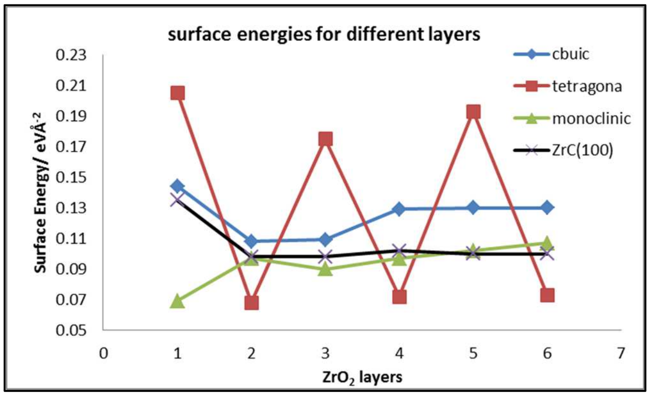

Figure 10. Calculated surface energies for different layers of ZrC (100) and *c*-, *t*-, *m*-ZrO$_2$ (001) surfaces

4.4 Structure and cohesion at the Interface

4.4.1 Rigid Work of Adhesion

In this section we give results for the rigid work of adhesion to provide understanding of the stability and mechanical behavior of the interface. As mentioned earlier, this work of adhesion is calculated by first obtaining the fully relaxed interface structure, then separating the two phases forming the interface and calculating their total energies without allowing them to relax. In this case, bulk properties of both ZrC and *c*-ZrO$_2$ are effectively cancelled out and the result depends purely on the interfacial properties. Table 4 provides a summary for the calculated rigid work of adhesion for the different interface models created. It is apparent from table 4 and figure 11(inset) that the Zr|OO|Zr|OO|Zr||oxidized-ZrC(100) interface has the strongest interaction at the interfacial region indicating this model as more stable with respect to cleavage. The calculated rigid work of adhesion (0.81 eV/Å^2) values are almost twice the values obtained for the other three interface structures. There is a convergence of the calculated values from 3 layers of *c*-ZrO$_2$ units.

4.4.2 Relaxed Work of Adhesion

The work of adhesion is calculated for the fully relaxed system in which the separated ZrC and *c*-ZrO$_2$ slabs are allowed to relax fully.

Table 4. The rigid work of adhesion W_{adh}^{rigid} and the relaxed work of adhesion $W_{adh}^{relaxed}$ for different layers of *c*-ZrO$_2$ (001) on ZrC (100). Interface model 1 is *Zr*|*OO*|*Zr*|OO||ZrC(100), model 2 is *O*|*Zr*|*OO*|*Zr*|O||ZrC(100), model 3 is *O*|*Zr*|*OO*|Zr||ZrC(100) and model 4 is *Zr*|*OO*|*Zr*|*OO*|Zr||oxidized ZrC(100)

c-ZrO$_2$ layers	Model 1	Model 2	Model 3	Model 4
Rigid Work of Adhesion (W_{adh}^{rigid})/ eV.Å^{-2}				
1	0.170	0.103	0.149	0.822
2	0.286	0.160	0.196	0.827
3	0.583	0.073	0.206	0.816
4	0.581	0.081	0.209	0.803
5	0.586	0.070	0.211	0.809
Relaxed Work of Adhesion ($W_{adh}^{relaxed}$)/ eV.Å^{-2}				
1	0.079	0.042	0.140	0.413
2	0.148	0.315	0.187	0.439
3	0.406	0.030	0.199	0.432
4	0.425	0.405	0.206	0.501
5	0.447	0.028	0.205	0.432

In table 4, the relaxed work of adhesion calculated for the four different interface structures are provided. It becomes immediately evident that the Zr|OO|Zr|OO|Zr||oxidized-ZrC(100) model is the most stable interface compared to the other three. Thus the relaxed work of adhesion confirms the most stable interface model obtained by the rigid work of adhesion. The relaxation process however results in a decrease of the work of adhesion as compared to the rigid model. The average difference between the rigid and relaxed work of adhesion is 0.40 eV/Å^2 for the Zr|OO|Zr|OO|Zr||oxidized-ZrC(100) system and this value is a result of interface slab relaxations. Thus after full relaxation, the resulting stable interface model is still Zr|OO|Zr|OO|Zr||oxidized-ZrC(100) and hence the relaxations do not affect the hierarchy of the works of separation.

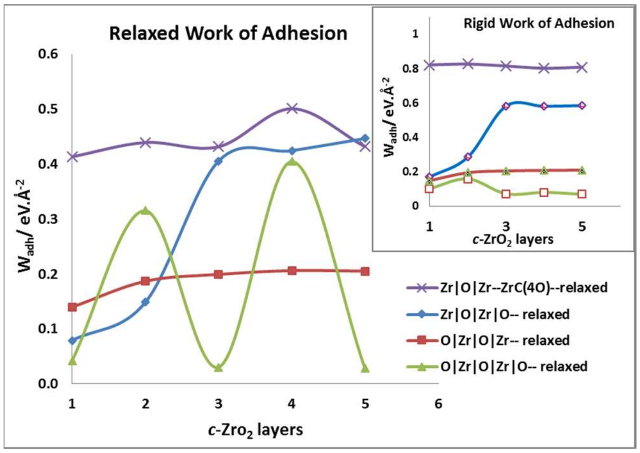

Figure 11. Calculated Work of Adhession (W_{adh}) of different number of *c*-ZrO_2 (001) layers on ZrC(100) surface

Figure 11 shows oscillation of the relaxed work of adhesion for the O|Zr|OO|Zr|OO|Zr|O- model. Thus even numbered layers of the *c*-ZrO_2(001) in this model forms stronger interface than odd numbered *c*-ZrO_2(001) layers. It is worth mentioning here that relaxation of the interface slab in the perpendicular direction to the interface results in transformation of the *c*-ZrO_2(001) phase into *t*-ZrO_2(001). As explained in section 4.3, the resulting *t*-ZrO_2(001) phase is similar to the *t*-ZrO_2(001) surface slab which terminates with O layers on both sides and we observed this odd/even nature of the surface energies which is related to difference in symmetry of the odd/even slabs.

It is observed in table 4 that the W_{ad} value is the same for all layers of *c*-ZrO_2(001) added (for the stable interface model). This pattern is however not the same for the other three interface models. Thus there is no systematic variation of the W_{ad} with the number of ZrO_2 layers and hence the chemistry of the ZrC(100)||*c*-ZrO_2(001) interface is local and defined by the ZrO_2 layer closest to the interface. In other words, long range interactions in the ZrO_2 does not significantly contribute to the interfacial strength. The thicker ZrO_2 layer produces almost the same electrostatic image in the ZrC as the thinner images and do not bond any stronger.

As defined in section section 3.4.3, the interface tension can also be used to determine the strength of the bonds formed at the interface compared to the corresponding bond strengths in the respective bulk phases. In this case, the criteria is $0 < \gamma_{int} < \sigma_{ZrC} + \sigma_{c-ZrO_2}$ corresponds to weakly coupled interface and $\gamma_{int} < 0$ to strongly coupled interfaces. Using σ_{ZrC} = 0.100 eV/Å^2 and σ_{c-ZrO_2} = 0.129 eV/Å^2 asymptotic values from table 3, with relaxed W_{ad} = 0.455 eV/Å^2 for the most stable Zr|OO|Zr|OO|Zr||oxidized-ZrC(100) interface model, the calculated interface tension γ_{int} = -0.226 eV/Å^2. Using value of σ_{t-ZrO_2} = 0.072 eV/Å^2 for even numbered layers and 0.175 eV/Å^2 for odd numbered layers, we still obtain γ_{int} = -0.283 eV/Å^2 and -0.180 eV/Å^2 respectively. Thus the negative sign of the interface tension shows that the interface bonds are stronger than the internal bonds in each ceramic phase.

4.4.2 Structure and properties at the Interface

In this section, we describe the structure and properties at the interface of the most stable model, Zr|OO|Zr|OO|Zr||oxidized-ZrC(100). In figure 12, the relaxed stable structures of the interface formed with 1, 2, 3, 4 and 5 layers of ZrO_2 are shown.

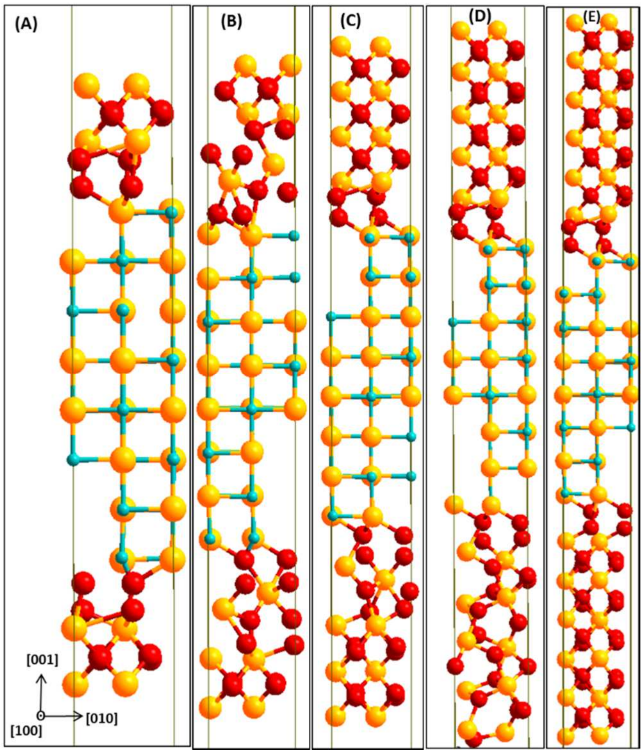

Figure 12. Lowest energy interface structures for 1 layer(A), 2 layers(B), 3 layers(C), 4 layers(D) and 5 layers(E) *c*-ZrO_2(001) for Zr|OO|Zr|OO|Zr||oxidized-ZrC(100) interface model. Yellow(Zr), light blue(C) and red(O)

During the relaxation process, the interfacial area is defined by the ZrC(100) substrate surface area and the pinned c-ZrO_2(001) overlayer is allowed to relax perpendicular to the interface. Figure 12 shows that, at all layers of ZrO_2 at the interface, there is the appearance of perpendicular distortions in the O atoms of ZrO_2. Thus *c*-ZrO_2 is transformed into *t*-ZrO_2 phase. The crystallinity of the ZrC phase is maintained while ZrO_2 phase is transformed. This is not surprising since the (*c*→*t*) ZrO_2 transformation is an easy process as can be seen from the calculated value of 0.054 eV/ ZrO_2 unit in table S.1. Thus even though the *c*-ZrO_2 is forced into registry with the ZrC lattice, the transformation into *t*-ZrO_2 is not inhibited.

We use the lowest energy 3-layer ZrO_2 interface slab to provide detailed description of the properties at the interface. Even though in *c*-ZrO_2 half of the oxygens are at the rear side of the other half forming a single layer, upon forming the interface, the oxygen layer is split into two. This splitting leads to inward relaxation (towards the ZrC side) of one of the Zr atoms (c-ZrO_2) and outward relaxation of the other Zr atom (*c*-ZrO_2). Even though the four O atoms forming the oxidized layer of the ZrC(100) surface are on the same plane, upon forming the interface, two half of the O atoms move upwards to form strong bonds with the Zr atoms from *c*-ZrO_2. These O atoms form direct bonds with Zr atoms (ZrC side) in addition to the interfacial bonds formed. The same phenomenon in the opposite direction is maintained for the two O atoms (c-ZrO2) which remains in their original planar positions. This explains the high work of adhesion calculated for this interface. There are twelve O – Zr bonds at the interface. The bond distances between the Zr (c-ZrO_2) atom closer to the interface and the interface O atoms (ZrC side) are 2.027 Å to 2.325 Å. The distances between the Zr (c-ZrO_2) atom far from the interface and the interface O (ZrC) atoms are 2.016 Å to 2.330 Å. At the region close to the interface (nearest first layer), there is the transformation of the *c*-ZrO_2 into *t*-ZrO_2 (101) with some three-fold and four-fold O atoms. Within this *t*-ZrO_2 (101) region, the three-fold O atoms have $d_{(O\text{-}Zr)\text{-}3f}$ bond distances of 2.027 Å, 2.051 Å and 2.189 Å while the four-fold O atoms have bond $d_{(O\text{-}Zr)\text{-}4f}$ of 2.161 Å, 2.271 Å, 2.232 Å and 2.799 Å.

After the first two layers of ZrO_2 at the interface, there is the transformation into *t*-ZrO_2(001). This can easily be seen by the tetragonal distortion observed in the last two oxygen layers away from the interface. Thus two phases of *t*-ZrO_2 are observed forming the interface: *t*-ZrO_2(101) and *t*-ZrO_2(001). The phase at the interface region is *t*-ZrO_2(101) and the phase at the exposed surface of the interface slab is *t*-ZrO_2(001). These transformations are results of compensating for the strain imposed on the c-ZrO_2 as it is pinned onto the ZrC surface. The observed ZrO_2 phases corroborate the experimental results in the TEM-ED analysis. Firstly, the ED analysis showed polycrystalline nature of the ZrO_2 and the d_{hkl} indexation revealed intense peaks for *t*-ZrO_2(101) phase. The transformation into *t*-ZrO_2 is necessary to alleviate part of the strain imposed on the *c*-ZrO_2 when forced into registry with the ZrC surface.

4.5 Thermodynamic Stability of Interface Models

Aside the use of the mechanical characterization parameters such as the work of adhesion and the interface tension, the significance of a thermodynamic analysis of stability of the different interface models considered is nevertheless an obvious one. The predominant parameter used in assessing the interfacial stability is the interface grand potential, $\Omega_{int}^{i/j}$ which is the interface analogue of surface energy or surface grand potential for non-stoichiometric surfaces. This parameter considers the bulk ZrC and *c*-ZrO_2 as the reference states in forming the interface. It is worth mentioning that the bulk *c*-ZrO_2 reference is in a strained state in order to accommodate the substrate ZrC phase. Thus the *a* and *b* lattice parameters of *c*-ZrO_2 are strained to those of ZrC(100) and the c lattice is allowed to relax in the z-direction of the bulk phase. The same strained *c*-ZrO_2 phase is used as the reference in calculating the surface energy, $\gamma_{ZrO_2}^{surf}$ (equation 8) of the exposed facets in the interface slab.

According to equation 7, the interface grand potential $\gamma_{int}^{i/j}$ is calculated for different values of $\Delta\mu_O$ and $\Delta\mu_{Zr}$ and a plot from the data is shown in figure 13.

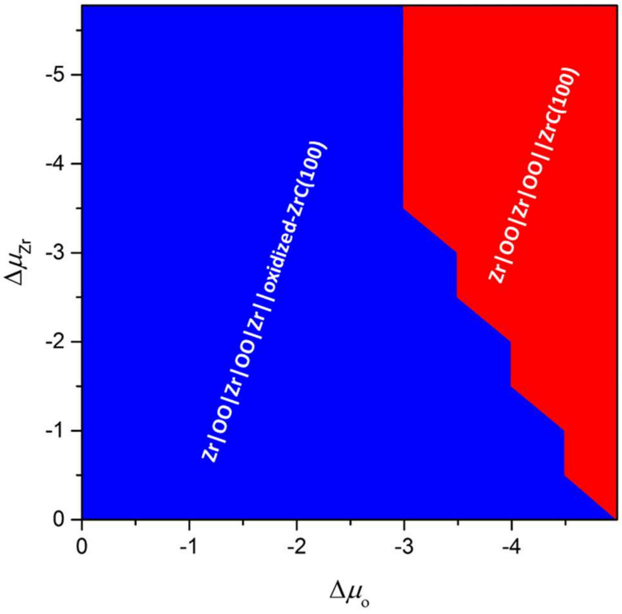

Figure 13. Stable interface models (lowest interface grand potential $\gamma_{int}^{i/j}$) for different interface models as a function of $\Delta\mu_O$ *and* $\Delta\mu_{Zr}$.

In this plot, low values of $\Delta\mu_O$ corresponds to oxygen poor environments and high values of $\Delta\mu_O$ corresponds to oxygen rich environments with similar criteria for the Zr chemical potential. According to the 2D plot in figure 13, two different interface models are stable at different combinations of Zr and O chemical potentials. The Zr|OO|Zr|OO||ZrC(100) interface model is stable for a narrow region of the Zr and O chemical potential combinations (oxygen poor and zirconium rich environments). However, in a wide combination of Zr and O chemical potentials, the Zr|OO|Zr|OO|Zr||oxidized-ZrC(100) interface model is the most stable, confirming the stability criterion established by both the work of adhesion and the interface tension. This can be explained by two factors. First in the Zr|OO|Zr|OO|Zr||oxidized-ZrC(100) model, there are more oxygen atoms at the interface than the other three models leading to the formation of more (12 Zr – O) bonds. In addition to this factor, in the Zr|OO|Zr|OO|Zr||oxidized-ZrC(100) model, the surface exposed to vacuum is Zr terminated which is less stable than the O terminated facets in ZrO_2. This leads to subsequent subtraction of a higher surface energy term in equation 8 than the other two models.

4.6 Electronic properties at the interface

4.6.1 Density of States

In this section, we describe the electronic features at the interface region, more specifically, the density of states and charge analysis.

We first provide a description of the density of states (DOS) at the interface. We use a total spectra obtained by projecting the electronic states onto all atoms in the interface and separate surfaces as well as atomic spectra obtained by projecting the density of states onto individual atoms. Figure 14 shows the total DOS (TDOS) for the interface structure with 3 layers of ZrO_2.

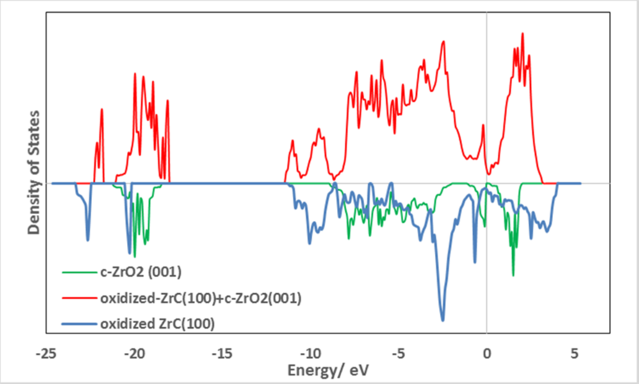

Figure 14. TDOS of interface model with 3 layers of *c*-ZrO_2(001) including the TDOS for the free oxidized ZrC(100) and *c*-ZrO_2(001) slabs

Included are the TDOS for the corresponding surface slabs for oxidized ZrC and ZrO_2 used in constructing the interface model. Figure 14 shows that upon forming the interface, *c*-ZrO_2 fixex both the valence band maximum and the conduction band minimum. The main interfacial features around -5 eV are mainly due to the ZrO_2 states while those at -11 eV are due to the oxidized ZrC(100) states. In figure 15, the DOS are projected onto each atom at the interface and the corresponding atom in the surface slab. This aids in understanding the shift in the bands when the atoms form the interface structure. The O (oxidized ZrC) atom which sits closer to the ZrC side upon forming the interface, in an mmc (three fold bonding between two metal(Zr) and one C atom) shift to higher energies in the core states and lower energies in the conduction band with the main interface features are at -11 eV and -22 eV (O s states are highly localized). This same localized band is found for the C and Zr (all oxidized ZrC side) at the interface at the same energy and shows the ionic nature of the C-O bond in the mmc configuration at the interface.

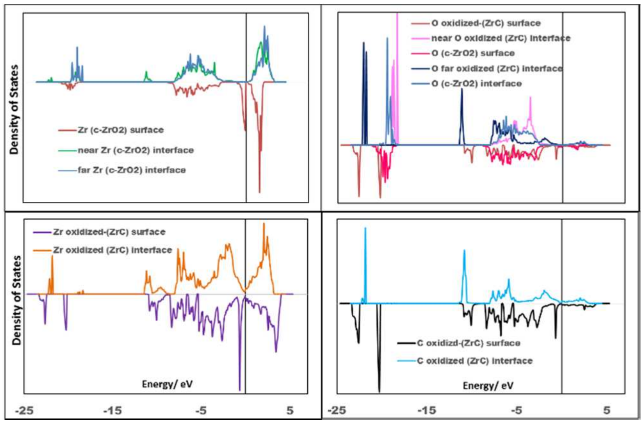

Figure 15. PDOS of each atom at the interface and in the corresponding surface slab. Spectra at the upper part of each plot are for atoms in the interface structure and those at the lower part are for the atoms in the corresponding surface slabs. Atoms labelled as near are closer to the interface plane than atoms labelled as far.

In the conduction band, these O atoms however contribute significantly to the lower end in forming covalent bonds with Zr atoms (*c*-ZrO_2 side). The mmc O (oxidized ZrC) which is closer to the interface plane also shifts to higher energies with the main feature at -18 eV and contributes to the upper part of the valence band as it also forms covalent bonds with Zr (*c*-ZrO_2 side) at the interface. The localized conduction band in Zr (ZrO_2) is broadened upon forming the interface while the higher states at the Fermi level (highly unstable Zr terminated *c*-ZrO_2 surface) are drastically reduced at the interface, stabilizing these atoms further. However, the Zr – O bond at the interface is highly covalent due to the diffuse nature of the bands Zr (*c*-ZrO_2) and O (oxidized ZrC) bands between -1 eV and -8 eV. In order to provide a good understand of the evolution of the electronic structure of atoms moving from bulk to surface and then forming interface, figure 16 aligns the Projected density of states (PDOS) for the atoms parallel to the interface plane showing the states for the atoms in both oxidized ZrC and *c*-ZrO_2 at the interface, in the bulk region of the slab and at the exposed surface in the vacuum area. The low energy area of the ZrO_2 bulk is made of much localized O 2s electrons and Zr 4d electrons at ~ -20 eV. However, the bulk ZrO_2 valence band is more covalent and made of O 2p and Zr 4d electrons and much more diffuse than the low energy ionic bands at -20 eV. The conduction band for this bulk region is mainly Zr 4d. Moving to the exposed surface region, the valence band is highly diffuse, made of Zr 4d electrons and the conduction band is shifted to lower energies with Zr 4d states occupying the Fermi level.

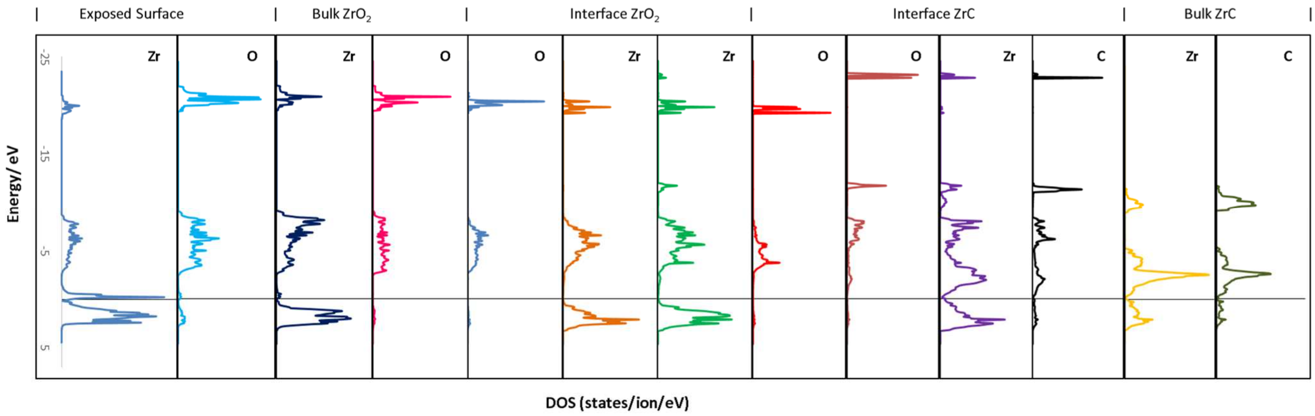

Figure 16. PDOS of atoms at the interface, in the bulk and the exposed surface of the three layer interface slab (Zr|OO|Zr|OO|Zr||oxidized-ZrC(100)). The states are aligned along the parallel plane to the interface with each region marked on the top layer. The Fermi level is aligned at the energy zero position

The high level of states at the Fermi level indicates a high reactivity of the exposed surface. The O 1s states at the lowest energy region are more diffuse than the bulk state, and the electrons are delocalized. In forming the interface, the O (oxidized ZrC side) adsorbed at the three fold mmc site exhibits highly localized electrons shifted to higer energies at around -18 eV. The newly formed states at the interface are derived from the O 2p and O 1s (oxidized ZrC side) electrons mixing with Zr 4d (*c*-ZrO_2). This band (-11 eV) is very narrow indicating highly localized electrons in some of the Zr – O bonds formed at the interface. The Zr - O valence electrons are highly delocalized while the bands due to the far O (penultimate O atom to the interface on the *c*-ZrO_2 side) are less affected by the interface. At the ZrC end of the interface, the valence band consisting of mixed Zr d, p and s states shift to higher energies towards the conduction band. The states arising from the mixing of the Zr (oxidized ZrC) and the far O (oxidized ZrC) at the interface are more diffuse and the electrons are delocalized. This stabilizes further the interface formed. In forming the interface, the C (oxidized ZrC) 2p states in the bulk become highly delocalized and shift to lower energies.

4.6.2. Charge Transfer Analysis

In this section, we provide analysis of charge transfer during formation of the interface. We use a somewhat intuitive idea of analyzing the charge transfer upon formation of the interface as described by Christensen and Carter[35] where the charge transfer values are arranged in a table in a form of spatial arrangement of the atoms from the surface to the respective layers of the phases forming the interface.

First we provide analysis of the charge distribution at the interface for the different layers, starting from one to five layers of ZrO_2 in a spatial profile, then we analysis the charge redistribution in the three layer ZrO_2 interface slab (Zr|OO|Zr|OO|Zr||oxidized-ZrC(100)) from the interface to the bulk like ions.

According to table 5, it is clear that there is significant amount of charge transfer when the free surfaces come in contact to form an interface.

Table 5. Charge transfer analysis of Interfacial structure between oxidized ZrC(100) surface and different number of layers of *c*-ZrO_2(001) in the Zr|OO|Zr|OO|Zr||oxidized-ZrC(100) interface model. Values reported are net charges (electrons/atom) obtained with respect to the charges on the atom in the corresponding surface slabs that form the interface.

	Ion type		ZrO_2 layers on ZrC				
			1	2	3	4	5
ZrO_2 layer at Interface		O	-0.06	-0.03	-0.03	-0.03	-0.06
	Zr		-1.11	-1.04	-1.05	-1.05	-1.08
		Zr	-1.11	-1.07	-1.07	-1.09	-1.11
Interface Plane							
Oxidized ZrC layer at Interface	O		0.18	0.10	0.10	0.11	0.15
		O	0.10	0.08	0.11	0.10	0.10
	Zr		0.02	0.01	0.02	0.01	0.02
		C	1.03	1.03	1.03	1.01	1.03

The cations close to the interface provides most of the charges. Moving from one layer of ZrO_2 upwards, there is essentially the same amount of charge transferred from Zr (c-ZrO2) atoms to the interface atoms.

Table 6. Spatial profile of Charge transfer arranged along the normal direction of the interface. *ΔQ_s* is difference in the charge of the ion with the corresponding ion in the isolated surface slab used to create the interface and *ΔQ_b* is the difference in charge between the ion and the corresponding ion in the bulk structure.

Layer in slab	3 (surface)			2 (bulk)				1 (interface)					1(interface)				2 (bulk)	
Ion type	Zr	O	O	Zr	O	O	Zr	O	O	Zr	Zr		O	O	Zr	C	Zr	C
Absolute Q	2.82	7.14	7.14	1.74	7.10	7.11	1.75	7.12	7.12	1.80	1.76		7.10	7.11	2.23	4.70	2.34	5.67
ΔQ_s (vs surface)	-0.01	0.00	0.00	0.00	-0.04	-0.03	0.01	-0.02	-0.02	-1.04	-1.08		0.10	0.11	0.03	1.03	-0.06	-0.06
ΔQ_b (vs bulk)	1.13	-0.01	-0.01	0.05	-0.05	-0.04	0.06	-0.03	-0.03	0.11	0.07		0.10	0.11	-0.11	-0.96	0.00	0.01

The splitting of Zr atoms (c-ZrO2) into near and far groups (with respect to the interface plane) does not result in any different in charge transferred by the two Zr groups. Nearly all the charge transferred from the interface cations are received by C atoms (oxidized ZrC side) resulting in an image charge phenomenon. This further explains why the interfacial strength is a local property confined to just the first and second ZrO_2 layers at the interface and does not depend on the number of layers added. The O atoms (oxidized ZrC side) receives the same amount of charge from the c-ZrO2 side corroborating the trend found using the mechanical property of the ideal work of adhesion (W_{ad}) in section 4.2.2.

In order to have an understanding of how the interface formation affects electronic properties of the bulk and surface, we provide a spatial profile using the interface formed from three ZrO_2 layers deposited on the ZrC(100) substrate in the Zr|OO|Zr|OO|Zr||oxidized-ZrC(100) model. Thus in table 6, the average charge distribution per layer is arranged from the interface region moving towards the bulk area. There is significant amount of charge transfer at the interface region with respect to the corresponding surface ions, originating mainly from the interface Zr (*c*-ZrO_2 side) atoms. The charges involved in the strong interface bonds are drawn from surface Zr atoms (*c*-ZrO_2 side) and placed at the interface C (oxidized ZrC side) atoms with some charge placed on the interface O atoms on the oxidized ZrC side as well. There is virtually no charge redistribution in the bulk and surface regions away from the interface plane. In this respect, the surface features of the isolated slabs are regained immediately moving away from the interface region into the vacuum area. The bulk features of both ZrC and *c*-ZrO_2 are regained from the second layer away from the interface plane due to no charge transfer in this region. Thus the interface formation has little effect on the ZrC and *c*-ZrO_2 layers farther from the interface. The Zr atom at the ZrO_2 surface side has a high charge due to its exposure to vacuum. The charge analysis in a spatial profile provides further evidence that the interface formation is a local effect, confined to the first one or two layers around the interface plane and that thicker *c*-ZrO_2 are not important.

5 Summary and Conclusions

A combination of experiments, namely XPS, ToF-SIMS, TEM-ED and DFT calculations have been used to characterize and study the oxidation process on ZrC nano crystallites.

According to the XPS analysis, two Zr $3d_{5/2}$ bands were observed and resolution showed the presence of two environments of Zr being ZrC and ZrO_2. A depth profiling showed ZrO_2 thickness on the ZrC surface to be 3.2 nm.

ToF-SIMS analysis of the nano crystallites revealed ZrO_2^- peaks and there was re-oxidation of the particles even with measurements under vacuum (1×10^{-8} mbar).

Using TEM experiments we further observed a different phase as a shell around the ZrC particles and EDX analysis showed this phase to be ZrO_2. Further ED analysis estimated the oxide layer to be about 5 nm and two different crystal orientations were observed showing the polycrystalline nature of the particles. The ED analysis revealed the presence of mainly cubic ZrO_2 with the presence of some tetragonal ZrO_2, mainly the (101).

Moreover, we used Finite temperature molecular dynamics to grow ZrO_2 on the ZrC surface from Zr and O atoms and we observed the formation of an ordered phase of cubic ZrO_2 on the ZrC (100) surface.

DFT was used to model the interface formed between ZrC and ZrO_2 phases and we observed the preferred interface consisting of ZrO_2 terminating with Zr atoms at the interface side on an oxidized ZrC (100) surface. The main mechanical property used to characterize the interfacial strength was the ideal work of adhesion (W_{ad}). The calculated W_{ad} values show that the interface strength remains fairly constant, moving from one layer ZrO_2 up to three layers ZrO_2 from which it converges. Thus the interfacial strength depend on only the first ZrO_2 layer and not on subsequent layers. Thermodynamic analysis using the interface grand potential, $\Omega_{int}^{i/j}$ provided further evidence of most stable interface formed. Further analysis on the electronic structure, using DOS and Bader charge analysis corroborated the local effect of the interface phenomenon.

ASSOCIATED CONTENT

Supporting Information. Equation of state fitting for lattice parameters and Bulk properties of m-, t- and c-ZrO2; A table containing all lattice and bulk parameters for the the three phases of ZrO2; A figure showing the energy versus volume plot used for fitting lattice parameters for the three phases of ZrO2. This material is available free of charge via the internet at http://pubs.acs.org

AUTHOR INFORMATION

Corresponding Author

* Corresponding author: tel +33 320 43 45 03, fax +33 320 43 65 61; email: sylvain.cristol@univ-lille1.fr

ACKNOWLEDGMENT

Numerical results presented in this paper were carried out using the regional computational cluster supported by Université Lille 1, CPER Nord-Pas-de-Calais/FEDER, France Grille, and CNRS. We highly appreciate and thank the technical staff of the CRI-Lille 1 center for their strong and helpful support. The project is supported by Agence Nationale de la Recherche under Contract No. ANR-12-BS08-004-02 (CollZSiC: Elaboration de nanocomposites coeur/coquille ZrC/SiC).
The Fonds Européen de Développement Régional (FEDER), CNRS, Région Nord Pas-de-Calais and Ministère de l'Education Nationale de l'Enseignement Supérieur et de la Recherche are acknowledged for fundings of XPS/LEIS/ToF-SIMS spectrometers within the Pôle Régional d'Analyses de Surface..

ABBREVIATIONS

UPS, Ultraviolet Photoemission Spectroscopy; XPS, X-ray Photoemission Spectroscopy; ToF-SIMS, Time of Flight Secondary Ion Mass Spectrometry; TEM, Transmission Electron Microscopy; ED, Electron Diffraction; EDX, X-ray Diffraction Analysis.

REFERENCES

(1) Gosset, D.; Dollé, M.; Simeone, D.; Baldinozzi, G.; Thomé, L. Structural Evolution of Zirconium Carbide under Ion Irradiation. *J. Nucl. Mater.* **2008**, *373* (1–3), 123–129.

(2) Gosset, D.; Dollé, M.; Simeone, D.; Baldinozzi, G.; Thomé, L. Structural Behaviour of Nearly Stoichiometric ZrC under Ion Irradiation. *Nucl. Instrum. Methods Phys. Res. Sect. B Beam Interact. Mater. At.* **2008**, *266* (12–13), 2801–2805.

(3) Das, T.; Deb, S.; Mookerjee, A. Study of Electronic Structure and Elastic Properties of Transition Metal and Actinide Carbides. *Phys. B Condens. Matter* **2005**, *367* (1–4), 6–18.

(4) Osei-Agyemang, E.; Paul, J.-F.; Lucas, R.; Foucaud, S.; Cristol, S. Stability, Equilibrium Morphology and Hydration of ZrC(111) and (110) Surfaces with H2O: A Combined Periodic DFT and Atomistic Thermodynamic Study. *Phys. Chem. Chem. Phys.* **2015**, *17* (33), 21401–21413.

(5) Arya, A.; Carter, E. A. Structure, Bonding, and Adhesion at the ZrC(1 0 0)/Fe(1 1 0) Interface from First Principles. *Surf. Sci.* **2004**, *560* (1–3), 103–120.

(6) Li, H.; Zhang, L.; Cheng, L.; Wang, Y. Oxidation Analysis of 2D C/ZrC–SiC Composites with Different Coating Structures in CH4 Combustion Gas Environment. *Ceram. Int.* **2009**, *35* (6), 2277–2282.

(7) Noda, T.; Yamazaki, M.; Ozawa, K.; Edamoto, K.; Otani, S. Oxygen Adsorption on a ZrC(111) Surface: Angle-Resolved Photoemission Study. *Surf. Sci.* **2000**, *450* (1–2), 27–33.

(8) Vojvodic, A.; Ruberto, C.; Lundqvist, B. I. Atomic and Molecular Adsorption on Transition-Metal Carbide (111) Surfaces from Density-Functional Theory: A Trend Study of Surface Electronic Factors. *J. Phys. Condens. Matter Inst. Phys. J.* **2010**, *22* (37), 375504.

(9) Noda, T.; Nakane, T.; Ozawa, K.; Edamoto, K.; Tanaka, S.; Otani, S. Photoemission Study of the Oxidation of ZrC(111). *Solid State Commun.* **1998**, *107* (4), 145–148.

(10) Ozawa, K.; Yoshii, T.; Noda, T.; Edamoto, K.; Tanaka, S. Coadsorption of Oxygen and Cesium on ZrC(1 1 1). *Surf. Sci.* **2002**, *511* (1–3), 421–434.

(11) Shimada, S.; Yoshimatsu, M.; Inagaki, M.; Otani, S. Formation and Characterization of Carbon at the ZrC/Zro2 Interface by Oxidation of ZrC Single Crystals. *Carbon* **1998**, *36* (7–8), 1125–1131.

(12) Shimada, S.; Inagaki, M.; Suzuki, M. Microstructural Observation of the ZrC/ZrO2 Interface Formed by Oxidation of ZrC. *J. Mater. Res.* **1996**, *11* (10), 2594–2597.

(13) Osei-Agyemang, E.; Paul, J.-F.; Lucas, R.; Foucaud, S.; Cristol, S. Oxidation and Equilibrium Morphology of Zirconium Carbide Low Index Surfaces Using DFT and Atomistic Thermodynamic Modeling. *J. Phys. Chem. C* **2016**, *120* (16), 8759–8771.

(14) Kitaoka, H.; Ozawa, K.; Edamoto, K.; Otani, S. The Interaction of Water with Oxygen-Modified

ZrC(100) Surfaces. *Solid State Commun.* **2001**, *118* (1), 23–26.

(15) Shin, K.; Ken-ichi, O.; Kazuyuki, E.; Shigeki, O. Photoelectron Spectroscopy Study of the Oxidation of ZrC(100). *Jpn. J. Appl. Phys.* **2000**, *39* (9R), 5217.

(16) Viñes, F.; Sousa, C.; Illas, F.; Liu, P.; Rodriguez, J. A. Density Functional Study of the Adsorption of Atomic Oxygen on the (001) Surface of Early Transition-Metal Carbides. *J. Phys. Chem. C* **2007**, *111* (3), 1307–1314.

(17) Rodriguez, J. A.; Liu, P.; Gomes, J.; Nakamura, K.; Viñes, F.; Sousa, C.; Illas, F. Interaction of Oxygen with ZrC(001) and VC(001): Photoemission and First-Principles Studies. *Phys. Rev. B* **2005**, *72* (7), 75427.

(18) Osei-Agyemang, E.; Paul, J. F.; Lucas, R.; Foucaud, S.; Cristol, S. Periodic DFT and Atomistic Thermodynamic Modeling of Reactivity of H2, O2, and H2O Molecules on Bare and Oxygen Modified ZrC (100) Surface. *J. Phys. Chem. C* **2014**, *118* (24), 12952–12961.

(19) Viñes, F.; Sousa, C.; Illas, F.; Liu, P.; Rodriguez, J. A. A Systematic Density Functional Study of Molecular Oxygen Adsorption and Dissociation on the (001) Surface of Group IV-VI Transition Metal Carbides. *J. Phys. Chem. C* **2007**, *111* (45), 16982–16989.

(20) Shimada, T.; Imamura, K.; Edamoto, K.; Orita, H. Electronic Structures of the Suboxide Films Formed on TiC(100) and ZrC(100) Surfaces: Density Functional Theory Studies. *Surf. Sci.* **2009**, *603* (15), 2340–2344.

(21) Shirley, D. A. High-Resolution X-Ray Photoemission Spectrum of the Valence Bands of Gold. *Phys. Rev. B* **1972**, *5* (12), 4709–4714.

(22) Hafner, J. Ab-Initio Simulations of Materials Using VASP: Density-Functional Theory and beyond. *J. Comput. Chem.* **2008**, *29* (13), 2044–2078.

(23) Mermin, N. D. Thermal Properties of the Inhomogeneous Electron Gas. *Phys. Rev.* **1965**, *137* (5A), A1441–A1443.

(24) Kresse, G.; Joubert, D. From Ultrasoft Pseudopotentials to the Projector Augmented-Wave Method. *Phys. Rev. B* **1999**, *59* (3), 1758–1775.

(25) Perdew, J. P.; Burke, K.; Ernzerhof, M. Generalized Gradient Approximation Made Simple. *Phys. Rev. Lett.* **1996**, *77* (18), 3865–3868.

(26) Methfessel, M.; Paxton, A. T. High-Precision Sampling for Brillouin-Zone Integration in Metals. *Phys. Rev. B* **1989**, *40* (6), 3616–3621.

(27) Monkhorst, H. J.; Pack, J. D. Special Points for Brillouin-Zone Integrations. *Phys. Rev. B* **1976**, *13* (12), 5188–5192.

(28) Haas, P.; Tran, F.; Blaha, P. Calculation of the Lattice Constant of Solids with Semilocal Functionals. *Phys. Rev. B* **2009**, *79* (8), 85104.

(29) Bouvier, P.; Lucazeau, G. Raman Spectra and Vibrational Analysis of Nanometric Tetragonal Zirconia under High Pressure. *J. Phys. Chem. Solids* **2000**, *61* (4), 569–578.

(30) Yashima, M.; Hirose, T.; Katano, S.; Suzuki, Y.; Kakihana, M.; Yoshimura, M. Structural Changes of ZrO2-CeO2 Solid Solutions around the Monoclinic-Tetragonal Phase Boundary. *Phys. Rev. B* **1995**, *51* (13), 8018–8025.

(31) Martin, L.; Vallverdu, G.; Martinez, H.; Cras, F. L.; Baraille, I. First Principles Calculations of Solid–solid Interfaces: An Application to Conversion Materials for Lithium-Ion Batteries. *J. Mater. Chem.* **2012**, *22* (41), 22063–22071.

(32) Yang, Y.-L.; Fan, X.-L.; Liu, C.; Ran, R.-X. First Principles Study of Structural and Electronic Properties of Cubic Phase of ZrO2 and HfO2. *Phys. B Condens. Matter* **2014**, *434*, 7–13.

(33) Christensen, A.; Carter, E. A. First-Principles Study of the Surfaces of Zirconia. *Phys. Rev. B* **1998**, *58* (12), 8050–8064.

(34) Liu, L. M.; Wang, S. Q.; Ye, H. Q. First-Principles Study of Metal/nitride Polar Interfaces: Ti/TiN. *Surf. Interface Anal.* **2003**, *35* (10), 835–841.

(35) Christensen, A.; Carter, E. A. First-Principles Characterization of a Heteroceramic Interface: ZrO2(001) Deposited on an Alpha-Al2O3(1(1)over-

bar02) Substrate. *Phys. Rev. B Condens. Matter Mater. Phys.* **2000**, *62* (24), 16968–16983.

(36) Wang, X.-G.; Smith, J. R. Si/Cu Interface Structure and Adhesion. *Phys. Rev. Lett.* **2005**, *95* (15), 156102.

(37) Hashibon, A.; Elsässer, C.; Mishin, Y.; Gumbsch, P. First-Principles Study of Thermodynamical and Mechanical Stabilities of Thin Copper Film on Tantalum. *Phys. Rev. B* **2007**, *76* (24), 245434.

(38) Hashibon, A.; Elsässer, C. Approaches to Atomistic Triple-Line Properties from First-Principles. *Scr. Mater.* **2010**, *62* (12), 939–944.

(39) Dalverny, A.-L.; Filhol, J.-S.; Doublet, M.-L. Interface Electrochemistry in Conversion Materials for Li-Ion Batteries. *J. Mater. Chem.* **2011**, *21* (27), 10134–10142.

(40) Malyi, O. I.; Chen, Z.; Shu, G. G.; Wu, P. Effect of Sulfur Impurity on the Stability of Cubic Zirconia and Its Interfaces with Metals. *J. Mater. Chem.* **2011**, *21* (33), 12363–12368.

(41) Dai, H.; Du, J.; Wang, L.; Peng, C.; Liu, X. First-Principle Study of the AlP/Si Interfacial Adhesion. *Phys. B Condens. Matter* **2010**, *405* (2), 573–578.

(42) Radican, K.; Berdunov, N.; Manai, G.; Shvets, I. V. Epitaxial Molybdenum Oxide Grown on $\mathrm{Mo}(110)$: LEED, STM, and Density Functional Theory Calculations. *Phys. Rev. B* **2007**, *75* (15), 155434.

(43) Hashibon, A.; Elsässer, C.; Rühle, M. Structure at Abrupt Copper–alumina Interfaces: An Ab Initio Study. *Acta Mater.* **2005**, *53* (20), 5323–5332.

(44) Finnis, M. W. The Theory of Metal - Ceramic Interfaces. *J. Phys. Condens. Matter* **1996**, *8* (32), 5811.

(45) Liu, M. W. and X. *Ultrathin Metal Films*; Springer-Verlag: Berlin, 2004.

(46) Suresh, L. B. F. and S. *Thin Film Materials: Stress, Defect Formation and Surface Evolution*; Cambridge University Press: Cambridge, England, 2003.

(47) Christensen, A.; Carter, E. A. Adhesion of Ultrathin ZrO2(111) Films on Ni(111) from First Principles. *J. Chem. Phys.* **2001**, *114* (13), 5816–5831.

(48) Craciun, D.; Socol, G.; Stefan, N.; Bourne, G.; Craciun, V. Chemical Composition of ZrC Thin Films Grown by Pulsed Laser Deposition. *Appl. Surf. Sci.* **2009**, *255* (10), 5260–5263.

(49) Lucas, R.; Pizon, D.; Laborde, E.; Trolliard, G.; Foucaud, S.; Maître, A. A Simple Route for Organic Covalent Grafting onto Zirconium Carbide Particles. *Appl. Surf. Sci.* **2013**, *287*, 411–414.

(50) Briggs, D.; Grant, J. . *Surface Analysis by Auger and XPS*; IM Publications and Surface Spectra Limited: UK, 2003.

(51) Grimblot, J. *L'analyse de Surface Des Solides*; Masson, 1995.

(52) Tanuma, S.; Powell, C. J.; Penn, D. R. Calculations of Electron Inelastic Mean Free Paths. V. Data for 14 Organic Compounds over the 50–2000 eV Range. *Surf. Interface Anal.* **1994**, *21* (3), 165–176.

(53) Piskorz, W.; Gryboś, J.; Zasada, F.; Cristol, S.; Paul, J.-F.; Adamski, A.; Sojka, Z. Periodic DFT and Atomistic Thermodynamic Modeling of the Surface Hydration Equilibria and Morphology of Monoclinic ZrO2 Nanocrystals. *J. Phys. Chem. C* **2011**, *115* (49), 24274–24286.

(54) Eichler, A.; Kresse, G. First-Principles Calculations for the Surface Termination of Pure and Yttria-Doped Zirconia Surfaces. *Phys. Rev. B* **2004**, *69* (4), 45402.

Insert Table of Contents artwork here

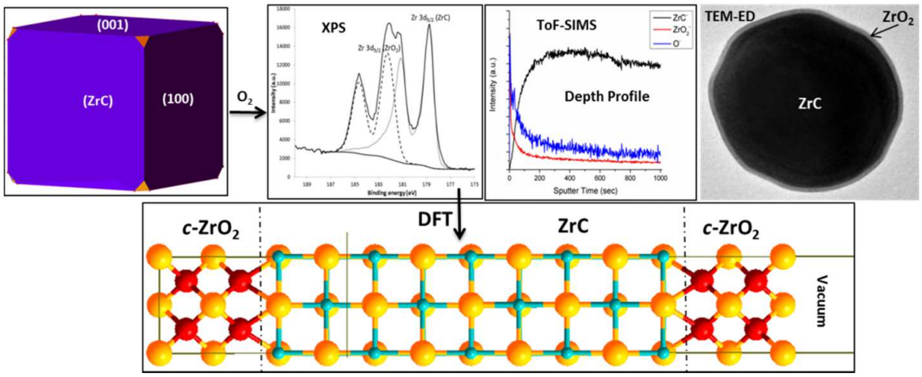

Supporting Information for

Structure and Energetics of ZrC(100)/*c*-ZrO_2(001) interface: A Combination of Experiments, Finite Temperature Molecular Dynamics, Periodic DFT and Atomistic Thermodynamic Analysis

Eric Osei-Agyemang[1], Jean-François Paul,[1] Romain Lucas,[2] Sylvie Foucaud,[2] Sylvain Cristol[1]*, Anne-Sophie Mamede[1], Nicolas Nuns[1], Ahmed Addad[3]

Detailed bulk and Lattice parameters for ZrO_2 polymorphs

For the *c*-ZrO_2 phase, the fitted lattice parameter is a slight overestimation of the experimental value of 5.085 Å[1], 5.110 Å[2] acceptable for GGA functional calculations. Our calculated lattice parameter of 5.143 Å is in very good agreement with other GGA calculations in the literature, 5.151 Å[3], 5.127 Å[4]. Both the bulk modulus and the equilibrium volume per ZrO_2 unit are well reproduced in this work. All the calculated parameters are shown in table S.1 and fitting of the lattice parameter is provided in figure 10.

The fitted lattice parameters were a = 3.649 Å and c = 5.257 Å which a slightly higher than experimental values, expected for using the GGA functional. The calculated lattice parameters however are in excellent agreement with other experimental data, a = 3.640 Å and c = 5.27 Å.[5] Other GGA calculated lattice parameters are highly comparable to our results (a = 3.645 Å and c = 5.289 Å,[6] a = 3.642 Å and c = 5.295 Å[7]). The calculated vertical displacement of the O atoms in the c direction Δz = 0.263 Å and the tetragonal distortion $d_z = \Delta z/c$ = 0.050 compared to the experimental value of 0.049[8] and other GGA calculated values of 0.050[9].

Our calculated lattice parameters are a = 5.243 Å, b = 5.307 Å, c = 5.412 Å and $\beta = 99.20^{o}$. This slight estimation of experimental parameters (a = 5.151 Å, b = 5.212 Å, c = 5.317 Å and $\beta = 99.23^{o}$)[10] but in excellent agreement with other calculations (a = 5.200 Å, b = 5.250 Å, c = 5.410 Å and $\beta = 99.60^{o}$)[11].

The structural energy difference between the cubic and tetragonal phases is 0.054 eV/ ZrO_2 unit as compared to the experimental value of 0.057[12] eV/ ZrO_2 unit while the energy difference between the tetragonal and the monoclinic phase is slightly over estimated, at 0.118 eV/ ZrO_2 compared to the experimental value of 0.061[12] eV/ ZrO_2 but in good agreement with other GGA calculated values of 0.100[13] eV/ ZrO_2 and 0.109[4] eV/ ZrO_2 .

Table S.1. Bulk parameters including Bulk modulus (B^o), Pressure derivative of the Bulk modulus (B'), Tetragonal distortion d_z and equilibrium volume V_{eq} for ZrO_2 phases

	a/ Å	c/ Å	b/a	c/a	B^o/ GPa	B'	d_z	V_{eq} (per ZrO_2)/ $Å^3$
				Cubic				
This work	5.143	5.143	1.000	1.000	235.35	4.027	-	34.013
Ref.	5.169[9] 5.151[3]				236.57[14], 251[15]	4.060[14]	-	34.530[9]
Expt.	5.086[10] 5.110[2]				194-25[16]		-	32.890[10]
				Tetragonal				
This work	3.649	5.257	1.000	1.441	178.85	4.496	0.050	35.010
Ref.	3.654[9] 3.642[7]	5.364[9] 5.295[7]		1.468[9]	226.10[14] 172.0[17]	3.810[14] 5.000[18]	0.050[9] 0.054[7]	35.940[9]
Expt.	3.640[5] 3.574[19]	5.270[5] 5.154[19]		1.448[10]	170[20] 190[21]	4.300[19]	0.065[5] 0.047[19]	33.660[10]
				Monoclinic				
This work	5.243	5.412	1.012	1.032	134.48	3.792	-	37.162
Ref.	5.242[9]	5.410[9]	1.012[9]	1.032[9]	157[22], 137[15]	2.38[22]	-	37.120

	5.235[4]	5.413[4]	1.012[4]	1.034[4]	185[18]	4.12[14]		
Expt.	5.150[10]	5.315[10]	1.012[10]	1.032[10]	95-189[8], 212[23]	4-5[24]	-	35.220[10]

$E^{c-ZrO_2} - E^{t-ZrO_2}$ (eV/ ZrO_2 unit)		$E^{t-ZrO_2} - E^{m-ZrO_2}$(eV/ ZrO_2 unit)
This work	0.054	0.118
Ref.	0.070[13], 0.063[4]	0.100[13], 0.109[4]
Expt.	0.057[12]	0.061[12]

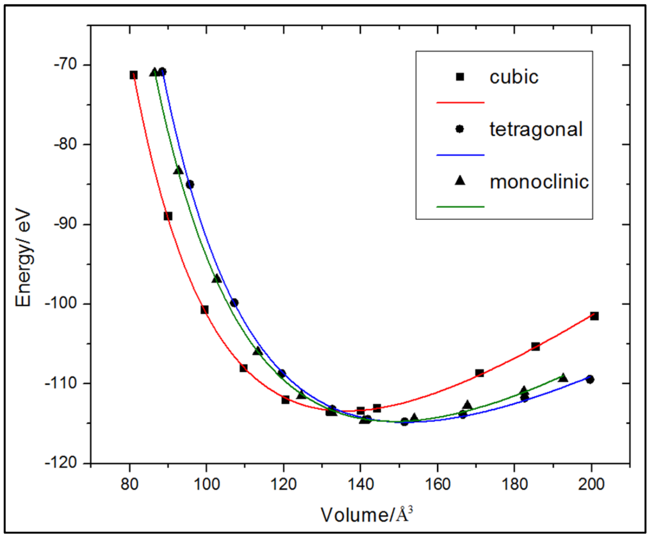

Figure S.1. Lattice parameter fitting for ZrO2 phases

References

(1) Scott, H. G. Phase Relationships in the Zirconia-Yttria System. *J. Mater. Sci. 10* (9), 1527–1535.

(2) Igawa, N.; Ishii, Y.; Nagasaki, T.; Morii, Y.; Funahashi, S.; Ohno, H. Crystal Structure of Metastable Tetragonal Zirconia by Neutron Powder Diffraction Study. *J. Am. Ceram. Soc.* **1993**, *76* (10), 2673–2676.

(3) Yang, Y.-L.; Fan, X.-L.; Liu, C.; Ran, R.-X. First Principles Study of Structural and Electronic Properties of Cubic Phase of ZrO2 and HfO2. *Phys. B Condens. Matter* **2014**, *434*, 7–13.

(4) Christensen, A.; Carter, E. A. Adhesion of Ultrathin ZrO_2(111) Films on Ni(111) from First Principles. *J. Chem. Phys.* **2001**, *114* (13), 5816–5831.

(5) Teufer, G. The Crystal Structure of Tetragonal ZrO2. *Acta Crystallogr.* **1962**, *15* (11), 1187.

(6) Eichler, A. Tetragonal Y-Doped Zirconia: Structure and Ion Conductivity. *Phys. Rev. B* **2001**, *64* (17), 174103.

(7) Kuwabara, A.; Tohei, T.; Yamamoto, T.; Tanaka, I. Ab Initio Lattice Dynamics and Phase Transformations of ZrO2. *Phys. Rev. B* **2005**, *71* (6), 064301.

(8) Aldebert, P.; Traverse, J.-P. Structure and Ionic Mobility of Zirconia at High Temperature. *J. Am. Ceram. Soc.* **1985**, *68* (1), 34–40.

(9) Jomard, G.; Petit, T.; Pasturel, A.; Magaud, L.; Kresse, G.; Hafner, J. First-Principles Calculations to Describe Zirconia Pseudopolymorphs. *Phys. Rev. B* **1999**, *59* (6), 4044–4052.

(10) Howard, C. J.; Hill, R. J.; Reichert, B. E. Structures of ZrO2 Polymorphs at Room Temperature by High-Resolution Neutron Powder Diffraction. *Acta Crystallogr. Sect. B* **1988**, *44* (2), 116–120.

(11) Walter, E. J.; Lewis, S. P.; Rappe, A. M. First Principles Study of Carbon Monoxide Adsorption on Zirconia-Supported Copper. *Surf. Sci.* **2001**, *495* (1–2), 44–50.

(12) Stefanovich, E. V.; Shluger, A. L.; Catlow, C. R. A. Theoretical Study of the Stabilization of Cubic-Phase ZrO2 by Impurities. *Phys. Rev. B* **1994**, *49* (17), 11560–11571.

(13) French, R. H.; Glass, S. J.; Ohuchi, F. S.; Xu, Y. N.; Ching, W. Y. Experimental and Theoretical Determination of the Electronic Structure and Optical Properties of Three Phases of ZrO2. *Phys. Rev. B* **1994**, *49* (8), 5133–5142.

(14) Terki, R.; Bertrand, G.; Aourag, H.; Coddet, C. Structural and Electronic Properties of Zirconia Phases: A FP-LAPW Investigations. *Mater. Sci. Semicond. Process.* **2006**, *9* (6), 1006–1013.

(15) Jaffe, J. E.; Bachorz, R. A.; Gutowski, M. Low-Temperature Polymorphs of ZrO2 HfO2: A Density-Functional Theory Study. *Phys. Rev. B* **2005**, *72* (14), 144107.

(16) Kandil, H. M.; Greiner, J. D.; Smith, J. F. Single-Crystal Elastic Constants of Yttria-Stabilized Zirconia in the Range 20° to 700°C. *J. Am. Ceram. Soc.* **1984**, *67* (5), 341–346.

(17) Fadda, G.; Colombo, L.; Zanzotto, G. First-Principles Study of the Structural and Elastic Properties of Zirconia. *Phys. Rev. B* **2009**, *79* (21), 214102.

(18) Stapper, G.; Bernasconi, M.; Nicoloso, N.; Parrinello, M. Ab Initio Study of Structural and Electronic Properties of Yttria-Stabilized Cubic Zirconia. *Phys. Rev. B* **1999**, *59* (2), 797–810.

(19) Bouvier, P.; Lucazeau, G. Raman Spectra and Vibrational Analysis of Nanometric Tetragonal Zirconia under High Pressure. *J. Phys. Chem. Solids* **2000**, *61* (4), 569–578.

(20) Bouvier. P, D. V. and L. G. The High-Pressure Phase Sequence in Nanocrystalline Zirconia. *Eur. Phys. J. B - Condens. Matter Complex Syst.* **2003**, *35* (3), 301–309.

(21) Fukuhara, M.; Yamauchi, I. Temperature Dependence of the Elastic Moduli, Dilational and Shear Internal Frictions and Acoustic Wave Velocity for Alumina, (Y)TZP and β′-Sialon Ceramics. *J. Mater. Sci.* **1993**, *28* (17), 4681–4688.

(22) Lowther, J. E.; Dewhurst, J. K.; Leger, J. M.; Haines, J. Relative Stability of ZrO2 and HfO2 Structural Phases. *Phys. Rev. B* **1999**, *60* (21), 14485–14488.

(23) Desgreniers, S.; Lagarec, K. High-Density ZrO2 and HfO2: Crystalline Structures and Equations of State. *Phys. Rev. B* **1999**, *59* (13), 8467–8472.

(24) Leger, J. M.; Tomaszewski, P. E.; Atouf, A.; Pereira, A. S. Pressure-Induced Structural Phase Transitions in Zirconia under High Pressure. *Phys. Rev. B* **1993**, *47* (21), 14075–14083.

3. Characterizing the ZrC(111)//c-ZrO$_2$(111) Hetero-ceramic Inter-face: A First Principles DFT and Atomistic Thermodynamic Modeling

This section contains a fully written research article submitted for publication in the American Chemical Society, Journal of Applied Materials and Interfaces.

Characterizing the ZrC(111)//*c*-ZrO_2(111) Hetero-ceramic Interface: A First Principles DFT and Atomistic Thermodynamic Modeling

Eric Osei-Agyemang,[1] Jean-François Paul,[1] Romain Lucas,[2] Sylvie Foucaud,[2] Sylvain Cristol[1]*, Anne-Sophie Mamede[1], Nicolas Nuns[1], Ahmed Addad[3]

[1] Université de Lille 1, Univ. Lille, CNRS, ENSCL, Centrale Lille, Univ. Artois, UMR 8181 - UCCS - Unité de Catalyse et de Chimie du Solide.

[2] Université de Limoges, CNRS, ENSCI, SPCTS, UMR 7315, F-87000 Limoges, France.

[3] Unité Matériaux et Transformations, Université Lille 1, CNRS-UMR 8207

ABSTRACT: Mechanical and physical properties of Zirconium Carbide (ZrC) is limited to its ability to deteriorate with respect to such properties in oxidizing environments. Low refractory oxides are typically formed as layers on ZrC surfaces when exposed to the slightest concentrations of oxygen. However, the carbide has a wide range of applications in nuclear reactor lines, nozzle flaps in the aerospace industry, just to name a few. In order to develop mechanically strong and oxygen resistant ZrC materials, the need for studying and characterizing the oxidized layers with emphasis on the interfacial structure between the ZrC phase and the oxidized phase cannot be understated. In this paper, we have studied and characterized ZrC (111)//c-ZrO_2 (111) interface using a combination of XPS, ToF-SIMS, TEM-ED experiments coupled with Finite temperature molecular dynamics simulation and DFT. The experimental technics revealed a ZrO_2 phase as a layer around the Zrc shell, with cubic and tetragonal ZrO_2 phases being predominant. The interfacial mechanical properties were characterized with the work of adhesion which revealed a Zr|OO|Zr|OO//ZrC (111) interface model as the most stable with an oxygen layer from ZrO_2 being deposited on the ZrC (111) surface. Further structural analysis at the interface revealed a crack in the first ZrO_2 layer at the interfacial region. Further analysis of the electronic structure using density of states calculations and Bader charge analysis revealed the interfacial properties as local effects with no significant effects in the bulk regions of the interface slab.

---

1 INTRODUCTION

Zirconium Carbide (ZrC), being a non-oxide ultra-high temperature ceramic is used for several special applications. It is mostly used in environmentally harsh and demanding conditions including cutting tools, nuclear plant inner coatings, turbine components in the aerospace industry and as refractory ceramics in the steel industries.[1,2] It fulfils all these application requirements to its excellent mechanical and physical properties with a high melting point of 3430ºC.

A serious problem however encountered with this material when used in harsh conditions is the proneness to oxidation. ZrC forms low refractory oxides 500 – 600ºC.[3] The oxide formed causes deterioration of the physical and mechanical properties and defeats the purpose for the applications generally used for. There is however the need to study the oxidation process and mechanism on the low index surfaces of this nanocrystallite material. ZrC being cubic has three distinct low index surfaces: (100), (110) and (111) surfaces with the (100) being the most stable. [4,5] Studies on the oxidation process has been carried out on the (100) surface[6–9] and all provides similar results: the ZrC(100) surface is extremely reactive to oxygen and easily oxidized by the smallest concentration of Oxygen. In a recent study, we observed the ZrC(110) surface to be easily oxidized with the formation of ZrO_2 on the exposed surface.[10] In another experimental study, the (110) orientation of *t*-ZrO_2 was observed to grow preferentially on the ZrC(100) surface.[11,12] Similar experiments[13–16] and theoretical[17] studies on the oxidation of the ZrC(111) surface have been conducted by several research groups. In all these studies, oxygen is observed to be very reactive on the (111) surface and dissociates completely into atomic species.

Cleaving ZrC bulk along the (111) normal plane produces a crystal with Zr and C layers terminating on opposite sides of the exposed surfaces. This renders the slab polar. However, experimentally findings show the surface to terminate preferentially with Zr layer.[18–20] In a recent theoretical study, we made several reconstructions on the ZrC(111) surface with different terminations and found the thermodynamically most stable surface to be terminated with four Zr atoms.[4] Thus this surface slab contains excess Zr atoms over C atoms.

Recent experimental analysis on ZrC nanocrystallites with XPS revealed the presence of another phase other than ZrC and TEM-ED analysis showed the presence of polycrystalline ZrO_2, mostly *c*-ZrO_2 with some amounts of *t*-ZrO_2.(our ZrC(100)/ZrO2(001) paper). The *c*-ZrO_2(111) phase was predominant. We studied the structure and energetics at the interface formed between the ZrC(100) and the *c*-ZO_2(001) and showed very strong interfacial bonds which are more stable than the bonds in the corresponding isolated surfaces .(our ZrC(100)/ZrO2(001) paper) This study also showed the interfacial strength and properties to be dependent on the first three layers of ZrO_2 deposited on the ZrC(100) surface.

Other theoretical studies have been carried out to study the heteroceramic interface of ZrO_2 deposited on α-$Al_2O_3(1\bar{1}02)$ substrate and found the stoichiometric $ZrO_2(001)/\alpha$-$Al_2O_3(1\bar{1}02)$ interface to be weakly bonded, regardless of the film thickness.[21] However, in another study where the $ZrO_2(111)$ ceramic was deposited on a metal (Ni) substrate, the $ZrO_2(111)$ was observed to adhere very strongly at the monolayer level but thicker films of the ceramic interacts very weakly with the Ni substrate.[22] The ZrO_2 overly was observed to transform partially into *m*-ZrO_2 but could not completely covert into *m*-ZrO_2 due to the constraints imposed by the periodic boundary conditions.

In Order to reduce the susceptibility of ZrC to easy oxidation, one method that can be used is to coat the surface with another ceramic material that forms a protective layer on the ZrC in oxidizing environments (SiC is a very good candidate). Moreover, it is necessary to study the oxidized layer, provide detail analysis on the structure, energetics and stability at the interfacial region between ZrC and the oxidized layer. This proper provides such information, complementing the study carried out on the interface formed on the ZrC(100) surface. (our ZrC(100)/ZrO2(001) paper)

The paper is organized as follows: Section 2 provides a brief description of the experimental conditions used in analysing the ZrC nanocrystallites. In section 3, Details about the Finite temperature molecular dynamics simulation and general calculation parameters as well as procedures for building the interface are provided. Section 4 provides the results obtained and discusses them accordingly. Section 5 gives the summary and conclusions on the current study.

2 EXPERIMENTAL PROCEDURES

A Kratos Analytical AXIS Ultra^{DLD} spectrometer was used in the XPS analysis of the ZrC nanocrystallites with an aluminium (Al Kα = 1486.6 eV) monochromatic source for excitation. Constant pass energy of 40 eV was used to operate the analyser with an analysis area of approximately 700 µm x 300 µm. Charge compensation was applied for the occurrence of charge effects during the analysis. O 1s binding energy (BE of 530.0 eV) of ZrO_2 phase was used as internal reference. CasaXP software was used to simulate and quantify the experimental photopeaks. A non-linear Shirley[23] background subtraction was taken into account for the quantification.

ToF-SIMS analysis was carried out in both positive and negative modes using (IONTOF GmbhH, Münster, Germany) equipped with a 25keV bismuth primary ion source. Pulsed low energy electrons (20 eV) were used to compensate for the charging effects due to the primary ion beam. Bi_3^+ ions were used in negative mode for both static and dynamic mode analysis. Tablet powder was used in the static mode to produce better mass resolution and secondary ion yield. The positive and negative spectra were compared with a reference of ZrO_2. During depth profiling, dual beam mode in which Cs^+ (0.5kV and 1kV) were used for sputtering in the non-interlaced mode in order to characterize the ZrO_2 layer on the ZrC.

TEM-ED experiments were conducted on the ZrC nanocrystals in order to ascertain the crystalline phases present. A powdered (dried) deposition on copper grid with carbon film was used.

3 STRUCTURAL MODELS AND CALCULATION SCHEMES

3.1 General Computational Details

Since ZrC was used as the substrate, all calculation parameters were based on optimized values for ZrC.

We performed all electron density functional calculations (DFT) using the Vienna ab initio Simulation Package (VASP)[24] based on Mermin's finite temperature DFT.[25] The following electronic configurations were used for Zr, C and O atoms respectively: $[Kr]4d^25s^2$, $[He]2s^22p^2$ and $[He]2p^6$. The pseudopotentials used were the Projected Augmented Wavefunction (PAW)[26] for describing the core electrons and the core part of the valence electrons wavefunctions and this aids in reducing the number of planewaves required in describing the electrons close to the nuclei. The Kohn-Sham valence states were expanded in a planewave basis set with a kinetic energy cutoff of 500 eV. The generalized gradient approximation (GGA), parametrized by Perdew, Burke and Ernzerhof (PBE)[27] was used for for the exchange correlation part. The Methfessel-Paxton[28] smearing scheme was used with the gamma parameter set to 0.1 eV. For all bulk calculations, a *k*-sampling of 9 x 9 x 9 mesh using the standard Monkhorst-Pack[29] special grid was employed. However, 9 x 9 x 1 *k*-points sampling was used for all surface and interface slab calculations. The Kohn-Sham equations were resolved using the self-consistent field (SCF) procedure and assumed to be converged when energy changes of 1 x 10^{-4} eV between two successive iterations is obtained.

3.2 Finite Temperature Molecular Dynamics

In order to confirm the experimental findings on the analysis of the ZrC nanocrystals, we performed finite temperature molecular dynamics simulation to provide a first approximation on the nature of ZrO_2 formed on the ZrC surfaces. We used a (2 x 2) supercell for all MD simulations. We started with a 9 layer thick of ZrC(111) substrate (terminating with 4 Zr atoms on both sides of the surface slab) by depositing Zr and O atoms onto the exposed ZrC(111) surface to form about two layers of ZrO_2. The ions were initially kept at T = 100 K within the micro canonical ensemble and the velocities was scaled upwards at different steps until a final temperature of 1000 K was reached. We selected this temperature to provide allowance for the possible formation of m-ZrO_2 phase which is stable at temperatures below 1450 K. 1 fs time step was used. The resulting equilibrium structure was then quenched from 1000 K to 500 K. Geometries at minima's on the potential energy surface were selected and optimized at higher precision of calculation to obtain a final structure.

3.3 Bulk ZrC and *c*-ZrO_2 phases.

In order to obtain parameters optimized for our system of calculations, we performed bulk calculations on the ZrC and c-ZrO_2 phases. Details on the bulk properties optimization are provided in a separate paper.$^{(100\text{ interface paper})}$ As such, we provide a brief description of the methodology use.

Energy Versus volume data were obtained for both ZrC and *c*-ZrO_2 and finally fitted with a Murnaghan's equation of state. The optimized lattice parameters are calculated from this fitting.

An optimized k-points of 5 x 5 x 5 Monkhorst-Pack grid producing 63 irreducible k-points was used for bulk ZrO_2 calculations and the same kinetic energy cut-off of 500 eV for the ZrC bulk was used for the ZrO_2 bulk. All *c*-ZrO_2 bulk used contains 4 formula units as shown in figure 1. Details on the Murnaghan's fitting and subsequent calculations for all lattice parameters for the c-, t- and m-ZrO2 used for this work are provided in a previous paper.$^{(100\text{ interface paper})}$

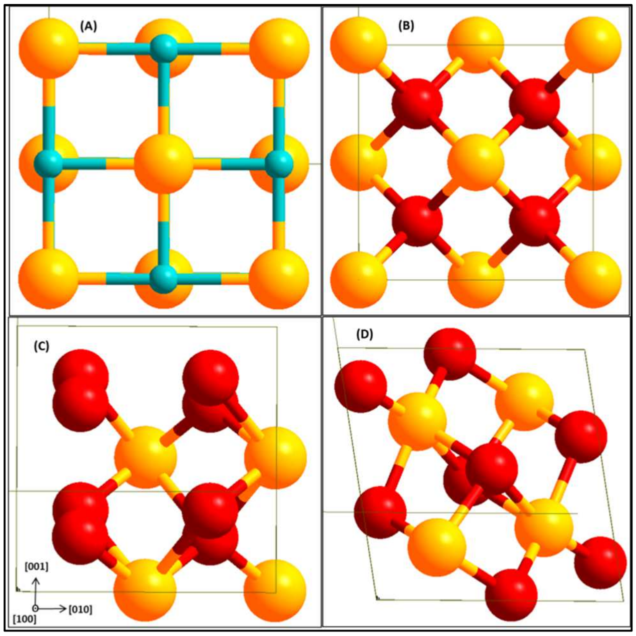

Figure 1. Bulk structures of ZrC(A), *c*-ZrO_2(B), *t*-ZrO_2(C) and *m*-ZrO_2(D). Yellow(Zr), light blue(C) and red(O).

3.4 Interface Model Construction

In order to construct the interface model, the stacking direction at the interface is initially selected and there should be proper commensurability factor between the two bulk phases with respect to the interface plane.[30] The required surfaces are subsequently cleaved from the two bulk phases along the selected surface normal. Each of the revealed surfaces will have different atomic arrangements and configurations. The interface is finally created by bringing the two surfaces in contact with each other and then fully relaxed to obtain a final optimized interfacial geometry.

3.4.1 Commensurate Phases and Surface Structures

Among the low index ZrC surfaces, the (100) surface being stoichiometric and non-polar is found to be the most stable.[4,5] However, even though the (111) surface is polar upon cleaving from the bulk phase by terminating on one side with carbon layer and the other side with Zirconium layer, surface reconstruction reveals a more stable surface terminated on both sides with Zr atom layers only second to the (100) surface in terms of stability.[4] With an a lattice parameter of 6.698 Å, *b* of 5.801 Å and $\beta = 60^o$, the exposed surface area of the ZrC (111) surface is 38.854 Å^2. On accounts of several studies made on the *c*-ZrO_2 surfaces, the (111) surface is found to be the most stable.[31,32] Surface energies are calculated for 1 layer up to 6 layers of ZrC to ascertain the effect of layer thickness on the surface energy. The surface energies are calculated as $E_{surf} = (1/2A)\ [E_{slab} - nE_{bulk}\ ]$ where E_{slab} is the total energy of the surface slab, E_{bulk} is the energy per formula unit of ZrC in the corresponding bulk, A is the surface area and n is the number of formula units in the surface slab.

Surface energies are also computed for the (111) terminations of *c*-ZrO_2.The surface energies were calculated for different number of layers, starting from 1 to 6 layers of ZrO_2. Upon cleaving the c-ZrO_2 along the [111] direction, a polar slab is obtained with an OO layer terminating on one side and Zr layer terminating on the other side. The slab can however be terminated in three different arrangements as OO|Zr|OO|Zr|OO-, Zr|OO|Zr|OO|Zr- and O|Zr|OO|Zr|O- (Figure 1). We used only symmetric slabs (slabs with mirror symmetry) in the calculation of the surface energy in order to eliminate the net dipole moment. The calculation of the interface tension defined in a subsequent section requires these surface energies. Thus surface energies of three different terminations were calculated: Zr- termination, O- termination and OO- termination.

In order to calculate surface energies of both stoichiometric and non-stoichiometric slabs, we define the surface grand potential, Ω^i which implies contact of the Zr and O reservoirs with the surface. It is defined as:

$$\Omega^i = \frac{1}{2A}\left[E^i_{slab} - N_{Zr}\mu_{zr} - N_O\mu_O\right] \ldots\ldots eq.(1)$$

N_{Zr} and N_O are the number of Zr and O atoms in the slab with μ_{Zr} and μ_O being the chemical potential of Zr and O respectively. E^i_{slab} is the total energy of the surface slab and A is the surface area. The chemical potentials of Zr and O are related by bulk ZrO_2 in the expression: $\mu_{ZrO_2} = E^{bulk}_{ZrO_2} = \mu_{Zr} + 2\mu_O$ with $E^{bulk}_{ZrO_2}$ being the total energy per bulk ZrO_2 unit. Rearranging this expression and substituting in equation 1, we obtain the following:

$$\Omega^i = \frac{1}{2A}\left[E^i_{slab} - N_{Zr}E^{bulk}_{ZrO_2} - N_O\mu_O + 2N_{Zr}\mu_O\right] \ldots eq.(2)$$

Defining the chemical potential of O in relation to the chemical potential of the reference state, O_2 which is defined as half the total energy of O_2 gas as $\Delta\mu_O = \mu_O - (\frac{E^{gas}_{O_2}}{2})$ and substituting in equation 2 with further rearrangements, we obtain:

$$\Omega^i = \frac{1}{2A}\left[E^i_{slab} - N_{Zr}E^{bulk}_{ZrO_2} + E^{gas}_{O_2}\left(N_{Zr} - \frac{N_O}{2}\right) + \Delta\mu_O(2N_{Zr} - N_O)\right] \ldots eq.(3)$$

If we make the following definition:

$$\gamma^i = \frac{1}{2A}\left[E^i_{slab} - N_{Zr}E^{bulk}_{ZrO_2} + E^{gas}_{O_2}\left(N_{Zr} - \frac{N_O}{2}\right)\right]..eq.(4)$$

Where Υ^i is the surface energy of the stoichiometric part of the selected slab and substituting equation 4 into equation 3, we obtain the following expression for the surface grand potential:

$$\Omega^i = \gamma^i + \frac{1}{2A}\left[\Delta\mu_O(2N_{Zr} - N_O)\right] \ldots\ldots eq.(5)$$

Thus the surface grand potential is defined in terms of the surface energy arising from the stoichiometric part of the slab and another part correcting for the extra number of Zr or O atoms.

From equation 5, a range of $\Delta\mu_O$ values can be accessed if we define the lower and upper limits. In defining the upper limit of the O chemical potential, we make the assumption that the chemical potential of O must be lower than the energy of O in its reference stable gaseous state. Thus we can write for the upper limit of the O chemical potential as:

$$\Delta\mu_O = \mu_O - \frac{E^{gas}_{O_2}}{2} < 0 \ldots..eq.(6)$$

For the lower limit of the O chemical potential, if we combine the expressions $\mu_{ZrO_2} = E^{bulk}_{ZrO_2} = \mu_{Zr} + 2\mu_O$ with $\Delta\mu_{Zr} = \mu_{Zr} - E^{bulk}_{Zr}$ and $\Delta\mu_O = \mu_O - (E^{gas}_{O_2}/2)$ and make rearrangements, we obtain the lower limit of the O chemical potential as:

$$\Delta\mu_O > \frac{1}{2}E^f_{ZrO_2} \ldots..eq.(7)$$

$E^f_{ZrO_2}$ is the formation energy of ZrO_2 defined as $E^f_{ZrO_2} = E^{bulk}_{ZrO_2} - E^{bulk}_{Zr} - E^{gas}_{O_2}$ and we calculated it as -9.97 eV. Thus the range of accessible chemical potential values of O is:

$$-4.98\,eV < \Delta\mu_O < 0 \ldots..eq.(8)$$

A plot of the surface grand potential Ω^i against the accessible range of o chemical potentials is obtained for both stoichiometric and non-stoichiometric slabs for easy comparison of surface energies.

Phase commensurability is one major problem which is encountered when forming interfaces. The two surfaces used in forming the interface must be coherent due to the periodic boundary condition imposed in the calculation. The surface misfit parameter, Ø can be used to select obtain highly coherent interfaces.[33] This parameter is defined as:

$$Ø = 1 - \frac{2S_{A-B}}{S_A + S_B} \ldots.eq.(9)$$

Thus a unit cell of *c*-ZrO_2 with surface area of S_B is forced into coherency onto a substrate ZrC(111) with surface area S_A and the resulting overlap area between the two surfaces is $S_{A\text{-}B}$. The misfit parameter rather measures the average length scale misfit between the two unit cells[21] rather than an area misfit. In table 1, the calculated misfit parameters between ZrC(111) substrate surface and all *c*-ZrO_2 surfaces are summarized. It is apparent from this table that, the ZrC(111)||*c*-ZrO_2(111) interface combination has the lowest misfit parameter of 8.2% and acceptable. The resulting interface unit cell defined by the substrate ZrC(111) is 6.698 Å x 6.698 Å which is small and can be easily managed by the DFT calculation.

Table 1. Surface mismatch parameter Υ calculated for different combinations of ZrC and c-ZrO_2 surface

ZrC	c-ZrO_2	Overlap area($S_{1\text{-}2}$)/Å^2	Misfit (Υ)
(111)	(001)	44.874	0.169
(111)	(110)	44.874	0.157
(111)	(111)	44.874	0.072

The misfit parameter, being a geometrical measure cannot be used alone in building the interface. It has to be combined with other models. Two models are widely known to be used in ensuring commensurability of two different phases when forming an interface. Within the first approach, the unit cells of the two phases are multiplied by a factor corresponding to the other unit cell until both cells are commensurate with each other. The resulting supercell is usually large and unbearable for ab initio calculations. However, the resulting interface is coherent with very small mismatch parameter.[34]

The second method is widely used[35–40] as it results in small and manageable interface supercells (a single unit cell), suitable for ab initio calculations. In this model the lattice parameters of the phase considered as the substrate are used for the interface with the lattice parameter of the other phase, scaled until a perfect match with the substrate lattice is obtained.

3.4.2 Geometrical Models for Interface

Within the slab model used to study the interface, a thickness of 10.945 Å of ZrC (9 layers) was used. This thickness was considered to be enough to mimic electronic structure when ionic positions in the bulk are relaxed. The *c*-ZrO_2 (111) units were then pinned into registry, layer by layer on the exposed ZrC(111) surface. Thus in straining the c-ZrO2 to match the dimensions of the ZrC surface, coherent interfaces are ensured. The interface unit cell is therefore determined by the bulk and surface parameters of the ZrC(111). In this manner, the unit cell lattice parameter of the *c*-ZrO_2 (111) is shrunk by about 8%. After fixing the geometries of the two surfaces are the interface, the remaining degrees of freedom in the resulting interface structure are the perpendicular direction to the interface and the interface chemical composition.[41] From one to five layers of the *c*-ZrO_2 (111) units were built on the ZrC(111) surface.

In figure 2, we provide side views of the interface models used, with the different number of ZrO_2 layers. Each c-ZrO2 bilayer is approximately 3.5 Å thick.

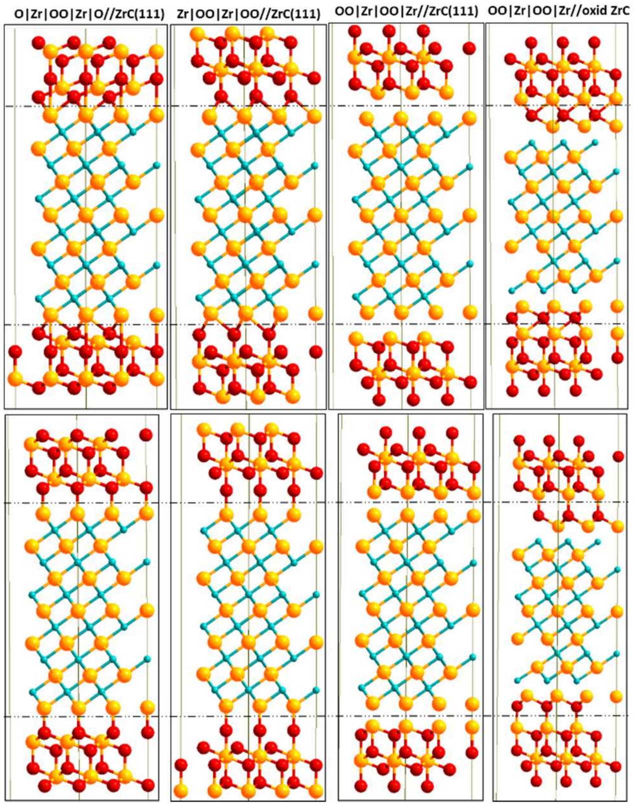

Figure 2. Side views of different interface model slabs using 2 layers of c-ZrO2 (111). Top structures are models with fcc bonding sites at interface with corresponding on-top interface bonding sites in the bottom structures

All interface models used were symmetric with respect to the center of the interface slab in order to remove any long range dipole-dipole interaction between exposed surfaces. 14 Å of vacuum was applied between two subsequent interface slabs in order to avoid any physical interactions between the slabs. The interface slab used thus has a configuration of: ---ZrC(111)|*c*-ZrO_2(111)|vacuum|ZrC(111)|*c*-ZrO_2(111)|vacuum|ZrC(111)|*c*-ZrO_2(111)|vacuum|ZrC(111)--. Since the ZrC(111) slab used is a reconstructed structure with four extra Zr atoms, the interface chemical composition is dependent on the number of Zr atoms (ZrC side) and the terminating layer of the *c*-ZrO_2(111) phase. In constructing the interface, three different terminations along the *c*-ZrO_2 [111] direction were considered: Zr|OO|Zr|OO|Zr|OO-, O|Zr|OO|Zr|OO|Zr|O-, OO|Zr|OO|Zr|OO|Zr-. We also considered the OO|Zr|OO|Zr|OO|Zr- on a ZrC(111) surface with an oxidized layer. A total of four different interface models were built as shown in figure 2.

3.4.3 Mechanics and Cohesion at the Interface

In defining the interface cohesion and stability, one important parameter mostly used is the interface tension γ_{int}, which is defined as the reversible work needed to separate the interface into two free surfaces.[42] According to this definition, an assumption made is that, both diffusional and plastic degrees of freedom are suppressed and hence negligible. The greater the γ_{int} value, the higher the energy needed to the separate the interface into two surfaces.

The interface tension can be defined according to the Dupre equation in terms of the interface and free surface energies as[43,44]

$$\gamma_{int} = \sigma_{ZrC} + \sigma_{c-ZrO_2} - \sigma_{ZrC||c-ZrO_2} \ldots\ldots eq.(10)$$

$\sigma_{ZrC||c-ZrO_2}$ is the interface energy also known as the adiabatic work of adhesion, $W_{ad} > 0$, σ_{ZrC} and σ_{c-ZrO_2} are the relaxed surface energies of the ZrC(111) and *c*-ZrO_2(111) surfaces respectively. In this definition, the relative strength of the interface versus the bulk bonds decides the preference for the formation of either the interface or the open surfaces.[22]

A measure of whether the interface formation or the free surfaces are the preferred can be determined by the interface tension. The magnitude and sign of γ_{int} (equation 10) provides a measure for whether the interface bonds are stronger than the internal bonds in the separate phases.[22] The criteria are that, $0 < \gamma_{int} < \sigma_{ZrC} + \sigma_{c-ZrO_2}$ corresponds to weakly coupled interface and $\gamma_{int} < 0$ to strongly coupled interfaces. The calculated values of σ_{ZrC} *and* σ_{c-ZrO_2} used here are obtained from their respective relaxed bulk equilibrium phases (Thus strain free surface slabs).

The adiabatic work of adhesion W_{ad} is however defined as:

$$W_{ad} = \frac{E^{tot}_{ZrC} + E^{tot}_{c-ZrO_2} - E^{tot}_{ZrC||c-ZrO_2}}{2A} \ldots. eq.(11)$$

$E^{tot}_{ZrC||c-ZrO_2}$ is the total energy of the fully relaxed interface slab, A is the interface area, E^{tot}_{ZrC} *and* $E^{tot}_{c-ZrO_2}$ are the total energies of the fully relaxed isolated ZrC(111) and *c*-ZrO_2(111) slabs respectively. Usually, the calculated W_{ad} value is a lower bound as compared to values obtained in cleavage experiments due to dissipative processes in physically separating the interface.[42] There is no relation between characterizing the interfacial strength and the bulk strain when depositing the *c*-ZrO_2. Hence, the $E^{tot}_{c-ZrO_2}$ value used is the total energy of the strained *c*-ZrO_2 for commensurability with the ZrC surface. In this manner, the strain energy component between $E^{tot}_{c-ZrO_2}$ and $E^{tot}_{ZrC||c-ZrO_2}$ is cancelled out due to the fact that the *c*-ZrO_2 is in the strain state.[22]

Aside the relaxed work of adhesion, the rigid work of adhesion W^{rigid}_{ad} can be used in characterizing the interface cohesion and stability. In this definition, the same strained state is ensured to exist in both the interface and the free surfaces. This provides maximum cancelation for the strain energy in the calculated interface energy.[45] This quantity provides information purely on the bonds formed at the interface irrespective of the free surfaces. It is calculated by separating the optimized interface structure into the different phases and rigidly calculating their energies without allowing the phases to fully relax. Equation 11 is finally applied in calculating the rigid work of adhesion.

A thermodynamic grand canonical ensemble treatment is used to compare the relative stabilities of the models with different chemical compositions. Within such ensemble, all models are assumed to be in chemical and thermal equilibria with bulk phases and the relevant thermodynamic quantity is the grand potential. An assumption made is that the entropic and volumetric contributions to the grand potential are negligible. For an interface of ZrC and *c*-ZrO_2, we define the interface grand potential as:

$$\Omega^{i/j}_{int} = \frac{1}{2}\left[\,\Omega^{i/j}_{slab} - N_{ZrC}\Omega_{ZrC} - N_{ZrO_2}\Omega_{ZrO_2}\right] - \Omega^{ZrO_2}_{surf} \;\ldots eq.(12)$$

$\Omega^{i/j}_{int}$ is the interface grand potential, $\Omega^{ZrO_2}_{surf}$ is the surface grand potential of the exposed *c*-ZrO_2 side of the interface slab, $\Omega^{i/j}_{slab}$, Ω_{ZrC}, Ω_{ZrO_2} are the grand potential of the interface slab, ZrC slab and ZrO_2 slabs respectively. N_{ZrC} and N_{ZrO_2} are the number of ZrC and ZrO_2 units in the respective slabs. Substituting the following:

$\Omega^{i/j}_{slab} = E^{i/j}_{slab} - \sum_k \mu_k N_k$, $\Omega_{ZrC} = E^{ZrC}_{bulk} - \mu_{ZrC}$, $\Omega_{ZrO_2} = E^{ZrO_2}_{bulk} - \mu_{ZrO_2}$, $\mu_{ZrC} = \mu_{Zr} + \mu_C$ and $\mu_{ZrO_2} = \mu_{Zr} + 2\mu_O$

Into equation 12, we obtain:

$$\Omega^{i/j}_{int} = \frac{1}{2}\Big[\,E^{i/j}_{slab} - N_{ZrC}E^{bulk}_{ZrC} - N_{ZrO_2}E^{bulk}_{ZrO_2} - \mu_{Zr}\left(N_{Zr} - N_{ZrC} - N_{ZrO_2}\right) - \mu_O\left(N_O - 2N_{ZrO_2}\right) - \left(E^{bulk}_{ZrC} - \mu_{Zr}\right)\left(N_C - N_{ZrC}\right)\Big] - \Omega^{ZrO_2}_{surf} \;\ldots\ldots\ldots eq.(13)$$

μ_{Zr}, μ_C, μ_O are the chemical potentials of Zr, C and O respectively. N_k is the number of that specie, $E^{i/j}_{slab}$ is the total energy of the interface slab, E^{ZrC}_{bulk} and $E^{ZrO_2}_{bulk}$ are the bulk energies of ZrC and ZrO_2 respectively. Upon rearrangement of equation 13, we obtain the following:

$$\Omega^{i/j}_{int} = \frac{1}{2}\Big[\,E^{i/j}_{slab} - N_C E^{bulk}_{ZrC} - N_{ZrO_2}E^{bulk}_{ZrO_2} - \mu_{Zr}\left(N_{Zr} - N_C - N_{ZrO_2}\right) - \mu_O\left(N_O - 2N_{ZrO_2}\right)\Big] - \Omega^{ZrO_2}_{surf} \;\ldots\ldots\ldots eq.(14)$$

If we make the following definition, $\Delta\mu_O = \mu_O - \mu^*_O$, and $\Delta\mu_{Zr} = \mu_{Zr} - \mu^*_{Zr}$with $\mu^*_{Zr} = E^{bulk}_{Zr}\, and\, \mu^*_O = E^{gas}_{O_2}/2$ and

3.5 Interfacial Thermodynamics

For each couple of interface model used, the most stable chemical composition of the interface is determined by a thermodynamic approach.

substituting in equation 14 with subsequent rearrangement, we obtain:

$$\Omega^{i/j}_{int} = \frac{1}{2}\Big[E^{i/j}_{slab} - N_{ZrO_2}E^{bulk}_{ZrO_2} - N_C E^{bulk}_{ZrC} - E^{bulk}_{Zr}\left(N_{Zr} - N_C - N_{ZrO_2}\right) - \frac{1}{2}E^{gas}_{O_2}\left(N_O - 2N_{ZrO_2}\right) - \Delta\mu_{Zr}\left(N_{Zr} - N_C - N_{ZrO_2}\right) - \Delta\mu_O\left(N_O - 2N_{ZrO_2}\right)\Big] - \Omega^{ZrO_2}_{surf} \;\ldots\ldots..eq.(15)$$

If we define another quantity:

$$\emptyset^{i/j}_{int} = \frac{1}{2A}\Big[E^{i/j}_{slab} - N_{ZrO_2}E^{bulk}_{ZrO_2} - N_C E^{bulk}_{ZrC} - E^{bulk}_{Zr}\left(N_{Zr} - N_C - N_{ZrO_2}\right) - \frac{1}{2}E^{gas}_{O_2}\left(N_O - 2N_{ZrO_2}\right)\Big] - \left(\Omega^{ZrO_2}_{surf}/A\right) \ldots\ldots..eq.(16)$$

Substituting equation 16 into equation 15, we obtain an expression for the Interface grand potential as:

$$\gamma^{i/j}_{int} = \frac{1}{A}\Omega^{i/j}_{int} = \emptyset^{i/j}_{int} + \frac{1}{2A}\Big[\Delta\mu_{Zr}\left(N_C + N_{ZrO_2} - N_{Zr}\right) + \Delta\mu_O\left(2N_{ZrO_2} - N_O\right)\Big] \ldots.eq.(17)$$

Thus for each overlayer termination i, the interface grand potential $\Omega^{i/j}_{int}$ depends on $\Delta\mu_O$ and $\Delta\mu_{Zr}$. A derivation of the upper and lower boundaries of the O and Zr chemical potentials is provided in the supplementary information 1(SI.1). We however state them here as follows:

For $\Delta\mu_{Zr}$, upper boundary is $\Delta\mu_{Zr} = \mu_{Zr} - E^{bulk}_{Zr} < 0$ and lower boundary is$\Delta\mu_{Zr} > {}^1\!/_2\left(E^f_{ZrC} + E^f_{ZrO_2}\right)$ where $E^f_{ZrC} and\ E^f_{ZrO_2}$ are the formation energies of ZrC and c-ZrO_2 respectively. Thus the Zr chemical potential range is defined as:

$$-5.78\,eV < \Delta\mu_{Zr} < 0 \ldots\ldots eq.(18)$$

Tapez une équation ici.

For O chemical potential, the upper limit is $\Delta\mu_O = \mu_O - {}^{1}\!/_{2}\,(E_{O_2}^{gas}) < 0$ and the lower boundary is $\Delta\mu_O > (E_{ZrO_2}^{f}/2)$ and the range of chemical potentials for O is:

$$-4.98 < \Delta\mu_O < 0 \ldots\ldots.eq.(19)$$

4 RESULTS AND DISCUSSION

4.1 XPS, ToF-SIMS and TEM-ED Experiments

Details on the experimental results are found in a previous paper. (100 interface paper)

4.2 Finite Temperature Molecular Dynamics Simulation

This section discusses the results obtained during the MD simulation. A haphazard ZrO_2 structure was observed to grow on the ZrC(111) surface at 1000 K. This structure shows O atoms forming three-fold hollow bonds between three Zr atoms of the ZrC(111) surface at the interface. The high temperature structure shows under coordinated Zr and O atoms.

Upon quenching to a T = 500 K, a more ordered structure was obtained (Figure 3).

The observed pattern of the ZrO2 atomic arrangements matches the crystal structure of *c*-ZrO_2 (111) and *t*-Zro_2 (101) structures. Thus the MD simulation confirms the formation of ZrO_2 on ZrC(111) surface from atomic depositions. This further complements the experimental results.

4.3 Surface and Bulk Properties of ZrC and ZrO_2

Details of the optimized lattice parameter, bulk modulus as well as the pressure derivative of the bulk modulus of ZrC is provided in a previous paper.[47] Thus the optimized lattice parameter for the ZrC bulk is 4.736 Å. The lattice parameter and all bulk characterizing parameters for the three phases of ZrO_2 are provided elsewhere.(100 interface paper) We however give a brief description of the computed values here. The fitted lattice parameter for the *c*-ZrO_2 is 5.143 Å. For the *t*-ZrO_2, the calculated *a* parameter is 3.649 Å and *c* = 5.257 Å and the tetragonal distortion $d_z = \Delta z/c = 0.050$. In case of the *m*-ZrO_2, the calculated values are: *a* = 5.243 Å, *b* = 5.307 Å, *c* = 5.412 Å and β = 99.20°. All these bulk parameters are well reproduced and are in excellent agreement with both experimental and other calculated values.

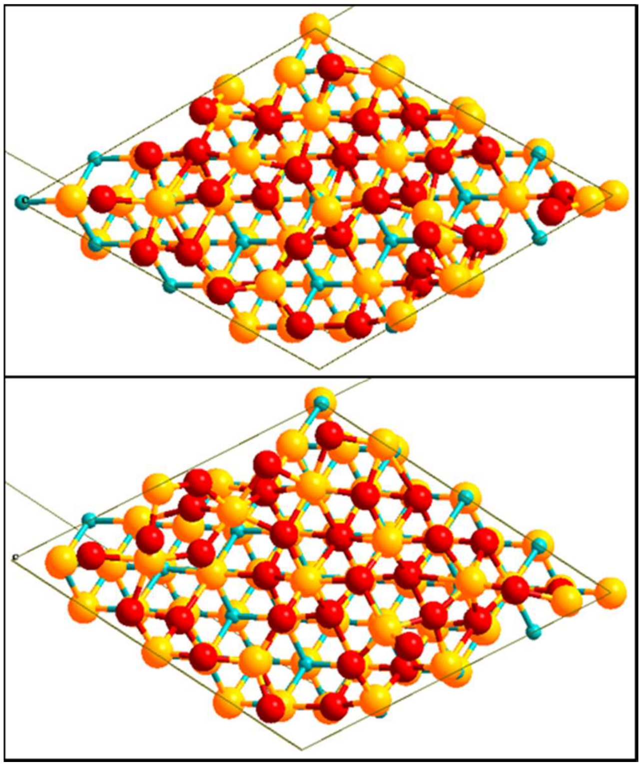

Figure 3. High temperature structure (top) and low temperature, T = 500 K (bottom) from MD simulation

In a previous paper[4], we calculated the surface energy for ZrC(111) surface terminating with four Zr atoms on both sides of the exposed surface at different chemical potentials of C. We calculated the surface energy as 0.169 eV/Å^2 at $\mu_C = E_C^{bulk}$. In figure 4, we provide a stability plot for the surface grand potential of each of the surface terminations of *c*-ZrO_2(111). The surface termination O|Zr|OO|Zr|O- is observed to be the most stable. The same stable termination is found in a different theoretical work.[32]

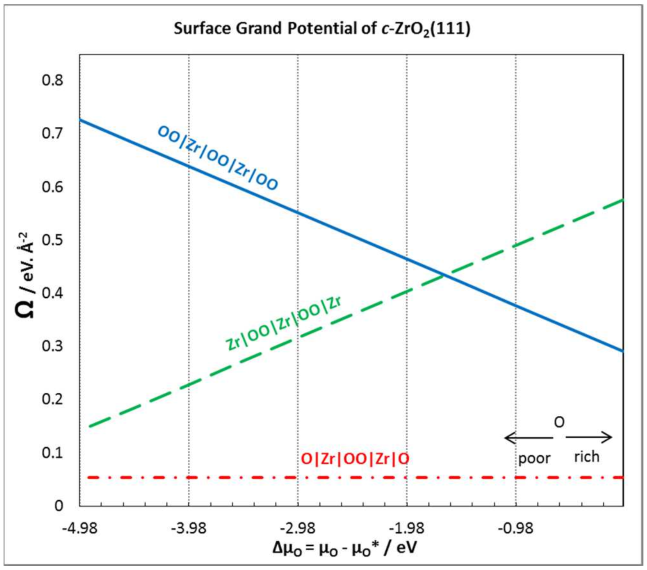

Figure 4. Surface Grand potential for different terminations of *c*-ZrO₂ (111) surface

For 6 layers of *c*-ZrO_2(111) with the O|Zr|OO|Zr|O-termination, the calculated surface grand potential at $\mu_O = E^{Gas}_{O_2}/2$ is 0.054 eV/Å^2 which agrees very well with 0.048 eV/Å^2 in a different work.[32] This is not surprising as this surface termination is the only stoichiometric structure used. Using the most stable surface termination, we calculated the surface energies with different number of ZrO_2 layers. Table 2 provides a summary for the surface energies with different number of layers. The surface energies of *c*-ZrO_2(111) surface with O|Zr|OO|Zr|O- termination converges after 3 layers. Thus we use a calculated surface energy 0.054 eV/Å^2 to compute the interface tension in equation 10.

Table 2. Calculated surface energies for O|Zr|OO|Zr|O termination of *c*-ZrO_2 (111) surface at all O chemical potentials

Number of layer	1	2	3	4	5	6
Ω^i/eVÅ^{-2}	0.068	0.053	0.055	0.055	0.054	0.054

4.4 Interface Cohesion and Structure

4.4.1 Rigid Work of Adhesion

Analysis of interfacial cohesion begins with the rigid work of adhesion, previously defined in section 3.4.3. With the rigid work of adhesion, bulk properties of ZrC and c-ZrO2 are cancelled out and the resulting parameter depends solely on interfacial properties. Table 3 provides summary for the rigid work of adhesion values. In this table, it is apparent that the rigid work of adhesion is always lower than the relaxed work of adhesion for nearly all the interface models considered. Thus the relaxation of the interface structure in the relaxed work of adhesion contributes significantly to the interface properties and results in a higher value than the rigid calculation. This relaxation is involved in releasing the strain imposed in the c-ZrO2 over-layer when it is forced into registry with the ZrC substrate.

Moreover, table 3 and figure 5 shows that, using the rigid work of adhesion, the most stable interface model is the *c*-ZrO_2 (Zr|OO|Zr|OO--) interface model compared to the other models. With this interface model, convergence of the W_{ad}^{rigid} rigid parameter begins at 3 *c*-ZrO_2 layers.

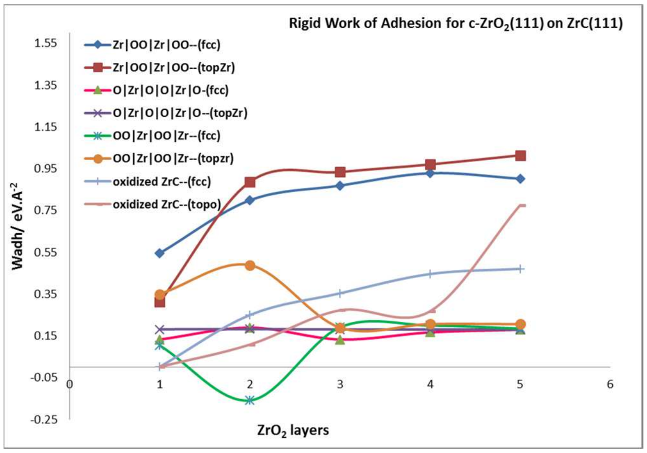

Figure 5. Rigid Work of adhesion for different interface models of *c*-ZrO₂ (111) on ZrC(111) surface

4.4.2 Relaxed Work of Adhesion

The relaxed work of adhesion is calculated for all the fully relaxed interfacial systems by allowing the separated ZrC and *c*-ZrO_2 slabs to fully relax. This parameter characterizes the interfacial bond strengths. In table 3, the relaxed work of adhesion calculated for the four interface models are summarized. According to table 3, the interface model involving two layers of oxygen from the ZrO_2 side (Zr|OO|Zr|OO--) is the most stable in terms of interfacial strength as observed in the calculated relaxed work of adhesion.

Figure 6 provides a pictorial view for the relaxed work of adhesion for all the interface models considered. For all models tested, there is convergence of the work of adhesion after three layers of ZrO_2 deposited on the ZrC. The W_{ad} values initially decrease from one layer to two layers of ZrO_2 and sharply rise at three layers of ZrO_2 from which point it converges. Looking at the most stable model (Zr|OO|Zr|OO--), the W_{ad} value sharply increases from 0.251 eVÅ^{-2} at two layers of ZrO_2 to 0.965 eVA^{-2} at three ZrO_2 layers for the on-top Zr mode of adsorption.

Table 3. Rigid, $W_{ad}^{relaxed}$ and Relaxed, $W_{ad}^{relaxed}$ work of adhesion for different interface models using different number of c-ZrO2 (111) layers at both fcc and on-top adhesion sites at the interface region

Interface model	OO|Zr|OO|Zr—ZrC(111)		Zr|OO|Zr|OO—ZrC(111)		O|Zr|OO|Zr|O—ZrC(111)		OO|Zr|OO|Zr—4O-ZrC(111)	
c-ZrO2(111) layers	fcc	top	fcc	top	fcc	top	fcc	top
Rigid work of Adhesion, W_{ad}^{rigid}								
1	0.104	0.350	0.545	0.312	0.132	0.182	0.002	0.002
2	-0.158	0.488	0.798	0.886	0.190	0.182	0.250	0.108
3	0.191	0.190	0.869	0.934	0.133	0.181	0.353	0.273
4	0.200	0.207	0.928	0.970	0.67	0.180	0.446	0.268
5	0.185	0.206	0.902	1.014	0.180	0.181	0.471	0.776
Relaxed work of Adhesion, $W_{ad}^{relaxed}$								
1	0.383	0.366	0.351	0.264	0.098	0.131	0.240	0.215
2	-0.682	-0.327	0.134	0.251	0.124	0.164	-0.252	-0.106
3	0.458	0.457	0.859	0.965	0.093	0.209	0.484	0.481
4	0.536	0.529	0.966	0.991	0.214	0.257	0.511	0.503
5	0.570	0.582	0.983	1.095	0.254	0.306	0.669	0.583

This phenomenon is exactly opposite to what is observed in ceramics deposited on metals where the first one and two layers of deposition are rather stronger than the deposition of three or more layers of ZrO_2.[22] Thus the interfacial strength depends on the first three ZrO_2 layers deposited. The same feature has been observed for metals deposited on ceramics where the metals are predicted to wet the ceramic surface but then ball up for more than one monolayer of metal deposited.[48–50] The on-top interface models form strong interface structures than the fcc models. Weak interfaces are formed when one and two layers of ZrO_2 are deposited but strong interfaces are obtained when three or more layers of ZrO_2 are deposited.

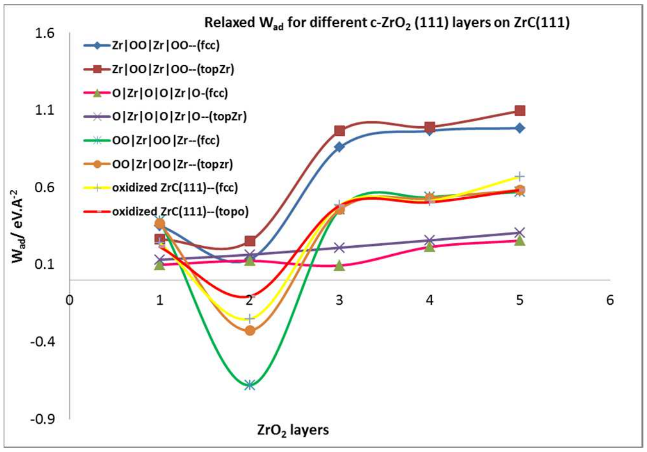

Figure 6. Relaxed Work of adhesion for different interface models of *c*-ZrO_2 (111) on ZrC(111) surface

The interface tension, defined in section 3.4.3 is a good parameter for assessing the interfacial mechanics and strength. It provides a measure for comparing the strength of bonds at the interface and in the corresponding bulk phases. According to the criteria defined, $0 < \gamma_{int} < \sigma_{ZrC} + \sigma_{c-ZrO_2}$ defines weakly coupled interface and $\gamma_{int} < 0$ to strongly coupled interfaces. With an asymptotic value of $\sigma_{ZrC(111)}$ = 0.169 eV/Å^2 and σ_{c-ZrO_2} = 0.054 eV/Å^2 combined with W_{ad} = 0.965 eV/Å2 for the most stable interface (Zr|OO|Zr|OO--), the calculated interface tension γ_{int} = -0.742 eV/Å^2. This shows that the interfacial bonds are stronger than the internal bonds in each ceramic bulk phase. When we consider the surface energy for the *c*-ZrO_2(111) with OO|Zr|OO|Zr|OO termination in an oxygen rich environment ($\Delta\mu_O$ = 0) as 0.292 eVÅ^{-2}, the calculated interface tension is still -0.504 eVÅ^{-2} which is still less than zero. Moreover, $\gamma_{int} \leq 0$ corresponds to a layer by layer growth of the ceramic known as the Frank-van-der-Merwe (FM) mode and the mixed mode also known as the Stranski-Krastanov (SK) growth mode.

4.4.3 Interfacial Structure Properties

A description for the structure and properties for the most stable interface models is provided here. The relaxed stable structures for the Zr|OO|Zr|OO//ZrC(111) interface model using 1, 2, 3, 4 and 5 layers of *c*-ZrO_2(111) are shown in figure 7. The interface structure appears to depend somehow on the number of ceramic layers. For this stable interface model, even though the starting geometry was O atoms from the ZrO_2 side adsorbed directly on top of Zr atoms of the ZrC, the final geometry was O atoms adsorbing at three fold hollow fcc sites between three Zr (ZrC) atoms. For all layers ZrO2, there is rearrangement of the Zr|OO|Zr|OO-- atoms upon forming the interface into a more stable O|Zr|O|Zr|OO— arrangement. Thus the exposed surface of the slab terminates with an O layer.

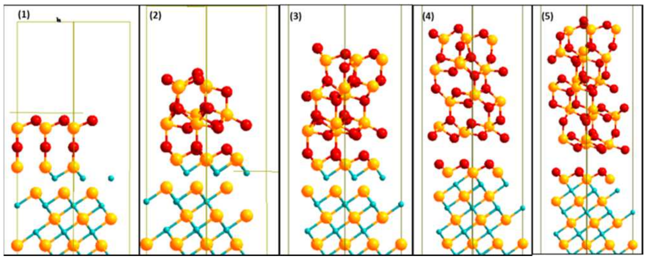

Figure 7. Relaxed stable structures for 1, 2, 3, 4 and 5 (from left to right) c-ZrO2(111) deposited on Zrc(111). The most stable interface model Zr|OO|Zr|OO—ZrC(111) is shown here

The crystal shape of the ZrC phase is maintained. However there is transformation of the *c*-ZrO_2 phase into *m*-ZrO_2. The phase transition is highly evident in the middle of the 3, 4, and 5 layer ZrO_2 interface structures with 3- fold and 4- fold O atoms as well as 6- fold and 7- fold Zr atoms. The (c→m) transformation is however not complete one due to the restraint imposed periodic boundary condition. At T= 0 K, the *m*-phase is about 7% large in volume than the c-phase and hence this transformation reduces the misfit of about 8% already calculated for this interface model. A similar transformation pattern in found in ceramics deposited on metals.[22]

Two type of oxygen bonds are observed at the interface: O1 atoms (ZrO_2) closer to the interface plane, bonding at fcc sites on the ZrC surface and O_2 atoms (ZrO_2) above the interface plane, bonding directly on top of Zr (ZrC) atoms. The fcc bonds are exactly the same found in a previous study when ZrC(111) surface was completely oxidized with a monolayer of oxygen.[10] It was also observed to passivate the ZrC(111) surface with no further diffusion of oxygen into the bulk. In the 1-layer ZrO2 interface, no fcc bonds of the O1 atoms are observed due to the O2 atoms pushing outwards from their bulk positions. These O2 atoms do not show any bonding with the Zr (ZrC) atoms in all layers of ZrO_2 deposited. The bond distances of the O2 type atoms with the Zr (ZrC) atoms have a minimum of 4 Å. Consequently, at $\geq 3\ ZrO_2$ layers, there is structural failure of ZrO_2 coating on the ZrC substrate. This crack is highly visible in the 4-ZrO_2 layer interface structure in figure 7. The crack leaves a monolayer of oxygen deposited on the ZrC. Thus there is a mixed mode of deposition of ZrO_2 on ZrC. A monolayer of oxygen is formed on the ZrC surface and the remaining ZrO_2 layers balls up. This is not surprising as the very negative interface tension calculated in section 4.4.2 suggests a mixed mode of deposition. Also the high work of adhesion, showing an over-adhered interface results in failure in the ceramic layer, a few Angstrom distance from the interface plane.

Using the 4-layer ZrO_2 interface model, the calculated bond distances for the O1 atoms at the fcc site of ZrC are $d_{(01\text{-}Zr)}$ fcc = [2.144 – 2.169] Å. These distances are in very good agreement with the calculated values O at fcc sites when ZrC(111) surface is fully oxidized by a monolayer of oxygen with distances of 2.144 Å and 2.145Å.[10]

4.5 Thermodynamic Stability of the Interface

In this section, analysis of the thermodynamic stability of the different interface models used are considered. The stability of the interface is calculated with respect to the respective bulk phases and not the surface slabs forming the interface. The interface grand potential $\Omega_{int}^{i/j}$ provides a measure of stability for the different interface models in different terminations. According to equation 17, the interface grand potential has an interface dependent term $\emptyset_{int}^{i/j}$ which only differs from the corresponding surface term γ^{i} in equation 4. As such, for the purpose of brevity and clarity, table 4 provides the $\emptyset_{int}^{i/j}$ values.

Table 4. Interface dependent terms of the interface grand potential $\emptyset_{int}^{i/j}$

Model site	$\emptyset_{int}^{i/j}$/ eV. Å^{-2}
O|Zr|OO|Zr|O-ZrC(111)	
fcc	-0.562
top	-0.605
Zr|OO|Zr|OO-ZrC(111)	
fcc	-1.555
top	-0.451
OO|Zr|OO|Zr-ZrC(111)	
fcc	-0.257
top	-0.251
Zr|OO|Zr-oxidized ZrC(111)	
fcc	-0.444
top	-0.434

This terms do not depend on the chemical potentials of excess Zr and O species. In table 4, it is apparent that interface is readily formed for all models (due to the negative values of the grand interface dependent terms) with the OO|Zr|OO|Zr--ZrC(111) model being the least stable amongst them. It is however evident from table 4 that the most stable model is the Zr|OO|Zr|OO//ZrC(111) fcc model, contradicting the the top Zr|OO|Zr|OO//ZrC(111) top model calculated to be the most stable using the relaxed work of adhesion parameter. However, it is worth pointing out that even though the fcc and top models used different starting point of interfacial atom adsorption, the two models resulted in the same configuration with interface O atoms bonding at fcc sites. In addition to this the difference between the calculated relaxed work of adhesion values for the two models is only 0.042 eV/ Å^2 using 4 layers of *c*-ZrO$_2$. The interface grand potential thus corroborates the stability criteria established in section 4.4.2 with Zr|OO|Zr|OO//ZrC(111) being the most stable. When the chemical potentials of excess O and Zr atoms are considered, the calculated $\Omega_{int}^{i/j}$ value when minimized for every ($\Delta\mu_{Zr}$, $\Delta\mu_{O}$) pair resulted in Zr|OO|Zr|OO//ZrC(111) being the most stable model formed.

4.6 Interfacial Electronic Properties

4.6.1 Density of States

The electronic features at the interface are analyzed by first considering the density of states when the free surfaces form the interface.

As an initial description of the density of states (DOS) at the interface, a total DOS (TDOS) obtained by projecting the density of states onto all atoms at the interface and compared with the DOS of the individual separate surfaces. In figure 8, the TDOS for the most stable interface model, Zr|OO|Zr|OO//ZrC(111) using 3 layers of ZrO$_2$ is shown.

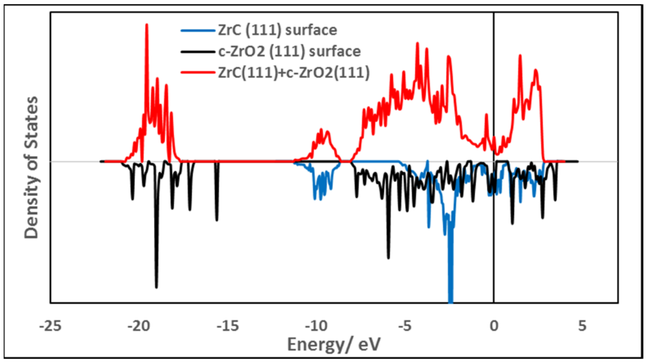

Figure 8. TDOS of interfacial structure Zr|OO|Zr|OO--ZrC(111) top site compared with DOS of corresponding surfaces. An interface model with 4 layers of c-ZrO$_2$ (111) is used

Figure 8 also includes the TDOS for the corresponding surface slabs used in constructing this interface model. In figure 8, the valence band maximum is fixed by both ZrC and c-ZrO$_2$ phases. However, the conduction band minimum is fixed by ZrC(111) surface upon forming the interface. No new interfacial states are observed in figure 8 and this is in agreement with the fact that c-ZrO$_2$ deposits a layer of oxygen on the ZrC(111) surface with the remain layers breaking off from the interface as explained in section 4.4.3

In order to understand the shift in bands when the surface atoms come together to form the interface, the DOS are projected onto the atoms at the interface and the corresponding atoms in the surface slabs in figure 9. Upon forming the interface, the Zr (ZrC) conduction bands shift to higher energies as they are filled with electrons from O (ZrO$_2$) with a dip at the Fermi level, stabilizing further the interface formed compared to the high level of states at the Fermi level of the corresponding surface. The Zr (ZrC) atoms form a new sharp core state at -18 eV corresponding to the Zr-O bonds formed at the interface. Thus the Zr (ZrC) – O (ZrO$_2$) bond closest to the interface plane is highly localized. There is no significant changes in the C (ZrC) states upon forming the interface with only the valence bands shifting slightly to higher energies. For Zr (ZrO$_2$) bands, they are shifted to lower energies upon forming the interface. The Zr (ZrO$_2$) sharp band at -15.6 eV which was initially mixed O (ZrO$_2$) closest to the interface plane is now lost upon forming the interface. This further explains the breakage of the c-ZrO$_2$ (111) phase after depositing an oxygen layer on the ZrC (111) surface. These Zr (ZrO$_2$) bands become diffuse upon forming the interface as their bonds with the closest O (ZrO$_2$) to the interface plane are broken and the electrons are delocalized. The high surface states of the O (ZrO$_2$) closest to the interface plane are quenched upon forming the interface and their sharp peaks at -15.6 eV are also lost as they break off from the c-ZrO$_2$ phase and deposit on the ZrC (111) phase. In the valence band, the O (ZrO$_2$) closest to the interface plane interacts strongly with the Zr (ZrC) bands due to their sharp peaks while the O (ZrO$_2$) far from the interface plane interacts weakly with its diffuse bands and delocalized electrons.

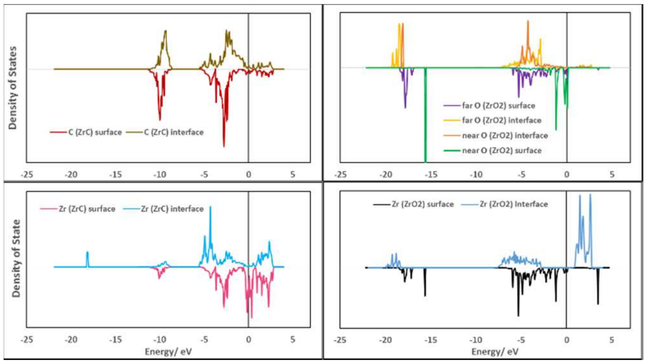

Figure 9. PDOS of each atom at the interface and in the corresponding surface slab for the Zr|OO|Zr|OO--ZrC(111) top site interface model. Upper part spectra of each plot are for atoms in the interface structure and those at the lower part are for the atoms in the corresponding surface slabs. Atoms labelled as near are closer to the interface plane than atoms labelled as far

Figure 10 provides a spatial profile of the electronic structure upon moving from the stable bulk faces to form the exposed surfaces and subsequently forming the interface. Thus in figure 10, the DOS are projected onto the atoms parallel to the interface plane, moving from bulk ZrC to the interface region and then bulk c-ZrO_2 and finally to the exposed c-ZrO_2 (111) surface. The C bands in bulk ZrC remains fairly the same upon forming the interface. In addition, the Zr valence band of ZrC are shifted to lower energies when they form the interface with the introduction of a sharp core state at -18.1 eV which mixes with the O core states of ZrO_2 closest to the interface plane. At the interface region, the valence band is a mixture of Zr (ZrC) d-bands and O (ZrO_2) p-bands with a covalent bonding nature. There is clearly diffuse interaction of the O (ZrO_2) p-bands far from the interface plane, explaining further the weak interaction of the second O layer (ZrO_2) far from the interface plane when the interface is formed.

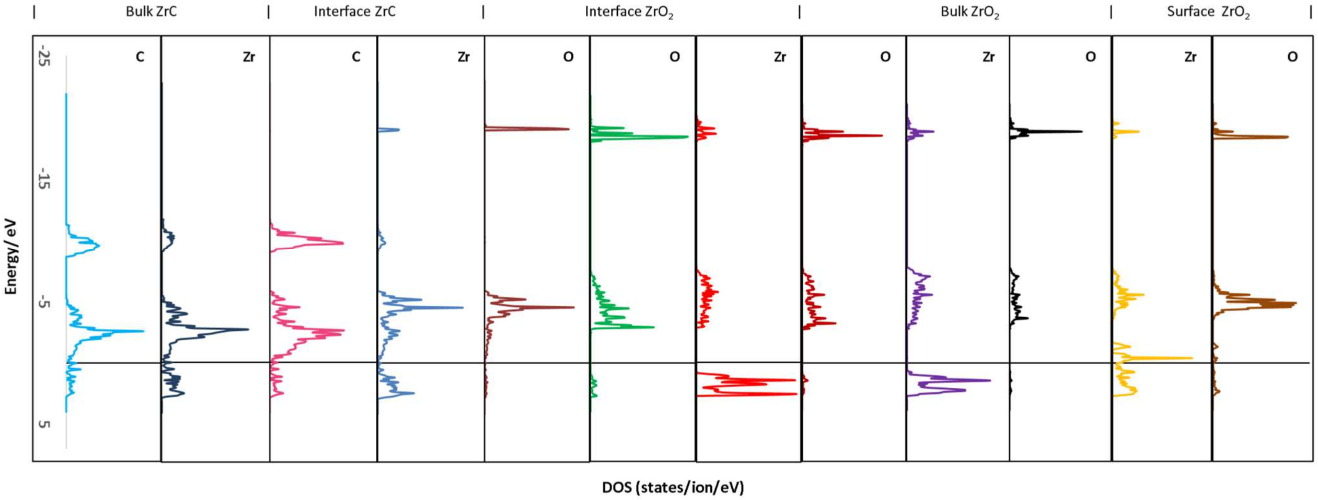

Figure 10. PDOS of atoms at the interface, in the bulk and the exposed surface of the 4 c-ZrO2 layer interface slab (Zr|OO|Zr|OO—ZrC (111)). The states are aligned parallel to the interface plane with each region marked on the top layer. The Fermi level is aligned at the energy zero position

It is also apparent that the O (ZrO_2) p-bands far from the interface maintains the bulk nature of such bands with a similar feature for the Zr (ZrO_2) d-bands far from the interface plane. The conduction band in this bulk ZrO_2 region is mainly Zr- d states. Moving to the exposed surface on the ZrO_2 side, the Zr –d states in the conduction band are reduced, shifted to lower energies and new states appear close to the Fermi level while the valence band become less diffuse. The exposed ZrO_2 surface is stabilized by the oxygen termination as there are fairly no states around the Fermi level. This termination is the same found for the most stable exposed surface of c-ZrO_2 (111).

4.6.2 Charge Transfer Analysis

A Bader charge analysis is provided in this section to understand how charges are transferred upon forming the interface from the cleaved surfaces. The charge transfer on the atoms are arranged in a spatial profile of the atoms from the surface to respective layers in the different phases forming the interface as described by Christensen and Carter.[51]

As a first step, we provide a charge transfer analysis for the most stable interface with different layers of *c*-ZrO_2 (111) starting from one to five in a spatial profile and finally analyze the four *c*-ZrO_2 (111) layer stable interface model, Zr|OO|Zr|OO//ZrC(111) top site.

Table 5 shows that upon forming the interface from the free surfaces, there is significant amount of charge transfer at the interfacial region. Nearly all the charge movement are from the cations (Zr) on the ZrC side of the interface plane to the O atoms (ZrO_2) closest to the interface plane. Initially with one layer of ZrO_2 deposited, there is the transfer of approximately 0.50 e^- from Zr (ZrC) to O atoms on ZrO_2 side of the interface. This value increases with the number layers and becomes fairly constant at three layers of ZrO_2 deposited. The high charge transfer of more than 0.90 e^- from Zr (ZrC) to O (ZrO_2) closest to the interface results in very strong interfacial bonds between the interface Zr and O atoms, subsequently causing breakage of the O layer (ZrO_2) closest to the interface from the remaining part of the ZrO_2 phase. In all layers of ZrO_2

deposited, there is essentially no significant charge redistribution in the atomic layers farther away from the interface moving toward the bulk region of the respective phases. With three or more ZrO_2 layers deposited, the high charge transferred from interface cations to anions releases part of the axial strain imposed on the ZrO_2 phase as it is brought into registry with the ZrC substrate upon forming the interface. The magnitude of the charges transferred from Zr (ZrC) to O (ZrO_2) for the different layers of ZrO_2 are in the same pattern as the relaxed work of adhesion computed for the different number of layers.

Table 5. Charge transfer analysis of Interfacial structure between ZrC(111) surface and different number of layers of *c*-ZrO_2(111) in the Zr|OO|Zr|OO—ZrC (111) top site interface model. Values reported are net charges (electrons/atom) obtained with respect to the charges on the atom in the corresponding surface slabs that form the interface.

	Ion type		ZrO_2 layers on ZrC				
			1	2	3	4	5
ZrO_2 layer at Interface		Zr	0.05	0.01	-0.09	-0.07	-0.08
	O		0.04	0.42	0.21	0.25	0.23
		O	0.38	0.73	0.67	0.75	0.75
Interface Plane							
ZrC layer at Interface	Zr		-0.49	-0.89	-0.94	-0.92	-0.93
		C	0.00	-0.04	-0.05	-0.07	-0.07

In table 6, a spatial profile of the charge transfer is provided in order to obtain further understanding of the electronic structure of the interface formed and how it affects the corresponding bulk and surface properties. The most stable Zr|OO|Zr|OO--ZrC(111) top site model with four layers of ZrO_2 is used in this analysis. In this table, the average charge distribution per layer is arranged in a profile moving from the interface plane towards the bulk and then the exposed surface regions. In this analysis, it is essential to compare utilize the ΔQ_s values of table 6 when analyzing the surface regions (these values are with respect to atoms in the corresponding surface slabs0 while ΔQ_b values are used when making bulk comparisons (ΔQ_b values are with respect to corresponding atoms in bulk phases). At the interfacial region, there is significant amount of charge transfer, compared to the corresponding free surface. This high amount of charge distribution originates mainly from Zr (ZrC) and placed on the O atoms (ZrO_2) at the interface. However, moving away from the interface into the bulk regions of both phases, and finally to the exposed surface area of ZrO_2, there is virtually no charge redistribution. The ΔQ_b values for the bulk regions also shows no charge redistribution upon forming the interface. This further ascertains the interface to be affected only by atomic layers closer to the interface plane.

5 Summary and Conclusion

Different experimental techniques have been used to characterize the oxide layer formed on ZrC nano particles. XPS, ToF-SIMS, TEM-ED experiments were used to analyze the oxide layer and confirmed the presence of ZrO_2, mainly cubic with some tetragonal ZrO_2 as a shell around the ZrC nano particles. Details of the experimental results are provided in a previous paper.[10]

Finite temperature ab initio molecular dynamics was used to build 2 layers of ZrO_2 on ZrC (111) surface. An ordered layer of ZrO_2 was observed to form on the ZrC(111) surface.

Periodic DFT was used to characterize the interface between ZrC (111) and c-ZrO_2 (111). The preferred interface observed was formed between Zr terminated ZrC(111) and an OO-terminated c-ZrO_2 (111) leading to a final interface model Zr|OO|Zr|OO//ZrC(111). The main mechanical property used to characterize the interface is the relaxed work of adhesion Wad. This value reveals the Zr|OO|Zr|OO//ZrC(111) model as the most stable interface with a high Wad value compared to the other models. A thermodynamic analysis using the interface grand potential also confirmed the Zr|OO|Zr|OO//ZrC(111) model as the most stable interface. A close examination of the structural properties revealed deposition of an oxygen layer from the ZrO_2 phase onto the ZrC(111) surface with the remaining part of ZrO_2 breaking off from the interface, suggestion a crack at this interface. This is also in very good agreement in a previous study on the oxidation of Zrc (111) surface which revealed the formation of an oxygen layer on the surface with further addition of O atoms leading to an endothermic reaction.

The electronic structure of the interface was analyzed using the density of states calculated for the interface models. The DOS showed no major changes in induced by the formed interface but only features of the deposited oxygen layer. Using Bader charge analysis, there is an enormous amount of charge transfer at the interface, originating mainly from cations on the ZrC side (Zr) to the O atoms from ZrO_2 at the interfacial region. Moreover, there is virtually no charge redistribution in the bulk regions of the interface slab. Thus the interfacial properties are governed by local effects, only confined to the first two atomic layers around the interface plane.

Table 6. Spatial profile of Charge transfer arranged along the normal direction of the interface. ΔQ_s is difference in the charge of the ion with the corresponding ion in the isolated surface slab used to create the interface and ΔQ_b is the difference in charge between the ion and the corresponding ion in the bulk structure.

Layer in slab	4 ZrO_2 (surface)			3 ZrO_2 (bulk)			2 ZrO_2 (bulk)			1 ZrO_2 (interface)				1 ZrC (interface)		2 ZrC (bulk)	
Ion type	O	Zr	O	Zr	O	O	Zr	O	O	Zr	O	O		Zr	C	Zr	C
Absolute Q	7.14	2.63	7.18	1.79	7.17	7.11	1.72	7.09	7.11	1.72	7.13	7.17		2.00	5.74	2.28	5.71
ΔQ_s (vs surface)	-0.04	0.07	0.01	0.04	0.09	-0.08	-0.01	-0.02	-0.07	-0.07	0.25	0.75		-0.92	-0.07	-0.07	-0.03
ΔQ_b (vs bulk)	-0.01	0.94	0.03	0.10	0.02	-0.04	0.03	-0.06	-0.04	0.03	-0.02	0.02		-0.34	0.08	-0.06	0.05

AUTHOR INFORMATION

Corresponding Author

* Corresponding author: tel +33 320 43 45 03, fax +33 320 43 65 61; email sylvain.cristol@univ-lille1.fr

Author Contributions

The manuscript was written through contributions of all authors. / All authors have given approval to the final version of the manuscript. / ‡These authors contributed equally. (match statement to author names with a symbol)

Funding Sources

Any funds used to support the research of the manuscript should be placed here (per journal style).

Notes

Any additional relevant notes should be placed here.

ACKNOWLEDGMENT

Numerical results presented in this paper were carried out using the regional computational cluster supported by Université Lille 1, CPER Nord-Pas-de-Calais/FEDER, France Grille, and CNRS. We highly appreciate and thank the technical staff of the CRI-Lille 1 center for their strong and helpful support. The project is supported by Agence Nationale de la Recherche under Contract No. ANR-12-BS08-004-02 (CollZSiC: Elaboration de nanocomposites coeur/coquille ZrC/SiC).

ABBREVIATIONS

TDOS, Total density of states; PDOS, Projected density of states; XPS, x-ray photoemission spectroscopy; DFT, density functional theory; PAW, projector augmented wavefunction.

REFERENCES

(1) Gosset, D.; Dollé, M.; Simeone, D.; Baldinozzi, G.; Thomé, L. Structural Behaviour of Nearly Stoichiometric ZrC under Ion Irradiation. *Nucl. Instrum. Methods Phys. Res. Sect. B Beam Interact. Mater. At.* **2008**, *266* (12–13), 2801–2805.

(2) Gosset, D.; Dollé, M.; Simeone, D.; Baldinozzi, G.; Thomé, L. Structural Evolution of Zirconium Carbide under Ion Irradiation. *J. Nucl. Mater.* **2008**, *373* (1–3), 123–129.

(3) Li, H.; Zhang, L.; Cheng, L.; Wang, Y. Oxidation Analysis of 2D C/ZrC–SiC Composites with Different Coating Structures in CH4 Combustion Gas Environment. *Ceram. Int.* **2009**, *35* (6), 2277–2282.

(4) Osei-Agyemang, E.; Paul, J.-F.; Lucas, R.; Foucaud, S.; Cristol, S. Stability, Equilibrium Morphology and Hydration of ZrC(111) and (110) Surfaces with H2O: A Combined Periodic DFT and Atomistic Thermodynamic Study. *Phys. Chem. Chem. Phys.* **2015**, *17* (33), 21401–21413.

(5) Arya, A.; Carter, E. A. Structure, Bonding, and Adhesion at the ZrC(1 0 0)/Fe(1 1 0) Interface from First Principles. *Surf. Sci.* **2004**, *560* (1–3), 103–120.

(6) Kato, S.; Ozawa, K.; Edamoto, K.; Otani, S. Photoelectron Spectroscopy Study of the Oxidation of ZrC(100). *Jpn. J. Appl. Phys.* **2000**, *39* (Part 1, No. 9A), 5217–5222.

(7) Viñes, F.; Sousa, C.; Illas, F.; Liu, P.; Rodriguez, J. A. Density Functional Study of the Adsorption of Atomic Oxygen on the (001) Surface of Early Transition-Metal Carbides. *J. Phys. Chem. C* **2007**, *111* (3), 1307–1314.

(8) Kitaoka, H.; Ozawa, K.; Edamoto, K.; Otani, S. The Interaction of Water with Oxygen-Modified ZrC(100) Surfaces. *Solid State Commun.* **2001**, *118* (1), 23–26.

(9) Rodriguez, J. A.; Liu, P.; Gomes, J.; Nakamura, K.; Viñes, F.; Sousa, C.; Illas, F. Interaction of Oxygen with ZrC(001) and VC(001): Photoemission and First-Principles Studies. *Phys. Rev. B* **2005**, *72* (7), 075427.

(10) Osei-Agyemang, E.; Paul, J.-F.; Lucas, R.; Foucaud, S.; Cristol, S. Oxidation and Equilibrium Morphology of Zirconium Carbide Low Index Surfaces Using DFT and Atomistic Thermodynamic Modeling. *J. Phys. Chem. C* **2016**, *120* (16), 8759–8771.

(11) Shimada, S.; Yoshimatsu, M.; Inagaki, M.; Otani, S. Formation and Characterization of Carbon at the ZrCZrO2 Interface by Oxidation of ZrC Single Crystals. *Carbon* **1998**, *36* (7–8), 1125–1131.

(12) Shimada, S.; Yoshimatsu, M.; Yunazar, F.; Otani, S. Deposition and Characterization of Carbon at the Interface by Oxidation of Single Crystals of Carbides (HfC, ZrC, TiC). *Tanso* **1999**, *1999* (190), 223–228.

(13) Noda, T.; Yamazaki, M.; Ozawa, K.; Edamoto, K.; Otani, S. Oxygen Adsorption on a ZrC(111) Surface: Angle-Resolved Photoemission Study. *Surf. Sci.* **2000**, *450* (1–2), 27–33.

(14) Noda, T.; Nakane, T.; Ozawa, K.; Edamoto, K.; Tanaka, S.; Otani, S. Photoemission Study of the Oxidation of ZrC(111). *Solid State Commun.* **1998**, *107* (4), 145–148.

(15) Ozawa, K.; Yoshii, T.; Noda, T.; Edamoto, K.; Tanaka, S. Coadsorption of Oxygen and Cesium on ZrC(1 1 1). *Surf. Sci.* **2002**, *511* (1–3), 421–434.

(16) Tokumitsu, S.; Anazawa, T.; Tanabe, A.; Sekine, R.; Miyazaki, E.; Edamoto, K.; Kato, H.; Otani, S. Interaction of Hydrogen with ZrC(111) Surface: Angle-Resolved Photoemission Study. *Surf. Sci.* **1996**, *351* (1–3), 165–171.

(17) Vojvodic, A.; Ruberto, C.; Lundqvist, B. I. Atomic and Molecular Adsorption on Transition-Metal Carbide (111) Surfaces from Density-Functional Theory: A Trend Study of Surface Electronic Factors. *J. Phys. Condens. Matter Inst. Phys. J.* **2010**, *22* (37), 375504.

(18) Aono, M.; Oshima, C.; Zaima, S.; Otani, S.; Ishizawa, Y. Quantitative Surface Atomic Geometry and Two-Dimensional Surface Electron Distribution Analysis by a New Technique in Low-Energy Ion Scattering. *Jpn. J. Appl. Phys.* **1981**, *20* (11), L829–L832.

(19) Hayami, W.; Souda, R.; Aizawa, T.; Otani, S.; Ishizawa, Y. Analysis of the HfC(111) Surface Structure by Impact Collision Ion Scattering Spectroscopy (ICISS). *Surf. Sci.* **1992**, *276* (1), 299–307.

(20) Hayami, W.; Souda, R.; Aizawa, T.; Otani, S.; Ishizawa, Y. Analysis of the NbC(111)-(√3 × √3)R30°-Al Surface Structure by Impact-Collision Ion-Scattering Spectroscopy. *Phys. Rev. B* **1993**, *47* (20), 13752–13758.

(21) Christensen, A.; Carter, E. A. First-Principles Characterization of a Heteroceramic Interface: ZrO2(001) Deposited on an Alpha-Al2O3(1(1)over-bar02) Substrate. *Phys. Rev. B Condens. Matter Mater. Phys.* **2000**, *62* (24), 16968–16983.

(22) Christensen, A.; Carter, E. A. Adhesion of Ultrathin ZrO2(111) Films on Ni(111) from First Principles. *J. Chem. Phys.* **2001**, *114* (13), 5816–5831.

(23) Shirley, D. A. High-Resolution X-Ray Photoemission Spectrum of the Valence Bands of Gold. *Phys. Rev. B* **1972**, *5* (12), 4709–4714.

(24) Hafner, J. Ab-Initio Simulations of Materials Using VASP: Density-Functional Theory and beyond. *J. Comput. Chem.* **2008**, *29* (13), 2044–2078.

(25) Mermin, N. D. Thermal Properties of the Inhomogeneous Electron Gas. *Phys. Rev.* **1965**, *137* (5A), A1441–A1443.

(26) Kresse, G.; Joubert, D. From Ultrasoft Pseudopotentials to the Projector Augmented-Wave Method. *Phys. Rev. B* **1999**, *59* (3), 1758–1775.

(27) Perdew, J. P.; Burke, K.; Ernzerhof, M. Generalized Gradient Approximation Made Simple. *Phys. Rev. Lett.* **1996**, *77* (18), 3865–3868.

(28) Methfessel, M.; Paxton, A. T. High-Precision Sampling for Brillouin-Zone Integration in Metals. *Phys. Rev. B* **1989**, *40* (6), 3616–3621.

(29) Monkhorst, H. J.; Pack, J. D. Special Points for Brillouin-Zone Integrations. *Phys. Rev. B* **1976**, *13* (12), 5188–5192.

(30) Martin, L.; Vallverdu, G.; Martinez, H.; Cras, F. L.; Baraille, I. First Principles Calculations of Solid–solid Interfaces: An Application to Conversion Materials for Lithium-Ion Batteries. *J. Mater. Chem.* **2012**, *22* (41), 22063–22071.

(31) Christensen, A.; Carter, E. A. First-Principles Study of the Surfaces of Zirconia. *Phys. Rev. B* **1998**, *58* (12), 8050–8064.

(32) Yang, Y.-L.; Fan, X.-L.; Liu, C.; Ran, R.-X. First Principles Study of Structural and Electronic Properties of Cubic Phase of ZrO2 and HfO2. *Phys. B Condens. Matter* **2014**, *434*, 7–13.

(33) Liu, L. M.; Wang, S. Q.; Ye, H. Q. First-Principles Study of Metal/nitride Polar Interfaces: Ti/TiN. *Surf. Interface Anal.* **2003**, *35* (10), 835–841.

(34) Wang, X.-G.; Smith, J. R. Si/Cu Interface Structure and Adhesion. *Phys. Rev. Lett.* **2005**, *95* (15), 156102.

(35) Hashibon, A.; Elsässer, C.; Mishin, Y.; Gumbsch, P. First-Principles Study of Thermodynamical and Mechanical Stabilities of Thin Copper Film on Tantalum. *Phys. Rev. B* **2007**, *76* (24), 245434.

(36) Hashibon, A.; Elsässer, C. Approaches to Atomistic Triple-Line Properties from First-Principles. *Scr. Mater.* **2010**, *62* (12), 939–944.

(37) Dalverny, A.-L.; Filhol, J.-S.; Doublet, M.-L. Interface Electrochemistry in Conversion Materials for Li-Ion Batteries. *J. Mater. Chem.* **2011**, *21* (27), 10134–10142.

(38) Malyi, O. I.; Chen, Z.; Shu, G. G.; Wu, P. Effect of Sulfur Impurity on the Stability of Cubic Zirconia and Its Interfaces with Metals. *J. Mater. Chem.* **2011**, *21* (33), 12363–12368.

(39) Dai, H.; Du, J.; Wang, L.; Peng, C.; Liu, X. First-Principle Study of the AlP/Si Interfacial Adhesion. *Phys. B Condens. Matter* **2010**, *405* (2), 573–578.

(40) Radican, K.; Berdunov, N.; Manai, G.; Shvets, I. V. Epitaxial Molybdenum Oxide Grown on $\mathrm{Mo}(110)$: LEED, STM, and Density Functional Theory Calculations. *Phys. Rev. B* **2007**, *75* (15), 155434.

(41) Hashibon, A.; Elsässer, C.; Rühle, M. Structure at Abrupt Copper–alumina Interfaces: An Ab Initio Study. *Acta Mater.* **2005**, *53* (20), 5323–5332.

(42) Finnis, M. W. The Theory of Metal - Ceramic Interfaces. *J. Phys. Condens. Matter* **1996**, *8* (32), 5811.

(43) Liu, M. W. and X. *Ultrathin Metal Films*; Springer-Verlag: Berlin, 2004.

(44) Suresh, L. B. F. and S. *Thin Film Materials: Stress, Defect Formation and Surface Evolution*; Cambridge University Press: Cambridge, England, 2003.

(45) Hashibon, A.; Elsässer, C.; Rühle, M. Structure at Abrupt Copper–alumina Interfaces: An Ab Initio Study. *Acta Mater.* **2005**, *53* (20), 5323–5332.

(46) Grimblot, J. *L'analyse de Surface Des Solides*; Masson, 1995.

(47) Osei-Agyemang, E.; Paul, J. F.; Lucas, R.; Foucaud, S.; Cristol, S. Periodic DFT and Atomistic Thermodynamic Modeling of Reactivity of H2, O2, and H2O Molecules on Bare and Oxygen Modified ZrC (100) Surface. *J. Phys. Chem. C* **2014**, *118* (24), 12952–12961.

(48) Bogicevic, A.; Jennison, D. R. Variations in the Nature of Metal Adsorption on Ultrathin A${\mathrm{l}}_{2}$${\mathrm{O}}_{3}$ Films. *Phys. Rev. Lett.* **1999**, *82* (20), 4050–4053.

(49) Musolino, V.; Selloni, A.; Car, R. Atomic and Electronic Structure of Cu Clusters on MgO. *Surf. Sci.* **1998**, *402–404*, 413–417.

(50) Pacchioni, G.; Rösch, N. Supported Nickel and Copper Clusters on MgO(100): A First-principles Calculation on the Metal/oxide Interface. *J. Chem. Phys.* **1996**, *104* (18), 7329–7337.

(51) Christensen, A.; Carter, E. A. First-Principles Characterization of a Heteroceramic Interface: ZrO2(001) Deposited on an α-Al2O3(1102) Substrate. *Phys. Rev. B* **2000**, *62* (24), 16968–16983.

Insert Table of Contents artwork here

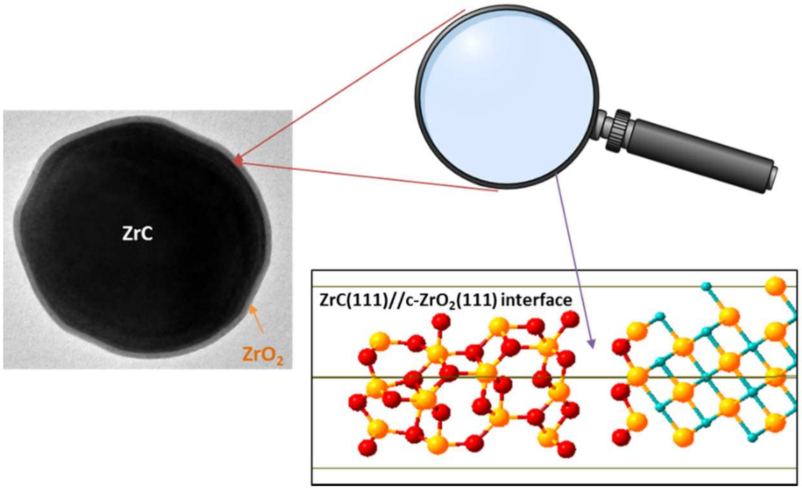

4. Conclusion

In this chapter the nature of the oxide layer formed on ZrC surfaces is determined through the combination of several experimental techniques. Through the use of XPS, the Zr, O and C peak analysis showed the presence of ZrO_2 with a thickness of about 3 nm on the ZrC substrates. However, it was observed that even at experimental conditions in ultra-high vacuum (UHV) during measurements, there was still the reformation of oxide after removal of the oxide layer. ToF-SIMS analysis was used to study this process and the depth profile of the oxide layer. TEM-ED analysis was also used to identify the crystal phases of ZrO_2 present on ZrC substrate. *c*-ZrO_2 with traces of *t*-ZrO_2 were observed as thin shells around the ZrC substrate surface.

Finite temperature ab-initio MD simulation was used to build a layer of ZrO_2 ontop of ZrC(100) surface and we observed the features of *c*-ZrO_2. Analysis of the interface between ZrC(100) surface and *c*-ZrO_2(001) revealed a strong interface formed. We observed interfacial properties to converge after three layers of *c*-ZrO_2(001) on ZrC(100) surface and the interfacial properties depend on only the first one or two ZrO_2 layers and not on subsequent layers.

For the interface formed between ZrC(111) surface and *c*-ZrO_2(111) surface, we observed a crack in the ZrO_2 phase formed on ZrC and this resulted in the deposition of an oxide layer ontop of ZrC as observed during the oxidation process of ZrC(111) surface in chapter IV. The interface is thus governed by local effects only confined to the first two atomic layers around the interface.

In conclusion, since a ZrO_2 layer is found around ZrC nano-crystallites, the interface model formed between ZrC(100) and ZrO_2(100) can be considered as the most stable. This is because the interface formed from the (111) surfaces of ZrC and ZrO_2 leads to deposition of an oxide layer ontop of ZrC with no ZrO_2 left.

Chapter VI: Grafting of Preceramic Polymeric Precursors on Functionalized Surfaces

Table of Contents

1. Introduction

This chapter concludes the project with a final part that involves grafting of polymeric precursors on exposed surfaces. Since studies in the previous chapter identified ZrO_2 layer on top of the substrate ZrC, studies in this chapter is carried out on the exposed surface of *t*-ZrO_2(001) on top of ZrC(100) substrate.

The chapter includes initial hydration of the exposed zirconia surface, followed by further functionalization with allyl(chloro)dimethylsilane. The final part along the steps of synthesizing ZrC/SiC core/shell nano-composites is to further graft the functionalized surface with a polymeric precursor, preferably polycarbsilanes. Other organic reagents are also explored for their functionalization.

The chapter is however made up of a fully written article which is under review for publication. The article is entitled "*Grafting of Preceramic Polymeric Precursors onto ZrC(100)//t-ZrO_2(001) using Grafting-to Approach en-route to Synthesizing ZrC/SiC Core/Shell Nano-composites: A Combination of Experiments and Theoretical Studies*". As the title implies, it is a combination of both experiments and theoretical studies. However the theoretical part is presented here and a combination with the experimental part will be made for the final published paper.

2. Grafting of Preceramic Polymeric Precursors onto ZrC(100)//*t*-ZrO_2(001) using Grafting-to Approach en-route to Synthesizing ZrC/SiC Core/Shell Nano-composites: A Theoretical Study

This section is made up of a fully written research article. The final published article will be a combination of experiments with theory and hence the theoretical part presented here will be combined with the experimental part from a different research group before publication. The article is presented here in the exact format as the journal that will publish it.

Grafting of Preceramic Polymeric Precursors onto ZrC(100)//*t*-ZrO$_2$(001) using Grafting-to Approach en-route to Synthesizing ZrC/SiC Core/Shell Nano-composites: A Theoretical Study.

Eric Osei-Agyemang[1], Dasan Arish,[2] Romain Lucas,[2] Sylvie Foucaud,[2] Jean-François Paul,[1] Sylvain Cristol[1]*

[1] Université de Lille 1, Univ. Lille, CNRS, ENSCL, Centrale Lille, Univ. Artois, UMR 8181 - UCCS - Unité de Catalyse et de Chimie du Solide.

[2] Université de Limoges, CNRS, ENSCI, SPCTS, UMR 7315, F-87000 Limoges, France.

KEYWORDS (Word Style "BG_Keywords"). Grafting, grafting-to, DFT, atomistic thermodynamic modeling, 3-butenoic acid, allyl(chloro)dimethylsilane, diphenylsilane, 1,4-diethynylbenzene,zirconium carbide, silicon carbide, zirconia, ZrC, SiC, ZrO$_2$.

ABSTRACT: Zirconium carbide (ZrC) being a non-oxide ceramic with a high melting point has excellent physical and mechanical properties that makes it applicable in harsh environmental conditions such as nuclear fuel reactor wall linen amongst others. However, there is a problem of oxidation as it forms low refractory oxides at temperatures of 500 – 600 °C. There is however no method described so far for controlling this oxidation and an anticipated method is to coat the surface with SiC which forms protective oxide layers at higher temperatures of 1400 °C. Silicon carbide (SiC) formed from polymeric precursors however has outstanding high temperature properties. This project therefore aims at grafting polymeric precursors on functionalized ZrC surface en-route to synthesizing ZrC/SiC core/shell nano-composites. In this study, the exposed surface on the zirconia side of t-ZrO$_2$(001) ontop of a ZrC(100) substrate is first modified with water. Water preferentially adsorbs molecularly and a subsequent functionalization with allyl(chloro)dimethylsilane (ACDMS) in a nucleophilic substitution reaction with the release of HCl was very weak. However, subsequent grafting of the polymeric precursor built from diphenylsilane and 1,4-diethynylbenzene monomers in a grafting-to approach through a hydrosilylation reaction was a highly favorable and exothermic reaction. As the main problem encountered is with nucleophilic substitution reaction of ACDMS and hydroxyl groups on the surface, a bifunctional organic molecule, 3-butenoic acid was exploited. 3-butenoic acid strongly adsorbed to surface Zr atoms through chelating effects of the carboxylic acid group and the subsequent hydrosilylation reaction with the preceramic precursor was also a favorable exothermic reaction.

1. INTRODUCTION

Zirconium carbide (ZrC) being a non-oxide Ceramic has a high melting point of 3400 °C and exhibits excellent mechanic and physical properties. The presence of these properties are advantageous and as such, ZrC is applied in several applications including the Aerospace industry and in cutting tools.[1,2] Advantage is also taken on the presence of extremely high melting point and as such, it is being considered in the nuclear industry as a structural and fission product barrier coating material for tri-isotropic (TRISO) coated nuclear fuel used in higher temperature reactors.[3] This makes it suitable for replacing or used in addition to the already used ceramic silicon carbide (SiC).[4–6]

Moreover, aside the aforementioned excellent properties that makes them applicable in a wide range of arenas, a major setback is the ease with which it oxidizes. ZrC, thus forms low refractory oxides at lower temperatures 500-600 °C.[7] This problem is a major setback in its numerous applications as the excellent physical and mechanical properties are deteriorated once it begins to oxide. Several accounts have been given on the oxidation process and mechanisms of ZrC. The various accounts have been given on oxidation at different conditions and also on the various low index surfaces of ZrC. All studies have shown extremely strong interaction of oxygen with ZrC surfaces. Both theoretical and experimental analysis have been done on the ZrC(111) surface.[8–12] All these studies showed complete dissociation of oxygen into atomic species and adsorption at three-fold hollow sites between three surface Zr atoms. On the ZrC(100) surface, several accounts has been given on the oxidation of this surface and all shows extremely reactivity of this surface with oxygen.[13–17] Oxygen dissociates completely on this surface into atomic species and adsorbs at an mmc site between two metal and one C atom on the surface. Only one theoretical account has been given on the oxidation of ZrC(110) surface and the observation is a strong reaction with oxygen in a dissociative manner leading to the final formation of ZrO$_2$ layer on the ZrC surface.[8]

Concerning the nature of oxide layer formed on ZrC surface, some researchers[14] observed the formation of a ZrO-like layer in the form of ZrO$_x$ ($1 < x < 2$) on the ZrC surface and the presence of this layer is observed to activate the ZrC(100) surface for further reaction with other molecules.[18] A separate study also found the formation of a monolayer of oxygen adsorbed on the ZrC (100) surface without any further diffusion of oxygen into bulk ZrC, thus passivating the ZrC surface.[8] A similar feature was also observed for the ZrC(111) surface[8]. Separate studies identified ZrO_2 as the oxide layer on ZrC and established crystallographic relationships between the ZrC and ZrO_2 facets that form the interface.[19,20] Several other experiments have revealed ZrO_2 as the oxide phase formed on ZrC with the appearance of cubic, tetragonal and monoclinic at different temperatures with the release of CO_2 gas.[21–26] In our recent studies(100 interface paper), a couple of experimental techniques such as XPS, ToF-SIMS and TEM-ED techniques were used to identify cubic ZrO_2 with traces of tetragonal ZrO_2 as shells around ZrC nano particles. Periodic DFT and atomistic thermodynamic modeling was then used to characterize the interface formed between ZrC and ZrO_2.

Aside all studies carried out on the oxidation of ZrC nano particles, no attempts have been made to control this oxidation and maintain and physical and mechanical properties that are required for the applications ZrC is known for. In this respect, it is therefore imperative to develop a technique that provides protection of oxidation on ZrC surfaces. A viable method is to coat ZrC nano particles with SiC. This is because SiC forms protective oxide layers at higher temperatures of 1400 °C but do not oxidize at lower temperatures. This is shown in figure 1. The conventional method for producing ZrC/SiC composites is to use conventional powders of SiC and Zr which are mixed and then sintered. Moreover, the problem with this method is homogenization of the sintered powder and hence makes it suitable to use pre-ceramic precursors[27,28]. SiC ceramics produced from polymeric precursors are known for their outstanding high temperature properties[29,30]. ZrC surfaces has to be modified for grafting of the polymeric precursors. However, there is no functionalization method described in the literature for ZrC with the exception of our recent functionalization[31,32] of all ZrC surfaces with water which yielded hydroxyl groups. Recent studies have revealed the interaction between vinyl groups of polycarbosilane and metallic Zr in ZrC[33]. Exploitation of the affinity of vinyl groups of polyvinylsilanes on ZrC has allowed improved microstructural homogeneity in the resulting composites[33]. The nature of the grafted polymer on the ZrC surface has however not been investigated. This work aims at providing details on the nature of grafting and properties of the grafted polymeric precursor.

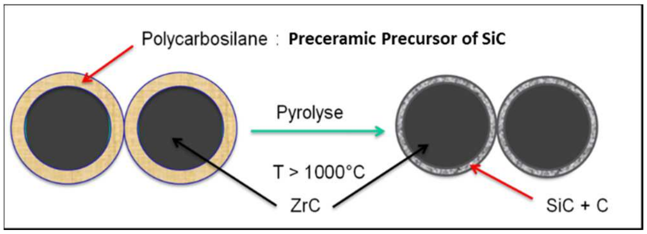

Figure 1. Synthesis of ZrC/SiC core/shell nano-composites

The initial part of the manuscript considers an oxidized ZrC surface with *c*-ZrO_2 as already studied in a previous paper. The next part then deals with functionalization of the exposed ZrO_2 surface with water, linkage to atomistic thermodynamics, further functionalization with allyl(chloro)dimethylsilane (ACDMS) and subsequent grafting of polymeric macromolecules. In the subsequent section, the functionalization process of ZrC is initiated with an organic compound with further direct grafting with the polymeric macromolecule. A final section gives conclusions and perspectives.

2 CALCULATION SCHEMES AND METHODOLOGY

2.1 General Calculation Method

The Vienna Ab-initio Simulation Package (VASP)[34] based on Mermin's[35] finite temperature DFT was used for all calculations. The electronic configurations used for Zr, C, O, H and Si are $[Kr]4d^25s^2$, $[He]2s^22p^2$, $[He]2p^6$, $1s^1$ and $[Ne]3s^23p^2$ respectively. The core electrons as well as the core part of the valence electrons were represented with the Projector Augmented Wave-function (PAW) pseudo-potential[36] in order to reduce the number of planewaves required for describing electrons close to the nucleus. The generalized gradient approximation (GGA) as parametrized by Perdew, Burke and Ernzerhof (PBE)[37] was used for the exchange correlation part of all calculations. The Methfessel-Paxton[38] smearing scheme was used by setting the gamma parameter to 0.1 eV and an optimized energy cut-off of 500 eV was used to expand the plane wave basis set in describing the valence electrons. This cut-off energy was that determined for ZrC as it is the substrate used in all structural models considered. A standard Mohkhorst-Pack[39] special grid of 9 x 9 x 9 k-points was used for all bulk calculations in integration of the Brillouin zone while all surface calculations was done with 9 x 9 x 1 k-point mesh. Within the self-consistent field (SCF) procedure for resolving the Kohn-Sham equations, convergence is assumed to be reached when two successive iterations have energy changes of 1×10^{-4} eV. In performing all surface calculations, the positions of all the ions in the three top most layers were allowed to relax until the net forces acting on them were smaller than 10-2 eV/Å while keeping all other atoms fixed to mimic bulk properties.

For all surface calculations, (1 x 1) unit cells were used except for lower coverages where other surface supercells are considered and a vacuum of 12 Å is used to separate two periodically repeated cells. This is done to prevent any unphysical surface-surface interactions. The slab used for all calculations is made up of a *t*-ZrO_2(001) phase ontop of a ZrC(100) substrate as shown in figure 2. The structure of such a slab has already been studied and determined in a previous study. An initial analysis showed ZrC substrate thickness to have negligible influence on the adsorption properties on the exposed ZrO_2 surface and hence only two layers of ZrC was used as substrates.

The (1 x 1) cell used has a lattice parameter of 4.736 Å and an exposed surface area of 22.433 $Å^2$. The (1 x 1) slab has two oxygen atoms exposed on the surface.

Both associated and dissociative modes of adsorption were used for adsorption and reactivity of molecules on the surface and the adsorption energy is calculated as in equation 1:

$$E_{ads} = -[E_{mol/Surf} - E_{Surface} - E_{mol}] \dots\dots\dots eq.(1)$$

In equation 1, $E_{mol/surf}$ is the DFT energy of the surface with adsorbed molecule on it, $E_{surface}$ is the energy of the free surface and E_{mol} is energy of the molecule in the gas phase.

The effect of different coverages are also calculated through the use of appropriate supercells to achieve different coverages of 0.25 monolayer (ML), 0.50 ML, 0.75 ML and 1.0 ML. The coverage is determined by the number of available adsorption sites. On this surface, the surface Zr atoms define the surface coverage. A similar approach as described above is used for further grafting of polymeric precursors on the functionalized surface.

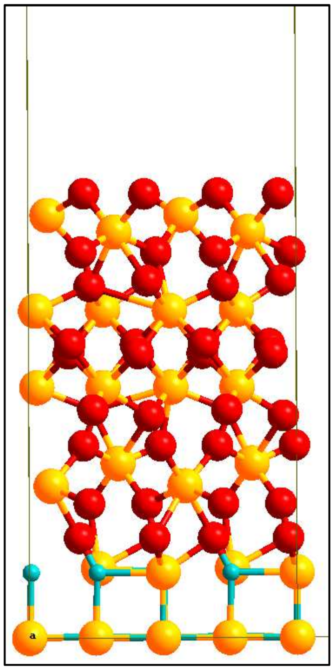

Figure 2. A (2 x 2) ZrC(100)/c-ZrO2(001) slab. Color scheme: Red = O atoms, Yellow = Zr atoms, light blue = C atoms

2.2 Atomistic Thermodynamic Model

In order to provide a relationship between the 0 K calculated properties in DFT and experimentally relevant conditions, the already well-established atomistic thermodynamic model[40] is used. The assumption is that, the adsorbed molecules on the surface are in thermodynamic equilibrium with the gas phase serving as a reservoir for the gas phase molecules. We can then define a Gibbs free energy of adsorption ($\Delta_r G$) as a function of thermodynamic parameters like temperature, pressure and chemical potential through equation 2:

$$\Delta_r G = \Big[\Delta E_O + E_{ZPE(mol/surf)} - \Delta \sum n\, \mu(T,\ p) \Big] \dots eq.(2)$$

The zero point energy (ZPE) contribution of the molecule upon adsorption on the surface is taken into account through the term $E_{ZPE(mol/surf)}$ while ΔE_O is the electronic energy difference between the surface with adsorbed molecule, the free surface and the free molecule in gas phase and is approximated by their respective DFT energies. Δμ (T,p) defines the difference in chemical potential of the gas phase molecules and all other released species in the reaction. ΔE_O is also given by the expression in equation 1. Changes in the chemical potential of gas phase molecules are brought about by the thermal contributions and hence contains temperature dependent terms as shown in equation 3:

$$\Delta\mu(T,P) = \Delta\mu^o(T) + RT \ln\left(\frac{P}{P^o}\right) \dots\dots\dots eq.(3)$$

However, statistical thermodynamics is used to calculate the changes in chemical potential of the gas phase molecules as follows:

$$\Delta\mu^o(T) = \left[E_{ZPE} + E_{vib(0\to T)} + E_{rot} + E_{trans} \right] + RT - T(S_{vib} + S_{rot} + S_{trans}) \dots\dots eq.(4)$$

These changes define the vibrational, rotational and translational degrees of freedom provided by the thermal contribution as well as the entropic contribution. These contributions can be obtained from standard statistical thermodynamic formulae through combination with calculated frequencies at equilibrium geometries. The values of $\Delta\mu^o(T)$ are calculated for the gas phase molecule at different temperatures. Thus the assumption made is that all contributions in the phase are considered while the adsorbed molecule is considered immobile with no rotational and translational degrees of freedom but only vibrational degrees of freedom. The pressure P^o in equation 3 is set to 1 atm and thermodynamic stability plots are obtained at different temperatures and pressures with the calculated ($\Delta_r G$) values. The plots include effects of the different coverages.

2. RESULTS AND DISCUSSION

2.1. Surface Functionalization with H_2O

The initial study involves functionalizing the exposed surface in the slab with an appropriate molecule such as water. The use of water is motivated by the fact that, in our previous studies[31,32], we achieved functionalizing the bare ZrC surfaces with water through the production of surface hydroxyl groups.

Considering both associative and dissociative modes of adsorption of water, the process is carried out in a step by step manner starting with one water molecule followed by another water molecule on the available site. The first water molecule was observed to adsorb in a dissociative mode with an OH ontop of Zr while the remaining H atom is adsorbed on surface O atom. The hydroxyl group is not bridged but a free OH with a bond distance of 2.114 Å between surface Zr and O atom of the OH group. The bond distance between H atom and the protonated surface O atom is 1.049 Å. The surface is hydrated surface is further stabilized by hydrogen bonding between the dissociated water species on the surface. In order to form a bond with the hydroxyl group, the surface Zr atoms are displaced from their equilibrium position and relaxes upwards from its buried initial positon.

The $\Delta_r G$ for this process is calculated to be -0.692 eV. This adsorption energy shows a strong interaction of H_2O with the surface and the equilibrium geometry of the dissociated water molecule for adsorbing 1 water molecule is shown in figure 3. This also defines 0.5 ML coverage as they are 2 sites available.

Upon the adsorption of a second water molecule resulted in associative mode of water adsorption. Thus the first adsorbed hydroxyl group is reorganized into molecular water while the second water molecule also adsorbs at the first Zr site in an associative mode. The presence of the second water specie causes changes in the adsorption mode of the first water molecule. There is further stabilization of the system by hydrogen bonding between the adsorbed water molecules and the surface O atoms. $\Delta_r G$ of the second water molecule is calculated to be -0.936 eV. This adsorption energy is however made up of strong hydrogen bonding with no hydroxyl groups present on the surface. There is an increase in bond distance between the surface Zr atom and O of the water molecule with distances of 2.367 Å and 2.439 Å. The second water molecule defines a coverage of 1.0 ML.

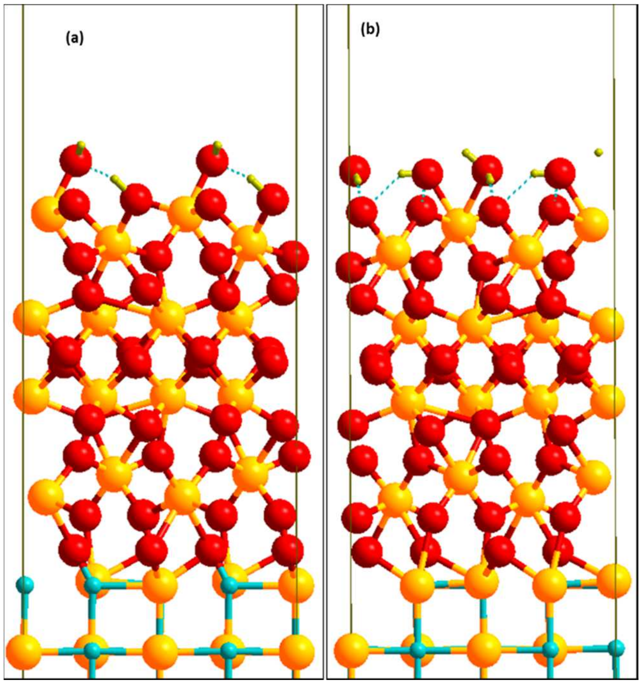

Figure 3. (2 x 2) ZrC(100)/c-ZrO2(001) surface with adsorbed water molecules. (a) is adsorption of 1 water molecule and (b) is adsorption of 2 water molecules. Color scheme: Red = O atoms, Yellow = Zr atoms, light blue = C atoms, Gold = H atom

The adsorption was continued with a third water molecule. However, as there are only two Zr sites available with one Zr buried within the surface in the direction of the second layer, a third water molecule has no available site to bind and hence forms a layer on top of the adsorbed water molecule with stabilization through hydrogen bonding. This process is accompanied by an adsorption energy of 0.457 eV. Thus any further addition of water will result in the formation of a water layer on top of the adsorbed water molecules and stabilized with hydrogen bonding. The adsorption is therefore stopped at 2 water molecules and different supercells were used to calculate the adsorption energies of water for 0.25 ML and 0.75 ML coverages. The calculated adsorption energies at different coverages is provided in table 1. There are easily observable changes in the adsorption energies at different coverages. At 0.25 ML where there is little interaction with other water molecules, the adsorption energy is high, decreases at a substantial amount to reach the 0.50 ML and begins to increase again. It is clear that there is the effect of lateral interaction on the adsorption energies of water on the exposed surface.

Figure 4 provides a density of states (DOS) plot for the adsorbed water on the surface. Figure 4 (top) shows a projected DOS for the surface atoms before adsorption of water molecules. As the exposed surface is made up of ZrO_2 units, the insulating nature of the surface is observed at the Fermi level where there is a gap between the conduction and valence bands. It is however clear from the total DOS (TDOS) plot that due to the substrate ZrC, the TDOS shows a metallic bonding nature at the Fermi level and hence the substrate effect is not negligible. The characteristic OH band in water is observed at -9.7 to -9.4 eV in figure 4. Interaction of water with the surface is very diffuse and the covalent nature of the bonding is obvious.

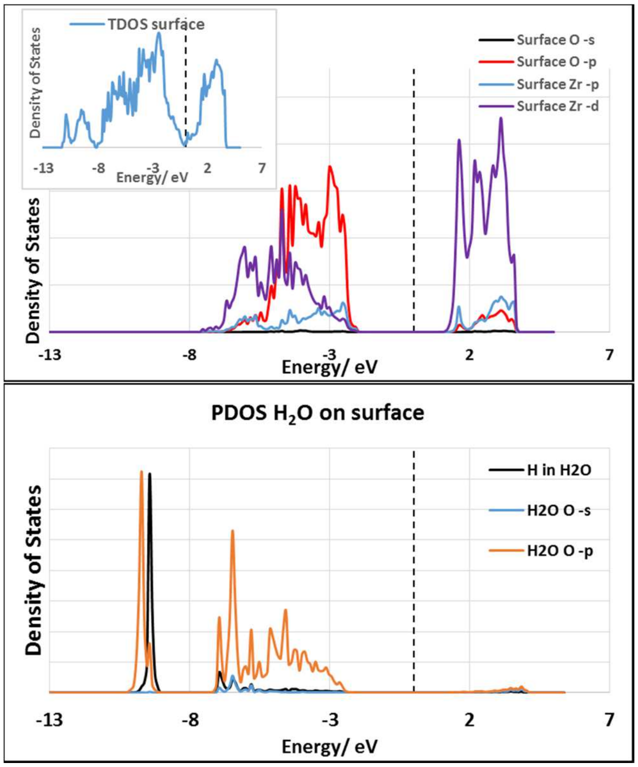

Figure 4. PDOS of surface (top) with TDOS of the exposed surface (insert of top figure), PDOS of H2O on exposed surface (bottom)

Table 1. Adsorption energies of water at different coverages on ZrC(100)/*t*-ZrO_2(001) exposed surface

Coverage	0.25 ML	0.50 ML	0.75 ML	1.00 ML
E_{ads}/ eV/ H_2O	1.025	0.692	0.889	0.936

A thermodynamic treatment of the adsorbed water molecule is also considered. The stability plot is given at three different temperatures by plotting the Gibbs free energy of the reaction Δ_rG against partial pressures of water at different coverages. The lowest lying of such plots is the most stable. The plots given in figure 5 are at room temperature (298.15 K), 400 K and 500 K of hydrating the exposed surface. It is clear that at room temperature, the surface is covered with water at full coverage at high pressures up to about $10^{-5.5}$ bar at which point a lower coverage is reached and the bare surface is recovered at ultra-high vacuum pressures. It is noteworthy that the surface can be hydrated at room temperature but with hydroxyl groups only within the range of $10^{-5.5}$ to 10^{-8} bar pressures. The water molecules are easily removed from the surface as temperature is increased due to the high vibrational degrees of freedom upon adsorption on the surface. By increasing the temperature to 400 K, hydroxyl groups can be obtained within $10^{-1.5}$ to $10^{-3.5}$ bar of pressure.

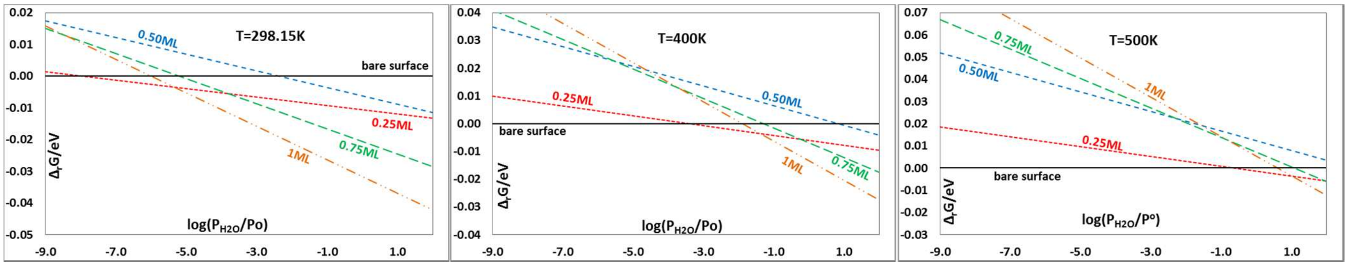

Figure 5. Stability plot for adsorption of water on ZrC(100)/*t*-ZrO_2(001) exposed surfac

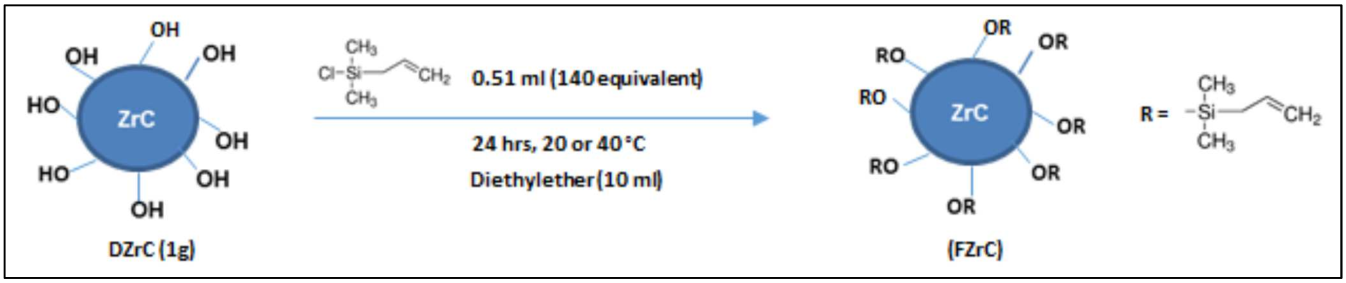

Figure 6. Functionalization with allyl(chloro)dimethylsilane (ACDMS). FZrC means functionalized ZrC and DZrC means deagglomerated ZrC. R = ACDM

2.2 Functionalization with Allyl(Chloro)dimethylsilane

With the main aim of grafting a preceramic polymeric precursor on the surface, the next step is gain further functionalization with allyl(chloro)dimethylsilane (ACDMS). This reaction is shown in figure 6. At this point, we used the fully hydrated surface for the functionalization with ACDMS. This is because as can be seen from figure 5, this coverage appears over a wide range of water partial pressures.

Interaction of the hydrated surface with ACDMS is analyzed through calculation of a reaction enthalpy. The reaction is considered to be a nucleophilic substitution reaction with the release of HCl gas. This reaction is shown in equation 5.

ZrC/ZrO_2—H_2O + ACDMS → ZrC/ZrO_2—HO—ACDMS + HCl ……………………………………eq. (5)

The calculated Δ_rG for the above reaction is -0.13 eV. This reaction energy shows the process is not strongly exothermic. As the starting point of the calculation was molecular water on the surface on which the ACDMS was grafted, there is further rearrangement to move one H atom (from H_2O) to a surface O atom and ACDMS reacting with the resulting OH group in the nucleophilic substitution reaction. It might be that, this rearrangement contributes to the -0.13 eV calculated. Thus, further functionalization with ACDMS is not a strong process and might not lead to highly functionalized surface. Even if the hydrated surface is functionalized, there number of functionalized molecules on the surface might be very low. The resulting structure after the surface is functionalized with

ACDMS is shown in figure 7. The bond distance between O (H_2O) and Si (ACDMS) is 1.679 Å.

2.3 Grafting of Preceramic Precursor using *Grafting-to* Approach

As the final step of achieving the synthesis aim as shown in figure 1, there is a further grafting of polycarbosilane precursor units onto the functionalized surfaced. The method of choice here is the *grafting-to* approach. In this approach, an already synthesized macromolecule is covalently bonded to the functionalized surface. Synthesis of the macromolecule is shown in figure 8. The macromolecule is synthesised from diphenylsilane and 1,4-diethynylbenzene monomer units. Due to the grafting-to approach used in the synthesis, we modelled the macromolecule as the grafting unit on the functionalized surface. The enthalpy of the reaction process is calculated. This reaction uses the final S-H bond of the macromolecule in a hydrosilylation reaction to attach the macromolecule to the alkene group of the ACDMS on the modified surface. This hydrosilylation reaction is observed to be a favourable exothermic reaction with a reaction enthalpy of -0.79 eV. As such, the grafting-to approach will yield the desired grafted preceramic precursor on the modified surface. The grafted macromolecule through the *grafting-to* approach is shown in figure 9. The grafting of the macromolecule results in blockage of several the sites available on neighbouring ACDMS sites. The bond distance between Si of the grafted macromolecule and the terminal carbon ACDMS is 1.891 Å.

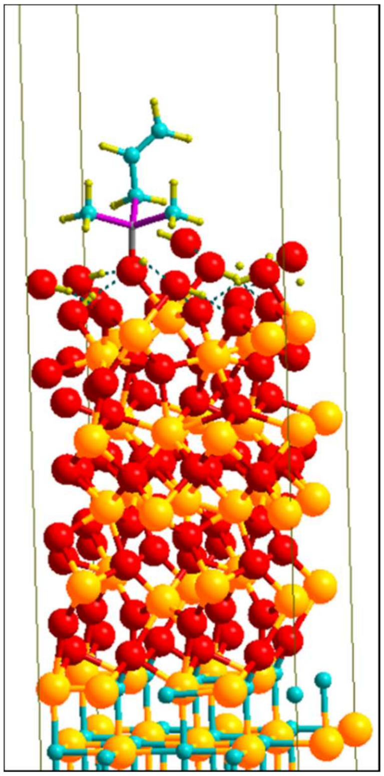

Figure 7. Hydrated ZrC(100)/t-ZrO2(001) exposed surface grafted with ACDMS. Color scheme: Red = O atoms, Yellow = Zr atoms, light blue = C atoms, Gold = H atom, Grey = Si atom

2.4 Functionalization with other organic compounds

As noted in sections 2.1 and 2.2, there might be problems with surface modification when water is used. Water will mainly exist as molecular species and the functionalization with ACDMS is not a highly favourable reaction due to the low exothermic nature of the adsorption and the removal at substantially low temperature. Another approach that can be considered is to explore other organic compounds that can be used for functionalization and by-pass the hydration step. In light of this, bifunctional organic molecules can be employed. Compounds with two functional groups can be used by using one part for binding to the surface and exploring the other functional group for further grafting.

Several organic molecules were screened for this purpose. These include compounds with OH groups and carboxylic acid groups. The compounds which were initially considered and tested are lactic acid, oxalic acid, ethanoic acid and 4-hydroxybenzoic acid. These compounds were selected as they contain OH groups and carboxylic acid groups.

All compounds exhibited strong interaction with the exposed surface through the carboxylic acid groups. We explored the adsorption through one O atom of the carboxylic acid group and the chelating effect of the two oxygen atoms. The chelating groups exhibited strong interaction with surface Zr atoms and protonation of surface O atoms. The calculated adsorption energies for the different molecules are given in table 2.

Further functionalization of with ACDMS on the second functional groups of the organic molecules through a nucleophilic substitution reaction were tested. This can be shown in table 2 as well. The reaction with ACDMS during nucleophilic substitution reaction through an OH group of all the molecules considered are endothermic as can be seen in table 2. It therefore becomes obvious that the nucleophilic substitution reaction of ACDMS and hydroxyl groups is not appropriate for further grafting as is evidenced by the hydrated surface and also through the bifunctional organic molecules.

From this point of view, it is therefore necessary to consider bypassing the nucleophilic substitution reaction of ACDMS and employing an organic reagent which is bifunctional and can be adsorbed directly onto the exposed surface while exploring the other functional group in the *grafting-to* approach for grafting the macromolecule.

2.4.1 Functionalization with 3-butenoic acid and further grafting of Macromolecule

As discussed in the previous section, there is the need to consider different groups functionalization. For the purpose of the work, 3-butenoic acid is a good candidate. This is because there is the availability of a carboxylic acid that can be utilized for adsorbing onto the exposed surface and the available double bond used for the hydrosilylation reaction in the *grafting-to* approach. The calculated adsorption energy for 3-butenoic acid on the exposed surface using the chelating properties of the carboxylic acid group is 0.997 eV. This shows a strong interaction with surface Zr atoms through two

O atoms of the organic molecule. The interaction is shown in figure 10. The calculated bond distances between the surface Zr atom and the chelating O atoms are 2.353 Å and 2.322 Å.

A DOS plot (figure 11) is obtained for the adsorbed 3-butenoic acid on the surface in order to check the electronic structure. The DOS shows the bonding between O atoms of the chelating group in 3-butenoic acid and Zr atoms on the exposed surface. The bond is typically of Zr –d mixing with O –p between -6.4 eV and -7.4 eV. The sharp nature of the peaks suggest ionic nature.

After functionalization with 3-butenoic acid, the *grafting-to* approach was used to graft the preceramic macromolecule as described in section 2.3 by utilizing the double bond of 3-butenoic acid for the hydrosilylation reaction. This reaction was highly favourable in an exothermic reaction as observed in section 2.3 when the hydrosilylation reaction was carried out through the use of ACDMS. The calculated $\Delta_r G$ for the hydrosilylation reaction is -0.942 eV.

3. SUMMARY AND CONCLUSION

DFT studies has been carried on functionalization of ZrC surfaces with further grafting of preceramic organic precursors with the aim of synthesizing ZrC/SiC core/shell nano composites.

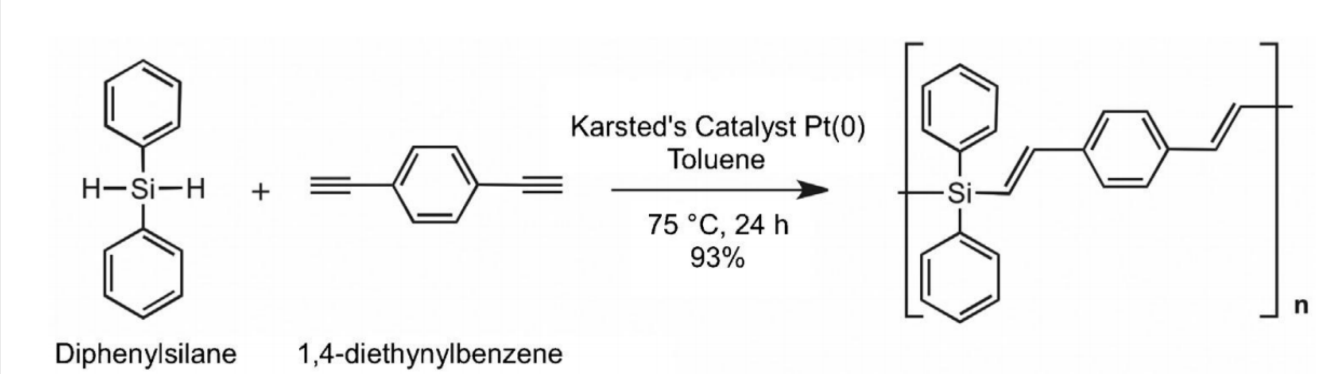

Figure 8. Synthesis of macromolecule used in *grafting-to* approach of synthesis

This analysis was carried out on the exposed surface of ZrO_2 on a ZrC substrate which was studied and described in a previous study. In the first part of the study, the exposed surface was modified with water. There is adsorption of molecular water at a wide range of pressures with hydroxyl groups appearing at extremely low water partial pressures. The resulting hydrated surface was further functionalized with allyl(chloro)dimethylsilane (ACDMS) in a nucleophilic substitution reaction with the release of HCl gas. There is rearrangement in the adsorbed molecular water to hydroxyl groups when ACDMS is adsorbed and the interaction of ACDMS with the OH groups is a rather weak one. However, further grafting of a polymeric precursor in a hydrosilylation reaction using a grafting-to approach was a highly favorable exothermic reaction.

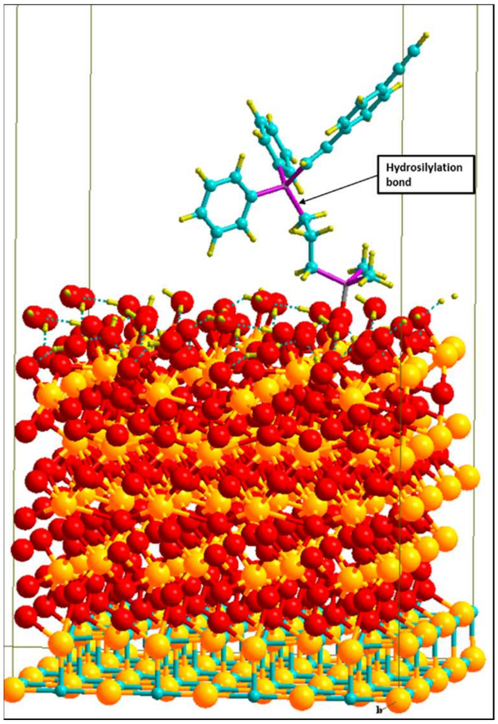

Figure 9. Grafted macromolecule through hydrosilylation reaction

Table 2. Adsorption energies for chelating group of different bifunctional organic molecules

Organic molecule	Oxalic acid	Lactic acid	Ethanoic acid	4-hydroxybenzoic acid
Eads/ eV/ molecule	1.260	0.994	1.027	0.840
Nucleophilic substitution reaction with ACDMS				
ΔrG	+0.585	+0.396	-	+0.146

Due to the poor nature of interaction between ACDMS and the hydroxyl groups on the surface, other alternatives were sought with different bifunctional organic molecules in which one functional group can be used to adsorb on the surface and the other functional group used to react with ACDMS. Lactic acid, ethanoic acid, oxalic acid and 4-hydroxybenzoic acid were all tested.

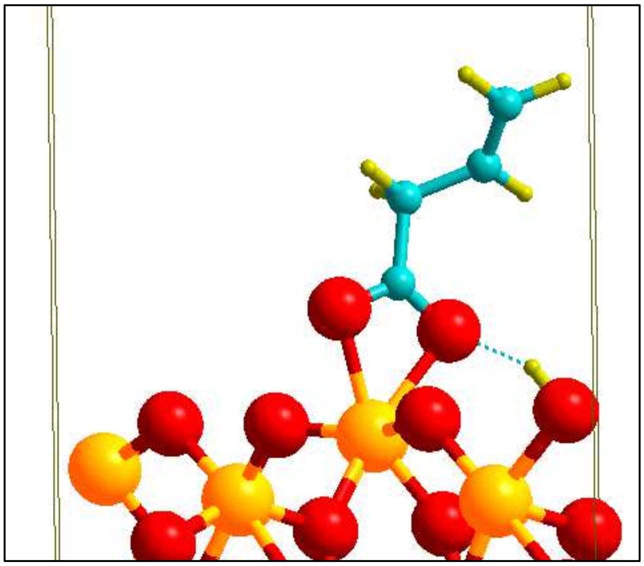

Figure 10. Adsorption of 3-butenoic acid on ZrC(100)/*t*-ZrO_2(001) exposed surface

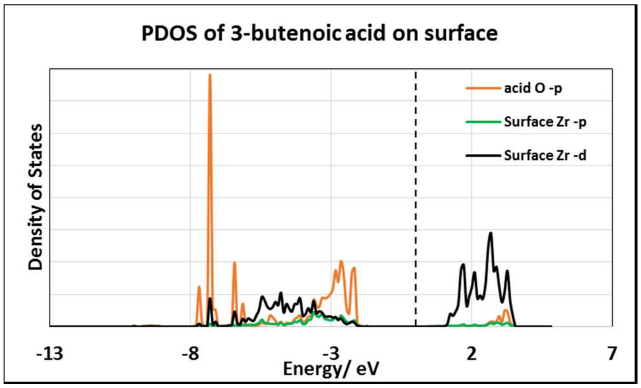

Figure 11. PDOS of 3-butenoic acid on ZrC(100)/*t*-ZrO_2(001) showing bonding with the surface

They all exhibited strong adsorption to the surface but the reaction with ACDMS was still weak and indicates the route of a nucleophilic substitution reaction using ACDMS as inappropriate for the intended goal.

3-butenoic acid was finally used to exploit the availability a carboxylic acid for strong gripping to the surface through chelating effect of the two oxygen atoms and a subsequent usage of the terminal alkene bond for the hydrosilylation reaction. This reagent gave excellent result with favorable adsorption onto the surface and a favorable exothermic hydrosilylation reaction in the *grafting-to* method.

ASSOCIATED CONTENT

(Word Style "TE_Supporting_Informati**on"). Supporting Information**. A brief statement in nonsentence format listing the contents of material supplied as Supporting Information should be included, ending with "This material is available free of charge via the Internet at http://pubs.acs.org." For instructions on what should be included in the Supporting Information as well as how to prepare this material for publication, refer to the journal's Instructions for Authors.

AUTHOR INFORMATION

Corresponding Author

* Tel: +33 320 43 45 03, fax +33 320 43 65 61; email: sylvain.cristol@univ-lille1.fr

Present Addresses

†If an author's address is different than the one given in the affiliation line, this information may be included here.

Author Contributions

The manuscript was written through contributions of all authors. / All authors have given approval to the final version of the manuscript. / ‡These authors contributed equally. (match statement to author names with a symbol)

Funding Sources

Any funds used to support the research of the manuscript should be placed here (per journal style).

Notes

The authors declare no competing financial interests.

ACKNOWLEDGMENT

Numerical results presented in this paper were carried out using the regional computational cluster supported by Université Lille 1, CPER Nord-Pas-de-Calais/FEDER, France Grille, and CNRS. We highly appreciate and thank the technical staff of the CRI-Lille 1 center for their strong and helpful support. The project is supported by Agence Nationale de la Recherche under Contract No. ANR-12-BS08-004-02 (CollZSiC: Elaboration de nanocomposites coeur/coquille ZrC/SiC).

ABBREVIATIONS

XPS, X-ray Photoemission Spectroscopy; ToF-SIMS, Time of Flight Secondary Ion Mass Spectrometry; TEM, Transmission Electron Microscopy; ED, Electron Diffraction; DFT, Density Functional Theory.

REFERENCES

(1) Gosset, D.; Dollé, M.; Simeone, D.; Baldinozzi, G.; Thomé, L. Structural Evolution of Zirconium Carbide under Ion Irradiation. *J. Nucl. Mater.* **2008**, *373*, 123–129.

(2) Gosset, D.; Dollé, M.; Simeone, D.; Baldinozzi, G.; Thomé, L. Structural Behaviour of Nearly Stoichiometric ZrC under Ion Irradiation. *Nucl. Instrum. Methods Phys. Res. Sect. B Beam Interact. Mater. At.* **2008**, *266*, 2801–2805.

(3) Katoh, Y.; Vasudevamurthy, G.; Nozawa, T.; Snead, L. L. Properties of Zirconium Carbide for Nuclear Fuel Applications. *J. Nucl. Mater.* **2013**, *441* (1–3), 718–742.

(4) Reynolds, G. H.; Janvier, J. C.; Kaae, J. L.; Morlevat, J. P. Irradiation Behavior of Experimental Fuel Particles Containing Chemically Vapor Deposited Zirconium Carbide Coatings. *J. Nucl. Mater.* **1976**, *62* (1), 9–16.

(5) Minato, K.; Ogawa, T.; Fukuda, K.; Nabielek, H.; Sekino, H.; Nozawa, Y.; Takahashi, I. Fission Product Release from ZrC-Coated Fuel Particles during Postirradiation Heating at 1600°C. *J. Nucl. Mater.* **1995**, *224* (1), 85–92.

(6) Ogawa, T.; Ikawa, K. *High Temp. Sci* **1986**, *22*, 179–192.

(7) Li, H.; Zhang, L.; Cheng, L.; Wang, Y. Oxidation Analysis of 2D C/ZrC–SiC Composites with Different Coating Structures in CH4 Combustion Gas Environment. *Ceram. Int.* **2009**, *35* (6), 2277–2282.

(8) Osei-Agyemang, E.; Paul, J.-F.; Lucas, R.; Foucaud, S.; Cristol, S. Oxidation and Equilibrium Morphology of Zirconium Carbide Low Index Surfaces Using DFT and Atomistic Thermodynamic Modeling. *J. Phys. Chem. C* **2016**, *120* (16), 8759–8771.

(9) Noda, T.; Yamazaki, M.; Ozawa, K.; Edamoto, K.; Otani, S. Oxygen Adsorption on a ZrC(111) Surface: Angle-Resolved Photoemission Study. *Surf. Sci.* **2000**, *450* (1–2), 27–33.

(10) Noda, T.; Nakane, T.; Ozawa, K.; Edamoto, K.; Tanaka, S.; Otani, S. Photoemission Study of the Oxidation of ZrC(111). *Solid State Commun.* **1998**, *107* (4), 145–148.

(11) Vojvodic, A.; Ruberto, C.; Lundqvist, B. I. Atomic and Molecular Adsorption on Transition-Metal Carbide (111) Surfaces from Density-Functional Theory: A Trend Study of Surface Electronic Factors. *J Phys Condens Matter* **2010**, *22* (37), 375504.

(12) Ozawa, K.; Yoshii, T.; Noda, T.; Edamoto, K.; Tanaka, S. Coadsorption of Oxygen and Cesium on ZrC(111). *Surf. Sci.* **2002**, *511* (1–3), 421–434.

(13) Kitaoka, H.; Ozawa, K.; Edamoto, K.; Otani, S. The Interaction of Water with Oxygen-Modified ZrC(100) Surfaces. *Solid State Commun.* **2001**, *118* (1), 23–26.

(14) Shin, K.; Ken-ichi, O.; Kazuyuki, E.; Shigeki, O. Photoelectron Spectroscopy Study of the Oxidation of ZrC(100). *Jpn. J. Appl. Phys.* **2000**, *39* (9R), 5217.

(15) Viñes, F.; Sousa, C.; Illas, F.; Liu, P.; Rodriguez, J. A. Density Functional Study of the Adsorption of Atomic Oxygen on the (001) Surface of Early Transition-Metal Carbides. *J. Phys. Chem. C* **2007**, *111* (3), 1307–1314.

(16) Rodriguez, J. A.; Liu, P.; Gomes, J.; Nakamura, K.; Viñes, F.; Sousa, C.; Illas, F. Interaction of Oxygen with ZrC(001) and VC(001): Photoemission and First-Principles Studies. *Phys. Rev. B - Condens. Matter Mater. Phys.* **2005**, *72* (7).

(17) Viñes, F.; Sousa, C.; Illas, F.; Liu, P.; Rodriguez, J. A. A Systematic Density Functional Study of Molecular Oxygen Adsorption and Dissociation on the (001) Surface of Group IV-VI Transition Metal Carbides. *J. Phys. Chem. C* **2007**, *111* (45), 16982–16989.

(18) Shimada, T.; Imamura, K.; Edamoto, K.; Orita, H. Electronic Structures of the Suboxide Films Formed on TiC(100) and ZrC(100) Surfaces: Density Functional Theory Studies. *Surf. Sci.* **2009**, *603* (15), 2340–2344.

(19) Shimada, S.; Inagaki, M.; Suzuki, M. Microstructural Observation of the ZrC/ZrO2 Interface Formed by Oxidation of ZrC. *J. Mater. Res.* **1996**, *11* (10), 2594–2597.

(20) Shimada, S.; Yoshimatsu, M.; Inagaki, M.; Otani, S. Formation and Characterization of Carbon at the ZrC/Zro2 Interface by Oxidation of ZrC Single Crystals. *Carbon* **1998**, *36* (7–8), 1125–1131.

(21) Miloserdin, Y. V.; Naboichenko, K. V.; Laveikin, L. I.; Bortsov, A. G. The High-Temperature Creep of Zirconium Carbide. *Strength Mater.* *4* (3), 302–305.

(22) Rama Rao, G. A.; Venugopal, V. Kinetics and Mechanism of the Oxidation of ZrC. *J. Alloys Compd.* **1994**, *206* (2), 237–242.

(23) Shimada, S.; Ishi, T. *J. Am. Ceram. Soc* **1990**, *73*.

(24) Bartlett, R. W.; Wadsworth, M. E.; Cutler, I. B. *Trans. Metall. Soc* **1963**, *227*.

(25) Bullock, R. E.; Kaae, J. L. *J. Nucl. Mater* **1983**, *115*, 69–83.

(26) Shimada, S. *Solid State Ionics* **1997**, *101–103*, 749–753.

(27) Gendre, M.; Maître, A.; Trolliard, G. A Study of the Densification Mechanisms during Spark Plasma Sintering of Zirconium (Oxy-)Carbide Powders. *Acta Mater.* **2010**, *58* (7), 2598–2609.

(28) Weimer, A. W. *Carbide, Nitride and Boride Materials Synthesis and Processing*, 80th ed.; Chapman and Hall, 1997.

(29) Li, H.; Zhang, L.; Cheng, L.; Wang, Y.; Yu, Z.; Huang, M.; Tu, H.; Xia, H. Effect of the Polycarbosilane Structure on Its Final Ceramic Yield. *J. Eur. Ceram. Soc.* **2008**, *28* (4), 887–891.

(30) Greil, P. Polymer Derived Engineering Ceramics. *Adv. Eng. Mater.* **2000**, *2* (6), 339–348.

(31) Osei-Agyemang, E.; Paul, J.-F.; Lucas, R.; Foucaud, S.; Cristol, S. Stability, Equilibrium Morphology and Hydration of ZrC(111) and (110) Surfaces with H2O: A Combined Periodic DFT and Atomistic Thermodynamic Study. *Phys. Chem. Chem. Phys.* **2015**, *17* (33), 21401–21413.

(32) Osei-Agyemang, E.; Paul, J. F.; Lucas, R.; Foucaud, S.; Cristol, S. Periodic DFT and Atomistic Thermodynamic Modeling of Reactivity of H2, O2, and H2O Molecules on Bare and Oxygen Modified ZrC (100) Surface. *J. Phys. Chem. C* **2014**.

(33) Pizon, D.; Lucas, R.; Chehaidi, S.; Foucaud, S.; Maître, A. From Trimethylvinylsilane to ZrC–SiC Hybrid Materials. *J. Eur. Ceram. Soc.* **2011**, *31* (14), 2687–2690.

(34) Hafner, J. Ab-Initio Simulations of Materials Using VASP: Density-Functional Theory and beyond. *J. Comput. Chem.* **2008**, *29* (13), 2044–2078.

(35) Mermin, N. D. Thermal Properties of the Inhomogeneous Electron Gas. *Phys. Rev.* **1965**, *137* (5A), A1441–A1443.

(36) Kresse, G.; Joubert, D. From Ultrasoft Pseudopotentials to the Projector Augmented-Wave Method. *Phys. Rev. B - Condens. Matter Mater. Phys.* **1999**, *59* (3), 1758–1775.

(37) Perdew, J. P.; Burke, K.; Ernzerhof, M. Generalized Gradient Approximation Made Simple. *Phys. Rev. Lett.* **1996**, *77* (18), 3865–3868.

(38) Methfessel, M.; Paxton, A. T. High-Precision Sampling for Brillouin-Zone Integration in Metals. *Phys. Rev. B* **1989**, *40* (6), 3616–3621.

(39) Monkhorst, H. J.; Pack, J. D. Special Points for Brillouin-Zone Integrations. *Phys. Rev. B* **1976**, *13* (12), 5188–5192.

(40) Reuter, K.; Scheffler, M. First-Principles Atomistic Thermodynamics for Oxidation Catalysis: Surface Phase Diagrams and Catalytically Interesting Regions. *Phys. Rev. Lett.* **2003**, *90* (4), 461031–461034.

Insert Table of Contents artwork here

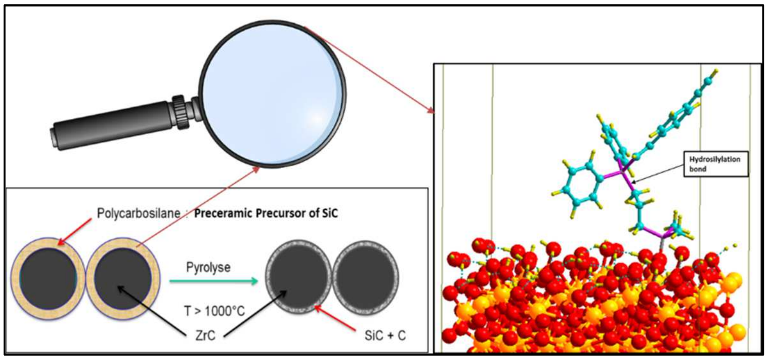

Conclusion

An exposed zirconia surface of ZrC(100)//*t*-ZrO_2(001) interfacial slab was initially modified with water. The adsorption of water resulted in hydroxyl groups at very low coverage and molecular water as the most stable total coverage at a wide range of temperatures. A thermodynamic treatment revealed availability of hydroxyl groups only at extremely low partial pressures of water and the bare surface can easily be regained at temperatures as low as 400 K.

Further functionalization of the hydrated surface with allyl(chloro)dimethylsilane (ACDMS) resulted in weak interaction through the nucleophilic substitution reaction envisaged. However, the further grafting of a preceramic polymeric precursor built from diphenylsilane and 1,4-diethynylbenzen monomers employed in a grafting-to method to yield a macromolecule on the functionalized surface was a highly favorable and exothermic reaction.

Due to the poor interaction of ACDMS with hydroxyl groups on the surface, other organic molecules with dual functional groups were exploited including lactic acid, oxalic acid, ethanoic acid and 4-hydroxybenzoic acid. All these compounds revealed strong chelating effect with surface Zr atoms using the carboxylic acid functional group but yet a poor interaction of their OH groups with ACDMS in a nucleophilic substitution reaction. Hence it is obvious the nucleophilic substitution reaction path is not appropriate for the purpose of the grafting.

Another organic compound, 3-butenoic acid was used by exploiting its bifunctional nature with both carboxylic acid and an alkene group. The carboxylic acid part exhibited a strong interaction with surface Zr atoms through a chelating effect and the remaining alkene group was used for the hydrosilylation reaction in grafting the polymeric macromolecule. This yielded excellent result with complete grafting on the surface.

General Conclusions and Perspectives

As zirconium carbide (ZrC) is known for excellent physical and mechanical properties, the non-oxide ultra-high temperature ceramic is however disadvantaged in the sense that, it is easily prone to oxidation by forming low refractory oxides at low temperatures which deteriorates the properties mentioned above and hampers applications. There are however no attempts providing a control for the oxidation process. This project therefore aims to fill this gap.

A proposed strategy is to coat ZrC nano-composite surfaces with silicon carbide (SiC) to form a core/shell nano material. This is because SiC forms a protective oxide layer at higher temperatures and resistant to oxidation at low temperatures as is the case for ZrC. As such, initial characterization of ZrC bulk is required followed by several studies on the surfaces to modification, functionalization before the final synthesis of SiC on the surface.

At the initial stage of the project, bulk studies on ZrC were carried out. This included calculation of lattice parameters, elastic constants, mechanical properties as well as studies on defects in ZrC bulk. The calculated lattice parameter of ZrC is 4.7363 Å and this value is in excellent agreement with experimental and other theoretically calculated values. The stress-strain approach was used to calculate the three distinct elastic constants of ZrC and all calculated values were in excellent agreement with literature values. These elastic constant values were used to estimate other bulk mechanical properties such as the bulk modulus, Young's modulus, shear modulus and Poisson's ratio. The calculated lattice parameters satisfied the Born stability criteria for cubic crystals. High mechanical property values were estimated for ZrC which is typical for the known mechanical strength. All estimated values agrees well with experimental and other calculated values.

Further studies were made on the formation of defects and we considered both carbon vacancy and carbon insertion defects. The analysis involved calculations in zirconium and carbon rich environments for different concentrations of the defect. Carbon vacancy is observed to be favorable in zirconium rich environments where the vacated carbon reacts with Zr in a reservoir to form stable ZrC. The vacancy is however stable for low concentration of defects such as 6% and 3% of carbon vacancies while higher concentration defects are not favorable. This is because the effect of the defect can be distributed within the supercell at lower concentrations than at higher concentrations of vacancy and stabilize further the system. Carbon insertion defects results in unstable structures and the effect of the defects is observed to be more local. Calculated values conforms to available literature values. All bulk properties are well described by the methodology used in this project.

After optimizing the bulk structure, studies into stability of the various low index surfaces of ZrC were carried out and the identified stability criterial was (100) > (111) > (110) with the (100) surface being the most stable. However, the as-cleaved (111) surface being polar is observed to terminate on both sides with zirconium layers upon various correction techniques used and this confirms the experimental observation of metallic termination on this surface. The (110) surface being the least stable is highly reactive with high amount of states at the Fermi-level and hence very reactive. A wulff construction of the nano-crystallites using the surface energy values at 0 K revealed a cubic structure made mainly of (100) facets with truncated corners of (111) facets which is less than 1% of the surface area.

We considered reduction of the (100) surface and observed a complete dissociation of H_2 into atomic species. However a calculated high activation barrier for the H_2 dissociation prevents the surface from being reduced at room temperature. Water is however observed to adsorb both as molecular water and dissociative mode into hydroxyl groups and CH. A low activation barrier is calculated for dissociation of the molecularly adsorbed H_2O into hydroxyl groups and hence the bare ZrC(100) surface can be hydroxylated with water. This study is the first to be presented for ZrC as no such determinations has been made previously. In combining the DFT calculations with atomistic thermodynamic modelling, we observed the (100) surface to be covered with hydroxyl groups at a wide range of water partial pressures up to 400 K until the bare surface can be recovered at temperatures above 500 K. Additionally, we covered the (100) surface with a ZrO-like layer as observed experimentally by some groups and we observed the surface to be further activated as it dissociates water into hydroxyl groups as well as complete dissociation into atomic O species with the release of H_2. The oxide-like layer further activates the surface for the hydration process. Thus the oxide covered surface is much easier to functionalize than the bare (100) surface.

Hydration of the (110) surface was also carried out and observed the formation of hydroxyl groups on this surface at higher coverage. However, at low coverages, there is complete dissociation of water into atomic O and H groups. The hydroxylated surface is stable at lower temperatures at a wide range of pressures of water while the surface covered with completely dissociated water into atomic species is stable between 700 K and 1000 K. The bare (110) surface is recovered at temperatures above 1000 K and lower partial pressures of water.

On the (111) surface, hydration led to complete coverage with hydroxyl groups accompanied by the release of hydrogen gas. The hydroxyl groups are in bridged positions on this surface between three surface Zr atoms. The hydrated properties of all three surfaces were used to construct an equilibrium morphology of the nano-crystallites. From 200-700 K, the ZrC nano-crystallites is made mainly of (111) surface with bridging hydroxyl groups while the (100) surface begins to appear at higher temperatures above 700 K with the introduction of dangling OH groups.

As the main concern of ZrC within the context of this project is oxidation, an analysis of oxidation on the various surfaces was carried out. Considering the (100) surface, adsorption of oxygen resulted in complete dissociation into atomic species adsorbing at mmc three-fold sites between two surface and one C atom. The oxidized surface is stable at a wide range of oxygen partial pressures and the bare surface is recovered at temperatures above 1500 K and low oxygen partial pressures. Oxygen however passivates the surface and there is no further diffusion of oxygen into the bulk. Oxidation on the (111) surface was also an extremely exothermic process with atomic oxygen adsorbing at fcc sites between three surface Zr atoms. Manipulation of temperature and pressure alone on this surface cannot be used to remove oxygen even at temperatures of 1500 K. The oxide layer passivates the (111) surface and there is no further diffusion of oxygen into the bulk. The (110) is the most reactive to oxygen and dissociates oxygen completely into atomic species. The surface can accommodate high amounts of oxygen. A step by step analysis of the oxidation process revealed removal all surface C atoms as CO_2 with a final formation of ZrO_2 layer on the surface. This process was observed as irreversible at all temperatures and oxygen partial pressures considered. The observation of ZrO_2 on ZrC has been documented in the literature. After considering oxidation on all three surfaces, a wulff construction was made for the equilibrium morphology of the nano-crystallites. Due to the high stability of the ZrO_2 formed on ZrC, only the (110) facets are revealed at all temperatures considered.

Since oxidation is inevitable on ZrC, it is necessary to determine the oxide layer experimentally. X-ray Photoemission spectroscopy (XPS) to analyze the oxide layer on top of ZrC. The analysis revealed the present of ZrO_2 with a thickness of about 3 nm. Further analysis was done with Time of Flight Secondary Ion Mass spectrometry (ToF-SIMS) and this also revealed the presence of ZrO_2. Removal of oxide layer and the experiments repeated in ultra-vacuum conditions revealed the reappearance of the oxide layer. The ZrO_2 phase was further determined with Transmission Electron Microscopy (TEM) and Electron Diffraction (ED) experiments. This revealed the presence of predominantly cubic ZrO_2 with traces of tetragonal ZrO_2. This further required studies on the interfacial structure and properties between ZrC and ZrO_2. Surface misfit calculations were done to determine which surfaces of ZrC and cubic ZrO_2 will form commensurate interfaces. This revealed the commensurability of ZrC(100) and cubic ZrO_2 (001), ZrC(111) and cubic ZrO_2(111) surfaces. Finite temperature molecular dynamics was used to build a zirconia layer on top of ZrC (111) surface from atomic species. This revealed the formation of ordered phase of cubic zirconia (111) phase. Several mechanical properties, thermodynamic characterization, density of states profile and charge transfer analysis was used to characterize the ZrC(111)//*c*-ZrO_2(111) interface. The analysis showed this interfacial properties to be governed by local effects and confined to only the first layer of *c*-ZrO_2(111) deposited on ZrC(111). There is a breakage within the first layer of the deposited zirconia leaving an oxygen layer on top of the ZrC(111) surface. This is in agreement with the results obtained on oxidation of the ZrC(111) surface. As such, ZrO_2 will not be observed on the ZrC(111) surface.

Similar interfacial studies was done for ZrC(100)//*c*-ZrO_2(001). The analysis showed convergence of the deposited zirconia up to 3 layers of *c*-ZrO_2(001) deposited. The strain imposed by the substrate ZrC(100) surface however transforms the *c*-ZrO_2(001) into *t*-ZrO_2(001) phase. The interfacial properties depend on only the first few 3 layers and not on subsequent layers of zirconia. Further density of states and charge transfer analysis revealed the local nature of the interfacial properties.

The stability strength of the ZrC(100)//*c*-ZrO_2(001) interface therefore makes it a suitable candidate for the next step of the project. The exposed surface on the zirconia side was then hydrated with water. The aim is to produce hydroxyl groups that can be used for grafting. However, the hydration revealed molecular water adsorbed on top of surface Zr atoms as the most stable. The water molecules are further stabilized by hydrogen bonding. Hydroxyl groups can only be obtained at very low coverages of water and low water partial pressure. The hydrated surface can also be cleaned of the water at temperatures as low as 400 K. Further functionalization of the hydrated surface was achieved with allyl(chloro)dimethylsilane (ACDMS) through a nucleophilic substitution reaction with the release of HCl. This was possible due to a rearrangement in the adsorbed water molecules to yield hydroxyl groups upon reacting with ACDMS. However, the interaction of ACDMS with water on the surface is very weak (reaction free energy of -0.13 eV). This energy could be mostly for the rearrangement in the water molecule and not on the reaction between the resulting OH and the ACDMS molecule. Moreover, the *grafting-to* method was used to graft a macromolecule (from diphenylsilane and 1,4-diethynylbenzene) onto the functionalized surface though a hydrosilylation reaction. This reaction was a highly favorable and exothermic reaction.

Due to the poor interaction of the water and the ACDMS, other bifunctional organic molecules were considered for the functionalization. Oxalic acid, lactic acid, ethanoic acid and 4-hydroxybenzoic acid were all used by exploiting their carboxylic acid groups for chelating surface Zr atoms and using the other functional group (OH or COOH) group for the nucleophilic substitution reaction with ACDMS. All the considered compounds showed excellent binding to the surface Zr atoms but poor interaction with ACDMS. This provided more insight into the fact that the nucleophilic substitution reaction between hydroxyl group and ACDMS might not be the appropriate route for grafting the preceramic polymeric precursor. Hence different compounds were tested for this purpose and 4-butenoic acid was finally used. The choice of this molecule is the fact that, the nucleophilic substitution reaction path can be by-passed and direct grafting of the macromolecule achieved. Initial binding to the exposed surface through chelating effects of the carboxylic acid was a highly favorable reaction and the subsequent hydrosilylation reaction in the *grafting-to* approach was successful.

At this point, theoretical studies have shown grafting of preceramic polymeric precursors to lead to favourable results. This is under experimental evaluations for validating the theoretical results.

Perspectives: With the success of achievement obtained on the theoretical study of grafting, further experimental analysis are on the way to confirm the grafted macromolecules on the surface. Laser pyrolysis will further be used to convert the grafted polymeric precursor into SiC with the release of free carbon. Additionally, theoretical studies have to be carried out on the interaction of SiC with ZrC. This will be specifically at the interface of ZrC and SiC.